

PURDUE UNIVERSITY
GRADUATE SCHOOL
Thesis/Dissertation Acceptance

This is to certify that the thesis/dissertation prepared

By Sameera Devsritha Wijeyakulasuriya

Entitled

Transient and Translating Gas Jet Modeling for Pressure Gain Combustion Applications.

For the degree of Doctor of Philosophy

Is approved by the final examining committee:

M. Razi Nalim

Chair

Stephen Heister

John Abraham

Likun Zhu

To the best of my knowledge and as understood by the student in the *Research Integrity and Copyright Disclaimer (Graduate School Form 20)*, this thesis/dissertation adheres to the provisions of Purdue University's "Policy on Integrity in Research" and the use of copyrighted material.

Approved by Major Professor(s): M. Razi Nalim

Approved by: David C. Anderson

Head of the Graduate Program

11/14/2011

Date

**PURDUE UNIVERSITY
GRADUATE SCHOOL**

Research Integrity and Copyright Disclaimer

Title of Thesis/Dissertation:

Transient and Translating Gas Jet Modeling for Pressure Gain Combustion Applications.

For the degree of Doctor of Philosophy

I certify that in the preparation of this thesis, I have observed the provisions of *Purdue University Executive Memorandum No. C-22*, September 6, 1991, *Policy on Integrity in Research*.*

Further, I certify that this work is free of plagiarism and all materials appearing in this thesis/dissertation have been properly quoted and attributed.

I certify that all copyrighted material incorporated into this thesis/dissertation is in compliance with the United States' copyright law and that I have received written permission from the copyright owners for my use of their work, which is beyond the scope of the law. I agree to indemnify and save harmless Purdue University from any and all claims that may be asserted or that may arise from any copyright violation.

Sameera Devsriitha Wijeyakulasuriya

Printed Name and Signature of Candidate

11/14/2011

Date (month/day/year)

*Located at http://www.purdue.edu/policies/pages/teach_res_outreach/c_22.html

TRANSIENT AND TRANSLATING GAS JET MODELING FOR PRESSURE GAIN
COMBUSTION APPLICATIONS

A Dissertation

Submitted to the Faculty

of

Purdue University

by

Sameera Devsritha Wijeyakulasuriya

In Partial Fulfillment of the

Requirements for the Degree

of

Doctor of Philosophy

December 2011

Purdue University

West Lafayette, Indiana

UMI Number: 3506196

All rights reserved

INFORMATION TO ALL USERS

The quality of this reproduction is dependent on the quality of the copy submitted.

In the unlikely event that the author did not send a complete manuscript and there are missing pages, these will be noted. Also, if material had to be removed, a note will indicate the deletion.



UMI 3506196

Copyright 2012 by ProQuest LLC.

All rights reserved. This edition of the work is protected against unauthorized copying under Title 17, United States Code.



ProQuest LLC.
789 East Eisenhower Parkway
P.O. Box 1346
Ann Arbor, MI 48106 - 1346

To my dad and mom who gave up everything to make me whom I am today

To my wife for her silent sacrifices and support

To my brother for his companionship

To my two sons for bringing joy and satisfaction to my life

ACKNOWLEDGEMENTS

This thesis is the final step of achieving a lifelong dream, not only mine, but of several others too. This journey began with the love for learning and reading I had even before I was able to read. My mum and dad did everything possible for them, to help me take each step of my life to come to where I am today. This was their dream and my mum will be the happiest mum in the world to hear the completion of my doctorate. I am not fortunate enough to tell my dad that I fulfilled his dream, did what he wanted me do, and made him proud, as he left me forever when I least expected, even without saying goodbye. Mum and dad, this is for you, the fruit of your hard work and I'm ever indebted to you for molding me, believing in me, and encouraging me. I'm also indebted to my dear wife Dinusha, for walking these 5 years with me and encouraging me day and night to walk towards my goal. Thank you for being with me, supporting me and most of all for your understanding and love.

I'd like to thank my advisor and mentor, Prof. Razi Nalim for his guidance in the last 5 years. His patience, advices, and understanding helped me immensely. I wouldn't have wished for a better mentor. Also I'd like to thank all my committee members for agreeing to be in my committee and for their valuable advices.

I'm very grateful for Rolls Royce North America for financial support for the majority of my work, and for an IUPUI fellowship and other internal funding. Finally my heartfelt gratitude goes to all my colleagues and friends at IUPUI and Purdue for their help, advices and company. Turning back I can tell without a doubt that I enjoyed my graduate life and will cherish every moment of it.

TABLE OF CONTENTS

	Page
LIST OF TABLES.....	viii
LIST OF FIGURES	ix
NOMENCLATURE	xviii
ABSTRACT.....	xxii
CHAPTER 1. INTRODUCTION.....	1
1.1 Introduction.....	1
1.2 Chapter Contents	3
CHAPTER 2. PRESSURE GAIN COMBUSTION.....	5
2.1 Pulse Combustors	8
2.2 Wave Rotor Constant Volume Combustors	10
2.2.1. Asea Brown Boveri (ABB) Test Rigs (1989 – 1994).....	12
2.2.2. Rolls Royce, IUPUI, and Purdue Test Rig (2009 – Present).....	16
2.3 Wave Rotors (Dynamic Pressure Exchanges)	26
2.4 Wave Disk Engines.....	27
2.5 Rotating Detonation Engines.....	28
CHAPTER 3. TURBULENCE MODELING OF GAS JETS.....	31
3.1 Introduction.....	31
3.2 Confined Turbulent Flow Modeling - Test Cases	36
3.2.1. Case 1- Steady Confined Co-flowing Jet.....	36
3.2.2. Case 2 – Transient Confined Multi-jet Mixing.....	43
3.2.3. Case 3 – Transient Confined Hot Gas Jet.....	47
3.3 Turbulence Modeling of Translating Gas Jets.....	51

	Page
CHAPTER 4. MOTIVATION AND CHALLENGE	54
4.1 Introduction.....	54
4.2 Mixing Processes in WRCVC	55
4.3 Mixture Stratification in WRCVC.....	57
4.4 Transient Translating Gas Jets in WRCVC	63
CHAPTER 5. IGNITION BY HOT GAS JETS.....	68
5.1 Introduction.....	68
5.2 Prior Work on Hot Gas Jet Assisted Ignition	69
5.3 Hot Gas Jet Assisted Ignition Test Rig at CPRL, IUPUI	73
5.4 Chemical Ignition Delay Time Analysis	80
5.4.1 Ethylene	84
5.4.2 Propane	88
CHAPTER 6. COMPUTATIONAL METHODS AND ACCURACY	92
6.1 Introduction.....	92
6.2 Computational Capabilities and Resources	93
6.3 Grid and Time Step Independence	96
6.4 Turbulence Model Selection.....	100
6.4.1. Zero-equation Models.....	101
6.4.2. One-equation Models.....	101
6.4.3. Two-equation Models.....	101
6.4.4. Reynolds Stress Models.....	108
6.4.5. Large Eddy Simulation Models	109
6.4.6. Direct Numerical Simulations	109
6.5 Gradual Opening and Closing of a Combustion Channel to a Port.....	112
CHAPTER 7. TRANSIENT TRANSLATING JETS IN A WRCVC.....	123
7.1 Introduction.....	123
7.2 Pilot Fuel Injection Analysis	124
7.2.1. Injector Orientation.....	126
7.2.2. Effect of Exhaust Port Closing to Subsequent Gas Injection	127
7.2.3. Effect of Jet Width and Pressure Ratio.....	131
7.3 Hot Gas Injection Analysis.....	135

	Page
7.3.1. Vortex Dynamic Dominated Mixing	136
7.3.2. Effect of Jet Momentum, Injection Pressure and Injected Gas Type	144
7.4 Jet Penetration from a Confined Traversing Hot Gas Injector	147
CHAPTER 8. EFFECT OF MIXTURE NON-UNIFORMITY ON IGNITION SUCCESS	151
8.1 Introduction.....	151
8.2 Test Cases Analyzed.....	152
8.3 One Dimensional Numerical Code.....	156
8.4 Two Dimensional Mixture Non-uniformity Analysis	159
8.4.1. Case A – Successful Combustion	159
8.4.2. Case B – Failed Combustion	169
CHAPTER 9. DESIGNING A TWO-DIMENSIONAL NOZZLE.....	177
9.1 Gas Dynamic Design of a 2D Nozzle.....	177
9.1.1. Diverging Section	178
9.1.2. Converging Section.....	179
9.2 Effect of Initial Injection Pressure Ratio	182
CHAPTER 10. HOT GAS INJECTION ANALYSIS IN 3D.....	196
10.1 Introduction.....	196
10.2 Problem Setup in 3D.....	197
10.3 The Transient Confined 3D Gas Jet.....	2066
10.4 Jet Penetration.....	211
10.5 Gas Mixing	218
CHAPTER 11. CONCLUSIONS AND RECOMMENDATIONS	2233
11.1 Conclusions.....	223
11.2 Recommendations.....	228
LIST OF REFERENCES.....	231
VITA.....	243
PUBLICATIONS.....	244

LIST OF TABLES

Table	Page
Table 2.1. A Representative Combustion Test Case of WRCVC.....	24
Table 5.1. ‘Ignition temperatures’ of different fuels (Van Dolah et al., 1965).....	72
Table 5.2. ‘Ignition temperature’ of mixture by inert hot jets, °C (hot jet flow rate = 35 cm ³ /s) (Wolfhard, 1958).....	72
Table 5.3. Ignition Delay Time Correlation Parameters.....	83
Table 5.4. Test Cases	86
Table 6.1. Cell Counts and Computational Times of the Grids used (Wijeyakulasuriya, 2009).....	97
Table 6.2. The Model Constants used in the SST k- ω Model	106
Table 7.1. Test Cases	133
Table 7.2. Test Cases	145
Table 8.1. Conditions and Configurations for Test Cases	154
Table 9.1. Initial and Boundary Conditions of Test Cases used in Numerical Computations	183
Table 10.1. Initial and Boundary Conditions.....	212

LIST OF FIGURES

Figure	Page
Figure 2.1. Simple Gas Turbine Efficiency versus Pressure Gain.....	7
Figure 2.2. Air-valved Direct Fueled Pulse Combustor	9
Figure 2.3. Wave Rotor Combustor Schematic and Developed View	11
Figure 2.4. ABB Single Combustion Channel CVC Test Rig.....	13
Figure 2.5. ABB 36 Combustion Channel, Counter Flow CVC.....	15
Figure 2.6. WRCVC Test Rig.....	16
Figure 2.7. Fuel Injectors Injecting Across the Inlet Air Flow	18
Figure 2.8. WRCVC Test Rig Instrumentation	20
Figure 2.9. WRCVC Channel Pressure Wave Analysis	21
Figure 2.10. Ion and Pressure Sensor Data of the Combustion Event	22
Figure 2.11. Repeatability of Combustion in WRCVC	23
Figure 2.12. The Total Pressure Measurements in the Exit Duct of the WRCVC	23
Figure 2.13. Experimental and Numerical Pressure Traces of Case 1.....	25
Figure 2.14. Schematic of a Four-port Dynamic Pressure Exchanger/Wave Rotor	27
Figure 2.15. Schematic of a Wave Disk Engine	28
Figure 2.16. Schematic of a Rotating Detonation Engine	30

Figure	Page
Figure 3.1. Steady Axis-symmetric Round Jet in a Co-flow	37
Figure 3.2. Grid Density Comparison.....	40
Figure 3.3. Radial Velocity Predictions at 2mm Downstream of Jet Exit	41
Figure 3.4. Radial Velocity Predictions at 70mm Downstream of Jet Exit for a Uniform Jet Inlet Velocity Profile	42
Figure 3.5. Radial Velocity Predictions at 70mm Downstream the Jet Exit for a Fully Developed Turbulent Jet Inlet Velocity Profile	42
Figure 3.6. Longitudinal Velocity Predictions.....	43
Figure 3.7. Configuration for Nitrogen & Helium Jet Mixing	44
Figure 3.8. Comparison of Experimental (PLIF) and Numerical Predictions of N ₂ Mass Fraction.....	45
Figure 3.9. Comparison of N ₂ Mole Fraction Variations at Two Locations, RB and LB in the Channel	46
Figure 3.10. Numerical Predictions and High Speed Camera Images of the Transient Jet, Generated in the Pre-Combustion Chamber Entering the Main Combustion Chamber	47
Figure 3.11. Transient Development of the Jet.....	49
Figure 3.12. Axial Jet Penetration Comparisons between Experiments and 3D URANS Simulations	50
Figure 3.13. Comparison of Jet Penetration using Injected Gas Mass Fraction Iso-surfaces	51
Figure 3.14. Translating Jet Behaving as a Wall Jet.....	52

Figure	Page
Figure 3.15. Translating Jet Behaving as a Sudden Expansion Flow	52
Figure 3.16. Translating Jet Behaving as a Wall Impinging Jet	53
Figure 4.1. Mixing Processes in a WRCVC	56
Figure 4.2. Mixing of Fuel and Air Downstream the Injection Point, in the Inlet Duct	56
Figure 4.3. Thermocouples, Pressure Transducers, and Ion Sensors Installed in the Combustion Channels 1 and 6 in the WRCVC.....	61
Figure 4.4. Temperature Measurements on the Inlet and Exit End Walls	61
Figure 4.5. Combustible Mixture Stratification in the Inlet Port.....	62
Figure 4.6. Avoiding Fuel Spillage by using Proper Mixture Stratification in the WRCVC	63
Figure 4.7. Fuel Jet Behavior of Translating and Stationary Planar Jets	67
Figure 4.8. High Speed Video Imaging of Translating and Stationary Round Jets.....	67
Figure 5.1. Limit Flame Temperatures and Hot Gas 'Ignition Temperatures' of Different Fuels	73
Figure 5.2. Single Channel WRCVC Test Rig	76
Figure 5.3. Variation of Ignition Delay Time with Pre-Chamber Equivalence Ratio	77
Figure 5.4. Variation of Ignition Delay Time with Main-Chamber Equivalence Ratios .	79
Figure 5.5. Local Chemical Ignition Delay Time Predictions for Ethylene-Air Mixtures	85
Figure 5.6. Ignition Delay Time of Ethylene for Equivalence Ratio of 1.0	87
Figure 5.7. Ignition Delay Time of Ethylene for an Equivalence Ratio of 0.6.....	90

Figure	Page
Figure 5.8. Ignition Delay Time Comparison of Ethylene	90
Figure 5.9. Prediction of Propane Ignition Delay According to the Correlation of Lamoureux et al. (2002)	91
Figure 6.1. Regions of Mixing, Diffusion, and Vorticity Requiring High Grid Resolutions	96
Figure 6.2. Locations where Axial Velocity Fluctuations are computed in a WRCVC Channel.....	98
Figure 6.3. Axial Velocity Variation with Grid Density	98
Figure 6.4. Axial Velocity Variation with Computational Time Step.....	99
Figure 6.5. Vorticity Predicted at Different Grid Densities, for $dt = 1E-06$	99
Figure 6.6. Vorticity Magnitude Contours.....	100
Figure 6.7. Comparison of Turbulence Model Predictions.....	111
Figure 6.8. Gradual Opening Time and Closing Time based on the Exit Port.....	114
Figure 6.9. Flow in a Gradually Closing WRCVC Channel.....	115
Figure 6.10. Pressure Contours of Instantaneous and Gradual Closing of a Combustion Channel.....	118
Figure 6.11. Pressure Contours of (a) Instantaneous and (b) Gradual Opening of a Channel (Larosiliere, 1993)	118
Figure 6.12. Vorticity contours of Gradual Opening and Closing Processes of a WRCVC Channel.....	119
Figure 6.13. Convection of the Deposited Vorticity along the Leading Wall	120
Figure 6.14. Gradual Opening Process	121

Figure	Page
Figure 6.15. Gradual Closing Process.....	122
Figure 7.1. Combustible Mixture Supplied from the Inlet Side not reaching the Igniter	125
Figure 7.2. Temporal Variation of Fuel Concentration with Different Injector Orientations.....	126
Figure 7.3. Schematic of the Numerical Setup to Evaluate the Effect of Preceding Exit Port to Fuel-Air Mixing by the Pilot Fuel Injector	129
Figure 7.4. Effect of Gradual Closing Process of the Exit Port on Pilot Fuel Injection.....	130
Figure 7.5. Vorticity Deposition and Convection along the Combustion Channel Leading Wall due to Exit Port Closure	131
Figure 7.6. Simulation Domain with the Pilot Fuel Injector.....	132
Figure 7.7. Fuel-air Mixing Predictions for Different Test Cases	134
Figure 7.8. Schematic of the Traveling Injector	136
Figure 7.9. Vortex Dynamic Interactions of the Translating Jet Injector	137
Figure 7.10. 3D Numerical Predictions of the Developing Vortex Structures from a Traversing Injector into a Long Combustion Channel	140
Figure 7.11. Experimental High Speed Video Images of the Developing Vortex Structures from a Traversing Injector into a Long Combustion Channel.....	141
Figure 7.12. Igniter Dimensions and Boundary Conditions	142
Figure 7.13. Vortex Formation and Interaction from a Translating Injector	143

Figure	Page
Figure 7.14. Flow Pattern shown by Injected Gas Mass Fraction during the Traverse of Injector.....	146
Figure 7.15. Axial Penetration of a Confined Traversing Jet for varying m/M.....	148
Figure 7.16. Transverse Penetration of a Confined Traversing Jet for Varying m/M	149
Figure 7.17. Interaction of Jet Exit Flow with Vortex V1	150
Figure 8.1. Different Fuel Filling Setups and One-dimensional Code Predictions for Axial Combustible Stratification	153
Figure 8.2. The Two Test Cases (A and B), Analyzed	155
Figure 8.3. One-dimensional Combustible Mixture Distribution Predictions of Cases A and B.....	158
Figure 8.4. C ₂ H ₄ (fuel) Mass Fraction of Case A.....	161
Figure 8.5. Mixing of Combustible Mixture and the Injected Gas.....	162
Figure 8.6. Modified Equivalence Ratio. Only the Cells whose Temperature is greater than 780 K is shown	163
Figure 8.7. The Mixed State of Gas with Modified Equivalence Ratios and possible Ignition Locations	165
Figure 8.8. 1D Combustion Modeling with the Inputs from the 2D Mixing Predictions for Case A	166
Figure 8.9. 1D prediction of Combustion in Case A	167
Figure 8.10. In-channel Pressure Comparisons at PT2 and PT5 for Case A	168
Figure 8.11. C ₂ H ₄ (fuel) Mass Fraction of Case B	170
Figure 8.12. The Temperature and Equivalence Ratio of the Mixed Gasses	171

Figure	Page
Figure 8.13. The Mixed State of Gas with Modified Equivalence Ratios and Possible Ignition Location for Case B	172
Figure 8.14. 1D Combustion Modeling with the Inputs from the 2D Mixing Predictions for Case B.....	173
Figure 8.15. Transient 1D Predictions of Combustion in Case B.....	174
Figure 8.16. In-channel Pressure Comparisons at PT2 and PT5 for Case B	175
Figure 9.1. Mach Number Distribution in the Injector	179
Figure 9.2. Jet Penetrations of 2D and 3D Jets	181
Figure 9.3. Boundary Condition and Problem Setup in the Computations of 2D Hot Gas Jet Injecting in to a Long Combustion Channel	184
Figure 9.4. Comparison of Axial Jet Penetration from the 2D Injector for Different Inlet Momentum Flow Rates	185
Figure 9.5. High Temperature Mixedness of Case 4	190
Figure 9.6. High Temperature Mixedness of Case 3	192
Figure 9.7. High Temperature Mixedness of Case 2	193
Figure 9.8. High Temperature Mixedness of Case 1	193
Figure 9.9. Time Evolution of the High Temperature Mixedness for Injected Gas Mass Fractions between $0.1 < Y < 0.8$	194
Figure 9.10. Time Evolution of the High Temperature Mixedness for Injected Gas Mass Fractions between $0.5 < Y < 0.9$	194
Figure 9.11. Time Evolution of the High Temperature Mixedness for Injected Gas Mass Fractions between $0.2 < Y < 0.5$	195

Figure	Page
Figure 10.1. Simulated Domain in 3D with the C-D Injector.....	198
Figure 10.2. Simulated WRCVC Domain in 3D with a Simplified Nozzle Geometry	198
Figure 10.3. 2D Representation of the Computational Domain for the Simplified Injector	199
Figure 10.4. Comparison of Jet Penetration and Jet Shape from a Stationary Round Cross Section and Square Cross Section Injector	201
Figure 10.5. Comparison of the Area Averaged Mass Flow Rates at the Injector Exits	202
Figure 10.6. Comparison of the Area Averaged Mach numbers at Injector Exits.....	202
Figure 10.7. Comparison of the Area Averaged Static Pressures at Injector Exits	203
Figure 10.8. Schematic of Transmitted and Reflected Pressure Waves depicting the Rise of Back Pressure in the Square Cross Section Injector sooner than that in the Circular One	204
Figure 10.9. Vortex Structures of Partially Opened Jet in to the Channel.....	207
Figure 10.10. Three-dimensional View of the Jet Entering the Channel.....	208
Figure 10.11. Fluid Mixing Assisted by 3D Vortices.....	209
Figure 10.12. The Development of the 3D Jet Depicted by 0.01 Iso-surface of the Injected Gas Mass.....	210
Figure 10.13. Comparison of 2D and 3D Cases in the Initial Phase of Injector Motion	213

Figure	Page
Figure 10.14. Comparison of 2D and 3D Cases in the Latter Part of Injector Motion	214
Figure 10.15. Comparison of Jet Penetration in two Orthogonal Planes in the 3D Case.....	214
Figure 10.16. Cross-channel Clearance	215
Figure 10.17. In-channel Thermocouple (TC) Data for Two Experimental Tests Compared with the 3D Axial Jet Penetration Predictions from Case 1	217
Figure 10.18. Comparison of 3D and 2D Jet Penetration from the C-D Injector	218
Figure 10.19. Level of Mixing of Injected Gas with Chamber Gas	220
Figure 10.20. Level of Mixing of Injected Gas with Chamber Gas that Resulted in High Temperature Mixtures.....	222

NOMENCLATURE

E_a	= Activation Energy
$[C_xH_y]$	= Concentration of C_xH_y
\dot{m}	= Mass flow rate
S_{ij}	= Mean Stress Tensor
$C_{\mu}, C_{\varepsilon 1}, C_{\varepsilon 2}, C_{\varepsilon 3}$	= Turbulence Model Constants
R_u	= Universal Gas Constant
2D	= Two Dimensional
3D	= Three Dimensional
Eqv_local	= Local Equivalence Ratio
Eqv_overall	= Overall Equivalence Ratio

HTM	= High Temperature Mixedness
I,IP	= Ion Probe
K	= Entrainment Constant
k	= Turbulent Kinetic Energy
LHV	= Lower Heating Value
M	= Mach Number
P	= Turbulence Production
P,PT	= Pressure Transducer
PDE	= Pulsed Detonation Engine
S	= Source Terms
t	= Time
T,TC	= Thermocouple
U, V	= Velocity
WRCVC	= Wave Rotor Constant Volume Combustor
ε	= Turbulent Dissipation

μ	= Viscosity
ρ	= Density
$\sigma_k, \sigma_\epsilon$	= Turbulence Model Constants
τ	= Ignition Delay Time
φ	= Equivalence Ratio
ω	= Specific Dissipation Rate

ABSTRACT

Wijeyakulasuriya, Sameera D. Ph.D., Purdue University, December 2011. Transient and Translating Gas Jet Modeling for Pressure Gain Combustion Applications. Major Professor: Razi Nalim. School of Mechanical Engineering.

Major mechanisms governing the mixing process of a gas injected into a long confined chamber is analyzed when there's a relative motion between the two. Such applications arise in a wave rotor combustor (WRCVC) where the moving combustion chambers receive gas from stationary injectors for fueling and ignition. Counter rotating vortices govern the mixing process in such problems, which moves across the channel enhancing mixing. The actions of vortices were seen to localize the injected gas in the vicinity of the injector end wall which can prove advantages during fueling to make a rich mixture near the ignition source and during hot gas injection for ignition to minimize the drop of temperature. The vortex structures can alter the exit conditions of the injector due to its strong near field interactions. The confinement is also important in which it suppresses the development and motion of such vortices and hence affect mixing. The thesis discusses several important features in a WRCVC. Namely, the effect of a combustion channel being opened to the preceding exit port prior to its opening to the gas injectors, on mixing of injected gas with channel gases.

This prior opening was seen to deposit vorticity on the channel wall which gets convected along them. This convecting vorticity resulted in enhanced jet penetration. The effect of combustible mixture non-uniformity on ignition success of a WRCVC was also analyzed using 2D and 1D computations. The predictions are validated against measured data from a WRCVC test rig. Ignition locations and combustion pressures were successfully predicted. Limited 3D computations of the hot gas jet mixing with the channel gases were carried out and measure temperature data from the WRCVC test rig was used to verify the axial penetration predictions of the jet. A methodology is proposed to quantify the level of mixing and ignition success by comparing the amount of injected gas inside the channel which is above a certain threshold temperature and mass fraction limits, to the total amount of injected mass trapped inside it at that particular time. Conclusions were made on the level of mixing and the ‘ignitability’ of the mixture by looking at the time variation of these defined quantities.

CHAPTER 1. INTRODUCTION.

1.1 Introduction

Turbulent passive scalar mixing takes place over a wide range of length scales. The largest length scale can be in the order of geometry length scales while the smallest be in the order of Kolmogorov length scale. At the largest length scales advection plays a decisive role in redistributing the scalar and gradient diffusion is observed, while at smallest length scales mass diffusion drives the scalar mixing. In order to accurately predict the scalar mixing process, all these length scales needs to be resolved in space and in time. This is a daunting process even for today's computers when the geometry length scales increase. This is why direct numerical simulations (DNS) are still not very common. The problem analyzed in this thesis is quite challenging to be solved using DNS due to geometry size (30" x 2.5" x 2.5"), transient mass addition, mesh motion and transonic flows, and available computational resources. Large eddy simulations would be the next to DNS in terms of accuracy of the predictions which also require substantial computational resources. The computational resources available and the expected turnover time to produce results only allowed the author to use URANS simulations. Chapter Six discusses the computational resources which were available to the author in detail.

The turnaround time for results were governed by the expectations of the industrial sponsor who sponsored this research and the time lines for set for the designing, manufacturing, testing, data analysis and reporting phases of the WRCVC test rig. This information is disclosed in expectation to better orient the reader in understanding the content of this thesis.

The originality of this thesis comes from the originality of the problem analyzed. Not often applications are found when there's relative motion between the combustion chamber and the ignition source. The only example other than the one being analyzed in this thesis which is known to the author is the rotary/wankle engine. Couple of marked differences between the rotary engine and the WRCVC is that the combustion chambers in the WRCVC are long (aspect ratio of the chambers are high) compared to the rotary engine and the use of shock waves for mixture compression in the WRCVC. A jet of hot combustion products was used as the ignition source of this combustor. Ignition by a hot gaseous jet has been analyzed by many in the past. However most of such applications were related to fire and explosion safety and hence inhibiting of ignition and combustion were focused upon. Although some knowledge existed in using such gas jets to promote ignition, a detailed analysis on the mixing process has not been carried out. This is the second contributing factor towards the originality of this work in which a detailed explanation is presented for the fluid dynamics governing the mixing of injected hot gas and chamber gases using numerical simulations. This developed methodology was used to predict ignition and combustion of the WRCVC in conjunction with other numerical codes and have shown to agree well with measured experimental data. The author could

not perform a direct verification of the predictions due to the unavailability of test results. However some experiments performed recently at the Combustion and Propulsion Research Laboratory (CPRL), Indiana University-Purdue University Indianapolis (IUPUI) on ignition of combustible mixtures using moving hot gas jets, verify the large scale structures of the jet as predicted by the simulations given in this thesis.

1.2 Chapter Contents

The thesis first introduces the notion of pressure gain combustion and discusses different ways in which it can be achieved in Chapter 2. A detailed description is provided on the WRCVC operation and performance based on the initial testing carried out in 2009. Other pressure gain devices such as pulsed combustors, pulsed detonation engines, dynamic pressure exchangers, wave disk engines and continuous detonation engines have been introduced briefly and referenced to popular work. This thesis analyses only the translating jet related issues in WRCVC.

Turbulent transient gas jet theory is reviewed briefly in Chapter 3. Since direct experimental results were not available to verify the numerical predictions of translating jets, the robustness and accuracy of the numerical code used was tested against three different jet flow problems for which experimental results were found. First a steady state jet in a co-flow was modeled for which published experimental and numerical results were available. Source terms were added in the turbulent diffusion equation to better predict the vortex stretching capability of the RANS turbulence model used. This correction was shown to improve predictions. The second and third cases used were of

transient jets. Satisfactory predictions were achieved which match the experimental data. The chapter is concluded by an introduction to the challenges of turbulence modeling of transient translating gas jets.

The motivation for the work and technical challenges faced is presented in Chapter 4. Mixing mechanisms in the WRCVC is discussed in detail followed by the need for combustible mixture stratification. The merits of mixture stratification are discussed and experimental data is presented to show how mixture stratification was achieved in the preliminary WRCVC tests. A formal introduction was given next, to the two translating gas jets found in a WRCVC. Relative importances of each are discussed. Hydrocarbon ignition delay time is discussed in Chapter 5 along with some preliminary analysis performed to predict the ignition delay times of hot gas jet ignited mixtures using empirical correlations. The computational resources available are presented in Chapter 6 along with the grid and time step independence studies carried out.

Translating gas jet analysis performed in 2D are presented in Chapter 7 while the 3D analysis is presented in Chapter 10. The effect of mixture non-uniformity near the ignition source is discussed in detail in Chapter 8 using 2D mixing predictions and 1D combustion predictions. The predictions are compared against experimental test data from the WRCVC. Due to the extremely high cost in performing 3D computations using the available resources, special emphasis was given to 2D analysis. In order to verify the applicability of the 2D results in representing the 3D problem a comparison was carried out using 2D and 3D predictions.

CHAPTER 2. PRESSURE GAIN COMBUSTION.

The scarcity and increased use of fossil fuels has been a concern all over the world for the last few decades. The adverse effects of greenhouse gasses and other emissions have added to the complexity of the problem and have increased the urge to find effective solutions. Generally continuous combustion processes generate no work output or pressure rise from the large gas expansion, resulting in loss of energy that could potentially be recovered. Industrial and home furnaces, gas turbine engines, and thermal power plants which account for the majority of fuel consumption worldwide, all significantly suffer from this energy conversion loss during the combustion processes.

Current combustion engine technologies have matured to a point where incremental improvements in performance are limited by available improvements in component efficiencies. Given the limitations of component efficiency and materials, there are fundamental thermodynamic limits on the performance of conventional gas turbine engine cycles based on the Brayton gas power cycle, i.e., those using constant-pressure heat addition processes. Alternatively, positive-displacement internal-combustion (IC) engines generate pressure-gain and increased work availability by utilizing confined intermittent combustion despite the relatively low-power density and low-piston speed limit their applicability.

Confined combustion processes have clear energy efficiency benefits and significant energy savings can be achieved from non-continuous, constant volume combustion processes. Inherently intermittent constant volume combustion combined with steady-flow compression and expansion turbomachinery can benefit from both gas turbine and IC engine operational principles. Combustion events temporarily confined in flow channels and aided by wave compression may provide a fundamental change in the gas power cycle.

Pressure gain combustion creates a rise in average total pressure at the exit of the combustor, compared to its inlet. Kentfield (1988) defines a pressure-gain combustor “as having substantially steady inflow and outflow, although nonsteady processes occur within the combustor system in order to generate a higher stagnation pressure at the outlet than at the inlet.” Pressure gain combustion can be achieved by either deflagrative or detonative combustion. Reciprocating IC engines, pulsed combustors, deflagrative WRCVCs, pulsed jets are examples of devices utilizing deflagrative pressure gain combustion. Pulsed detonation engines, rotating detonation engines, and detonative WRCVCs are examples of developed non-steady engines to achieve detonative pressure gain.

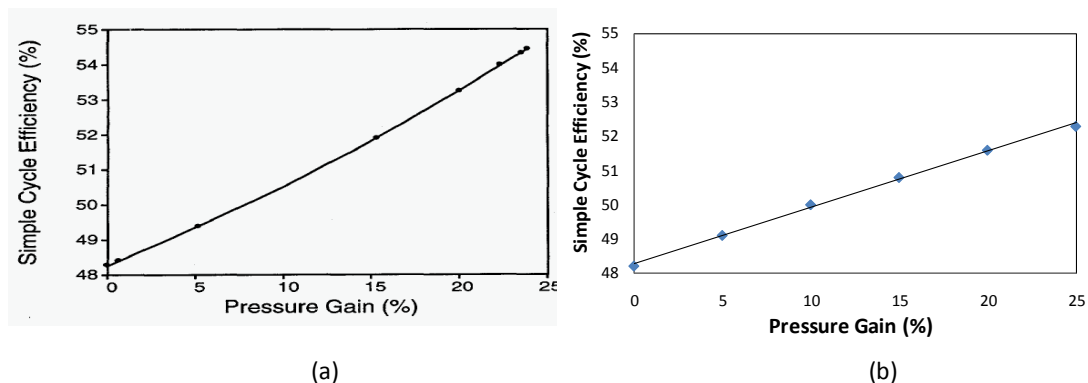


Figure 2.1. Efficiency of a simple gas turbine versus pressure gain (Figure (a) taken from Gemmen et al., 1995 and (b) calculated by the author for the same input values specified by Gemmen et al., 1995).

Compared with constant pressure combustion systems, constant volume combustion systems produce a greater available energy in the end-state gas. Figure 2.1 shows how the efficiency of a simple-cycle gas turbine can be increased with pressure gain across the combustion chamber. Here, the pressure gain is shown as percent increase from compressor exit stagnation pressure to turbine inlet stagnation pressure. The figure was based on an analysis assuming thermodynamically ideal conditions for all components and a specific heat ratio of 1.4. The compressor pressure ratio was assumed to be 10, and the temperature ratio across the combustion chamber was assumed to be 4.5. Figure 2.1 (a) shows that at the maximum pressure gain achieved (about 25%), the efficiency is more than 54% as compared to the ideal constant pressure cycle efficiency of about 48%. Hence, if the maximum pressure gain can be achieved, then a boost of nearly 6% can be obtained. Such an increase in efficiency can reduce fuel consumption by more than 12% for comparable systems (Gemmen et al., 1995).

2.1 Pulse Combustors

Pulse combustion and its application has been widely recognized, tested, and reported (Porter, 1958, Thring, 1961, Muller, 1971) and experimentally demonstrated (Kentfield & Yerneni, 1985, Kentfield & O'Blenes (1987), Kentfield & Fernandes (1990), and Kentfield, 1990) to achieve pressure-gain combustion in gas turbines. The oscillatory combustion process in the combustor can produce a stagnation pressure gain, rather than a pressure loss, associated with conventional, steady combustion. If properly utilized, this pressure gain can improve the cycle efficiency, depending on the operating conditions (Richards, et al., 1994) and lower NO_x emissions in some applications (Corliss et al., 1984). Using the same type of combustor, pulsejet engines have been used to power pilotless aircraft. For instance, the 'buzz-bomb' of WW-II was powered by a pulsejet engine.

Using analytical methods, Lampinen et al. (1992) found that the cycle efficiency of a gas turbine engine can be improved by as much as 8% in certain applications. Kentfield & Fernandes (1990) achieved a pressure gain of 4% of the gas turbine compressor delivery pressure for a mass flow rate of 0.15 kg/s. Valved pulse-jet combustors have a set of one-way valves through which the incoming air enters, illustrated in Figure 2.2. When the air-fuel mixture is ignited, the valves slam shut which means that the hot gases can only leave through the tailpipe, thus creating forward thrust and/or high pressure. Combustion is re-ignited by the interaction of fresh mixture with the hot combustion products from the previous cycle. In a valve-less (aerodynamically valved) pulse combustor, oscillating gas motion is used to sustain the combustion process. With appropriate timing of the

unsteady gas flows, the fluid motion is similar to the piston and valve assembly in an IC engine, yet without the complexity of moving parts. After confined combustion producing pressure-gain, the subsequent wave motion exhausts the combustion products, then recharges and compresses the combustor for the next cycle. A related device is the pulse detonation engine (PDE), which has achieved some prominence in military research (Roy et al., 2004).

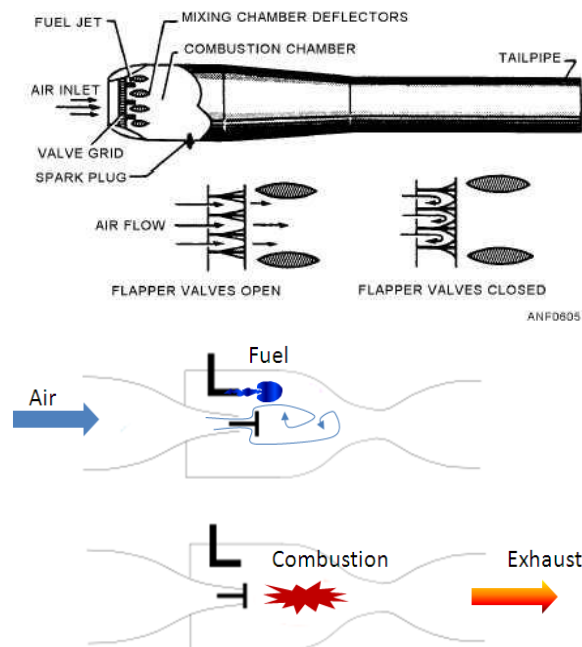


Figure 2.2. Air-valved direct fueled pulse combustor, typical layout (Top) and main phases (Bottom).

2.2 Wave Rotor Constant Volume Combustors

The Wave Rotor Constant Volume Combustor (WRCVC) exploits pressure waves to accomplish shock-wave pre-compression, constant-volume combustion, and rapid expansion of combustion gases all in one unit. It is a compact, high-flow rate pressure-gain combustor, consisting of an array of combustion channels arranged around the axis of a cylindrical drum. As schematically shown in Figure 2.3, the drum rotates between two end plates each of which has a port controlling the fluid flow through the combustion channels. The inlet port allows premixed air-fuel mixture to flow sequentially into the rotating combustion channels as they come into alignment with the port. After combustion within the rotating channels, exhaust gases are purged through the exit port. Combustion channels are periodically charged and discharged as they rotate and meet inlet and outlet ports, initiating compression and expansion waves within the WRCVC channels. Combustion in each channel is ignited either by a mounted igniter or by injected gases from a previously combusted channel. Based on design objectives, combustion modes may include premixed turbulent deflagration or detonation (Nalim, 1999).

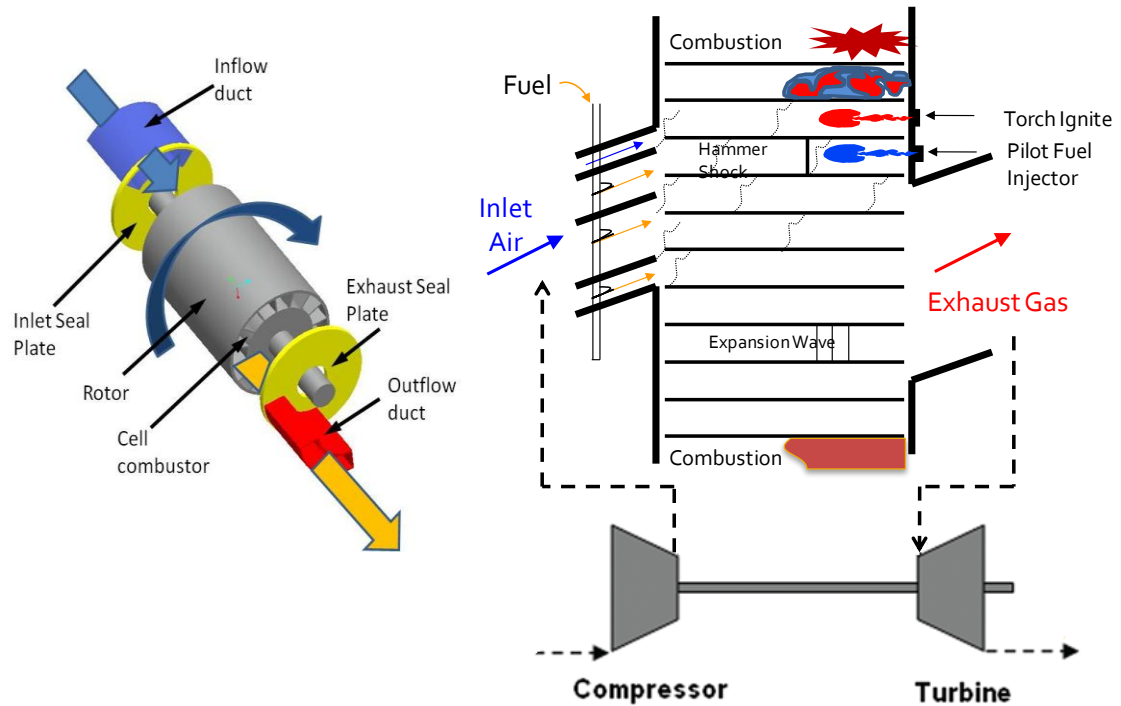


Figure 2.3. Wave Rotor Combustor Schematic and Developed View of a Typical Cycle.

Fast combustion combined with quick gas expansion would allow reduction in hot gas residence time that dominates nitrogen oxide formation. Akbari & Nalim (2006) numerically showed that the outlet flow of a detonative WRCVC is more uniform than of a comparable PDE, due to the fast rotation and large number of combustion channels. This favors turbine blades in gas turbine applications. Additionally, higher pressure gain is produced due to the mixture pre-compression by a hammer shock which does not exist in typical PDEs.

There had been only two major reported WRCVC test rigs built anywhere in the world. The first one was built and tested in the early 1990s by Asea Brown Boveri (ABB) in Zurich, Switzerland. The program was abandoned in 1994 due to lack of commercial

viability foreseen. The second test rig was built by Rolls Royce, North America in collaboration with IUPUI and Purdue University in mid 2000s. This test rig was built and tested in 2009 successfully. The program is still active. The work presented in this thesis was done in support of this test rig

2.2.1. Asea Brown Boveri (ABB) Test Rigs (1989 – 1994)

In the period of 1991 – 1992, ABB built a single-channel constant volume combustor (CVC) test rig to investigate fundamental aspects of CVC, such as conditions for reliable ignition and the level of NO_x emissions. The test rig was a stationary single combustion channel with revolving slotted disks functioning as the inlet and exit valves. The combustion channel was designed stationary to facilitate optical observation of ignition and combustion. The combustion channel was 165 mm long with cross sectional area dimensions of 15×15 mm using a quartz window on one side for optical access. Initially, ignition was initiated using three conventional automobile spark plugs placed along the bottom surface of the combustion channel. Premixed air and Propane was used as reactants. The revolving disks were rotated by an electric motor. An optimum ignition method was sought by varying parameters such as the disk rotational speed, supply pressure of the combustible mixture, and the air fuel ratio. It was later decided to employ the spark plugs only during start-up and auto-ignition by a re-circulated hot gas jet during the full operation, which would prove the test rig to be self-sustaining. Thus, a separate combustion channel as ignition source was used for ignition in the steady operation. Turbulent flame speeds of 15 – 44 m/s were observed with equivalence ratios up to 1.6 resulting in successful combustion. The maximum combustion pressure was observed at

an equivalence ratio of 0.9. A NO_x emission value of 20 ppm was measured which was attributed to short combustion durations (1- 6 ms)

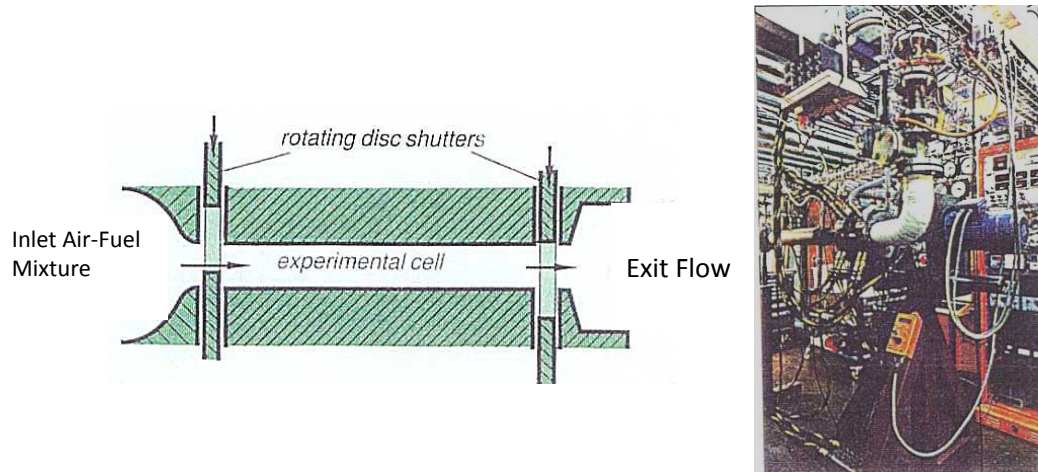


Figure 2.4. ABB Single combustion channel CVC test rig designed and tested during 1991-1992. The test rig permitted to vary the pressure and temperature of the air-fuel mixture, mixture equivalence ratio, the rotational speed of the disks which acted as ports. The quartz window facilitated optical access.

With the experience and knowledge gained from the single channel test rig, ABB designed a rotating, 36 combustion channel CVC test rig in 1991 and tests started in 1992. It was a counter flow design where the inlet and exit ports were on opposite sides of the rotor. Same combustion channel dimensions as the stationary single channel were retained, i.e. 165 mm length and 15×15 mm cross section. The rotor diameter was 200 mm and the wall thickness between two combustion channels were 2 mm. Single channel tests had shown that direct injection of fuel into the channel produced an inhomogeneous mixture and resulted in a very slow diffusion flame. Hence in the 36 cell rotating channel design, a homogeneous mixture of air-fuel was used by injecting fuel into air upstream of

the rotor plane and also by using vortex generators to enhance fuel-air mixing. Combustible mixture stratification was achieved by using four different injection nozzles. Complete scavenging of the exhaust gasses were not achieved in one single sweep (Weber, 1997). For complete scavenging two exit ports, one at high pressure and one at low pressure was used. Combustion using different kinds of fuels was investigated. A mixture of natural gas, propane, and hydrogen improved flammability. Similar to the single-channel rig, during startup spark plugs were used to ignite the mixture. There was one spark plug at each end of the combustion channel to simultaneously initiate ignition from both ends, and another pair for the second cycle.

An ignition burner using pressurized air and propane was used as an alternative to the spark plugs. These burners were mounted in the stator where the spark plugs were mounted, and injected exhaust gas into the combustion channels. However these did not give successful combustion initiation (Weber, 1997). For continuous self sustained operation, recirculated hot gas, taken at the end of the combustion zone was injected back to the combustible mixture to be ignited. Maximum combustion pressure of 9 bar recorded. Weber (1997) discusses several issues faced during experiments which had limited the attainable maximum combustion pressures. Despite relatively successful preliminary results, the management discontinued the project in 1994.

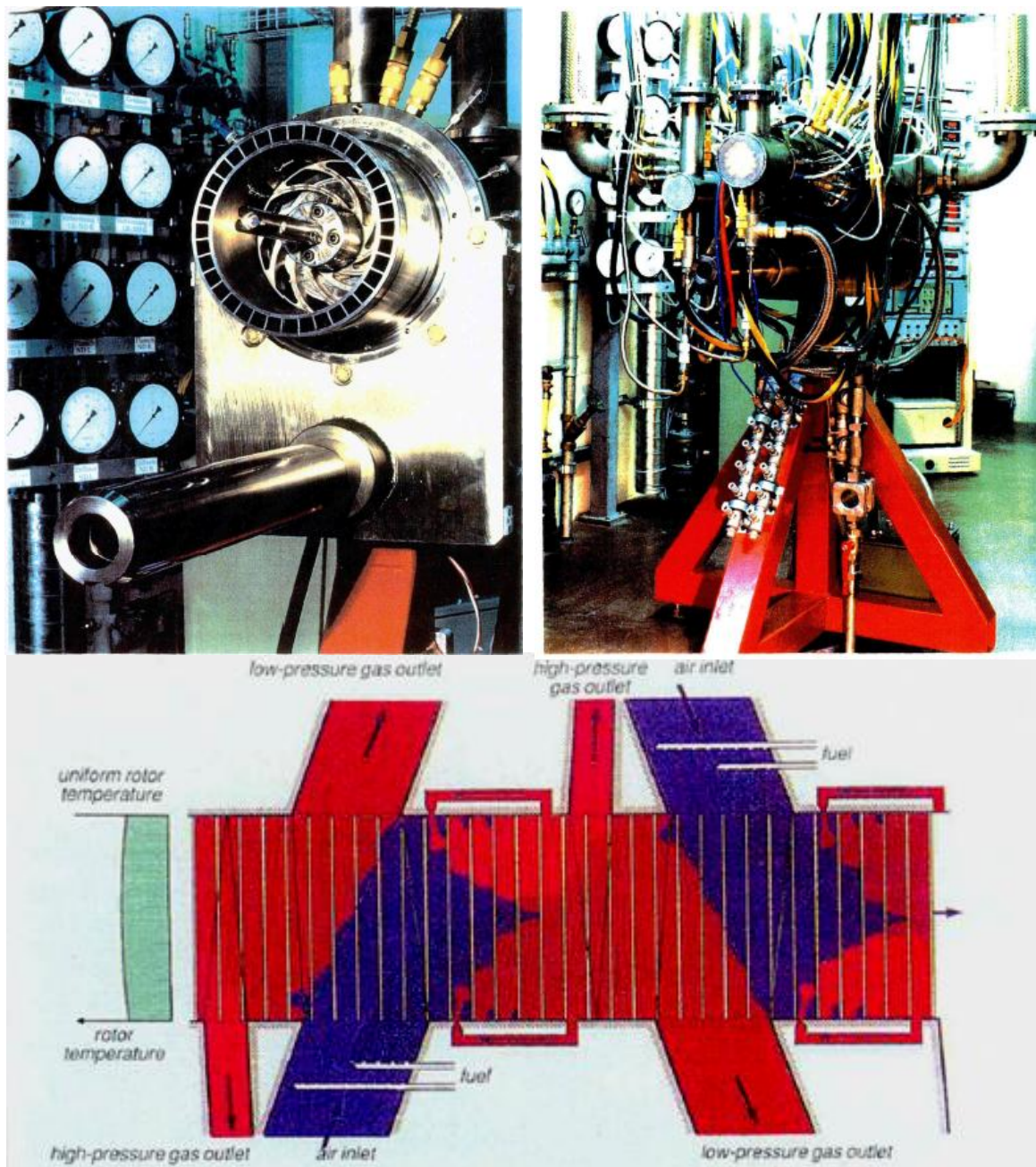


Figure 2.5. ABB 36 Combustion Channel, Counter Flow CVC (Walraven, 1994).

2.2.2. Rolls Royce, IUPUI, and Purdue Test Rig (2009 – Present)

A wave rotor constant volume combustor was designed, built and successfully tested as a collaborative work between Rolls-Royce North America, Indiana University-Purdue University Indianapolis (IUPUI), and Purdue University (Figure 2.6). Initial tests were conducted in 2009 to investigate operational characteristics of the combustor. Successful combustion was achieved at multiple test conditions enabling to assess the effects of fuel-air ratio, and the level of combustible mixture stratification on combustor performance. The viability of the concept for use in a pressure-gain engine has been demonstrated. Matsutomi et al. (2007) give details of the design of this test rig and the experimental data are presented and analyzed by Matsutomi et al. (2010), Elharis et al. (2010) and Elharis et al. (2011).

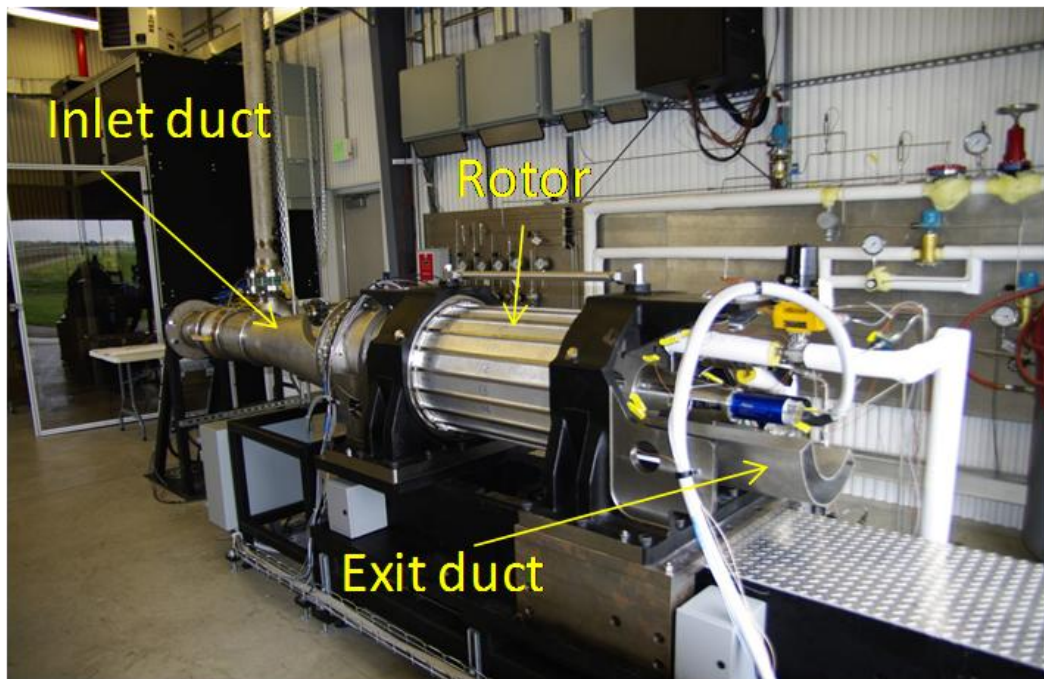


Figure 2.6. WRCVC Test Rig.

The rig included the inlet, exhaust, rotor, seal plates, ignition source, fuel injectors, and the electrical motor. The WRCVC used ethylene as the fuel due to its low ignition delay times. The test rig was run at 2100 rpm during the initial tests with mass flow rates of 9-10 lbm/sec. Experiments were run for short combustion durations (on the order of 1-3 seconds) to keep the rotor temperature within the design limit, which was demonstrated to be sufficient time to establish a repeating cycle. The inlet port was circumferentially 1040 in extent and the exit port was 1190 allowing the combustible mixture to enter and exit the combustion channels. The inlet flow was turned through inlet guide vanes to match the rotor tangential velocity. The fuel injection tubes were located on the upstream side of the inlet port. There were 15 fuel injectors in the circumferential direction (Figure 2.7).

The fuel distribution is controlled by the number and location of active fuel injectors. The injectors are designed to promote a uniform reactant mixture at the entrance to the rotor. The rotor consisted of 20 circumferentially located combustion channels, at a radius of 9 inches. The approximate size of each combustor was 2.5 x 2.5 x 31 inches. Selected combustion channels were instrumented with thermocouples, pressure transducers, and ion probes along the flow path as shown in Figure 2.8. Channels 1, 6, 11, and 16 were instrumented which were at 90° intervals. Several thermocouples and pressure transducers were installed in the inlet duct, exit duct, and on end plates as well. The exhaust duct was mounted on the opening of the seal plate. It routed the exhaust products away from the test rig and as designed did not attempt to capture work available in the exhaust gases. The exhaust was connected to ambient. A converging-diverging nozzle

was used as the torch igniter, burning propane/air which was used as the ignition source for the rig. The igniter was mounted on the exhaust end seal plate. The torch igniter was designed to operate continuously regardless of the unsteady events occurring within the WRCVC passages. The continuous operation of the igniter eliminated the need for motion synchronization with the rotor. It operates at approximately one percent of the WRCVC mass flow.

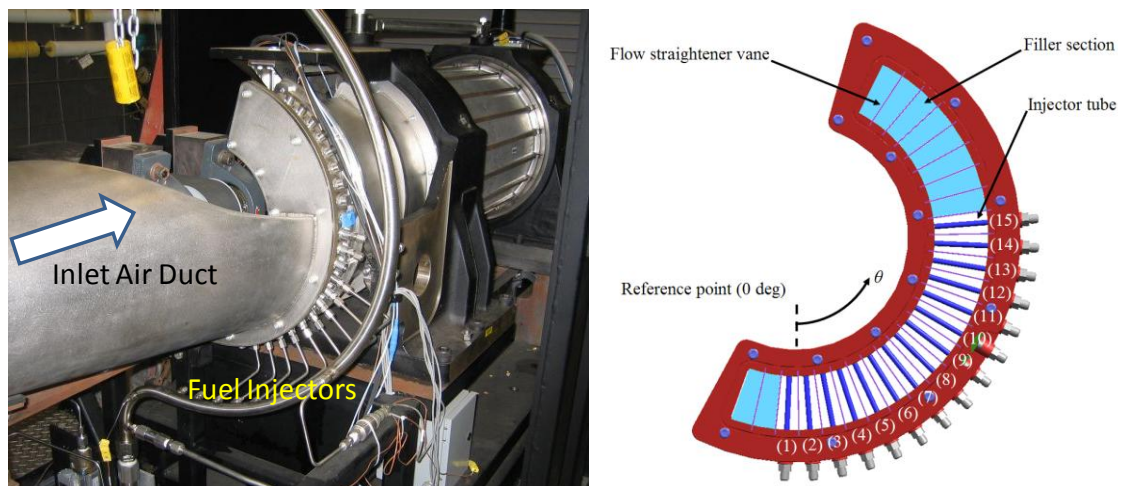


Figure 2.7. Fuel Injectors Injecting Across the Inlet Air Flow. The Injectors are placed in the Air Flow Path inside the Inlet Air Duct (right).

Figure 2.9 illustrates channel pressure variation at 7 inches away from the inlet end wall for 3 different operating conditions along with a one dimensional numerical simulation which were matched for experimental test conditions (Elharis et al., 2010). A strong expansion fan is generated (1 in Figure 2.9) upon the opening of the combustion channel into the exit port in the firing phase. It can be seen how the channel pressure goes below

the supplied pressure from the inlet when combustion takes place. This creates the pumping action of WRCVC. This affects the inlet flow rate into the test rig and since the flow rate was held constant, total pressure was seen to drop in the inlet duct. This pressure drop was an indication of the pressure gain achieved by this test rig and Matsutomi et al. (2010) reports it to be 1.5 psia for the conditions tested and with open clearances. The wave denoted by '3' is the hammer shock generated due to stopping of flow, when exit port closes. This wave is reflected off of the inlet side end wall (denoted by '4') as the inlet port is closed before this hammer shock reaches the inlet end. Under perfect flow conditions, considering only one single shock wave traveling from the exit end to the inlet end stopping the flow behind it, wave '4' should not exist. This exists because there are residual waves traveling in the combustion channel giving rise to non-zero gas velocity, even when both ends of the channel are closed. Wave '4' can be seen to reflect off of the exit end of the combustion channel as '5'. The multiple waves seen here is due to the initiation of the torch igniter which gives rise to subsequent ignition as indicated using '6' and '7'.

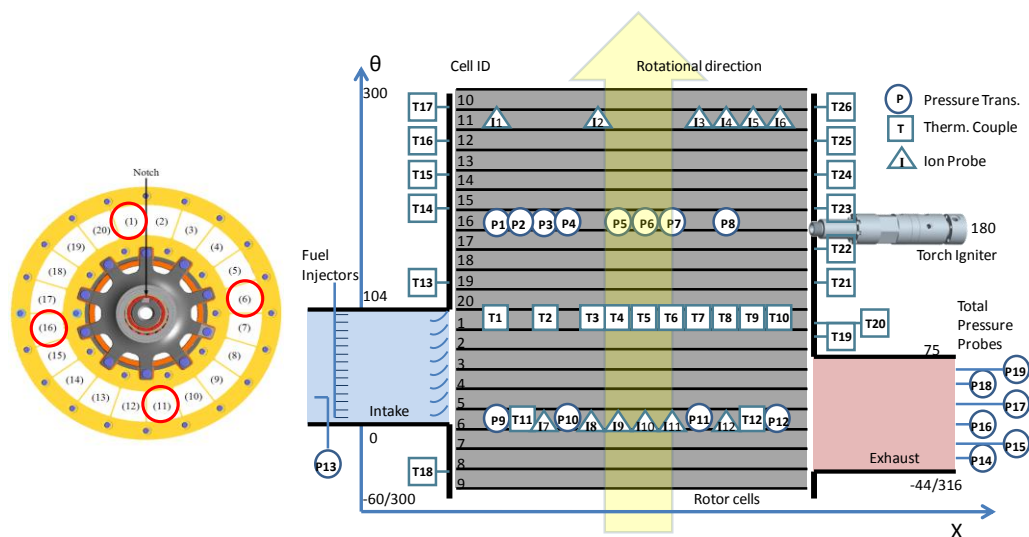


Figure 2.8. A developed view of the WRCVC test rig (right) showing the instrumentation on 4 combustion channels which are 90° apart (left).

Sustainable combustion was achieved successfully as can be seen from the high frequency (10K Hz), in-channel pressure transducers and ion sensors in Figure 2.10. High frequency pressure data from two different channels (at similar locations on the combustion channel) is shown in Figure 2.11. The repeatability of the combustion process is further illustrated from this as the pressure data from these transducers is seen to overlap precisely on one another. Ethylene was used as the fuel for all the tests and the combustion failed to occur for mixtures with overall equivalence ratio below 0.7 and local equivalence ratio 1.2. Overall equivalence ratio was calculated using the total amount of fuel and air supplied, where as local equivalence ratio only takes into account the air from the portion of the duct with active fuel injectors.

Total pressure measurements at the exit duct are shown in Figure 2.12. Total pressure probe P14 records the highest pressure while the probes in the middle of the channel records almost atmospheric pressure. Probes P18 & P19 which are towards the trailing edge of the exit duct record ~ 18 psia. An arithmetic average of the area weighted pressures gives a discharge pressure of 18 psia (Matsutomi et al., 2010). Using one dimensional numerical simulations to provide a distribution of the mass flow out of the device, the mass averaged total discharge pressure is 20 psia (Snyder et al., 2011).

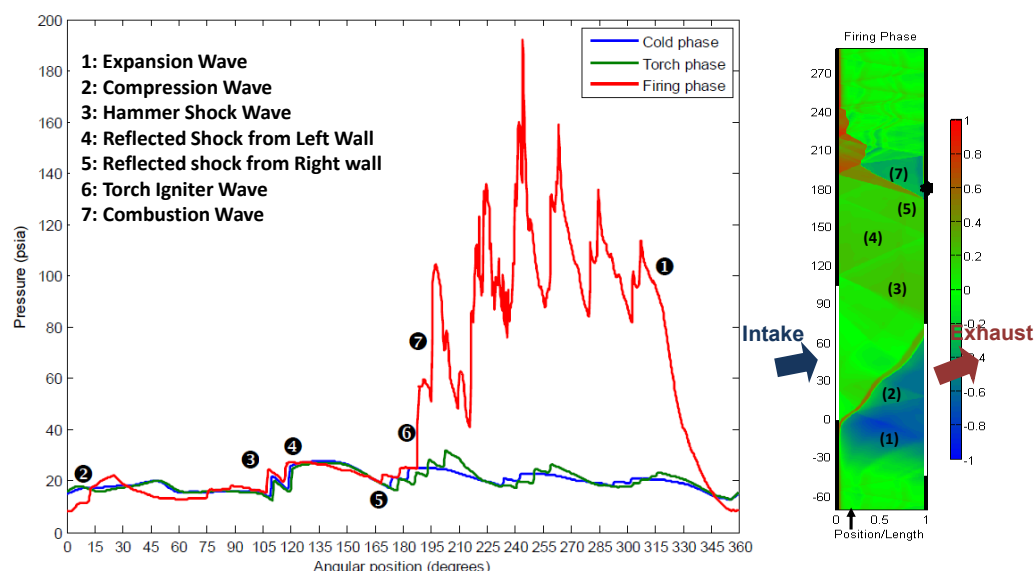


Figure 2.9. Pressure variation at a location 7 inches away from the inlet end wall (shown using the black arrow on the contour plot (right)). The numbers in the line plot (left) and on contour plot of log density (right) shows the major pressure waves of interest. The three phases shown in the line plot (left) corresponds to; Cold phase – only air was supplied through the WRCVC, Torch phase – torch igniter was turned on while the air flows through the WRCVC, Firing phase – Fuel is turned on while both the torch igniter and air flow is turned on. Combustion happens in the Firing phase.

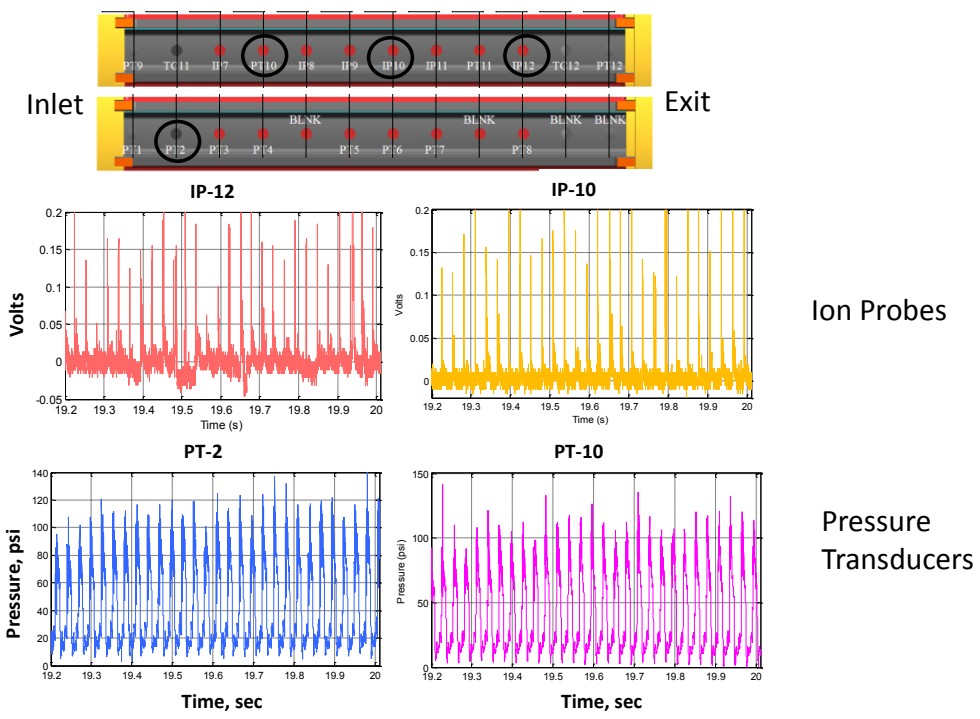


Figure 2.10. Ion and pressure sensor data showing the repeatability of the combustion event. The combustion period shown is ~0.8sec which includes 28 combustion cycles. The locations of measurement are shown highlighted in black circles (top).

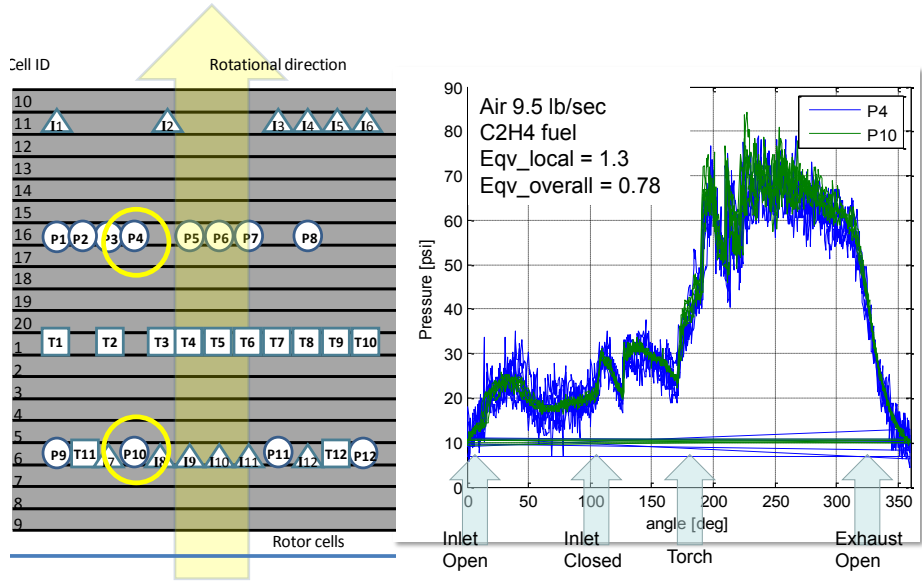


Figure 2.11. The combustion lasted for 1 second in this test. The two channels 6 and 16 are 180° apart on the rotor. (Figure taken from Matsutomi et al., 2010).

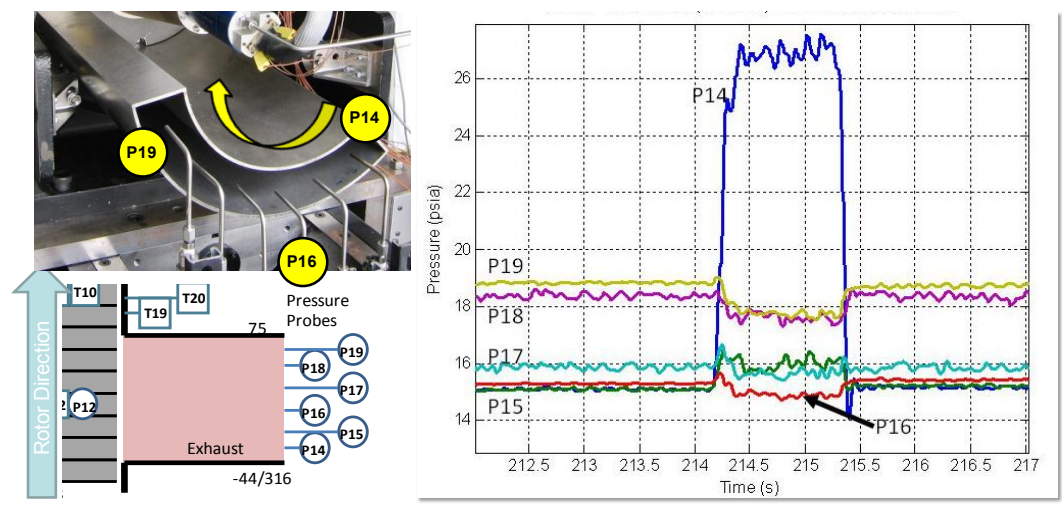


Figure 2.12. The total pressure measurements in the exit duct showing that the major variations in pressure are spatial not temporal. The area averaged total pressure at the exit is 18.1 psia showing pressure gain.

The percentage of chemical energy in fuel, used for pressure rise of the gasses in the WRCVC, is calculated next. A wide range of test cases were run using the current WRCVC (Matsutomi, et al., 2009) and one representative test case (Table 2.1) was selected to carry out this analysis.

Table 2.1. A Representative Combustion Test Case of WRCVC.

Case	Phase	Air flow	Fuel flow	Torch flow	Intake Air Pressure	Local equivalence ratio	Combustion	Combustion Duration	RPM	Fuel Injectors	Fuel Composition
		lbm/s	lbm/s	lbm/s	psia			sec			
1	Firing	9.42	0.562	0.17	20.17	1.46	Yes	1.2	2078	3 - 11	C ₂ H ₄

Case 1 given in Table 2.1 corresponds to case A in Elharis et al., 2011, where the gas dynamics and combustion performance of which are discussed in detail.

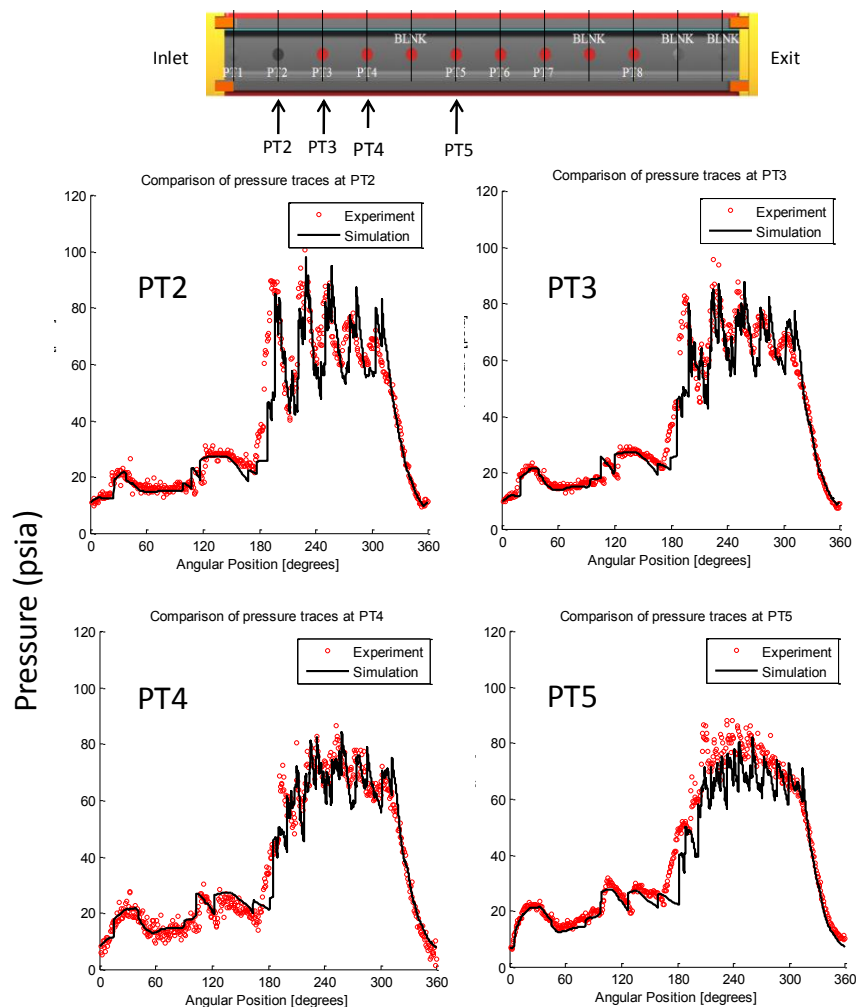


Figure 2.13. Experimental and numerical pressure traces of Case 1 along the combustion channel. The experimental pressure traces plotted were that for a single cycle to better illustrate the pressure waves (Elharis, et al., 2011).

It can be seen from Figure 2.13 (taken from Elharis, et al., 2011), that the pressure inside the combustion channel just before the exit opens (at 316°) was ~ 90 psia. Assuming this is the average pressure on the entire cycle (which is a pretty good assumption when looking at the pressure tracers in figure 2.13), the pressure rise inside the combustion channel due to combustion is ~ 60 psia (pre-combustion pressure is 30 psia). The total

volume of the combustion channel is $3.17 \times 10^{-3} \text{ m}^3$. In order to raise the pressure of this volume by 60 psia, the energy needed is 1.3 kJ. Assuming all fuel supplied from the inlet port was retained inside the channel without any spillage (as per Elharis, et al., 2011), $1.6 \times 10^{-3} \text{ kg}$ of fuel was trapped inside a single combustion channel (as per 2078 rpm, fuel supplied from injectors 3-11 and 0.562 lb/sec fuel flow rate) prior to combustion. Taking the LHV of ethylene to be 47MJ/kg, the energy released from the fuel is 60 kJ, assuming complete combustion of all fuel. The percentage of energy released from the combustion, used for pressure rise in a single combustion channel then comes out to be 2.2%.

2.3 Wave Rotors (Dynamic Pressure Exchanges)

Dynamic pressure exchangers or wave rotors use pressure waves to exchange energy between two gasses with minimal mixing between the two. Wave rotors operating under a variety of wave cycles have been successfully used for different applications such as the Compres® automotive diesel engine supercharger (Berchtold, 1985), and the ‘wave superheater’ - a unique high-enthalpy continuous-flow wind tunnel for studying atmosphere re-entry aerodynamics (Rose, 1979). A comprehensive review on the wave rotors is reported by Akbari et al. (2004). Figure 2.14 is a schematic of a four-port dynamic pressure exchanger integrated with an external combustion chamber. Despite the pressure loss in the combustor, the turbine inlet stagnation pressure can still be more than the compressor exit pressure placing the dynamic pressure exchange in the category of pressure gain devices. Snyder (1996) predicted that the wave-rotor-topped Allison 250-C30 turbo shaft engine can produce 11.4% more shaft horsepower (+20% specific power)

with a 22% decrease in engine SFC at a 100% power setting (at 1930⁰F turbine inlet temperature).

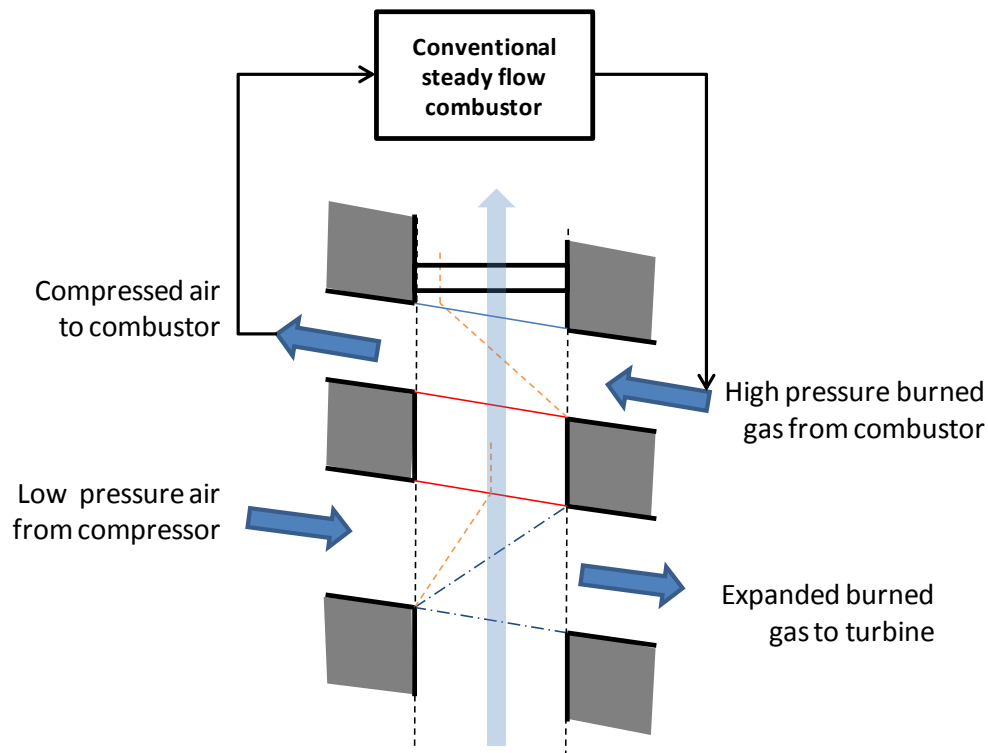


Figure 2.14. Schematic of a four-port Dynamic Pressure Exchanger/Wave Rotor.

2.4 Wave Disk Engines

The Wave Disk Engine (WDE) is a WRCVC with radial combustion channels. It takes advantage of centrifugal forces to improve the compression process and flow scavenging. Curved channels of the WDE further can allow direct work extraction due to change in angular momentum of the exiting flow. Fresh fuel-air mixture enters from the inner radius and mixes rapidly with hot residual gas from previous combustion (Figure 2.15). In contrast to the axial-flow WRCVC, the radial inflow and centrifugal motion of denser

fresh mixture can aid rapid mixing in the flow direction. The combusted products leave as a jet with both radial and tangential momentum, imparting a reaction force that spins the rotor and generates work output. Piechna et al. (2004), and Akbari et al., (2008) provide further details on this concept.

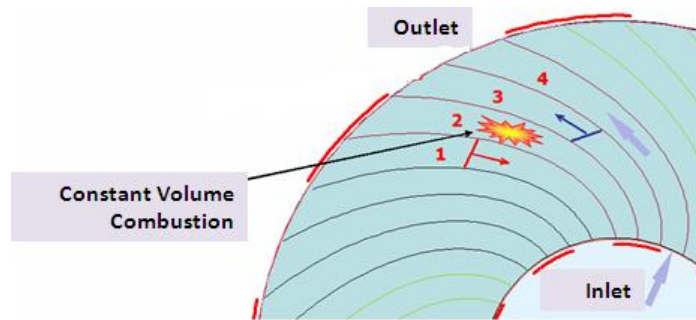


Figure 2.15. Schematic of a Wave Disk Engine
 (1) Hot burnt gas moving towards the inner radius. (2) Combustion. (3) Fresh combustible mixture moving towards the outer radius.

2.5 Rotating Detonation Engines

In the past, the focus of detonation research has primarily been on pulsed detonation engines (PDEs). Recently, however, detonation research has begun to also focus on rotating, or continuous, detonation engines (RDEs). Since RDEs do not need long exhaust tubes, RDEs can be shorter than equivalent PDEs (Russo, 2011). Also, RDEs could work more efficiently with a turbine since the exhaust from the RDE would provide the turbine a continuous stream instead of a series of pulses. The Rotating Detonation Engine (RDE) represents a new method of detonation-based engines. It provides the thermodynamic advantages of detonation-based combustion with nearly constant thrust and a simpler overall design (Lim, 2010). RDE has the potential to be employed in a wide range of platforms such as missiles, fighter aircraft and unmanned

aerial vehicles (Lim, 2010). The RDE relies on a detonation mode of combustion similar to what is used on the Pulse Detonation Engine (PDE).

A rotating detonation engine is a relatively simple mechanical device that feeds propellants axially into an annular combustion chamber. The basic idea behind the RDE is the generation of a detonation wave that rotates around an annular combustion chamber formed by two concentric cylinders, producing thrust that is nearly continuous as combustion products are expelled out of the RDE. The detonation wave propagates around the annulus of the combustion chamber near the propellant injector holes (Figure 2.16). The detonation wave does not exit the RDE as it would in a PDE. The detonation products flow axially downstream in the combustion chamber, following the bulk flow, and exit the open end of the combustion chamber. Unlike a PDE, RDEs have no check valve to ensure there is no back flow into the feed lines. Therefore, the propellant feed pressure must be high enough to prevent any hot detonation products from flowing back into the propellant lines. Additionally, the propellant feed pressure needs to be large enough to reestablish flow into the combustion chamber after the detonation wave has passed. The final restriction on the propellant feed pressure is that it must be high enough such that an adequate amount of combustible mixture has refilled the combustion chamber by the time the detonation wave has completed one revolution of the annulus.

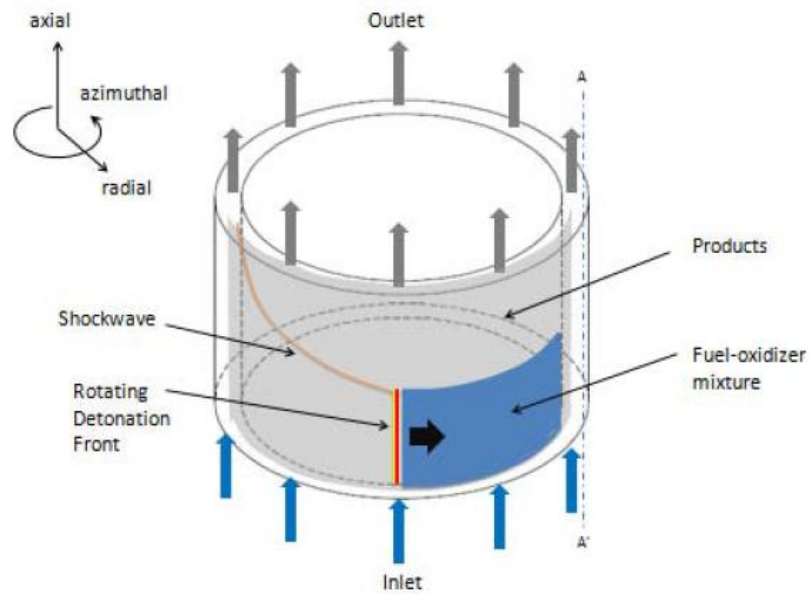


Figure 2.16. Schematic of a Rotating Detonation Engine (Lim, 2010).

The process is initiated by injecting a combustible mixture via the inlets into the chamber. Once the chamber is sufficiently filled, a detonation wave initiator will send a detonation wave tangentially into the mixture. A high-pressure deflagration wave then propagates for a short distance and forms a rotating detonation wave. The rotating detonation wave will continuously propagate at the CJ velocity. The detonation wave will be continually supplied with freshly injected combustible mixture. The products and oblique shock waves will exit from the outlet. Thrust is generated by the acceleration of the combustion products.

CHAPTER 3. TURBULENCE MODELING OF GAS JETS.

3.1 Introduction

The turbulent free jet has been analyzed extensively in the past using analytical (Fanil and Dash, 1983), experimental (Townsend, 1956, Hinz, 1959, Schlichting, 1958), and numerical (Kawanabe, et al., 2007) approaches. The behavior of the jet in terms of its mean and fluctuating velocities, temperatures and concentrations of chemical species have been studied using the above approaches. The problem of a jet flow in the presence of confining walls is also studied in the past, although may not be up to the extent of a free jet. The two-dimensional, or plane, jet immersed in a secondary stream of approximately uniform and constant velocity has been studied experimentally by Weinstein, Osterle & Forstall (1956). His results, for various ratios of secondary and jet velocities, have been shown by Spalding (1958) to be essentially functions of a single independent variable. Ferguson (1949) has measured the mean velocity field of a two-dimensional jet immersed in a duct. Curtet (1958) has also reported measurements for this case, and Craya & Curtet (1955) have developed a method of calculating the flow field assuming the external stream to be a potential flow.

Experimental data on the axisymmetric jet in an external stream of approximately constant velocity have been provided by Forstall & Shapiro (1950), Landis & Shapiro (1951) and Pabst (1944). Using Prandtl's mixing length theory, Squire & Trouncer (1944) and Szablewski (1946) have developed momentum integral equations with which to calculate the flow field. Considerable data has been provided by Hembold, Luessen & Heinrich (1954) and Becker, Hottel & Williams (1962) for confined axisymmetric flows on which the walls exert a dominating influence. Arcoumanis et al. (1988) analyzed the penetration of high density transient jets injected into quiescent chamber containing air at atmospheric temperature and various pressures has been measured by using laser beam deflection. They showed that the jet penetration increased with jet to chamber density ratio and decreased with chamber pressure.

It is important to understand and determine the entrainment of surrounding gas into the injected gas jet in many applications. In the current WRCVC (Matsutomi, et al., 2010), the primary fuel is injected into the main air flow and is expected to mix well, before it enters the combustion chambers (Wijeyakulasuriya, and Nalim, 2008). The pilot fuel injected just before the igniter is expected to mix well with the combustion chamber gas to make a locally rich combustible mixture near the igniter. The injected hot gas jet used as the igniter is expected to increase the temperature of the combustible mixture in the channels without diluting it much. All these different processes have different requirements on mixing and hence on the amount of gas entrained. Direct injected IC engines (gasoline and diesel) are some other applications where the surrounding gas entrainment into the transient jets is of importance. Several works can be found in the

open literature on the determination of entrainment in steady free gas jets. Ricou and Spalding (1961) measured the mass entrainment rate in gas jets as a function of axial distance and the ratio of injected gas density to the surrounding gas density, using a porous cylinder and estimating the mass flux into it as a function of axial distance. They came up with the following equation which expresses the normalized entrained mass flux in terms of the normalized axial distance:

$$\frac{\dot{m}(x) - \dot{m}_i}{\dot{m}_i} = K \left(\frac{x}{d} \right) \left(\frac{\rho_a}{\rho_i} \right)^{1/2}, \quad (3.1)$$

where K is the entrainment constant whose value was equal to 0.32 according to Ricou and Spalding (1961). However Abraham (1996) found that this measured entrainment constant can vary in the range of 0.2 to 0.457 in the far field of steady gas jets. Crow and Champagne (1971) showed that the entrainment in the near field is less than in the far field of a steady, free gas jet. Hill et al. (1972) also showed experimentally that the entrainment is less in the near field than the far field, and the value of the entrainment constant increases with axial distance in the near field. This increase of entrainment constant with the axial distance in the near field, was confirmed by Wall et al., (1980). Song and Abraham (2003) present mathematical equations for entrainment for transient round, radial, and wall impinging jets. They (Song and Abraham, 2003) further compared the entrainment characteristics of these three types of jets and found that the radial jet penetrates less but entrains more mass than the round jet. The wall impinging jet, approximated as a half-radial jet was found to penetrate less and entrain more mass than

the round jet. It can be seen from Equation (3.1), the amount of gas entrained increases with the increase of surrounding gas density. In a WRCVC, the hot gas jet is injected into the combustion channel, after the hammer shock has compressed it. Hence the density of the combustion channel gas is higher than that of ambient gas which results in higher gas entrainment into the hot gas jet.

The standard k- ϵ turbulence model calculates the velocity field of a two-dimensional plane jet quite accurately, but large errors occur for axisymmetric jets (Pope, 1978), with spreading rate overestimated by about 40%. Experimental data indicate that the round jet spreads about 15% less rapidly than the plane jet; yet, its calculated spreading rate using k- ϵ model is 15% greater. Pope (1978) attributed this discrepancy to ring vortex stretching in axisymmetric jets by the action of strain rate produced by the velocity gradients. The vorticity of the large turbulent motions tends to be aligned with the mean-flow vorticity in the mean flow, and is stretched with it, leading to greater scale reduction, greater dissipation, less kinetic energy, and so to a lower effective viscosity, and incorrect spreading rates of axisymmetric jets. Pope proposed a modification to the diffusion equation in the standard k- ϵ model, to capture vortex stretching phenomena in flows such as round jets and radial jets. Using this modification, Rubel (1985) calculates the growth rate of a round jet to be 28% less than that predicted from the standard k- ϵ model, and very good agreement with experiments is shown for round jets (Rodi, 1972), but not so well for radial jets experiments (Tanaka, 1976 & Witze, 1976).

The standard k - ϵ turbulent model also works poorly for complex turbulent shear layers, such as flows subjected to curvature and rotation. Cheng (1990) described how the streamline curvature alters the turbulent structure. Cheng & Farokhi (1992) proposed a modification to the standard k - ϵ model by incorporating an extra rate of strain to calculate the eddy viscosity, using the Jones-Launder length-scale model and Prandtl-Kolmogorov formula. The high Reynolds number k - ϵ model, used in this analysis (see Equations 7.1 and 7.2) incorporates compressible effects in the turbulent diffusion equation (Tahry, 1983). However, this model does not take into account the effects of streamline curvature or vortex stretching.

The RANS turbulent models usually require wall functions to model the flow within the boundary layer where the molecular and turbulent effects are comparable in magnitude. The widely used standard wall functions assume that the flow property variations are predominantly one dimensional and normal to the wall, negligible pressure gradients and body forces inside the layer, shear stresses and velocity vectors are aligned inside the layer, balance of turbulent production and dissipation and linear variation of turbulent length scales. A “non-equilibrium wall function” can also be used, where the assumption of negligible pressure gradients inside the layer is relaxed. This type of a formulation might be important in modeling a propagating shock wave through an already established flow (and hence a boundary layer).

3.2 Confined Turbulent Flow Modeling - Test Cases

Three test cases were selected to model using the same numerical code used in this thesis, to verify its applicability and the quality of its predictions in modeling confined shear flows, by comparing against measured test data. First, a co-flowing steady, confined air jet is modeled using modifications to the RANS turbulence models. This is relatively a simple shear flow problem involving the development of the shear layer between the jet and the co-flowing air. The second case was a transient 2D multiple confined jet mixing problem which involves multiple shear layer development and gas mixing. Finally a transient hot gas jet used for igniting a combustible mixture is used to model the development of this high temperature jet in a confined volume. Measured jet penetration until the combustion was initiated was used to verify the non-reacting flow numerical predictions.

3.2.1. Case 1- Steady Confined Co-flowing Jet

The first representative problem was analyzed (Bouzada et al., 2010) to evaluate the applicability and limitations of the RANS models for a confined shear flow. The case selected was an air jet interacting with a co-flowing air stream inside a confined chamber (Figure 3.1, not to scale). The radial and longitudinal profiles of axial velocity were compared against the measured experimental data.

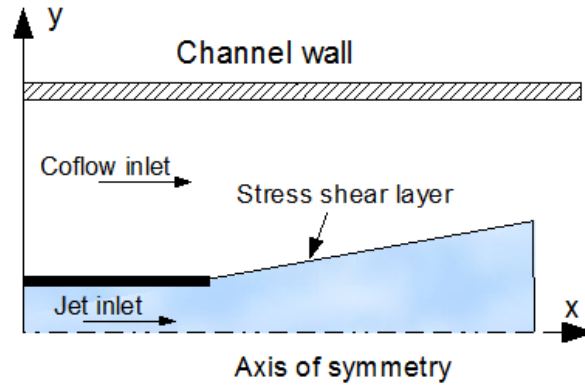


Figure 3.1. Steady Axis-symmetric Round Jet in a Co-flow (Pagè, 1998).

In this analysis, the vortex stretching correction for the turbulent diffusion equation was used to improve the predictions. Pope(1978) corrects for vortex stretching by adding a term in the right hand-side of the transportation equation for the dissipation rate (Equation 3.2):

$$\frac{D\varepsilon}{Dt} = \frac{\partial}{\partial x} \left(\frac{\mu_{eff}}{\sigma_\varepsilon} \right) \frac{\partial \varepsilon}{\partial x_i} + \frac{\varepsilon^2}{k} \left(C_{\varepsilon 1} \frac{P}{\varepsilon} - C_{\varepsilon 2} + C_{\varepsilon 3} \chi \right), \quad (3.2)$$

where

$$\chi = \frac{1}{4} \left(\frac{k}{\varepsilon} \right)^3 \left(\frac{\partial U_i}{\partial x_j} - \frac{\partial U_j}{\partial x_i} \right)^2 \frac{U_j}{x_j}. \quad (3.3)$$

A linearized form of the source terms was implemented in this analysis for greater numerical stability. This correction term (χ) in the dissipation equation (Equation 3.3) gives rise to numerical convergence issues, and hence many (Davidenko, 2005) have used a limiter to achieve convergence (Equation 3.4):

$$\chi \Rightarrow \text{sign}(\chi) \cdot \min(|\chi|, \chi_{lim}). \quad (3.4)$$

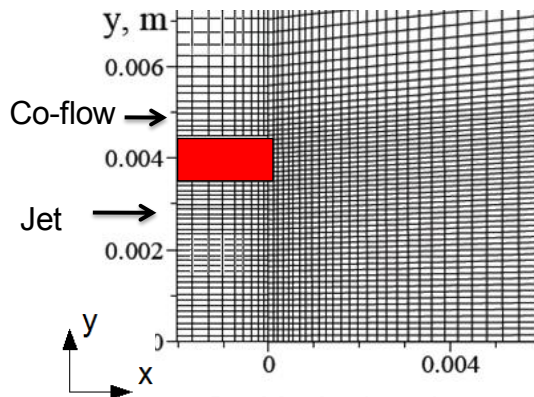
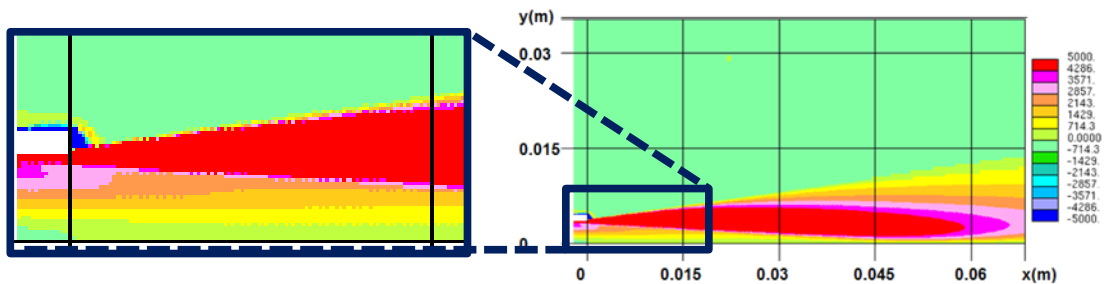
The linearization of the three source terms are performed as follows:

$$\begin{aligned}
 S &= S1P - S2P \times \varepsilon, \\
 S1P &= C_{\mu} C_{\varepsilon 1} \rho k P, \\
 S2P &= C_{\varepsilon 2} \rho \frac{\varepsilon}{k} \frac{1}{4} \rho C_{\varepsilon 3} \left(\frac{\partial U_i}{\partial x_j} - \frac{\partial U_j}{\partial x_i} \right)^2 \frac{U_j}{x_j} \frac{k^2}{\varepsilon^2}.
 \end{aligned} \tag{3.5}$$

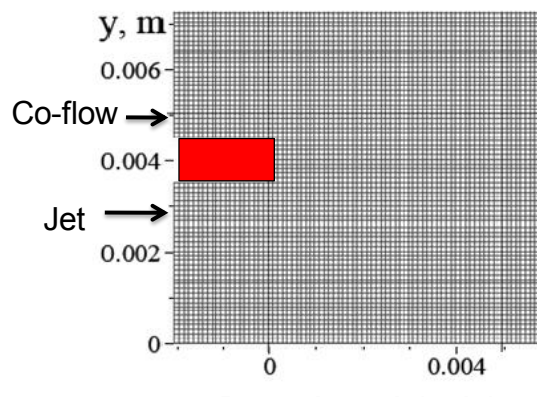
As shown in Equation 3.5, S represents the source terms in the turbulent dissipation equation. $S1P$ is the constant term and $S2P$ is the linear term with respect to ε . A subroutine was written to add the correction term into the turbulent diffusion equation as shown in Equation 3.5. Davidenko (2005) presents an excellent description of this limiting vortex stretching formulation, along with a comparison of different limiters. The method proposed by Davidenko(2005) to limit the vortex stretching correction is adopted in the current analysis with more careful grid generation in regions with high shear stress gradients.

With a turbulent inlet velocity profile specification, it was found that the model predictions for the radial velocity, agreed well with the experimental results at 2 mm downstream the injector (Figure 3.3). The current analysis is done on a much refined mesh than the one used by Davidenko (2005) (Figure 3.2), which has resulted in better predictions as can be seen in Figure 3.3. Figures 3.4 & 3.5 show the radial velocity at a further downstream centerline location (70 mm from injector exit) with uniform and fully developed turbulent inlet velocity profiles respectively. For the uniform velocity profile, the predictions from the high Reynolds number k - ε model used, matches very well with the experimental data than other models considered (Figure 3.4). However away from the

centerline, the model predictions are more comparable for the same problem. The standard $k-\varepsilon$ model with limited Pope correction ($\chi_{lim}=0.143$) shows very good agreement to the experimental results of centerline axial velocity (Figure 3.6). However, this model shows a slight over prediction of axial velocity beyond ~ 180 mm, in which regions the SST $k-\omega$ (Menter, 1994) and the high Reynolds number $k-\varepsilon$ (Tahry, 1983) models showed good agreement with experimental data (Figure 3.6). The Standard $k-\varepsilon$ model with limited Pope correction ($\chi_{lim}=0.143$) can be seen superior in predicting the radial flow in the case of a turbulent inlet velocity profile, compared to other turbulence models used.



Davidenko (2005)



Bouzada et al. (2010)

	Davidenko [2005]	Bouzada et al. (2010)
Total number of cells	15,600	295,000
Min cell size (mm)	0.1	0.1
Max cell size (mm)	13.2	2
Cells across injector	30	35

Figure 3.2. Grid Density near Injector, where the Vorticity Gradients are high.

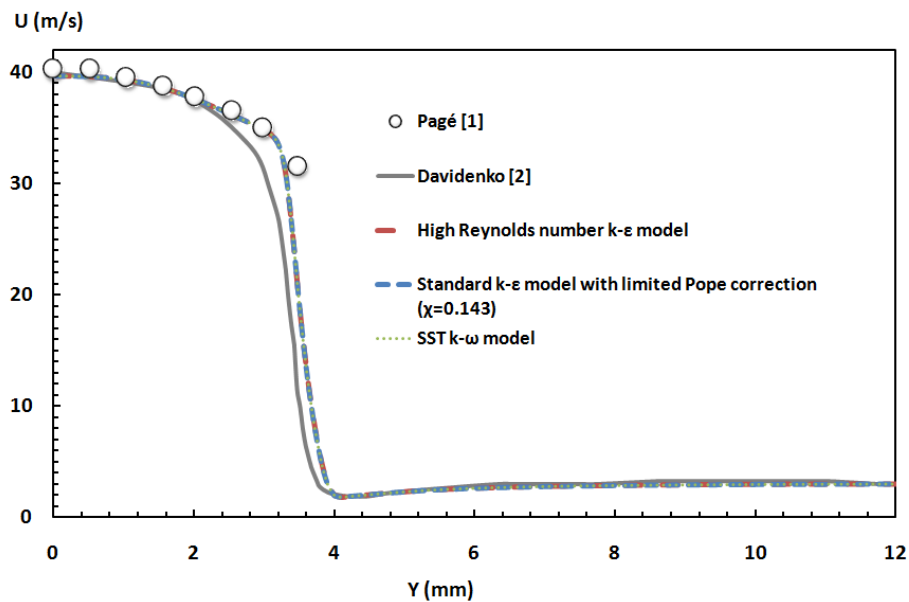


Figure 3.3. Radial Velocity Profile Predictions using Different RANS Models, at 2mm Downstream of Jet Exit for a Fully Developed Turbulent Jet Inlet Velocity Profile, compared with Experimental Data (experimental data was unavailable beyond ~ 3.5 mm) (Bouzada, 2010).

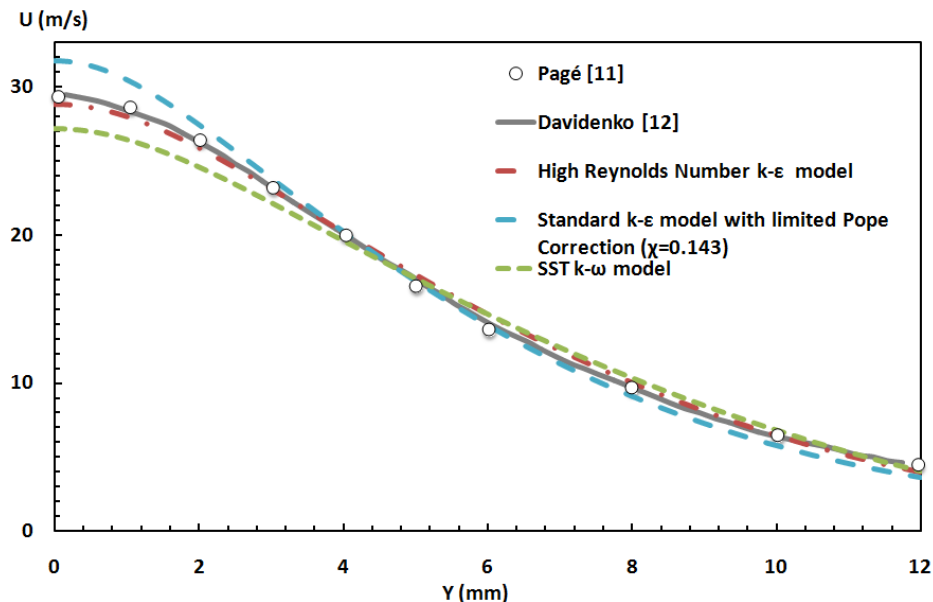


Figure 3.4. Radial Velocity Distribution Predictions using Different RANS Models, at 70mm Downstream of Jet Exit for a Uniform Jet Inlet Velocity Profile compared with Experimental Data (Bouzada, 2010).

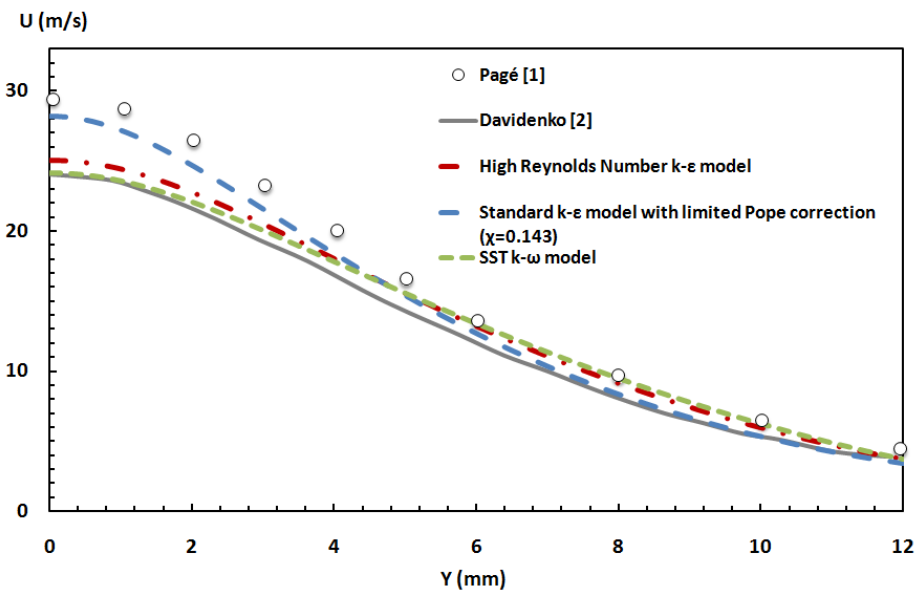


Figure 3.5. Radial Velocity Distribution Predictions using Different RANS Models at 70mm Downstream the Jet Exit for a Fully Developed Turbulent Jet Inlet Velocity Profile compared with Experimental Data (Bouzada, 2010).

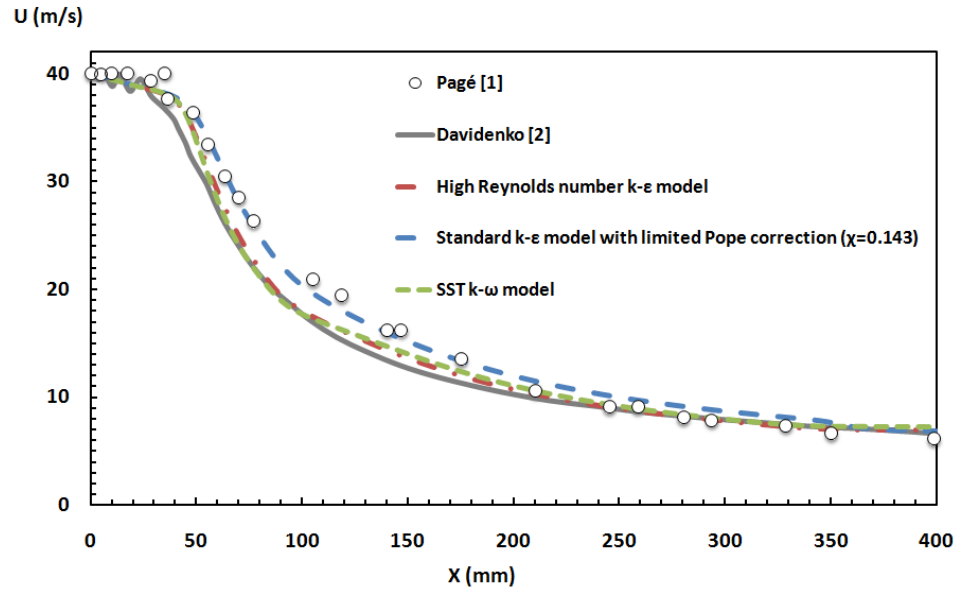


Figure 3.6. Longitudinal Velocity Distribution Predictions using Different RANS Models, on the Jet Axis ($Y=0$ mm) for a Fully Developed Turbulent Jet Inlet Velocity Profile, compared with Experimental Data (Bouzada, et al., 2010).

3.2.2. Case 2 – Transient Confined Multi-jet Mixing

The second type of confined shear flow investigated is the mixing of two gaseous jets of different compositions inside a confined channel. This was experimentally and numerically investigated by Tseng et al., (2009). The problem was set up two-dimensionally and solved using a time accurate implicit solver. The two gases being injected are nitrogen and helium, while the chamber is initially filled with nitrogen. The experimental setup was arranged horizontally with a nitrogen inlet in the center, while two helium jets flowed on either sides of it (Figure 3.7). Initially, the chamber was filled with nitrogen, under atmospheric conditions; nitrogen is injected first into the chamber, followed by the injection of helium. The experimental results show that the fluid behavior

is not symmetrical although the geometry is symmetrical: the nitrogen jet deviates from the centerline toward the top confining walls (Figure 3). In the experiment (Tseng, 2009), the time-dependent nitrogen mole fraction was measured at four downstream locations from the jet exit plane which are used for comparison with numerical results.

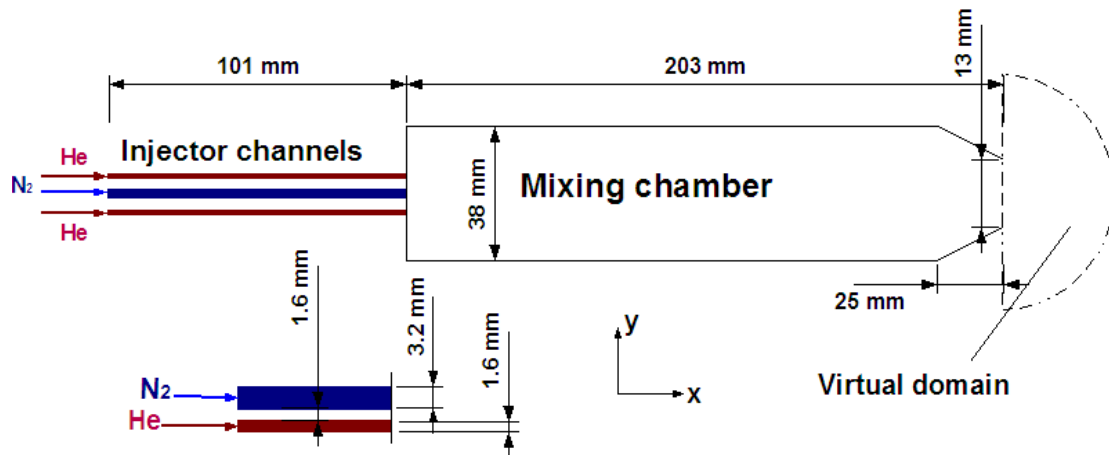


Figure 3.7. Configuration for Nitrogen & Helium Jet Mixing (Reproduced from Tseng et al.,2009).

The results presented here are using a preliminary coarse grid. An extra semi-circular domain was added at the end of the computational domain to allow for pressure variations at the exit of the channel. In order to correctly predict the fluctuations seen in the experiments, a much finer grid is required. This is left as future work.

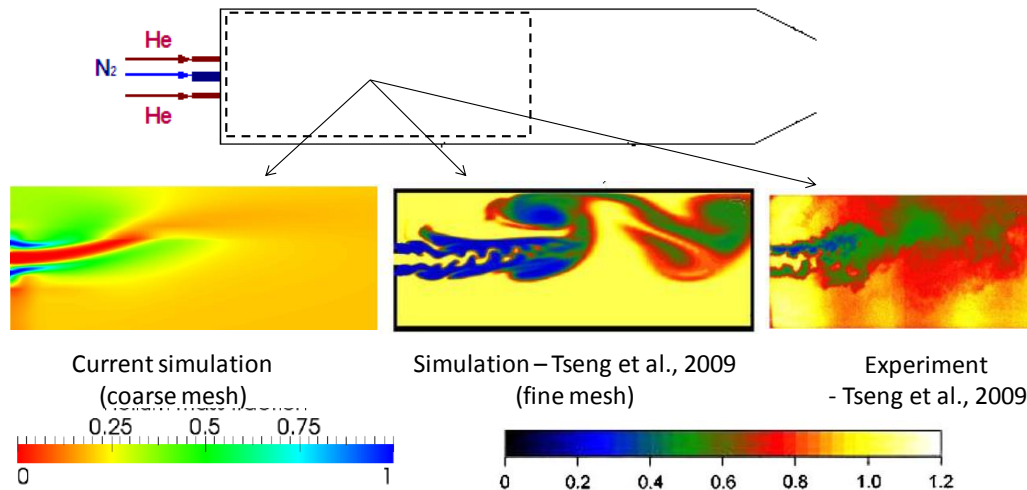


Figure 3.8. Comparison of Experimental (PLIF) Mass Fraction of N_2 and Numerical Predictions of N_2 .

It can be seen from Figure 3.8 that the coarse mesh used in the current simulation did not capture small scale vortices and their behavior. However, the large scale behavior (the asymmetry of the jet) was captured in this simulation. This asymmetric jet behavior was seen by many (De Zilwa et al., 2000, Sheen et al., 1997, Fearn, et al., 1990, Patel and Drikakis, 2003, Drikakis, 1996) in sudden expansion flows and was attributed to unstable flow bifurcation occurring beyond a certain critical flow Reynolds number at jet exit. It can be seen from Figure 3.9 that the coarse mesh predictions are able to capture the trends of N_2 mole fraction variations. Although the numerical simulations of Tseng et al., (2009) was using a finer computational mesh than the one used in the current analysis, the predictions of which do not match the experiments well.

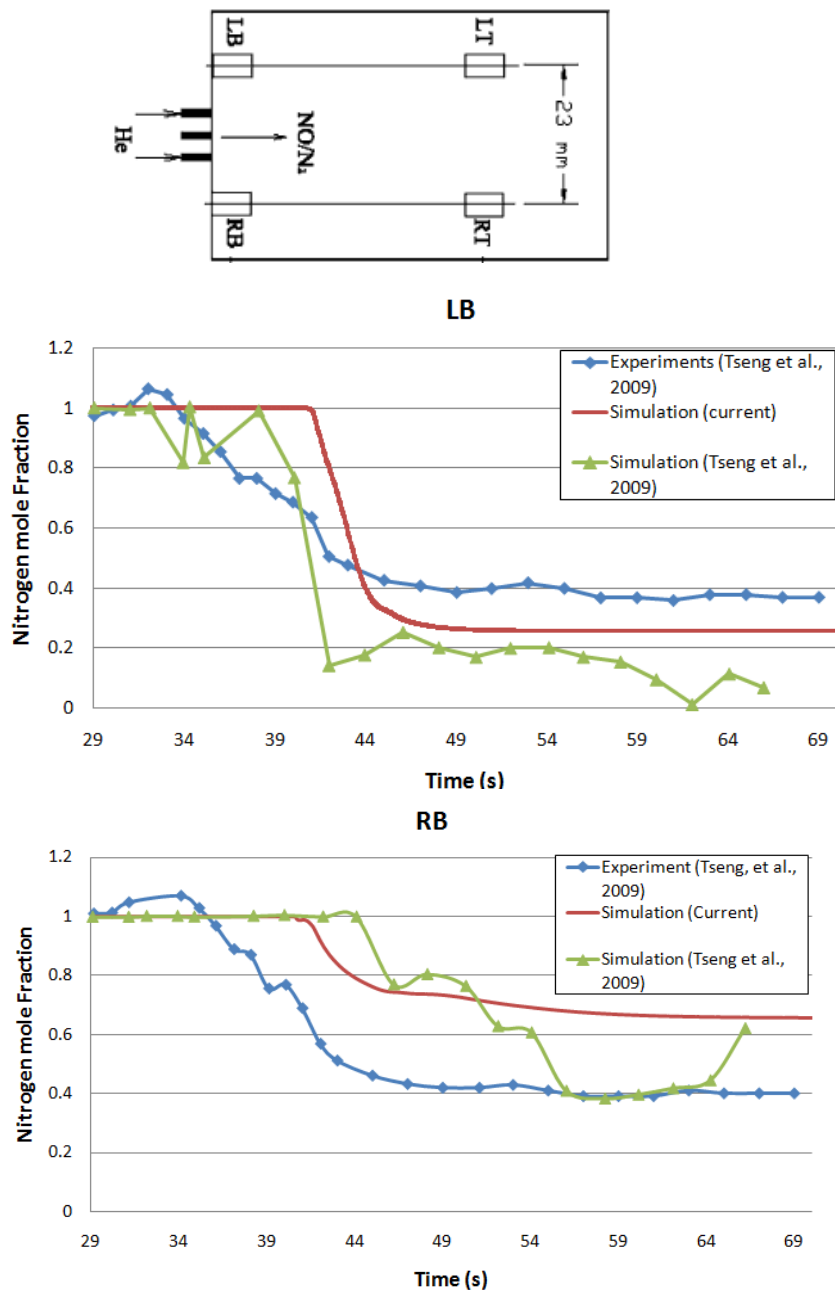


Figure 3.9. Comparison of N₂ Mole Fraction Variations at Two Locations, RB and LB in the Channel.

3.2.3. Case 3 – Transient Confined Hot Gas Jet

The third case simulated was of a transient jet generated from a pre-combustion chamber, igniting a fuel air mixture inside a long combustion chamber. For the purpose of this thesis, only non reacting jet penetration results are presented. The test rig used is described briefly in Chapter 5, and in detail in Perera, 2010.

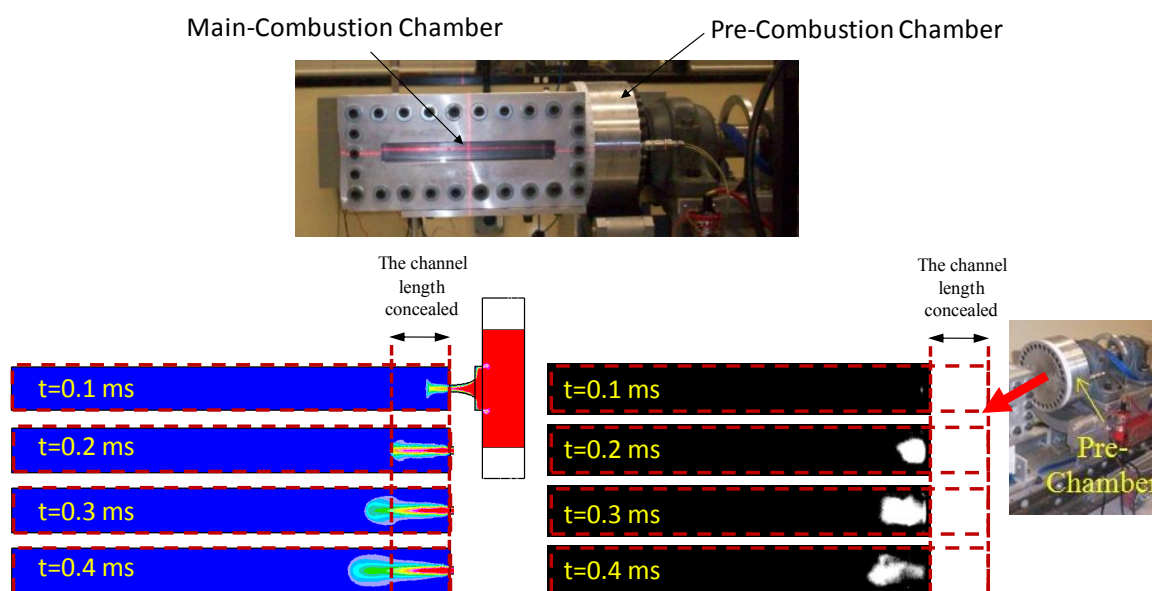


Figure 3.10. Numerical Predictions and High Speed Camera Images from Experiments of the Transient Jet, Generated in the Pre-Combustion Chamber Entering the Main Combustion Chamber.

As can be seen in Figure 3.10, ~2 inches of the main-combustion chamber is concealed from the injector side. The four red vertical dotted lines in Figure 3.10 mark this concealed 2 inches. The dotted line boxes (also in red) mark the boundaries of the main-combustion chamber. The numerical simulation performed was a 3D URANS simulation.

The pre-combustion chamber was initialized with an averaged total pressure during a selected time duration. This duration is from the time the diaphragm (which is in between the pre-combustion chamber and the main-combustion chamber) ruptures until combustion starts in the main-combustion chamber. This time is also defined as ignition delay time for these experiments by Perera, 2010. The total temperature inside the pre-chamber was initialized at the adiabatic flame temperature of the mixture used. The main-chamber was initialized with atmospheric pressure and temperature as were used in the experiments by Perera, 2010. SST k-omega turbulence model was used for modeling turbulence with the standard wall functions being used to better predict near wall flow. Since the transient jet is not a continuous jet, the numerical formulation of the problem as an initialization problem is satisfactory. Combustion kinetics was not modeled in the numerical computations. Figure 3.11 shows the development of the jet in 3D using the 0.01 iso-surface of the injected gas mass fraction.

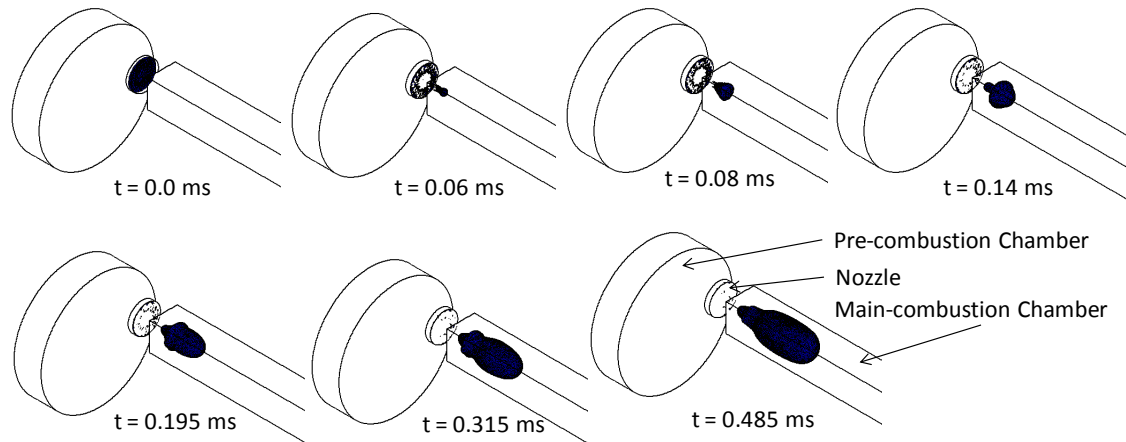


Figure 3.11. Transient Development of the Jet. Time $t=0$ ms Corresponds to the Diaphragm Rupture Event.

The comparison of axial penetration predictions of the jet with that of the experiments is shown in Figure 3.12. The experimental data for jet tip penetration was obtained by visual inspection of the high speed camera images. It can be seen from Figure 3.12 that there's quite a variability of the experimental axial penetration data. The three tests presented in Figure 3.12 had the same pre-chamber and main chamber equivalence ratios, which were the variables of the tests by Perera, 2010. However, the dynamics of ignition and combustion inside the pre-combustion chamber, and the time and nature of diaphragm rupture cannot be controlled in the tests. The nature of diaphragm rupture has direct influence to the jet dynamics and momentum transfer rate, which can effect axial penetration. However, the measured pressure histories inside the pre-chamber were similar in these cases. It is interesting to see how the CFD predictions are bounded by the experimental data. The unavailability of some data points at the start and end of the tests

might be due to the variability in diaphragm rupture and combustion inside the main chamber. The jet penetration is depicted in Figure 3.13 using two different iso-surfaces of the injected gas mass fraction, 0.1 and 0.01. It can be seen that the iso-surface corresponds to 0.01 encompass the iso-surface of 0.1.

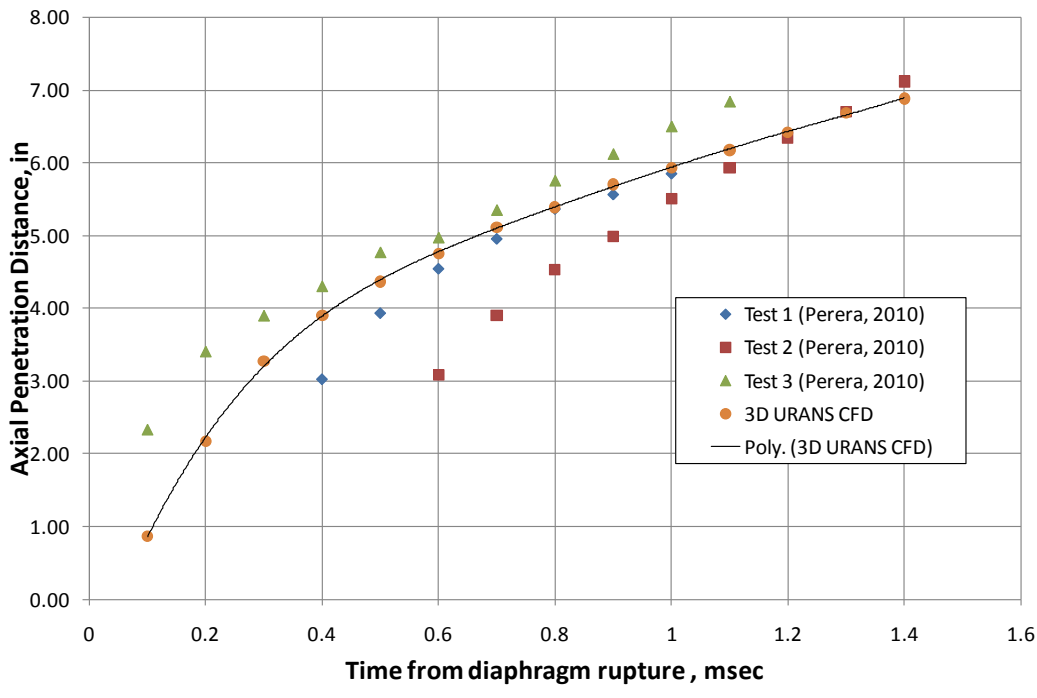


Figure 3.12. Axial Penetration Comparisons between Experiments (Perera, 2010) and 3D URANS Simulations. The Black Line corresponds to the Polynomial Curve Fit to the Simulation Predictions.

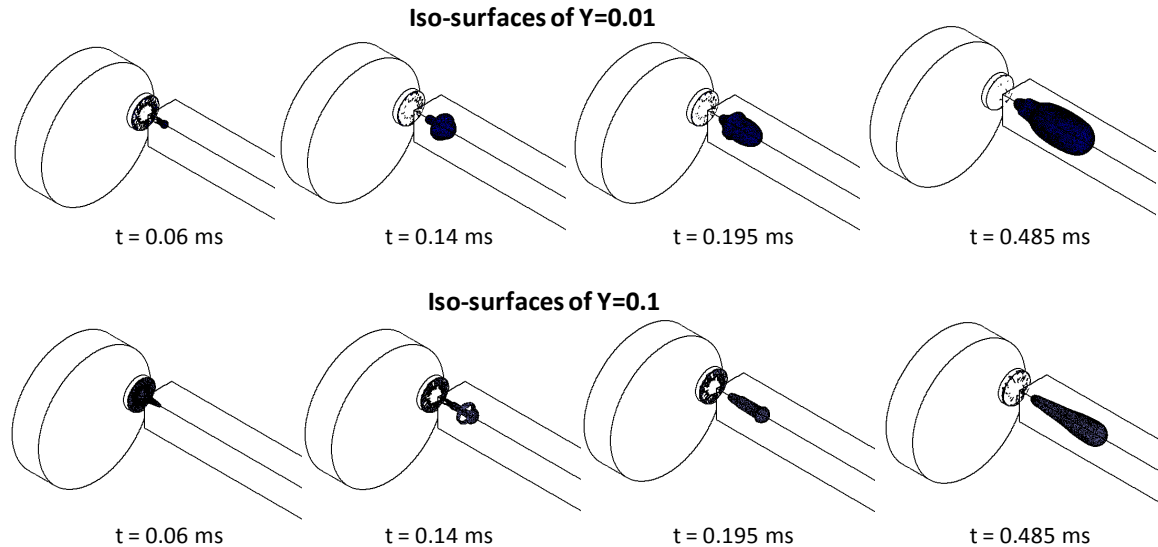


Figure 3.13. Comparison of Jet Penetration using of Two Different Injected Gas Mass Fraction (Y) Iso-surfaces, 0.1 and 0.01.

3.3 Turbulence Modeling of Translating Gas Jets

The traversing jet behaves like a jet parallel to a wall at the start and end of a channel traverse. The spreading rates of a jet discharged parallel to a wall are considerably different from the rates observed for free jets (Craft et al., 2001). Many (Newman et al. 1972; Davis, 1980; Fujisawa, 1989; Abrahamson et al., 1997) have observed larger growth rates (5-9 times) parallel to the plane wall than the rates normal to it. Some (Davis, 1980) attribute this difference to the enhanced turbulent diffusion parallel to it while others (Craft, 2001; Abrahamson et al., 1997) argue that this anisotropic growth rates are due to a resulting secondary flow causing substantial lateral outflow parallel to the wall with a strong entrainment velocity being induced normal to it. Launder & Rodi (1983) attribute

these anisotropic growth rates of the shear boundary to vortex-line bending. Craft et al., (2001) use several turbulent closure models to conclude that these large lateral spreading rates are due to anisotropic Reynolds stresses, creating streamwise vorticity. In this sense, using linear eddy/turbulent viscosity RANS models to model the turbulent closure in the traversing jet would be questionable in its initial and later parts of the travel across a channel, which can be approximated by “parallel wall jets”. Non-linear eddy/turbulent viscosity models or Reynolds stress model (RSM) which does not assume a linear relation between the Reynolds stresses and the mean strain tensor would be more accurate in this case as these can capture anisotropic turbulence and streamline curvature effects better. However, the addition of another set of equations to solve for Reynolds stresses in RSM, increases computational time and cost.



Figure 3.14. Translating Jet Behaving as a Wall Jet.

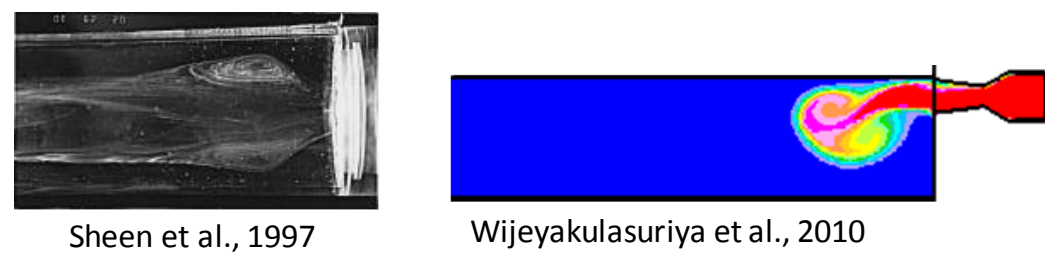


Figure 3.15. Translating Jet behaving as a Sudden Expansion Flow.

Further into its traverse, the jet is relatively ‘free’ and is characterized by classic vortex ring (round jet) or counter-rotating vortex pair (2-d slot jet) structures (Figure 3.15). Due to the translation of the injector and the interaction of the vortex structures with confining leading wall, the jet may at times behave like a ‘wall impinging jet’ (Figure 3.16).

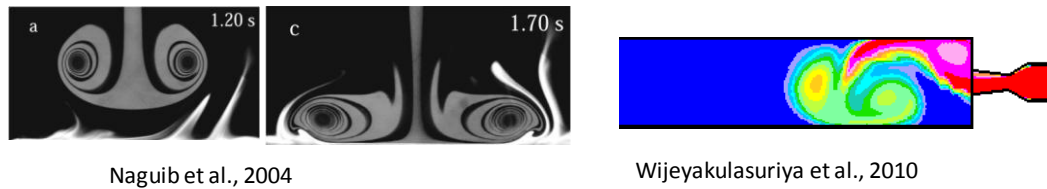


Figure 3.16. Translating Jet behaving as a Wall Impinging Jet.

Son and Abraham (2003) explain in detail about transient round, radial and wall jets and provide a very good list of prior work (modeling and experimental) on these jets.

Modeling these different jet phenomena requires different turbulence modeling strategies and this is identified as one of the greatest challenges in modeling transient translating and confined jets which are currently analyzed.

CHAPTER 4. MOTIVATION AND CHALLENGE.

4.1 Introduction

This chapter explains the motivation for the work done in this thesis and gives an outline of the challenges in each of them. Understanding the different mixing mechanisms available in the WRCVC and their effect on its performance is important in either promoting them or to minimizing them. Another goal was to achieve a stratified mixture inside the combustion channels which has numerous benefits such as lowering the post combustion temperature, which in turn lowers NO_x emissions, avoid back fire in the inlet duct and also avoid combustible mixture spillage during the charging process. Section 4.2 presents experimental data which help understand how some of these benefits were achieved in the current WRCVC test rig, using mixture stratification. Section 4.3 presents experimental and numerical results of transient jets which translates relative to the combustion channels. WRCVC has two such jets, namely the pilot fuel jet which supplies a small amount of fuel (apart from the main fuel) in making a fuel rich zone near the igniter to facilitate ignition and the hot gas jet which is used as the igniter.

4.2 Mixing Processes in WRCVC

There are several mixing mechanisms in the WRCVC as shown in Figure 4.1. Primary (main) fuel is supplied using injectors placed in the air stream. The fuel injectors have several injection holes along its length, injecting gaseous fuel perpendicular to the air stream to evenly distribute the fuel and facilitate mixing (Wijeyakulasuriya, 2008). Mixing due to fuel injection and upstream turbulence is marked as 'A' in Figure 4.1. The mixing mechanism marked as 'B' takes place when the fuel-air mixture from the inlet duct enters the channels. The gradual opening of the channels into the inlet duct generates vortices which results in mixing of the gases already within the channels with the first incoming gases. The level and intensity of mixing depends on the speed of channel rotation, relative size of the channel compared to the inlet duct and the driving pressure differential of the inlet gases. Mechanisms 'C' & 'D' mix gases injected directly in to the channels, with gases already in them, which is the main focus of this thesis and will be analyzed and discussed in detail later. Vortex dynamic interactions are shown to govern these mixing processes (Wijeyakulasuriya, 2009 & 2010). Further mixing takes place via mechanism 'E' through pressure waves traversing the channel. These pressure waves interact and reflect at channel walls and density interfaces (flames in the case of WRCVC) (Kilchyk,2010) giving rise to gas mixing.

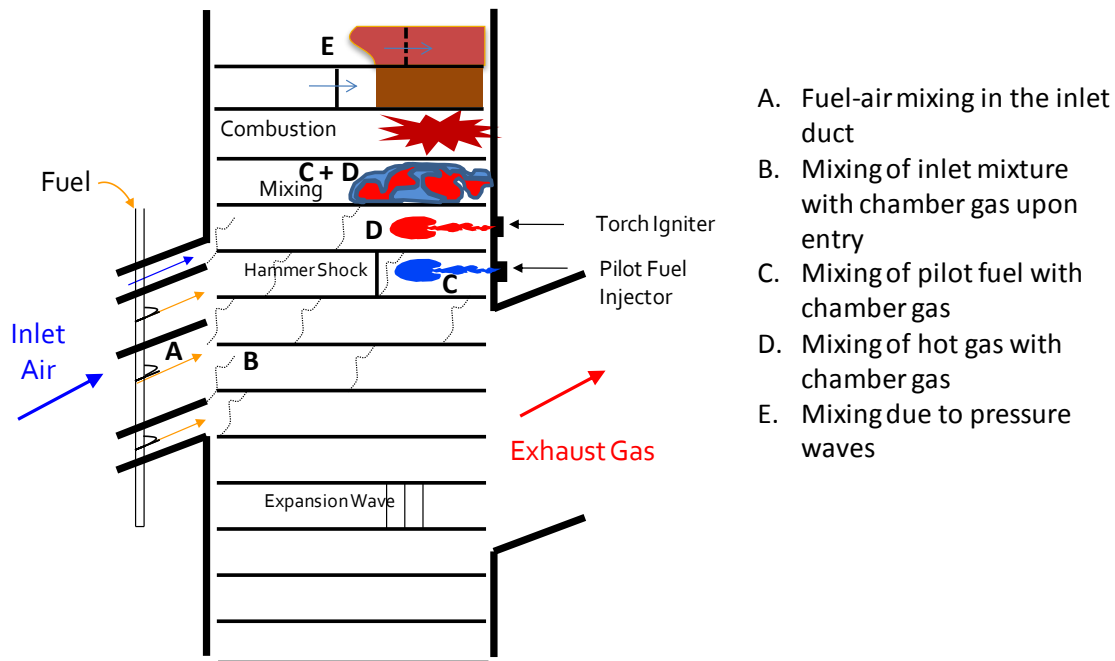


Figure 4.1. Mixing Processes in a WRCVC.

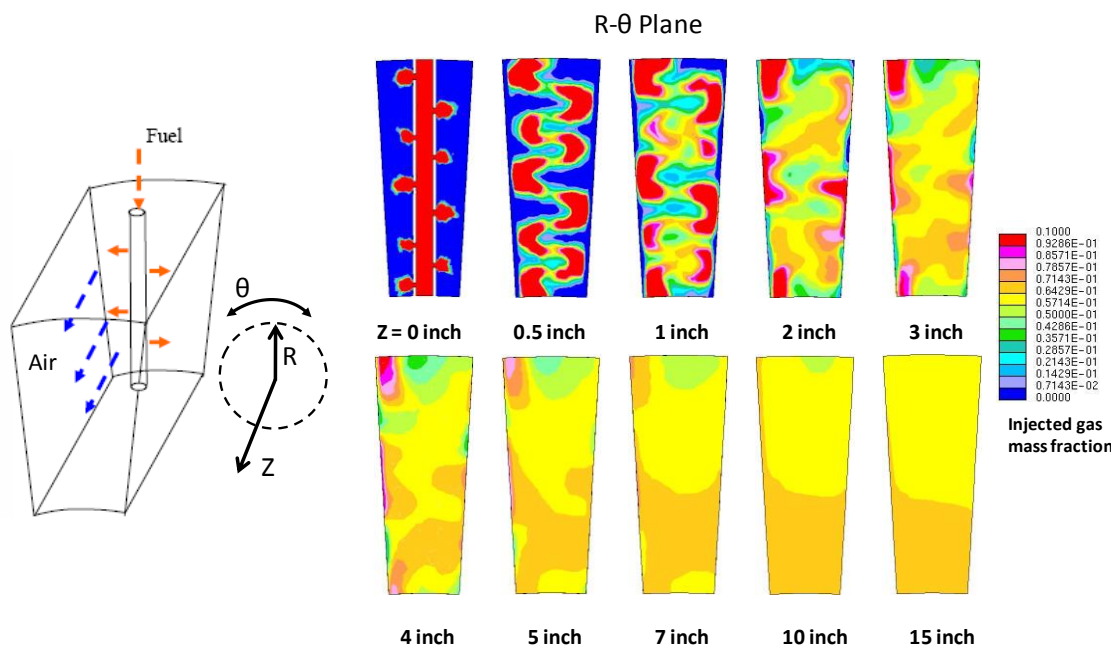


Figure 4.2. Mixing of Fuel and Air Downstream the Injection Point, in the Inlet Duct.

4.3 Mixture Stratification in WRCVC

Conventional gas turbine combustors operate with overall lean mixtures under all operating conditions, with the overall fuel-air ratio usually below the lean flammability limit of typical fuels. This necessitates the use of a richer primary zone for stable combustion with additional air being mixed downstream to bring the overall mixture temperature to the limit of turbine inlet temperature. Mixture stratification in a WRCVC allows lowering the turbine inlet temperature by burning an overall lean mixture. This further assists in lowering NO_x emissions. Having a very lean mixture (non-combustible) near the inlet duct (which supplies the fuel air mixture) will avoid the presence of flame, and hence back fire into the inlet duct.

Nalim developed fueling strategies (Nalim, 1997, Nalim, 2000) in longitudinal and radial directions of rotor channels that concentrate fuel at the specific regions of the channel for improving the combustion process and thermal management of end wall temperatures, respectively. Employing circumferential partitions in the inlet duct, longitudinal mixture stratification provides richer fuel concentration near the igniter which results in a more stable combustion while lowering NO_x emissions in the leaner main mixture (Nalim, 1997). Additionally providing fresh air in the first few partitions of the inlet duct will help in avoiding preignition and prevent any fuel spillage through the exhaust port.

Pekkan and Nalim (2003) studied fuel stratification in the radial direction of the channels by using circumferential partition walls. The partition walls provide a limited region of the channel to be charged with a near-stoichiometric or enriched mixture that ensures ignition or initiation of a deflagrative or detonative combustion process. The enrichment

may be with fuel, oxidant or both. The combustion in this region is controlled by the provision of circumferential partition walls in the rotor channels that extend a relatively short distance into the length of the channel.

The current WRCVC test rig used mixture stratification successfully to achieve several favorable working conditions, such as stable combustion, avoid spillage, prevent back fire in the inlet duct and burn a lean mixture. These aspects are explained in detail below. It is shown in Figure 4.1 how a number of fuel injectors in the inlet duct can be used to obtain an axially stratified mixture in the channel. One such injector is shown in Figure 4.2 where the fuel is injected in gaseous form from a strut placed in the air flow. Several injection holes which are staggered along the length of the injector are used to inject fuel into the air flow, which is supplied from the top. The fuel mass fraction contour plots downstream of the injector shows how this injected fuel mixes with the air (Wijeyakulasuriya & Nalim, 2008).

Thermocouple and ion sensor data will be used below to show the effect of mixture stratification on WRCVC performance. These thermocouples and ion sensors are placed in the combustion channels and rotate with them, providing data via slip rings as explained in Chapter 2. The temperature rise recorded in the inlet and exit seal plate thermocouples are shown in Figure 4.4. In the current WRCVC, the combustion was initiated from the exit end. The exit wall thermocouples in the vicinity of combustion recorded high temperatures of over 1000⁰ F, while the inlet wall thermocouples only recorded temperatures of less than 200⁰ F. It can be deduced from this that the flames

were not seen in the vicinity of the inlet wall. In the particular test case, shown in Figure 4.4, the first 9 injectors (injectors 1-9) had been used to supply the fuel while injectors 10-15 did not supply any fuel. This resulted in a stratified mixture in the combustion channel where nearly 7 inches of the combustion channel from the inlet end wall, had very little (if not none) fuel in it and avoided flame from propagating all the way to the inlet end wall. This point is further illustrated in Figure 4.5. The placement of several thermocouples, ion sensors and pressure transducers in two combustion channels (numbered 1 and 6 in the figure) is shown in Figure 4.3. TC2 in combustion channel 1 and IP7 in combustion channel 6 are both placed 7 inches from the inlet side end wall. Combustion occurred in the time period 214 sec – 215 sec of the period recorded in Figure 4.5(a). It can be seen from Figure 4.5 (a) thermocouple data that TC3-TC10 recorded higher temperatures during the combustion period. However TC1 and TC2 both recorded lower temperatures during this period, which was placed with 7 inches from the inlet end wall.

Ion sensor data for three consecutive cycles is shown in Figure 4.5(b) for transducers I7 – I12. The vertical axis of Figure 4.5(b) corresponds to the rotational angle, while the horizontal axis denotes sensor voltage for different transducers. The peaks of this figure correspond to the availability of ions in the vicinity of the transducers. It can be seen that except I7, all other ion sensors recorded a flame. I7 is placed at 7 inches from the inlet side end wall, and this further supports the idea that the combustion in the channel, in this particular test case was contained from the exit side end wall till 7 inches from the inlet side end wall. Hence the cross channel flow in the inlet side (cross channel flow would

still happen in the inlet side due to the propagation of shock waves throughout the combustion channel) did not contain any radicals nor was it at sufficient temperature to result in back fire in the inlet duct. Figure 4.5 is an illustration of the use of fuel distribution to control ignitability and fuel spillage, as well as the potential use of stratified mixture.

The effect of fuel spillage on pressure rise within the combustion channels is examined using numerical and experimental measurements. Two different fueling arrangements are compared with each other. First, only injectors 1 through 9 were used to supply fuel in the inlet port and the one-dimensional modeling and experimental pressure measurements are shown on the top row. The white lines in the fuel-flow prediction plots from one dimensional modeling show the locations of inlet and exit ports. In these two plots, the color red denotes the combustible mixture of a known equivalence ratio, while the color blue denotes air without fuel. As seen from these fuel-flow predictions, combustible mixture spills from the exit port during filling process when fuel is supplied from the injectors 1-9. This spillage was avoided when fuel was supplied from injectors 3 through 11 in the inlet port as shown on the bottom row of Fig. 4.5 These stratification setups are also shown in Figure 4.5. It was estimated that about 7.5% spillage of combustible mixture in the first case, resulted in a peak pressure rise difference in the combustion channel of ~50% between these two cases (Elharis, 2010).

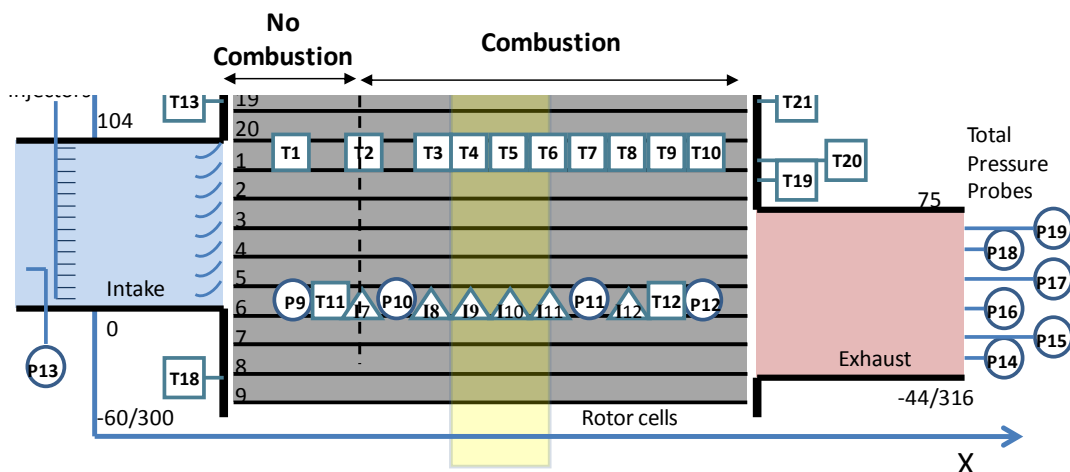


Figure 4.3. Thermocouples, pressure transducers, and ion sensors installed in the combustion channels 1 and 6 in the WRCVC (figure from Mastutomi, et al., 2010).

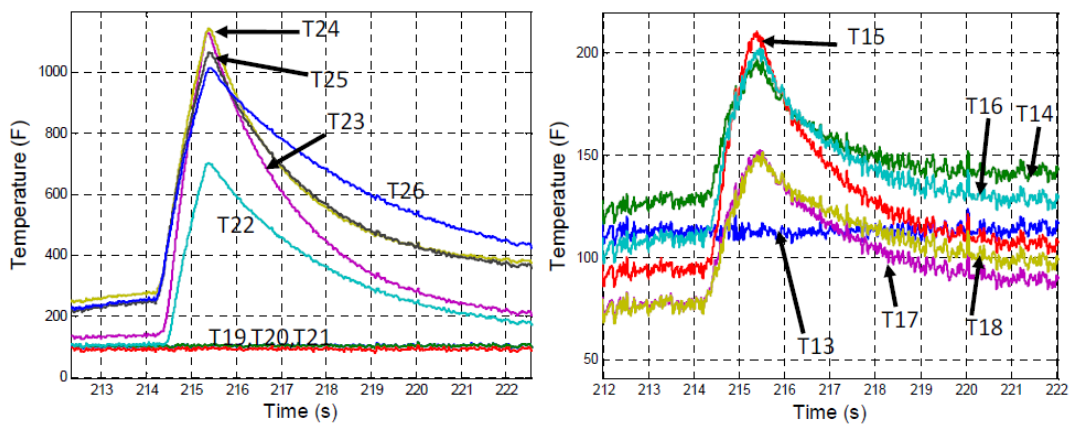
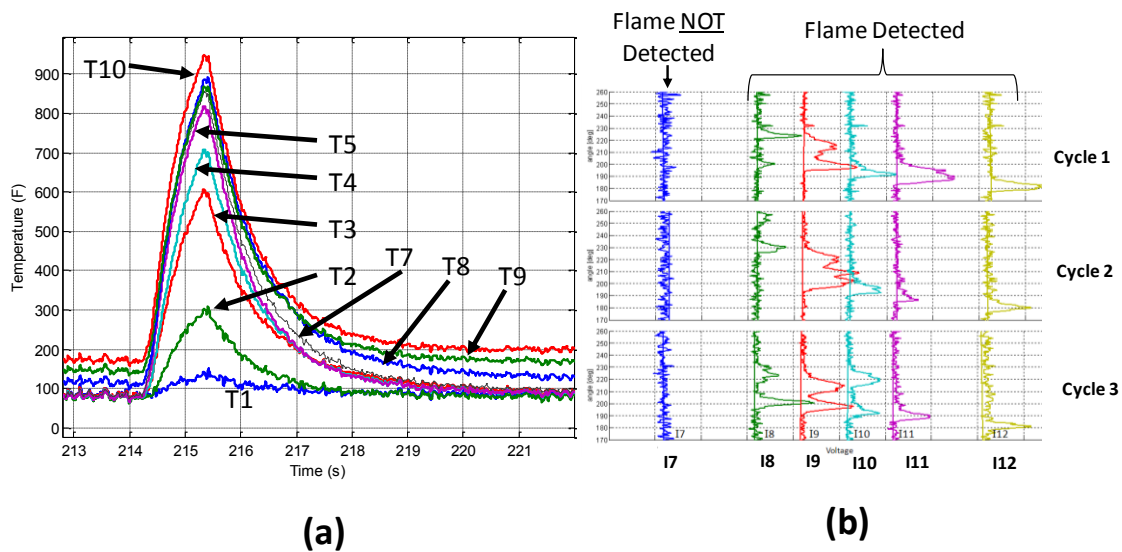


Figure 4.4. Temperature measurements on the inlet and exit end walls. Refer to Figure 4.3 for thermocouple (Ti) locations.



(a) Thermocouple Data from Combustion Channel 1
 (b) Ion sensor Data from Combustion Channel 6 for Three Consecutive Cycles

Figure 4.5. Combustible Mixture Stratification in the Inlet Port, used to Avoid Back Fire. Refer to Figure 4.3 for Thermocouple (Ti) and Ion Sensor (Ii) locations.

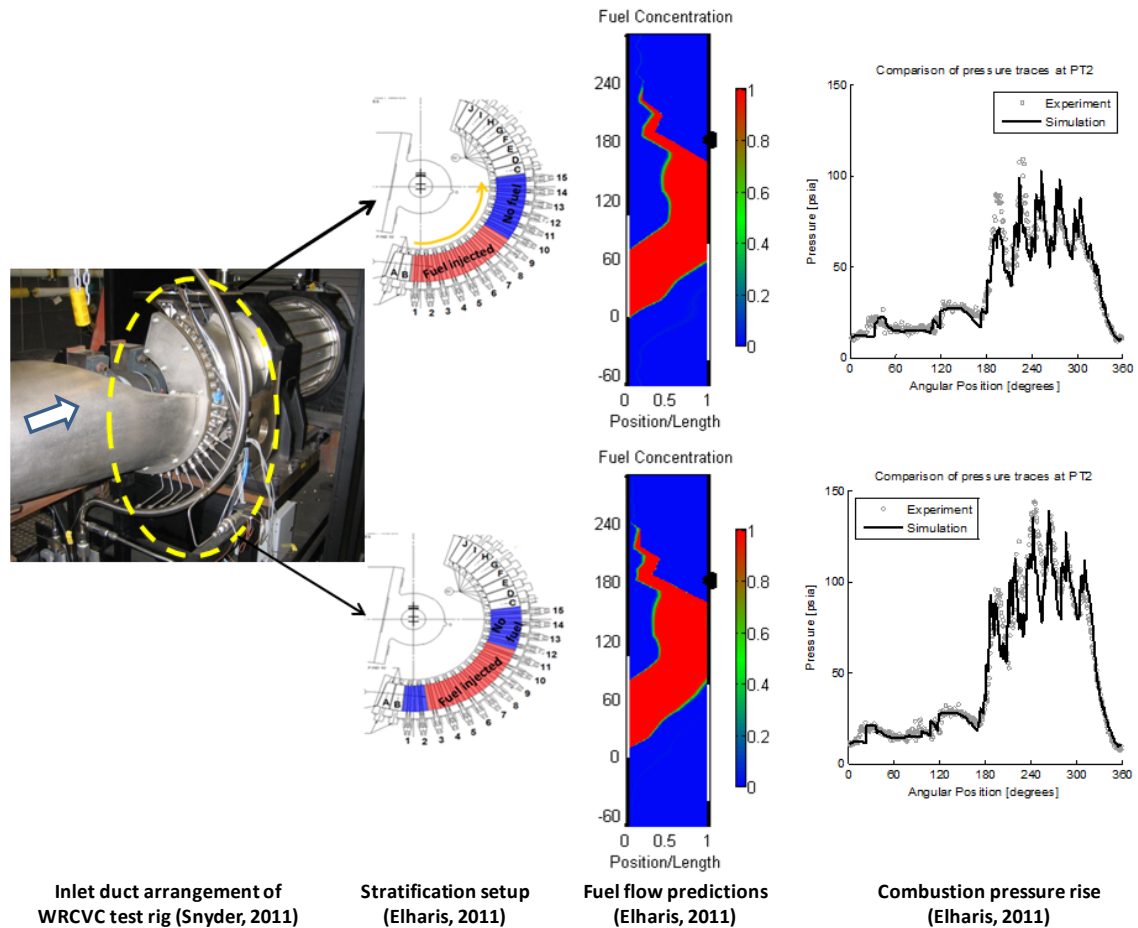


Figure 4.6. Avoiding fuel spillage by using mixture stratification in the WRCVC.

4.4 Transient Translating Gas Jets in WRCVC

Transient gas and liquid jets in confined cavities are common in combustion engines and other applications, but are usually stationary. Such jets are generally initiated and terminated by upstream valve operation or pressure modulation. This thesis describes transient jets that sweep a cavity by translation of a carrier wall, with jet upstream conditions generally constant. This was motivated by the need to design pilot fuel and ignition gas jets, to initiate combustion inside a WRCVC as schematically shown in

Figure 4.1. To ensure reliable ignition and complete combustion, pilot fuel injection and subsequent torch ignition may be key design features. A relatively small amount of fuel gas (pilot fuel) is injected from an end wall, to create a relatively fuel rich zone (Akbari et al., 2006). Pilot fuel injected should mix rapidly with air near the exit side end wall, thereby making a fuel rich zone, ready to ignite. Shortly afterward, this mixture is to be ignited by a transient jet of hot gas from a torch igniter. The ignition gas should be sufficiently hot and have the right momentum and mass to create an explosive mixture with the fuel-air mixture in the channel.

The ignition of pilot fueled zone will allow the flame to reach the primary fuel mixed with the inlet air. The pilot fuel injector and the igniter can be placed at the exit end wall (Matsutomi et al, 2010), at the inlet end wall (ABB, 1994), or at both ends (ABB, 1994). This depends broadly on the overall objectives, application, emissions, thermal management, and other specific design needs. In a typical WRCVC, the average combustion time is in the order of a few milliseconds, after which the exhaust port opens. This time is governed by the rotational speed and the location of the exhaust port in the WRCVC. For rapid combustion, successful ignition should be followed by flame acceleration with assistance from turbulence and flame area increase due to wave interaction, or other means. Ideally, the hot jet should penetrate sufficiently far into the mixture in the long combustion chamber. However the amount of mixture entrained with the jet should be limited, so as to raise the temperature of the combustible mixture with a minimum delay time.

Transient jet ignition is determined by a complex vortex mixing process, made more complex when the jet is traversing relative to the mixture and is confined by nearby walls. A qualitative comparison of two simulations is depicted in Figures 4.7. In this comparison all parameters (mass flow rate, injection pressure, and injector width) are kept the same except for the translation of the injector. The translating jet distributes fuel over the combustion channel width in the near injector region. The axial jet penetration of the translating jet is not very different from a stationary jet at the mid section of the channel although the transverse penetration is enhanced by the translating jet. Figure 4.8 presents experimental data using a high speed imaging, of a stationary jet and a translating jet injecting into a long combustion channel.

The experimental results by Perera (2010) uses a stationary jet of hot combustion products via a converging nozzle, generated in a pre-combustion chamber, to ignite a mixture inside the long combustion channel, while Murphy (unpublished) uses the same test rig and jet conditions, with the pre-chamber rotating and hence producing a translating jet, injecting into the combustion channel. The numerical predictions given in Figure 4.7 are not matched with the experimental data in figure 4.8 and hence a validation of the penetration characteristics is not intended. Only the dominant coherent structures and the nature of jet spread are compared. The advantage of the translating jet in producing a near homogeneous mixture near the end wall is apparent from this comparison. The traversing jet keeps a larger fraction of the fuel injected near the end wall which is crucial in combustion initiation of the WRCVC. In this comparison all

parameters (mass flow rate, injection pressure, and injector width) are kept the same except for the translation of the injector.

The high speed video imaging of translating (Left) round jet shown in Figure 4.8 was traversing at 150 rpm and hence has more time to inject gas in to the combustion channel, compared to the numerical prediction of the traversing jet (Figure 4.7), whose injector was traversing at 2100 rpm. The jet injects more gas to a particular region in the channel, when the injector is traversing at low rpm, and hence the greater penetration of the experimentally observed translating jet, as seen in Figure 4.8.

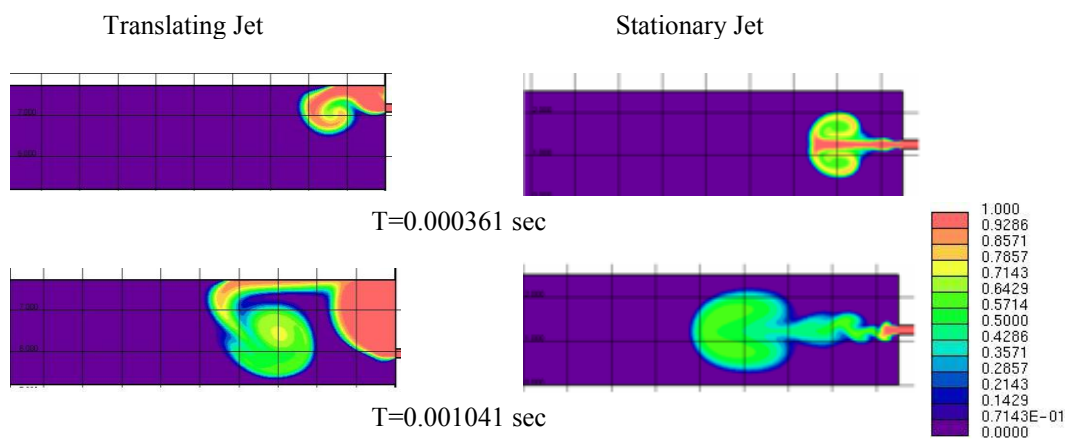


Figure 4.7. Fuel jet behavior of translating and stationary planar jets (Contours of injected gas mass fraction).

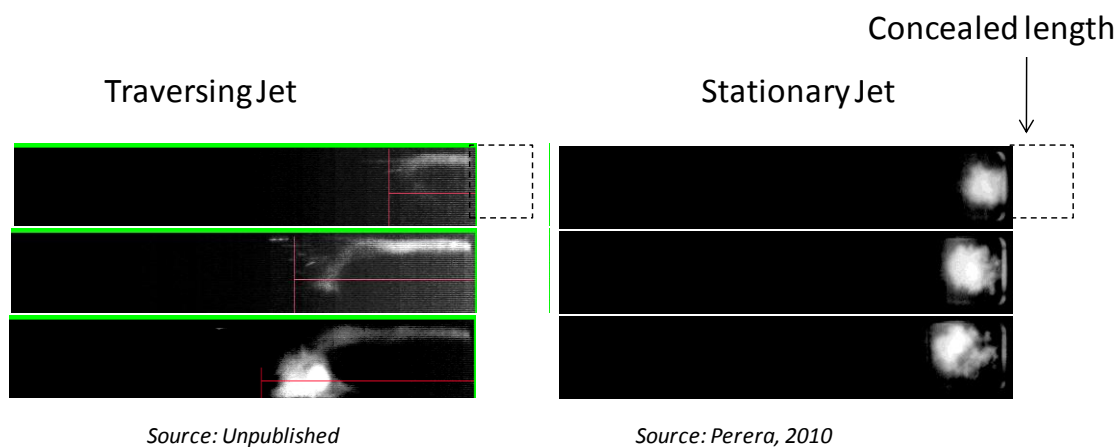


Figure 4.8. High speed video imaging of translating (Murphy, unpublished) and stationary (Perera, 2010) round jets. The jets are injected from the right.

CHAPTER 5. IGNITION BY HOT GAS JETS.

5.1 Introduction

Ignition of fuel-air mixtures by hot turbulent gas jets is important for fire and explosion safety, internal combustion engines, pulse detonation engines, wave rotor combustors, and other related systems. In a volume containing a combustible gas mixture, ignition may occur through contact and mixing with hot burned gases admitted as a jet. Ignition by a jet of hot gas is assisted by a mixing process, and thus differs from ignition by a hot surface, spark, or compression (Table 1). The chapter begins with a literature review on hot gas jet assisted ignition and its performance compared to other ignition methods. Many prior studies have been done in relation to fire and explosion safety whose prime objective was to inhibit ignition by hot gas jets, unlike in the current study where promotion of ignition is pursued. The single channel hot gas jet assisted combustion experiment at the combustion and propulsion research lab (CPRL), IUPUI is explained in the second part of the chapter. The chapter is concluded by an ignition delay time analysis using empirical correlations developed for ignition behind reflected shock waves. The viability and challenges in using such correlations are also discussed.

5.2 Prior Work on Hot Gas Jet Assisted Ignition

Early experiments of ignition of combustible mixtures by hot gases were studied in relation to safety in mines, by the U.S. Bureau of Mines (Wolfhard, 1958, Van Dolah et al., 1965, Vanpee & Wolfhard, 1959, Bruszak et al., 1959, Fink & Vanpee, 1975, Cato & Kuchta, 1966). These experiments used a non-reactive hot gas jet injected continuously into a uniform quiescent combustible mixture. Wolfhard (1958) defined ignition temperature as the steady jet-base temperature at which the luminous region in the combustible mixture transforms into ignition. This definition of ignition temperature is different from the one used in the current work, where the predicted local temperatures at the onset of ignition are sought. Further Wolfhard's (1958) definition might be different from several other works cited in this thesis.

The minimum jet temperature needed to ignite hydrocarbon combustible mixtures appeared to be much higher than their auto-ignition temperatures, but much lower than the adiabatic flame temperatures of stoichiometric mixtures and close to flame temperatures for flammability limit mixtures (Vanpee & Wolfhard, 1959). Vanpée and Wolfhard (1959) showed a correlation between the ignition temperature and the "limit flame temperature" for most combustible mixtures as seen in Figure 5.1. This limit flame temperature was measured using a diffusion flame around a stainless steel hemisphere (Simmons & Wolfhard, 1957). Fink and Vanpée (1975) developed an overall rate expression for describing the ignition of methane, ethane, and ethylene fuel-air mixtures by a hot inert gas injected at relatively low velocities, similar to laminar flame simplified reaction rate expressions (Westbrook & Dryer, 1984). The required jet temperature was

found to depend on the dimensions of the jet, composition and velocity of the jet, and combustible mixture (Cato & Kuchta, 1966). Low flow velocities provide low air dilution rates, slower temperature drop due to reduced mixing, and long contact times with the combustible mixtures. Similarly, studies on resumed detonation of fuel-air mixtures when hot detonation products are injected indicates that a range of ignition energy deposition, injected gas mass, and premixed fuel-air composition can initiate combustion (Tarzhanov, 2006). It is expected that relatively high fuel concentrations, high jet temperature, and low jet flow velocities would promote ignition.

Cato and Kuchta (1966) found that fuel-air mass ratio has little influence on the minimum jet temperature for ignition of several heavy hydrocarbons, except that an increase in this critical temperature was observed with decrease of fuel-air mass ratio below 0.3. The same trend of this critical jet temperature (called 'ignition temperature' by some authors) with fuel-air mass ratio was observed for different jet diameters, and the critical temperatures decreased consistently as the jet diameter was increased for a constant jet flow rate. Further, the critical jet temperature was higher than the temperature needed using wire ignition or the auto-ignition temperatures for the same mixture and heat source diameter (Cato & Kuchta, 1966).

Wolfhard (1958) experimentally observed that a jet of hot air slightly below a threshold temperature introduced into a cold fuel left little visible traces of ignition. When the air jet temperature was raised, a small flame appeared above the jet, and then disappeared when the temperature was reversed. However, when the temperature was increased above

a higher critical temperature, this flame became self-propagating and was not extinguished with the reduction of jet temperature. The weak dependence of critical jet temperature on mixture concentration was also observed by Wolfhard (1958), noting that several hydrocarbons ignite slightly better under fuel rich conditions, with the exception of ethylene for which the minimum is on the fuel lean side. This is consistent with the findings of Cato & Kuchta (1966) for heavy hydrocarbons (e.g. hexane, octane, and decane), which ignited better under fuel rich conditions.

Ignition of a combustible mixture by a turbulent jet of radical-laden gas generated in a pre-chamber was studied by Gussak (1975), Oppenheim (1978), Murase et al. (1984), Murase et al. (1998) Wallesten and Chomiak (2000), Valle et al. (2003), Toulson et al. (2009), Attard et al. (2010), and Yamaguchi et al. (1985). This method of ignition described as avalanche activated combustion or LAG (a Russian acronym) aims to initiate combustion using highly active radicals generated in a fuel-rich pre-chamber. Gussak (1975) reported a 5-7 fold reduction in ignition delay time and 3-4 fold reduction in combustion duration with the LAG method relative to conventional spark ignition systems. Versions of the LAG concept (Murase et al., 1998) include expanding the jet to quenching conditions and using electrical discharge to produce a plasma jet Wallesten and Chomiak (2000). In these versions, the pre-chamber was much smaller than the main combustion chamber. Radicals in the jets appear to initiate ignition of very fuel-lean mixtures.

Mayinger et al. (1999) found a correlation between the induction time (ignition delay time/flame re-ignition delay time, accounting for heat transfer to solid walls) and mixing time of the jet (characteristic flow time, obtained by using correlations for vortex structures) and adiabatic ignition delay time (ignition time delay neglecting heat transfer to solid walls) for fuel-air mixtures of hydrogen, methane, and propane.

Table 5.1. 'Ignition temperatures' of different fuels (Van Dolah et al., 1965).

Fuel in fuel-air mixture	Hot surface ignition temperature, deg C	Hot gas ignition temperature, deg C	Lower limit flame temperature, deg C
Methane	537	1325	1518
Benzene	562	1018	1540
n-Butane	405	990	1422
Diethyl ether	-	956	1386
Ethane	515	915	1363
Ethylene	-	900	1422
Carbon monoxide	-	870	1177
Hydrogen	520	<755	811

Table 5.2. 'Ignition temperature' of mixture by inert hot jets, °C (hot jet flow rate = 35 cm³/s) (Wolfhard, 1958).

Fuel	Nitrogen	Argon	Helium	Carbon dioxide
Ethane	1100	1175	1290	1100
Ethylene	1100	1165	1265	1075
Carbon monoxide	900	925	1000	870

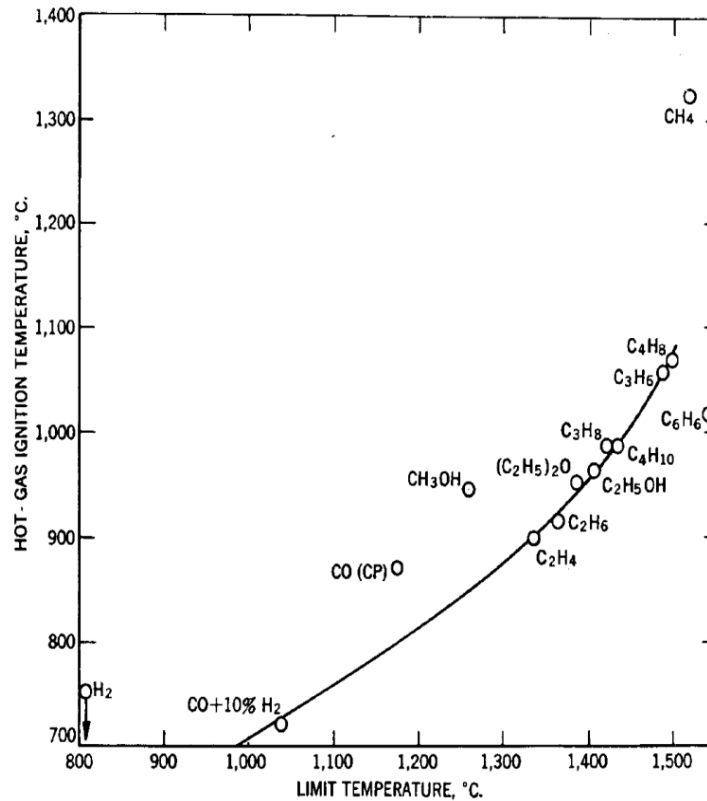


Figure 5.1. Limit Flame Temperatures and Hot Gas 'Ignition Temperatures' of Different Fuels.

5.3 Hot Gas Jet Assisted Ignition Test Rig at CPRL, IUPUI

Combustion and Propulsion Research Lab (CPRL) at IUPUI has an experimental test rig to evaluate the ignition and combustion characteristics of fuels using a jet of hot combustion products. The single channel wave-rotor combustion rig (SCWRC) was designed (Bilgin et al., 1998 and Bilgin, 1998) to examine the fundamental ignition processes in a stationary chamber using imaging and pressure measurements (Figure 5.2). The SCWRC rig has two combustion chambers: the pre-chamber which houses the

nozzle and the main chamber (Figure 5.2 (a)). The pre-chamber is a cylindrical chamber with an internal volume of 52.48 in³, while the main chamber is a rectangular channel of square cross-section with internal dimensions of 1.57 in × 1.57 in × 16.0 in. The distance between the chambers can be adjusted with the main chamber entrance oriented to the pre-chamber nozzle exit. Perera (2011) reports experiments using this rig for different fuel types for which the gap between the pre-chamber and the main chamber was maintained at a mean of 0.008 in with a variation ranging 0.003 to 0.010 in. Ambient gas can be prevented from going into the two chambers using two diaphragms (Figure 5.2 (c) and (d)) which is important when fueling. The type and thicknesses of the diaphragm used is explained by Perera (2010). The diaphragms used were made to rupture upon the impingement of the torch jet, generated in the pre-chamber.

Details of the setting up and preparation of these diaphragms are explained by Perera (2010). A conventional spark ignition system is employed in the pre-chamber to initiate combustion. The pressure rise in the pre-chamber ruptures the aluminum diaphragm (in the pre-chamber) delivering the combustion products through a convergent nozzle. This torch jet impinges on the main chamber latex diaphragm rupturing it in the process and entering the main chamber which contains the prepared premixed combustible fuel-air mixture. The nozzle exit (Figure 5.2 (a) is aligned with the longitudinal-axis of the main chamber for stationary tests (Perera, 2010) and offset by a known angle for rotary combustion tests (Murphy, unpublished) . Stationary tests corresponds to cases when the jet is stationary and rotary tests corresponds to cases when the pre-chamber (and hence the hot jet) was rotating while the hot combustion products were injected. The main

chamber is equipped with dynamic pressure transducers and also provides visual access through a Pyrex[®] viewing window (Figure 5.2 (a) and (c)). High-speed data recorded from high-frequency pressure transducers and a high-speed camera was used to visualize the complex flame and combustion phenomena in the main chamber.

The pressure history inside both the pre-chamber and the main chamber are acquired using PCB 113A32 high-frequency dynamic pressure sensors with one pressure transducer allocated to the pre-chamber (PT0) and the other four positioned along the main chamber (Figure 5.2 (c)). The visualization of the combustion in the main chamber is captured with a Phantom[®] v9.0 high-speed video camera. The camera is capable of capturing high-speed video at 144,175 frames per second (fps) and has the maximum resolution of 1632×1200 pixels. Perera (2010) recorded the high-speed video images at 10,000 fps due to elongated nature of the viewing window which limited the capture rate. Therefore, the high-frequency pressure measurements were also limited to 10,000 Hz to ease of matching the data between the high-speed video images and pressure measurements.

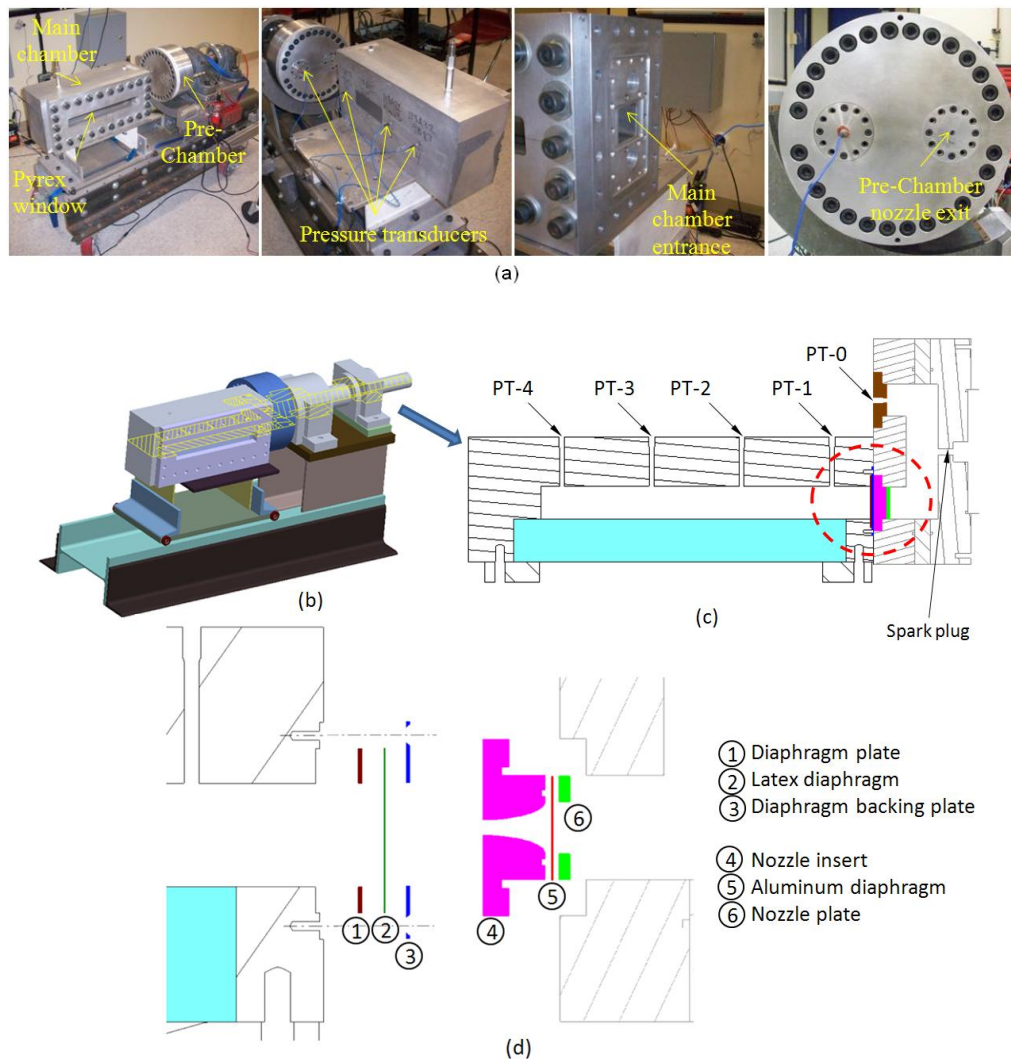


Figure 5.2. Single Channel WRCVC Test Rig: (a) indicating the main components (b) indicating computer aided design (CAD) model of the SCWRC rig, (c) indicating the pressure transducer locations and designations on the cross-section indicated of the CAD model, and (d) detailed view of the diaphragm assemblies used in the pre-chamber and the main chamber (Reproduced from Perera et al., 2011).

In the studies of Perera (2010) and Murphy (unpublished) using this test rig, ignition was detected by the luminosity in the main chamber gas mixture, emitting in the range from 400-1,000 nm of the electromagnetic spectrum which the high speed camera was able to detect. The evolution of the luminous region was used to identify the self-propagating flame that traverse the main chamber both downstream as well as upstream. In addition to this optical method, the spatial pressure measurements from the pressure transducers in the main chamber were used to validate the ignition and subsequently the ignition delay time (Perera, 2010). Perera (2010) defines the ignition delay time as the time between the diaphragm rupture in the pre-chamber and time of detection of the luminous flame observed in the captured high-speed video images.

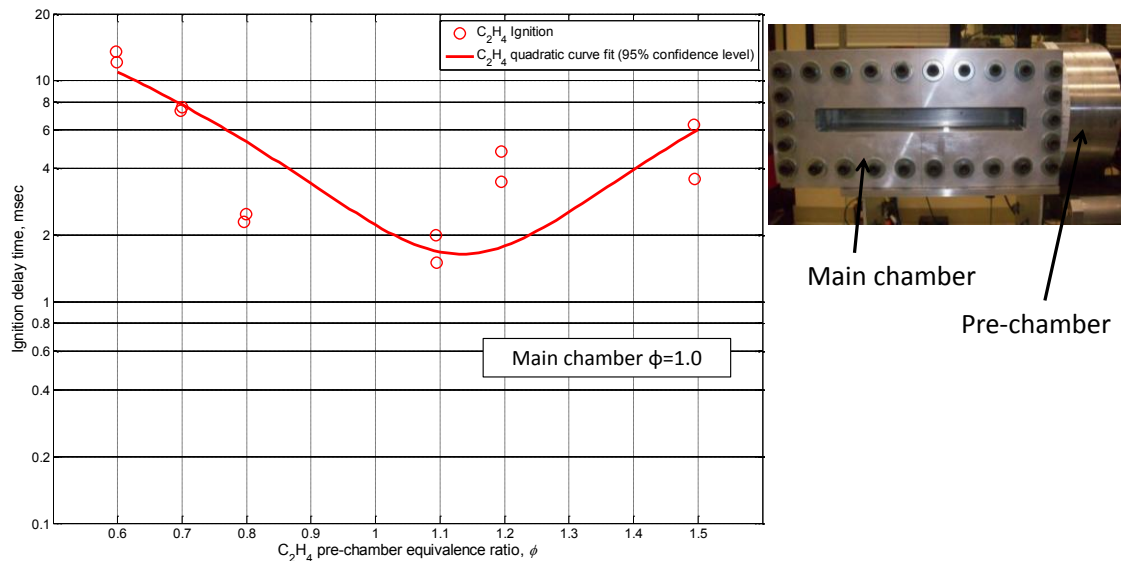


Figure 5.3. Variation of ignition delay time with pre-chamber equivalence ratios for a main chamber equivalence ratio of 1.0. (Perera et al., 2011).

For stationary tests (Perera, et al., 2011 and Perera, 2010) using ethylene as fuel in both the chambers, it was found that a pre-chamber equivalence ratio of 1.1 produced the least ignition delay time in the main chamber for a main chamber equivalence ratio of 1.0 (Figure 5.3). Perera (2010) and Perera et al., (2011) further studied the effect of main-chamber equivalence ratio on ignition delay time for a fixed pre-chamber equivalence ratio of 1.1. It was found that fuel lean mixtures (equivalence ratios 0.6 – 0.8) produced the lowest ignition delay times as shown in Figure 5.4. Stoichiometric mixtures had nearly 1 ms more ignition delay times compared to these lean mixtures. Mixtures with equivalence ratios lower than 0.4 and greater than 2.4 failed to ignite in a consistent manner (Perera, 2010). It is noted that the equivalence ratio noted here represent the mixtures before the injection of the hot gas jet and the local equivalence ratios at the points of ignition might be different than these values due to mixing with the injected hot gas jet. The current experimental setup is not capable of measuring the local, transient equivalence ratios.

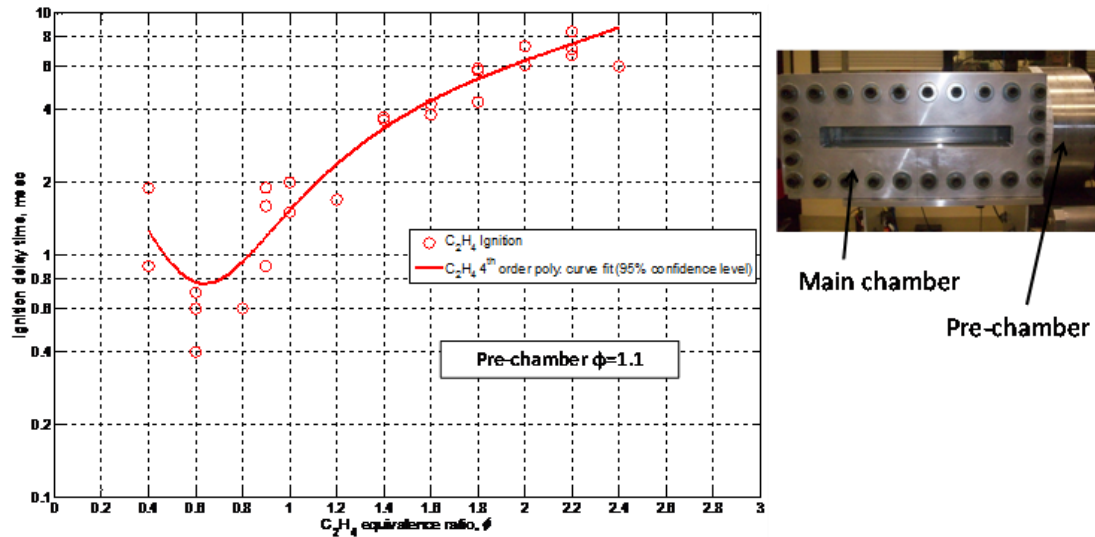


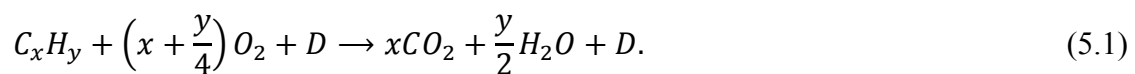
Figure 5.4. Variation of ignition delay time with main-chamber equivalence ratios for a pre chamber equivalence ratio of 1.1. (Perera et al., 2011).

Murphy (unpublished) conducted experiments with rotating hot gas jet ignition for several pre-chamber speeds up to 750 rpm. The author's private communications with Murphy K. (unpublished), have shown that similar trends of ignition delay times to pre-chamber and main-chamber equivalence ratios exist and the ignition delay time increases with the increasing of rotational speed. This can be explained in light of energy deposition at a local position in the main-chamber by the hot combustion gas jet. When the jet moves faster, the energy deposited at one single point by the jet is low and hence the ignition delay time increases.

5.4 Chemical Ignition Delay Time Analysis

Most of the experimental studies (Fink & Vanapee, 1975, Lamoureux et al., 2002, Lifshitz, 2001, Baker and Skinner, 1972, Brown and Thomas, 1999, Würmel et al., 2007, Burcat et al., 1971, Hidaka et al., 1974) on chemical ignition delay time measurement of hydrocarbons have used shock tubes due to their simplicity and their ability to increase the temperature of the combustible mixture instantaneously behind shock waves. The ignition delay time has been determined from pressure changes or the emission or the absorption profiles of specific chemical species. These pressure signals or chemical species are observed behind the reflected shock waves in shock tube experiments. In numerical simulations, the delay time is determined from the calculated temperature profiles, species concentrations, and pressure. It is defined either as the time at which the rate of temperature rise reaches its maximum value ($d^2T/dt^2 = 0$) (Murase et al., 1998), or the sudden pressure rise from its initial value (Lifshitz, 2001).

The overall reaction of hydrocarbon fuels (C_xH_y) and oxygen in the presence of an inert diluent gas (D) can be represented by a global reaction equation, such as:



The global reaction equation represents completion of reaction to form final products, but for ignition studies, the initiation of reaction to the point where significant heat release is evident is of interest. Here, the ignition delay time is evaluated using shock-tube

experimental correlations with initial mixture temperature and species concentrations. It is estimated by an Arrhenius-type model (Lifshitz, 2001):

$$\tau = 10^a \exp\left(\frac{E_a}{R_u T}\right) \cdot [C_x H_y]^a [O_2]^b [D]^c, \quad (5.2)$$

where 10^a is the pre-exponential rate constant coefficient, E_a is the activation energy of the reaction, and R_u is the universal gas constant, T is the local, pre-ignition temperature of the reactants, $[C_x H_y]$, $[O_2]$ and $[D]$ are molar concentrations of reactants and diluent, and a , b , and c are constants.

The inclusion of the diluent concentration in the ignition delay equation is debated in the literature. Some suggest that the diluent concentration affects the ignition time delay (Lamoureux et al., 2002, Lifshitz, 2001, Baker and Skinner, 1972), while others (Fink & Vanapee, 1975, Lamoureux et al., 2002, Burcat et al., 1971, and Hidaka et al., 1974) do not include the diluent concentrations in their models. The effect of diluent gases on the ignition delay time is explained by Lifshitz (2001) through two different roles: the first is a third body effect in disassociation-recombination reactions where the diluents enhance the recombination rather than disassociation, reducing the radicals that promote the reactions which reduce the ignition delay. Second is a cooling effect of the diluents during the ignition process. The heat released in the reactions increases the temperature of the reactants, but the heat capacity of the diluent gases inhibits the increase in temperature, reducing the rate of reactions, increasing the ignition delay time.

The particular diluent gas present appears to have an effect on the delay time, depending on the ignition method (Würmel et al., 2007). Würmel et al. (2007) observed longer ignition delay times with increasing relative concentrations of Argon compared to N_2 , purportedly due to their different thermal capacities and the thermal diffusivities.

Reflecting subtle effects of device timescales, the same study concludes that Argon prolongs ignition delay time in rapid compression machines but shortens the ignition delay time in shock tube experiments under specific conditions. In experiments using a hot inert gas as the source of ignition (Wolfhard, 1958), the critical gas temperature of the core of the jet base varies with the type of diluent gas (Table 2), possibly due to the effect of thermal capacity and /or the thermal diffusivity of the diluent.

Local chemical ignition delay times are predicted in this study using the correlations developed for ignition of hydrocarbon fuels behind reflected shock waves. Three such correlations are used for ethylene and propane. Although the degree, mechanism, and uniformity of heating may be different in shock-assisted ignition and hot-gas jet ignition, local chemical ignition kinetics should be similar. The correlations remain the best available data for ethylene and propane ignition. The ethylene ignition delay was modeled according to the correlation given by Baker and Skinner (1972) which models the ignition delay of ethylene behind reflected shock waves as a function of temperature, concentrations of oxygen, ethylene, and argon (diluent). Propane ignition delay was modeled using correlations by Lamoureux et al. (2002) and Burcat et al. (1971) which use the temperature and concentrations of oxygen and propane to model ignition delay.

Wijeyakulasuriya (2010) analyses the rate and extent of mixing of the hot gas and the combustible fuel-air mixture. The temperature distribution of the mixture is analyzed with time, to determine the tendency for ignition. The spatial and temporal temperature variation in the channel upon injection is studied for different hot gas mass flow rates and for different combustible mixtures inside the channels. This helps to understand the optimal injection conditions (velocity, jet temperature) needed to raise the temperature of the combustible mixture to its ignition temperatures in the time available for ignition. Only homogenous combustible mixtures were considered in this study.

It is emphasized that these computations do not include combustion. The local transient concentrations and temperatures during mixing are used to predict local chemical ignition delay times within the jet. This is consistent with the use of pre-combustion temperature and concentrations in the experimentally derived correlations. The parameters used in each correlation according to Eq. 2 are summarized in Table 3. The numerical method for deriving ignition delay times is explained in Chapter 8.2

Table 5.3. Ignition Delay Time Correlation Parameters.

	Fuel	A	E_a/R_u (K)	a	b	c
Baker and Skinner (1972)	C_2H_4	$10^{-11.9}$	17222	0.30	-1.10	0.4
Lamoureux et al. (2002)	C_3H_8	5.06×10^{-15}	28450	0.85	-1.30	0
Burcat et al. (1971)	C_3H_8	4.40×10^{-14}	21250	0.57	-1.22	0

5.4.1 Ethylene

The chemical ignition delay correlation developed by Baker and Skinner (1972) for shock-wave assisted ignition of ethylene-oxygen-argon mixtures is used here:

$$\tau = 10^{-11.9} [C_2H_4]^{0.3} [O_2]^{-1.1} [Ar]^{0.4} e^{34200/RT}. \quad (5.3)$$

The correlation given in Equation 5.3 is expressed using mole fractions and pressure (Equation 5.4), revealing significant pressure dependence:

$$\tau = 10^{-11.9} [\chi_{C_2H_4}]^{0.3} [\chi_{O_2}]^{-1.1} [\chi_{Diluent}]^{0.4} (P/RT)^{-0.4} e^{34200/RT}. \quad (5.4)$$

Time-dependent local mass fractions of hot gas injected and the air in the combustors are used to estimate the ignition delay time according to Equation 5.4. It is acknowledged here that in order to determine the ignition location and delay time precisely, particles of mass has to be tracked individually to see how their energy is increased over time. This requires a lagrangian formulation of the problem, which is not discussed in this thesis. The analysis done here looks at the problem in an eularian perspective. The fuel and oxidant concentrations, temperature and the predicted ignition delay time for Case 4 introduced in Table 5.4 with injected CO₂ at a mass flow rate of 72 g/sec (Wijeyakulasuriya, et al., 2010) is compared in Figure 5.5. The effect of temperature can be seen to dominate over other parameters, from the density contours as the pressure rise due to injection is minimum. The effect of gas mixing, facilitated by two counter rotating

vortices, which can be seen from the injected gas (CO_2) mass fraction plots and the oxygen and ethylene plots is also very pronounced.

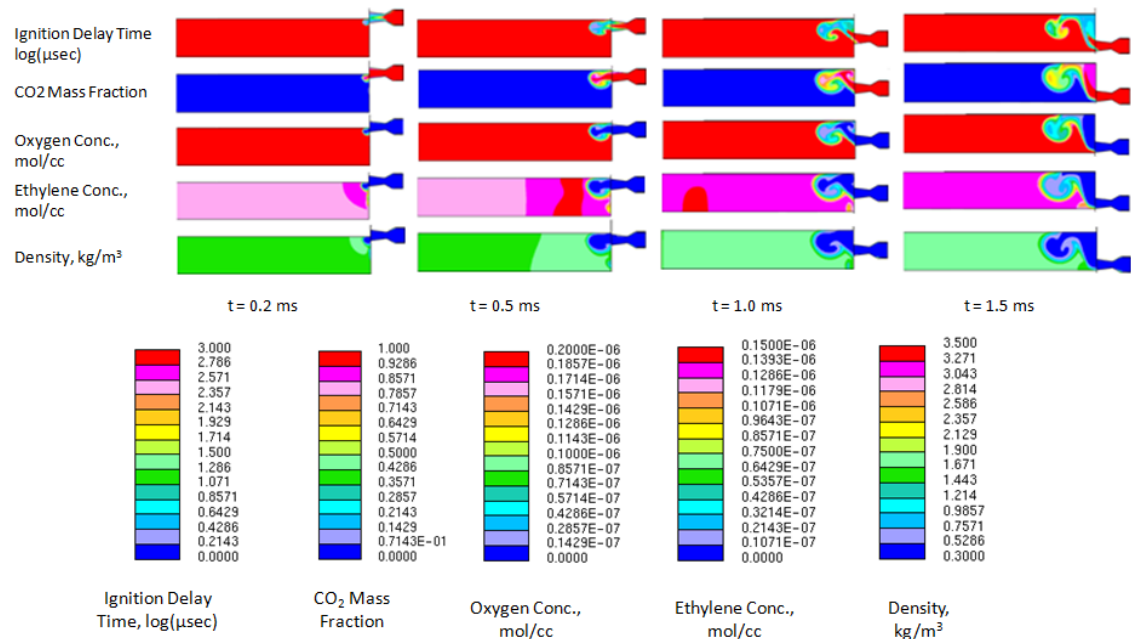


Figure 5.5. Local Chemical Ignition Delay Time Predictions for Ethylene-Air Mixtures (Wijeyakulasuriya, 2010).

It was assumed that a well mixed, stoichiometric air-fuel mixture exists in the combustion channels when the hot gas jet is introduced. The correlation for ethylene ignition delay in mixtures of ethylene, oxygen and argon, with more than 95% argon. In the computations, the diluent was considered to consist of the nitrogen in the air, plus the hot gas injected from the injector. The gas before the hot gas injection was assumed to be a mixture of air (consisting of 23% O_2 and 77% N_2 by volume) and ethylene of a known equivalence ratio. Once the hot gas is injected, it dilutes the combustible mixture and provides a third body effect for the chemical reactions. Hence injected gas was considered as a diluent, along with the N_2 in the air. Knowing the correct species concentrations required for

successful ignition is a challenge as there have been no previous experimental investigations into understanding the local parameters necessary for successful ignition. Given such a correlation exist, the current numerical method accurately predicts the ignition success/failure and the ignition delay time, based on the local concentrations, pressures and temperatures resulted from an accurate mixing calculation. The user coding was used in conjunction with the numerical code, to calculate the ignition delay time.

It is shown in Figure 5.6 how ignition location(s) can be qualitatively identified from the ignition delay time plots. The hot gas starts entering the first combustion chamber at $t = 0.1$ ms. The ignition delay predicted at that time is $\sim 200 \mu\text{s}$ and drops to about $\sim 3 \mu\text{s}$ at $t = 0.15$ ms, indicating ignition might initiate soon after the hot gas starts entering the combustion chamber. As explained above, a lagrangian form of analysis is needed for precise identification of the local ignition locations.

Table 5.4. Test Cases.

Case	Injected Gas	Injector Inlet Boundary Conditions			\dot{m} (kg/s)	$\left(\frac{P_{injection}}{P_{initial}} \right)_{Static}$
		U (m/s)	ρ (kg/m ³)	T (K)		
Case 1	N ₂	28.5	1.3	2200	0.058	6.16
Case 2	N ₂	72.3	1.3	2200	0.150	6.16
Case 3	N ₂	145.4	1.3	2200	0.300	6.16
Case 4	CO ₂	95.0	0.3	2200	0.072	1.00

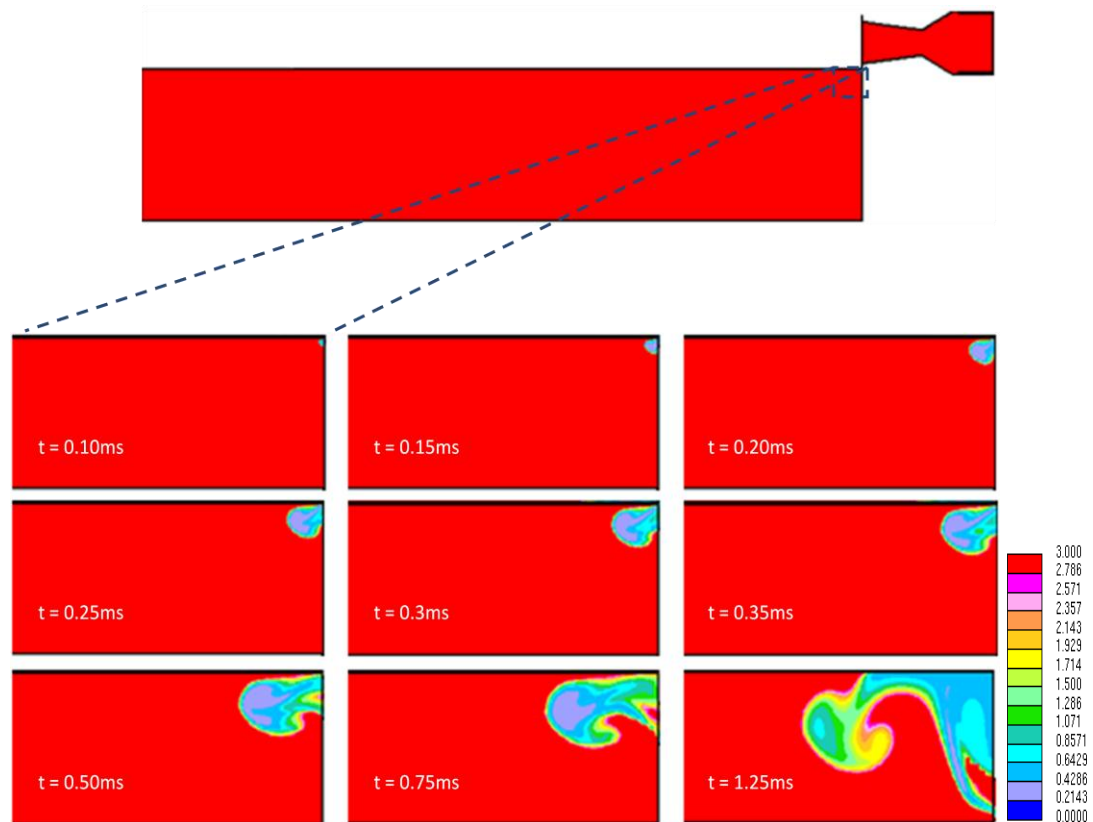


Figure 5.6. Ignition Delay Time of Ethylene for Equivalence ratio of 1.0, in $\log(\mu\text{s})$.

In a typical WRCVC, the fueling and mixing processes may not lead to a well-mixed, stoichiometric mixture near the ignition source. The ignition of the combustible mixture might be negatively affected if a very lean mixture exists in the vicinity of the ignition source. Therefore, the ignition delay time was also calculated for a mixture equivalence ratio of 0.6 in the combustor, shown in Figure 5.7. The predicted shortest ignition time delay is $\sim 50 \mu\text{s}$.

The predicted ignition delay times for Cases 1, 2, and 3 introduced in Table 4 are compared in Figure 5.8. It can be seen that the ignition delay in Case 1 is the lowest and in Case 3 is the highest. This difference is very pronounced at times $t = 0.25$ ms and $t = 0.35$ ms. Such a difference may be due to the differences in the exit flow velocities between the three cases. Case 1, with the lowest velocities, does not entrain the cold combustible mixture into the hot jet as much as Case 3 does, thereby not ‘cooling’ the hot jet to a greater extent. If a stratified combustible mixture was assumed to exist in the combustion chambers, with a relatively fuel-lean region near the igniter carrier wall (which is a possible operating condition for WRCVC), the igniter in Case 1 might fail to ignite the combustible mixture away from the igniter carrier wall due to its low penetration. Comparing the three cases after $t = 0.75$ ms confirms this conclusion clearly.

5.4.2 Propane

In order to assess the ignition delay time when propane is used as the fuel, correlations developed by Lamoureux et al. (2002) and Burcat et al (1971) for propane ignition behind reflected shock waves were used.

The correlations are as follows:

$$\tau = 5.06 \times 10^{-15} \exp\left(\frac{28450}{T}\right) [C_3H_8]^{0.85} [O_2]^{-1.3}, \quad (5.5)$$

$$\tau = 4.4 \times 10^{-14} \exp\left(\frac{42.2 \times 10^3}{RT}\right) [C_3H_8]^{0.57} [O_2]^{-1.22} [Ar]^0. \quad (5.6)$$

The ignition delay predictions from the correlation by Lamoureux et al. (2002) (Equation 5.5) are shown in Figure 5.9. The ignition delay time predicted according to the correlation of Burcat et al. (1971) (Equation 5.6) showed similar results. Comparing this figure to Figure 5.6 shows the difference in ignition time delays of ethylene and propane. The shortest ignition delay time predicted for ethylene was in the order of 10 μs while the shortest ignition delay time predicted for propane was in the order of 300 μs . This order of magnitude difference in ignition delay times was also observed by Perera (2010), using a hot gas jet assisted ignition experiment. The numerical methodology used can be used to predict the ignition success or failure accurately. In conjunction with well defined experiments, that measure local concentrations of the jet mixing region, these computations can be used to predict the local temperatures of the mixture in the ignition regions and the ignition delay times which might be difficult to obtain experimentally. The numerical simulations can be tuned to match the measured local concentrations of species prior to ignition and the predictions can be used to get accurate estimations of ignition temperatures and precise ignition delay times.

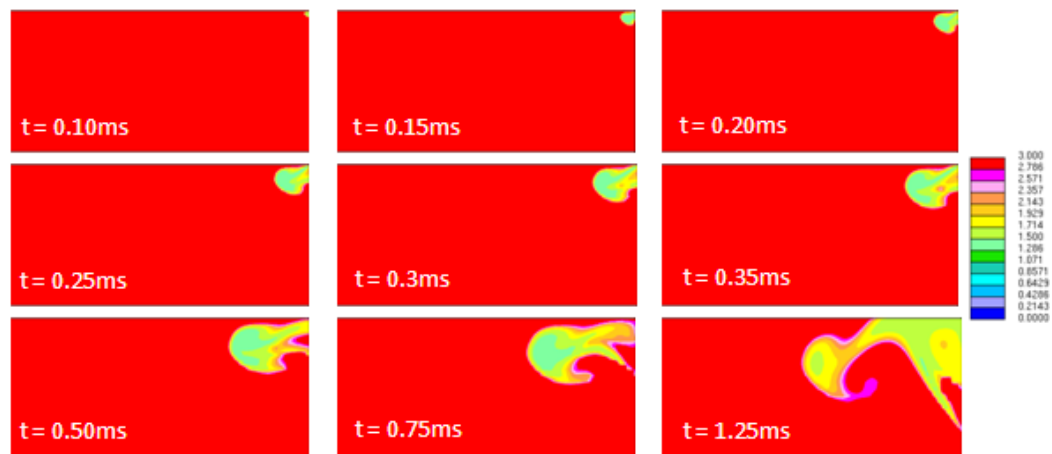


Figure 5.7. Ignition Delay Time of Ethylene for Equivalence ratio of 0.6 in $\log(\mu\text{s})$.

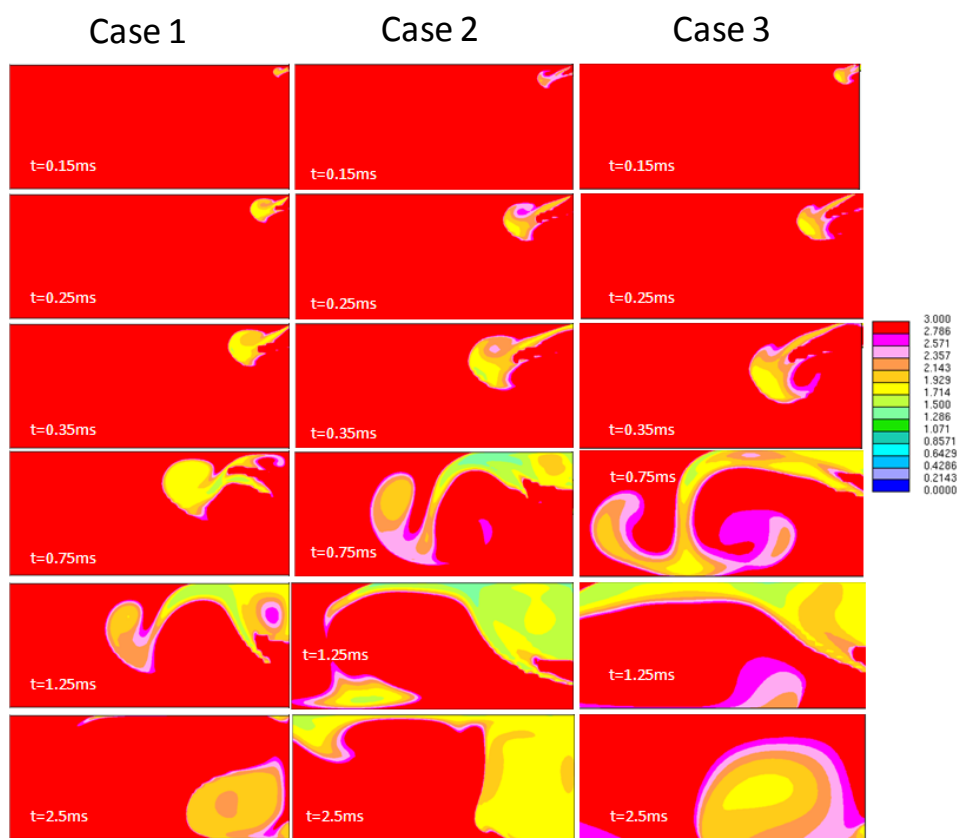


Figure 5.8. Ignition Delay Time (in $\log(\mu\text{s})$) Comparison of Ethylene.

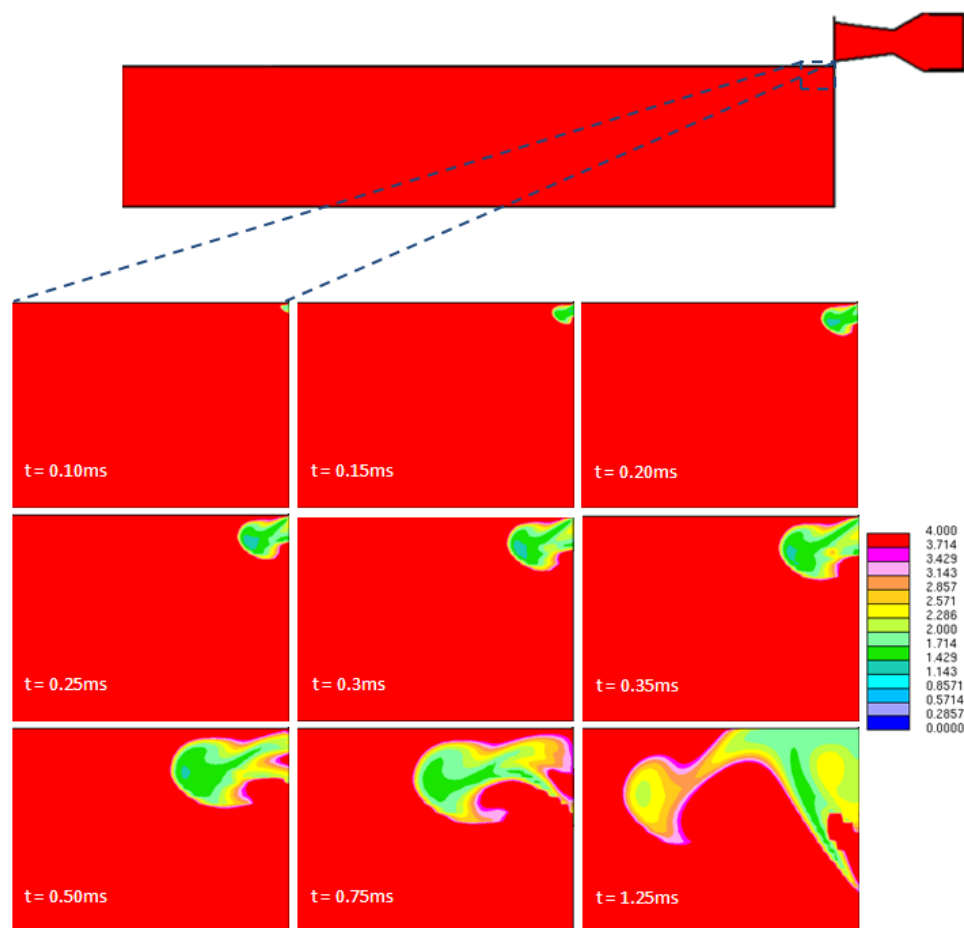


Figure 5.9. Prediction of Propane Ignition Delay According to the Correlation of Lamoureux et al. (2002).

CHAPTER 6. COMPUTATIONAL METHODS AND ACCURACY.

6.1 Introduction

The computational resources which were available and the numerical methods used for the work in this thesis is discussed in this chapter. The hardware and software resources available to the author during the course of this thesis are discussed in the first part of the chapter, followed by the grid independence studies performed for representative cases used in the thesis. A short discussion on the turbulence models is presented next, followed by some reasoning on the URANS models used in this thesis. The chapter is concluded with a discussion on the importance of modeling the preceding exit port for translating jet injection modeling of a WRCVC.

6.2 Computational Capabilities and Resources

The commercial code StarCD was used for the current analysis. The code uses a finite-volume formulation of the Navier-Stokes equations. A second-order accurate spatial differencing scheme was used for the momentum, energy, turbulence, and species transport equations, while an implicit temporal discretization was used for transient computations. The code uses a pressure based solver, where the governing equations are solved sequentially (i.e., segregated from one another). Unlike in density-based solvers, the pressure is not obtained directly from the continuity and state equations, but by using a pressure correction equation, derived using the continuity and momentum equations. Due to the non-linear and coupled nature of the governing equations in compressible flows, the solution loop must be carried out iteratively in order to obtain a converged numerical solution. The segregated algorithm is memory-efficient, although, the solution convergence is relatively slow, due to decoupling of the equations. The solution algorithms employed in the code are applicable to both incompressible and compressible flows (subsonic, transonic, and supersonic). A shock capturing technique is used to handle shock waves but may not provide as sharp a resolution of shocks as density-based solvers without very fine grids.

The computations were run on two dedicated 8-processor Dell Precision 690 machines (64 bit architecture, 2.66 GHz processor and 24 Gig RAM) as well as on ‘Quarry,’ one of the high performance computer clusters at the Indiana University. Quarry is a cluster composed of IBM HS21 Blade servers and IBM iDataPlex dx340 rack-mounted servers

running Red Hat Linux. Job management is provided by the TORQUE resource manager (also called PBS) and the Moab job scheduler. Quarry consists of two types of machines:

- 140 IBM HS21 Blade servers, each containing two Intel Xeon 5335 quad-core processors, 8 or 16 GB of memory, a 36 or 73 GB locally attached SAS disk for local scratch space, and gigabit Ethernet for system interconnects
- 230 IBM iDataPlex dx340 rack-mounted servers, each with two Intel Xeon E5410 quad-core processors, 16 GB of memory, 98 GB locally attached scratch space, and gigabit Ethernet for system interconnects

The number of processors used in this analysis was limited by the number of commercial licenses available. During the tenure of this thesis, there were 40 ‘hpc’ licenses and 10 general licenses. Each processor run would utilize one ‘hpc’ license. A script file which has details on the number of processors the analysis would be run on, estimated time required for the analysis, execution commands of the software, location to store the data, and some other control commands had to be submitted into the queuing system of the supercomputing cluster “Quarry.” The job scheduler assigns the requested amount of processors and computing time, based on server availability. Two files pbs.sh and star.sh contained these commands:

The file pbs.sh contains the following lines:

```
#!/bin/bash
#PBS -l nodes=4:ppn=8,walltime=10:00
#PBS -m ae
```

```
#PBS -N star.sh

STARINI="Default"; export STARINI

/N/hd00/rmeagher/Quarry/starcd/highRePart3PressureBased/star.sh
```

The file star.sh contains the following lines:

```
#!/bin/bash

cd /N/u/rmeagher/Quarry/starcd/highRePart3PressureBased

./N/soft/linux-rhel4-x86_64/starcd/starcd_4.10.019_x64/etc/setstar

star -mpi=lam -decompmeth=x -nodefile=$PBS_NODEFILE
```

The author had access to two mass storage systems at Indiana University which were used as backup storage. The Scholarly Data Archive (SDA) is primarily a tape-based archive storage system. Currently SDA has a raw tape capacity of 5.7PB. It has over 200TB of spinning disk space that operates as a cache for files moving to or from tape. SDA is geographically distributed between the IUPUI and IUB campuses. By default, a file stored in SDA has a copy on each campus. This protects from minor problems like tape failures to major ones like a site disaster. Each campus has an automated tape library capable of holding over 5,000 tapes and 24 high speed tape drives. SDA has an aggregate transfer rate of over 2GB per second. It is capable of storing files from about 1MB to over 5TB in size. The Research File System (RFS) is a spinning disk system with currently 30TB of total capacity. RFS can be mounted on the desktop or accessed over the web or SFTP protocol. RFS supports active editing of files and documents, unlike the SDA. Files are backed up on a nightly basis from RFS. RFS has robust support for

project work as well. Quotas start at 10GB for personal space and 50GB for project space.

6.3 Grid and Time Step Independence

The region of jet and vortex dynamics that is of most interest and with the sharpest gradients requires careful grid generation. This is illustrated in Figure 6.1, for stationary and traversing injector cases. Unlike in a stationary jet, the shear layer of the moving jet is not confined to a conical region that diverges into the chamber starting from the jet exit. The translating jet covers the entire width of the chamber and hence requires adequate refinement throughout the width of the chamber to accurately capture the essential jet physics.

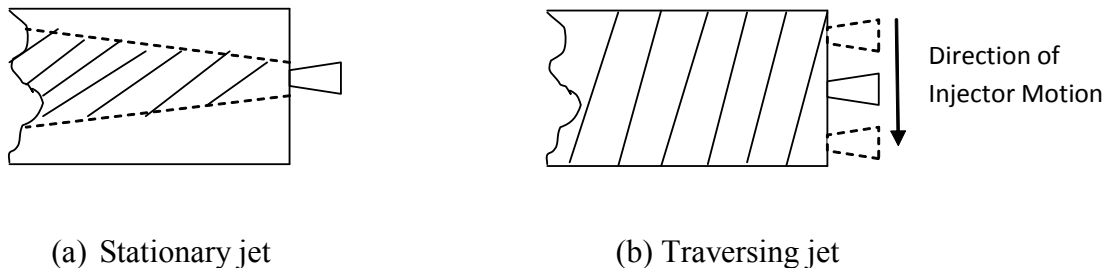


Figure 6.1. Regions of Mixing, Diffusion, and Vorticity requiring High Grid Resolutions (hashed).

- (a) Conical Region of interest in the Stationary Jet
- (b) The Entire Combustion Channel Width becomes the Region of Interest due to Injector Motion

Velocity vector plots and vorticity contour plots were compared visually and the axial velocity variation was compared using different computational cell sizes and time steps.

The time step and the grid size analysis showed that a maximum Courant number about

0.5 produces time-step independent results, if the grid is sufficiently fine. The grid should be able to resolve at least the large scale flow structures. Five successively finer grids are compared in Figure 6.5. It is seen that Grid 1 cannot capture the large scale structures. Grid 3 to Grid 5 exhibit only finer scale differences in vorticity contours. It is interesting to see that the vortices appear ‘stretched’ in coarse grid computations. This can affect mixing of the injected gas, as the vortices are responsible for the local mixing, underlining the importance of adequate spatial and temporal resolution. Taking into account the computational cost, Grid 4 was selected with a computational time step of 5×10^{-7} . Three different time steps were compared, using Grid 3. It can be seen from Figure 6.5 that there is no significant change in the results when reducing the time step from 10^{-6} (corresponds to Courant No. = 0.5) to 2.5×10^{-7} .

Table 6.1. Cell Counts and Computational Times of the Grids used
(Wijeyakulasuriya, 2009).

Grid	No. of cells	Time per iteration (sec)	Total simulation time (hrs)
Grid 1	17700	1	1.5
Grid 2	74300	2	3
Grid 3	157800	4	7
Grid 4	263500	5	15
Grid 5	328000	7	20

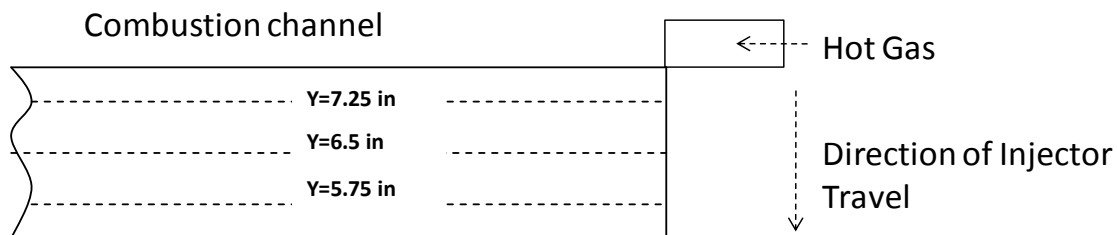


Figure 6.2. Part of the Wave Rotor Channel in which Axial Velocity Fluctuations are Analyzed.

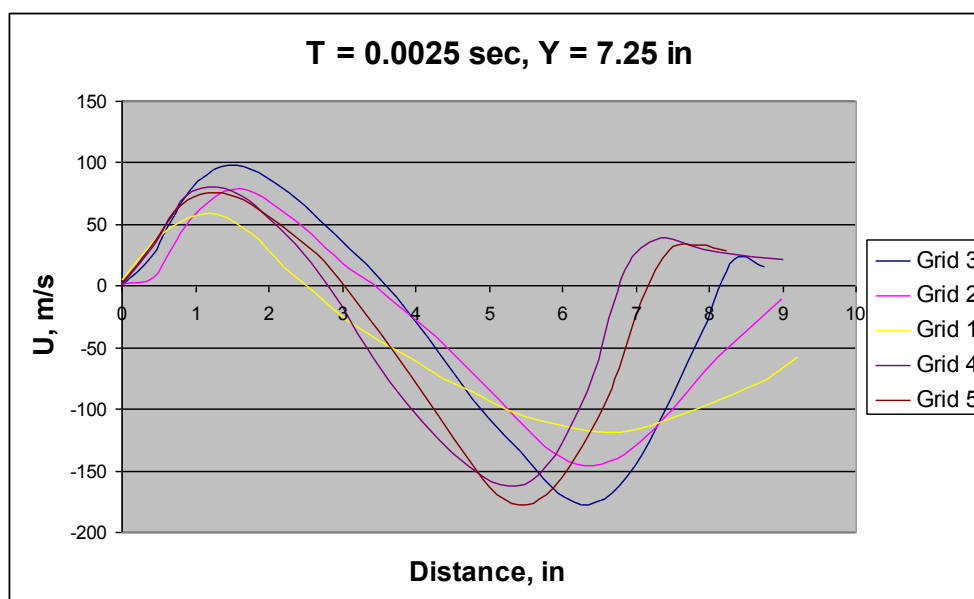


Figure 6.3. Axial Velocity Variation with Grid Density.

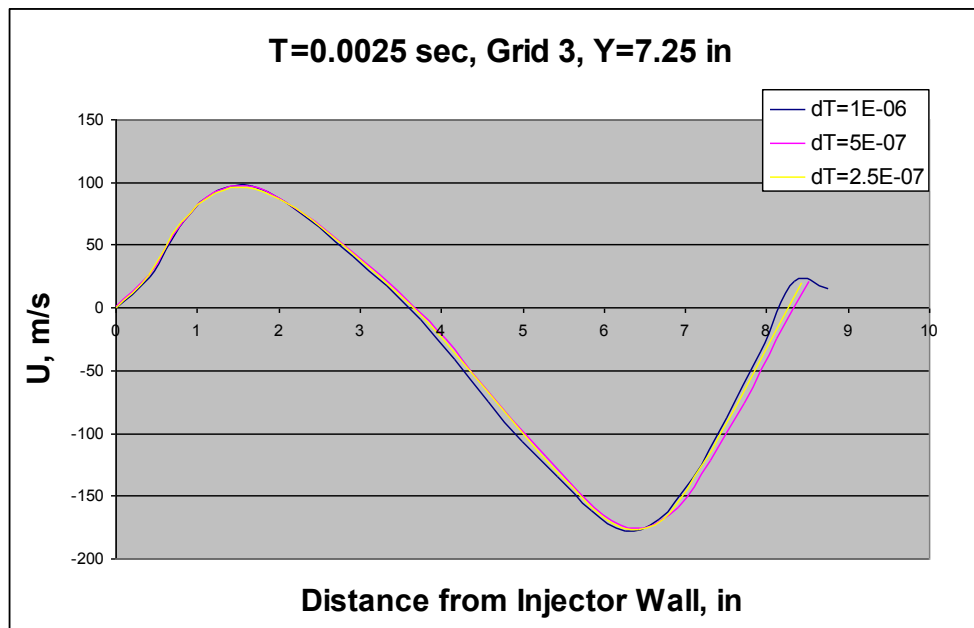


Figure 6.4. Axial Velocity variation with Computational Time Step.

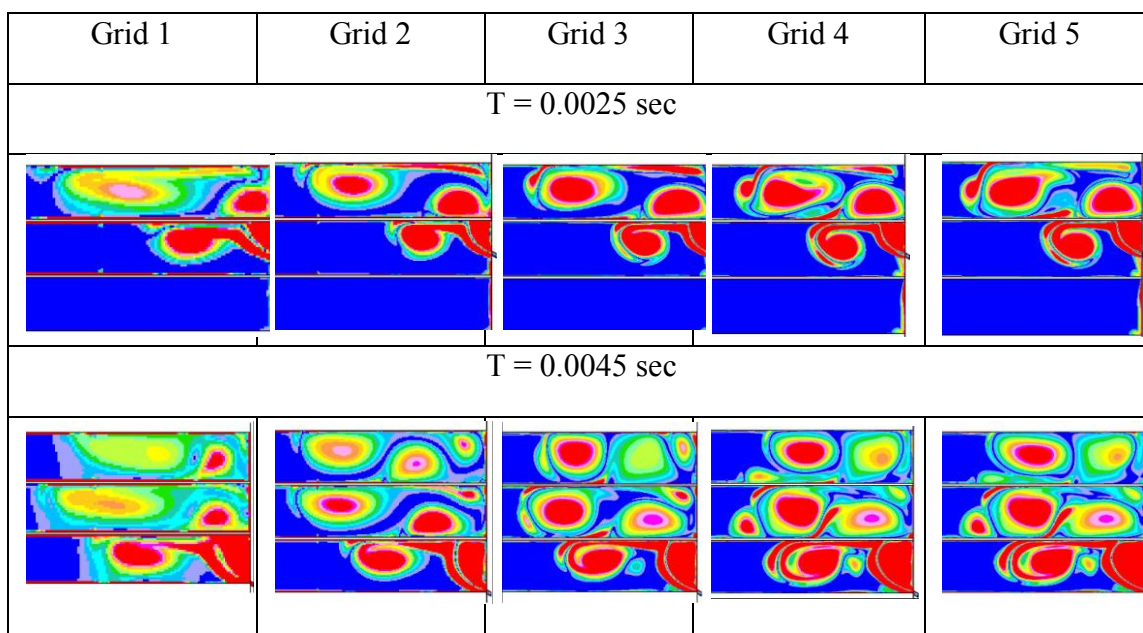


Figure 6.5. Vorticity predicted at Different Grid Densities, $dt = 1E-06$ (color scheme same as Fig. 6.6).

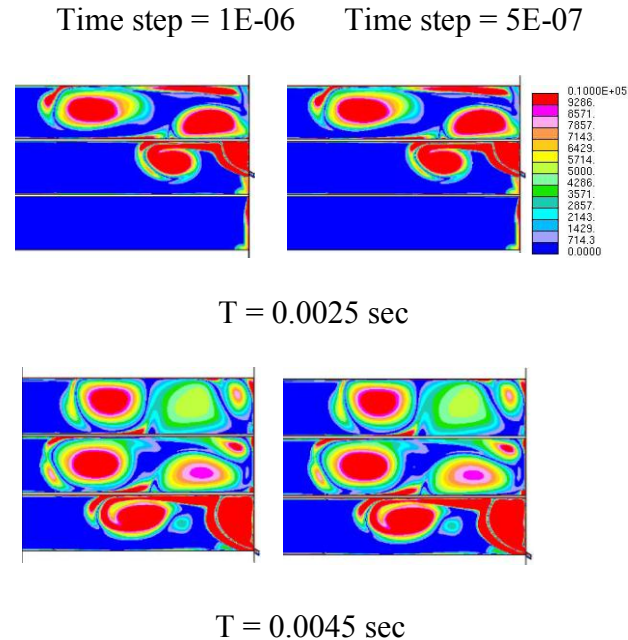


Figure 6.6. Vorticity Magnitude Contours, Grid.

6.4 Turbulence Model Selection

Turbulent flows are characterized by fluctuating velocity fields. These fluctuations mix transported quantities such as momentum, energy, and species concentration, and cause the transported quantities to fluctuate as well. Since these fluctuations can be of small scale and high frequency, they are too computationally expensive to simulate directly in practical engineering calculations. Instead, the instantaneous governing equations can be time-averaged, ensemble-averaged, or otherwise manipulated to remove the small scales, resulting in a modified set of equations that are computationally less expensive to solve. However, the modified equations contain additional unknown variables, and turbulence models are needed to determine these variables in terms of known quantities.

For most engineering applications it is sufficient to resolve the mean flow, without resolving the details of the turbulent fluctuations. A turbulence model can be defined as a computational procedure to close the system of mean flow equations. Classical turbulence models based on Reynolds Averaged Navier-Stokes (RANS) equations are given below.

6.4.1. Zero-equation Models

Zero-equation models or algebraic turbulence models are models that do not require the solution of any additional differential equations, and are calculated directly from the flow variables. E.g.: Baldwin-Lomax model (Baldwin and Lomax, 1978) and Cebeci-Smith model (Smith and Cebeci, 1967).

6.4.2. One-equation Models

One-equation models solve one turbulent transport equation, usually the turbulent kinetic energy. E.g.: Baldwin-Barth model (Baldwin and Bath, 1990) and Spalart-Almaras model (Spalart and Almaras, 1992).

6.4.3. Two-equation Models

Two-equation models include two transport equations to represent the turbulent properties of the flow which account for history effects like convection and diffusion of

turbulent energy. The first transport variable is usually turbulent kinetic energy, k , while popular choices for the second variable are the turbulent dissipation, ε , or the specific dissipation, ω . E.g.: k - ε model and k - ω model.

As explained in Chapter 3, different jet flows require different modeling techniques to be able to predict their characteristics accurately. Turbulence model selection is key in trying to predict different jet flow conditions. The growth of the shear layer varies in different types of jet flows and hence requires different turbulence models which can predict these behaviors accurately. The shear layer of the free jet develops freely in the absence of the confining walls and requires a model which can model the free stream flow accurately (e.g.: standard k - ε model). On the other hand the shear layer growth is disrupted by the confining walls in confined jet flows. A turbulence model which can predict near wall flows accurately is required for accurate prediction in these situations. Wall functions can also be used in conjunction with the turbulence models to better predict the near wall flows. The following presents a brief discussion on several popular turbulence models used in modeling various types of jet flows.

Based on the Boussinesq eddy-viscosity assumption, the Reynold's stress tensor τ_{ij} is taken to be proportional to the mean stress tensor, S_{ij} in all turbulent viscosity models as shown in Equation 6.1 (Pope, 2000):

$$\tau_{ij} = 2\mu_t S_{ij} - \frac{2}{3}\rho k \delta_{ij}. \quad (6.1)$$

Using the definitions for Reynold's stress tensor and mean stress tensor, Equation 6.1 becomes,

$$-\overline{\rho u_i u_j} = \mu_t \left(\frac{\partial U_i}{\partial x_j} + \frac{\partial U_j}{\partial x_i} \right) - \frac{2}{3} \rho k \delta_{ij}. \quad (6.2)$$

Different turbulence models listed above model the turbulent viscosity, μ_t differently. The effect of turbulence on mean flow is modeled similar to molecular viscosity. Although the validity of Boussinesq approximation is questionable in complex flow situations, this simplification is widely used.

Two-equation models are single-point closure models, and hence contain no direct length-scale information. In single-point closures, we cannot directly account for spectral dynamics features such as energy transfer between scales of different sizes. Instead we have to assume a self-similar type of development of the energy spectra, where the development is governed by a single length scale. Two differential equations are solved for quantities that can be used to form a velocity scale and a length scale, which in turn are used in the eddy viscosity. The velocity scale is usually determined from the turbulent kinetic energy, k , and several methods can be used to calculate the second quantity which is used to find the length scale. Of the many two-equation models in the literature, two popular models are used extensively in this thesis and presented below.

6.4.3.1. Shear Stress Transport (SST) k - ω Model (Menter, 1993)

Developed by Menter in 1993 the SST model is formulated to retain the robust and accurate formulation of the Wilcox k - ω model (Wilcox, 1998) in the near wall region and to take advantage of the free-stream independence of the k - ϵ model (Launder, 1974) in the outer part of the boundary layer. Hence the SST k - ω model is virtually identical to the k - ϵ model (in a k - ω formulation) for free shear layers and has the additional ability to account for the transport of the principal turbulent shear stress in adverse pressure gradient boundary layers. In order to achieve the blend between these two models, the original k - ω model (Equations 6.3 and 6.4) constants (σ_{k1} , $\sigma_{\omega1}$, etc.) are multiplied by a function $F1$ and the transformed model (k - ϵ model in the k - ω formulation – Equations 6.5 and 6.6) constants (σ_{k2} , $\sigma_{\omega2}$, etc.) by a function $(1-F1)$, and both are added together (Equation 6.9) to obtain the SST model constants given in Table 6.2. The model is based on Bradshaw's assumption (Bradshaw et al., 1967) that the principal shear-stress is proportional to the turbulent kinetic energy, which is introduced into the definition of the eddy-viscosity. The predictions of the SST model are also independent of the free-stream values but show better agreement with experimental data for adverse pressure gradient boundary-layer flows (Menter, 1993):

Original k - ω model (Wilcox, 1998):

$$\frac{D\rho k}{Dt} = \tau_{ij} \frac{\partial u_i}{\partial x_j} - \beta^* \rho \omega k + \frac{\partial}{\partial x_j} \left[(\mu + \sigma_{k1} \mu_t) \frac{\partial k}{\partial x_j} \right], \quad (6.3)$$

$$\frac{D\rho \omega}{Dt} = \frac{\gamma_1}{\nu_t} \tau_{ij} \frac{\partial u_i}{\partial x_j} - \beta_1 \rho \omega^2 + \frac{\partial}{\partial x_j} \left[(\mu + \sigma_{\omega1} \mu_t) \frac{\partial \omega}{\partial x_j} \right]. \quad (6.4)$$

Transformed $k - \varepsilon$ model (Menter, 1993):

$$\frac{D\rho k}{Dt} = \tau_{ij} \frac{\partial u_i}{\partial x_j} - \beta^* \rho \omega k + \frac{\partial}{\partial x_j} \left[(\mu + \sigma_{k2} \mu_t) \frac{\partial k}{\partial x_j} \right], \quad (6.5)$$

$$\frac{D\rho \omega}{Dt} = \frac{\gamma_2}{\nu_t} \tau_{ij} \frac{\partial u_i}{\partial x_j} - \beta_2 \rho \omega^2 + \frac{\partial}{\partial x_j} \left[(\mu + \sigma_{\omega 2} \mu_t) \frac{\partial \omega}{\partial x_j} \right] + 2\rho \sigma_{\omega 2} \frac{1}{\omega} \frac{\partial k}{\partial x_j} \frac{\partial \omega}{\partial x_j}. \quad (6.6)$$

SST $k - \omega$ model (Menter, 1993):

Turbulent kinetic energy equation:

$$\frac{\partial}{\partial t} (\rho k) + \frac{\partial}{\partial x_j} \left[\rho u_j k - \left(\mu + \frac{\mu_t}{\sigma_k^\omega} \right) \frac{\partial k}{\partial x_j} \right] = \mu_t P - \rho \beta^* k \omega + \mu_t P_B, \quad (6.7)$$

Specific dissipation rate ($\omega = \varepsilon/k$) equation:

$$\frac{\partial}{\partial t} (\rho \omega) + \frac{\partial}{\partial x_j} \left[\rho u_j \omega - \left(\mu + \frac{\mu_t}{\sigma_\omega^\omega} \right) \frac{\partial \omega}{\partial x_j} \right] = \alpha \frac{\omega}{k} \mu_t P - \rho \beta \omega^2 + \rho S_\omega + C_{\varepsilon 3} \mu_t P_B C_\mu \omega, \quad (6.8)$$

where,

$$\beta = \beta_0 f_\beta \beta^* = \beta_0^* f_\beta^* \beta^* \chi_\omega = \frac{|\Omega_{ij} \Omega_{jk} S_{ki}|}{(2\beta_0^* \omega)^3} \beta^* f_\beta = \frac{1 + 70\chi_\omega}{1 + 80\chi_\omega} \beta^* = \begin{cases} 1, & \chi_k \leq 0 \\ \frac{1 + 680\chi_k^2}{1 + 400\chi_k^2}, & \chi_k > 0 \end{cases}$$

$$\chi_k = \frac{1}{\omega^3} \frac{\partial k}{\partial x_j} \frac{\partial \omega}{\partial x_j},$$

$$C_\phi = F_1 C_{\phi 1} + (1 - F_1) C_{\phi 2}. \quad (6.9)$$

Model constants ($C_{\phi 1}$) (Wilcox, 1998):

$$\sigma_{k1} = 0.5, \sigma_{\omega 1} = 0.5, \beta_1 = 0.0750, \beta^* = 0.09, \kappa = 0.41, \gamma_1 = \frac{\beta_1}{\beta^*} - \frac{\sigma_{\omega 1} \kappa^2}{\sqrt{\beta^*}}$$

Model constants ($C_{\phi 2}$) (Standard $k - \varepsilon$):

$$\sigma_{k2} = 1.0, \sigma_{\omega 2} = 0.856, \beta_2 = 0.0828, \beta^* = 0.09, \kappa = 0.41, \gamma_2 = \frac{\beta_2}{\beta^*} - \frac{\sigma_{\omega 2} \kappa^2}{\sqrt{\beta^*}}.$$

$$F_1 = \tanh(\arg_1^4), \arg_1 = \min \left[\max \left(\frac{\sqrt{k}}{0.09\omega y}, \frac{500\nu}{y^2\omega} \right); \frac{4\rho k}{\sigma_{\omega 2}^\omega CD_{k\omega} y^2} \right],$$

$$CD_{k\omega} = \max \left(\frac{2\rho}{\omega \sigma_{\omega 2}^\omega} \frac{\partial k}{\partial x_j} \frac{\partial \omega}{\partial x_j}, 10^{-20} \right), \alpha_1 = \frac{\beta_1}{\beta_1^*} - \frac{1}{\sigma_{\omega 1}^\omega} \frac{\kappa^2}{\sqrt{\beta_1^*}}, \alpha_2 = \frac{\beta_2}{\beta_2^*} - \frac{1}{\sigma_{\omega 2}^\omega} \frac{\kappa^2}{\sqrt{\beta_2^*}},$$

$$S_\omega = 2(1 - F_1) \frac{1}{\sigma_{\omega 2}^\omega} \frac{1}{\omega} \frac{\partial \omega}{\partial x_j} \frac{\partial k}{\partial x_j}, \mu_t = \rho \frac{a_1 k}{\max(a_1 \omega, \Omega^* F_2)}, F_2 = \tanh(\arg_2^2),$$

$$\arg_2 = \max \left[\left(2 \frac{\sqrt{k}}{0.09\omega y}, \frac{500\nu}{y^2\omega} \right) \right].$$

Table 6.2. The Model Constants used in the SST k- ω Model.

α	β_0	β_0^*	α_k^ω	α_ω^ω	σ_{k1}^ω	$\sigma_{\omega 1}^\omega$	β_1	β_1^*	κ	σ_{k2}^ω	$\sigma_{\omega 2}^\omega$	β_2	β_2^*	a_1
0.52	0.072	0.09	2.0	2.0	1.176	2.0	0.075	0.09	0.41	1.0	1.168	0.0828	0.09	0.31

6.4.3.2. High Reynolds Number k- ε Model (Tahry, 1983)

The standard k- ε model (Jones and Launder, 1972, Launder and Sharma, 1974) has several advantages over simpler models like the zero-equation model (e.g., the mixing length model) or a one-equation model, but it still has shortcomings. The most fundamental criticism of the model is its basic assumption that turbulence reacts to the mean strain rate in a similar manner to a Newtonian molecular response. The validity of such an assumption rests on a variety of factors (Tennekes, H. and Lumley, 1974, Lumley, 1967). The most relevant among them is the magnitude of the ratios of time and length scales between turbulent and mean motions. The model is most accurate when these ratios are small compared to unity. Morel and Mansour (1982) reported that the k- ε model

originally was developed and tested (see Launder and Spalding(1972) and Rodi (1972)) in incompressible flows of a relatively simple nature (mainly of the boundary-layer type). It subsequently has been used with various degrees of success in more complicated recirculating flows that included density variation caused by thermal stratification (Khalil et al., 1975) and free shear flows influenced by Mach number effects (Launder et al., 1973). Tahry (1983) modified this standard k - ε model to incorporate compressibility effects, so that it can be used in compressible flow problems with confidence. The code used in this thesis uses a similar compressible version of the standard k - ε model, called ‘high Reynolds number k - ε model.’

The turbulent kinetic energy and dissipation rate equations of the high Reynolds number k - ε equation is given in Eq. (6.5) and Eq. (6.6). The four terms on the right side of the kinetic energy equation represent, in order, turbulent production, viscous dissipation, compressibility effects, and non-linear contributions. The third term, which takes into account the amplification and attenuation of turbulence due to compressibility effects, is important in modeling variable density turbulent shear flows. The spreading rate of compressible mixing layers decreases sharply with Mach number (Bogdanoff, 1983, Papamoschou and Roshko, 1988). Sarkar (1995) showed that this is due to a reduction in the amount of turbulent kinetic energy produced by mean shear, leading to a reduction of turbulent mixing in variable density compressible shear flows:

$$\frac{\partial}{\partial t}(\rho k) + \frac{\partial}{\partial x_j} \left[\rho u_j k - \left(\mu + \frac{\mu_t}{\sigma_k} \right) \frac{\partial k}{\partial x_j} \right] = \mu_t (P + P_B) - \rho \varepsilon - \frac{2}{3} \left(\mu_t \frac{\partial u_i}{\partial x_i} + \rho k \right) \frac{\partial u_i}{\partial x_i} + \mu_t P_{NL}, \quad (6.10)$$

where,

$$P \equiv \left(\frac{\partial u_i}{\partial x_j} + \frac{\partial u_j}{\partial x_i} \right) \frac{\partial u_i}{\partial x_j} \quad - \text{Turbulence production by shear and normal stresses,}$$

$$P_B \equiv -\frac{g_i}{\sigma_{h,i}} \frac{1}{\rho} \frac{\partial \rho}{\partial x_i} \quad - \text{Turbulence production by buoyancy forces,}$$

$$P_{NL} = -\frac{\rho}{\mu_t} \overline{u_i u_j} \frac{\partial u_i}{\partial x_j} - \left[P - \frac{2}{3} \left(\frac{\partial u_i}{\partial x_i} + \frac{\rho k}{\mu_t} \right) \frac{\partial u_i}{\partial x_i} \right] \quad - \text{Non-linear contributions.}$$

The turbulent dissipation rate equation used in the current analysis is given by Equation

(6.11):

$$\begin{aligned} \frac{\partial}{\partial t} (\rho \varepsilon) + \frac{\partial}{\partial x_j} \left[\rho u_j \varepsilon - \left(\mu + \frac{\mu_t}{\sigma_\varepsilon} \right) \frac{\partial \varepsilon}{\partial x_j} \right] &= C_{\varepsilon 1} \frac{\varepsilon}{k} \left[\mu_t P - \frac{2}{3} \left(\mu_t \frac{\partial u_i}{\partial x_i} + \rho k \right) \frac{\partial u_i}{\partial x_i} \right] + C_{\varepsilon 3} \frac{\varepsilon}{k} \mu_t P_B \\ - C_{\varepsilon 2} \rho \frac{\varepsilon^2}{k} + C_{\varepsilon 4} \rho \varepsilon \frac{\partial u_i}{\partial x_i} + C_{\varepsilon 1} \frac{\varepsilon}{k} \mu_t P_{NL}, & \end{aligned} \quad (6.11)$$

where σ_ε is the turbulent Prandtl number, and $C_{\varepsilon 1}, C_{\varepsilon 2}, C_{\varepsilon 3}, C_{\varepsilon 4}$ are model coefficients

These model coefficients are:

$$C_{\varepsilon 1} = 1.44, C_{\varepsilon 2} = 1.92, C_{\varepsilon 3} = 1.44, C_{\varepsilon 4} = -0.33, C_\mu = 0.09, \sigma_k = 1.0, \sigma_\varepsilon = 1.22.$$

6.4.4. Reynolds Stress Models

Reynolds stress models do not use the Boussinesq approximation and solve differential equations for the Reynolds stresses. This replaces the k-equation with 6 Reynolds stress equations, and hence introduces many new terms that have to be modeled. The dissipation equation is still solved for in a similar manner as in RANs models.

6.4.5. Large Eddy Simulation Models

Large Eddy Simulation (LES) models use a spatial filter to remove the small length scales from the flow and use a subgrid-scale (SGS) model to determine how the small eddies influence the resolved ones, solving directly for the motion of the large eddies. Usually the SGS model is an eddy viscosity model, although there are variations to this. For an eddy viscosity model, the length scale is provided by the grid spacing or the filter width of an explicitly applied solution filter.

6.4.6. Direct Numerical Simulations

This approach does not use a turbulence model. It requires solving the time dependent Navier-Stokes equations and resolving all of the relevant length scales in the flow.

Valentino et al. (2007) compared Reynolds-averaged Navier-Stokes (RANS) and large eddy simulation (LES) approaches to modeling confined axisymmetric gas jets, using the same numerical algorithm and spatial resolution. LES resolved vortical structures and predicted jet mixing and entrainment better than RANS, without the excessive dissipation of RANS. However, unsteady RANS calculations by Song and Abraham (2003) achieved good agreement of jet penetration with the experimental data, using an empirical pipe-flow formula and a $1/7$ power-law velocity profile for the near wall region of impinging jets. Their review of transient round, radial and wall jets acknowledge that turbulence closure is the key challenge in modeling confined jets.

Poroseva & Bezard (2001) report different sets of k- ϵ model coefficients for various jet flows, keeping $C_{\epsilon 2} = 1.9$ & $C_{\mu} = 0.09$ of the standard model and varying the other coefficients to match experimental findings ($C_{\epsilon 3}, C_{\epsilon 4}$ are not included in this analysis). They show that these modified k- ϵ equations predict shear dominated flows (plane wake, mixing layer, plane jet, and round jet) better than the standard k- ϵ model and k- ω turbulent models. For a plane jet they recommend $C_{\epsilon 1} = 1.45, \sigma_k = 0.67, \sigma_{\epsilon} = 1.0$. Figure 6.7 shows a comparison of the axial velocity variation in a channel due to gas injection predicted by the standard k- ϵ method (yellow curve), using the standard coefficients given in high Reynolds number k- ϵ method (blue curve), and a modified k- ϵ model using coefficients proposed by Poroseva and Bezard (2001) for a plane jet (pink curve). There is good agreement between the predictions using the high Reynolds number method and the empirically-modified coefficients Poroseva and Bezard (2001), even while the latter do not use the term for compressibility effects on turbulence structure. Predictions from standard k- ϵ equations show considerable deviation. The high Reynolds number k- ϵ method with its standard coefficients is used in this chapter.

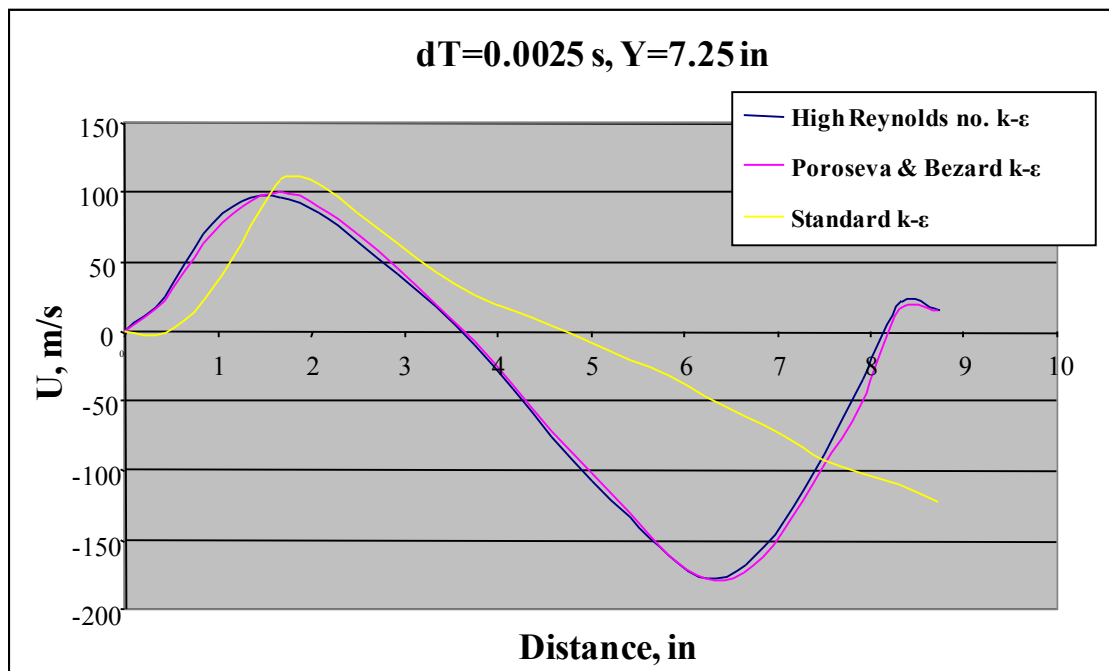
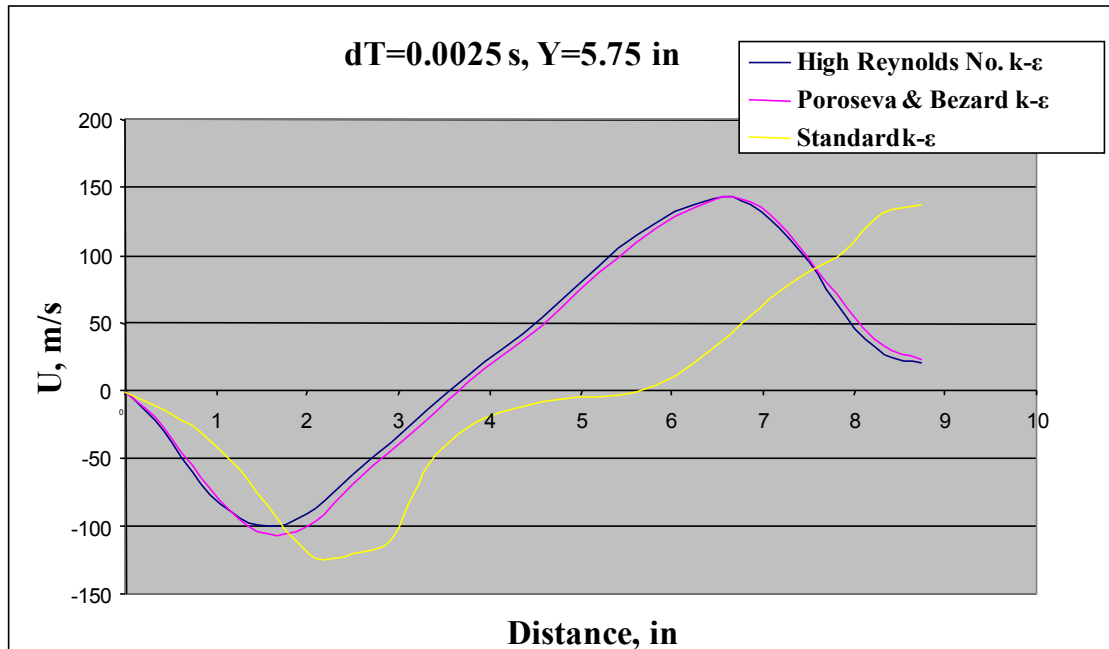


Figure 6.7. Comparison of turbulence model predictions (part of the channel analyzed – Refer Figure 6.2).

6.5 Gradual Opening and Closing of a Combustion Channel to a Port

It is important to understand the multidimensional flow effects taking place inside a WRCVC channel to better predict its performance. Some of the prominent and important multidimensional flow phenomena taking place inside a WRCVC channel are due to, gradual opening and closing of combustion channels to the inlet and exit ports, pilot fuel and hot gas injection, shock wave and flame interactions, centrifugal and Coriolis accelerations. Accurate modeling of these flow phenomena is important in predicting the performance of a WRCVC. Modeling multidimensional flow effects due to fluid injection is discussed in detail in latter chapters. Shock wave and flame front interactions increase the flame area and give rise to baroclinic vorticity which in turn give rise to multidimensional flow effects. Kilchyk (2009) presents detailed numerical analyses of this phenomenon in relation to WRCVC. This section discusses the multidimensional flow generated due to the other two phenomena.

Since both the pilot fuel and hot gas injection are placed after the exhaust port, they can be affected by the blow down process. When a combustion channel rotates into alignment with an inlet/exit port, it is gradually exposed to the port flow. This is called the gradual opening (if the channel meets a port) and gradual closing (if the channel leaves a port). The effects of gradual opening/closing of a channel into a port have been studied before, numerically (Larosiliere, 1993, and Eidelman, 1985). Eidelman (1985) models opening of a single wave rotor channel to its inlet port using unsteady two-dimensional Euler equations, assuming the flow is inviscid. He argues that the pressure waves are not one dimensional throughout the channel in the gradual opening case compared to a suddenly

opened channel and it takes a finite length for the pressure waves to “straighten-up” and be considered one dimensional. The gradual opening process results in a significant distortion of the fluid interface and further delays the formation of the shock wave (Eidelman, 1985). The flow field behind these moving pressure waves (which subsequently coalesce into a shock wave) attains a complex flow structure due to multiple reflections of the shock and pressure waves from passage walls.

These events can adversely affect the performance of a wave rotor (Larosiliere, 1993). Eidelman (1985) attributes this loss of performance to the rotational nature of the flow and the existence of pressure waves which interact strongly with channel walls, preceding the formation of the one-dimensional flow pattern. These behaviors contribute to significant mixing between the fresh combustible mixture and the exhaust gasses from the previous cycle and cause performance losses. The simulations presented in this chapter, and the simulations by Eidelman (1985) were two dimensional, and did not take into account some of the important three-dimensional effects of Coriolis and centripetal accelerations resulted through wave rotor rotation (Larosiliere, 1993). The gradual opening time (defined as the time between the leading and trailing edges of a rotor channel moving past a solid end wall) and the gradual closing time (Figure 6.8) are inversely proportional to the rotational speed of the wave rotor, and hence channel rotation becomes important. Larosiliere and Mawid (1993) have shown how the centripetal and coriolis accelerations affect the interface distortion and the unsteady gasdynamics within the channel. Larosiliere (1993) investigated the impact of Coriolis

and centripetal accelerations on the flow inside a gradually opening wave rotor channel using a three-dimensional Euler code.

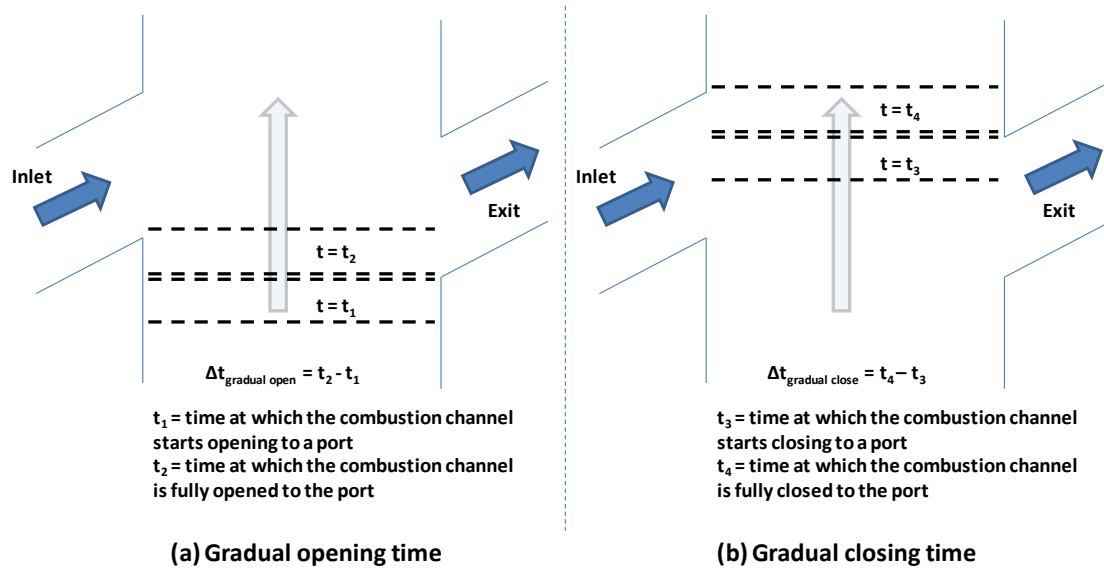


Figure 6.8. Gradual Opening Time and Closing Time based on the Exit Port. The times shown represent the Instantaneous Times when the Combustion Channels are in the Locations shown.

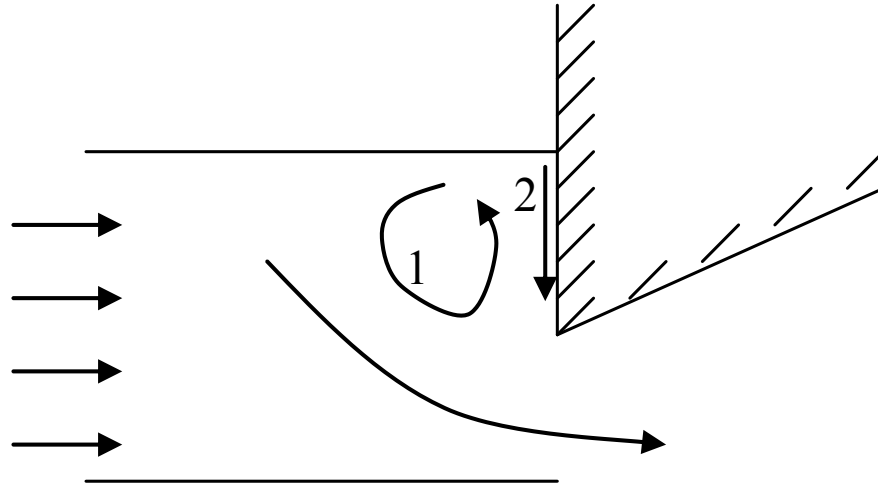


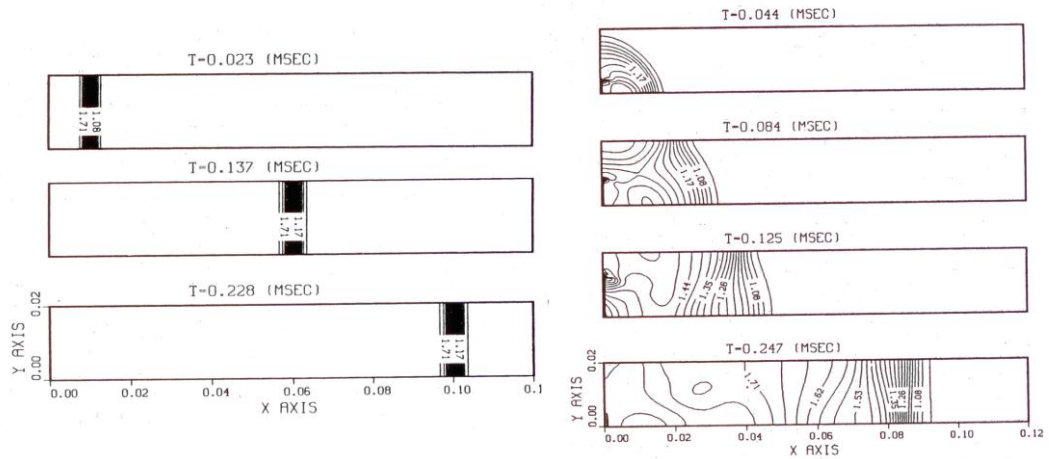
Figure 6.9. Flow in a Gradually Closing Wave Rotor Channel.

In a gradually closing channel, unlike in a gradually opening channel, no dominant axial velocity exists behind the shock wave due to the wall boundary condition. However the flow in the vicinity of the wall is governed by the vorticity induced by the gradual closure (denoted by 1 in Figure 6.9) and the circumferential velocity (denoted by 2 in Figure 6.9) due to channel rotation relative to the stationary end wall. Since these two motions oppose each other, the flow behind the shock wave depends on the relative magnitudes of the vorticity generated tangential flow and the circumferential flow due to channel rotation (Wijeyakulasuriya, 2009). However the Coriolis acceleration cannot be neglected during the period of gradual closing. Due to the rotation of the WRCVC, the gas inside the combustion channel is subjected to Coriolis acceleration (in the rotating frame of reference). The axial flow which comes out of the exit port during the gradual closing process (as viewed in the stationary, exit/inlet port of reference) is viewed as rotational flow by the gas inside the combustion channel due to this Coriolis acceleration. This

circumferential velocity in the rotational frame of reference, generated by the presence of the stationary wall and the outflow through the partial opening, contributes to vorticity inside the combustion channel.

To better understand the effect of gradual closing of the exit port on the channel flow, pressure wave propagation inside the channel due to a gradual closing and sudden closing is compared (Figures 6.10 and 6.11). In the case of Figure 6.11, the channels were initialized with the same velocity in both the cases and in the suddenly closed channel case, the right-hand-side boundary condition is changed to “no-slip wall” from “pressure” boundary condition (exit port was not modeled). In the gradually closed channel case, the exit port was made to slide past the channel. The formation of the shock waves in both cases is similar to what was modeled by Larosiliere (1993) (Figure 6.12). As the passage gradually closes, a series of curved compression waves start forming attached to the leading wall and the end wall. These waves travel into the channel and reflect from the trailing wall to interact with the other oncoming waves. Larosiliere (1993) explains that in a gradual opening situation, these reflected waves interact with the interface between the driver gas and the driven gas and give rise to baroclinic vorticity. However this phenomenon is absent here due to the lack of an interface in the exit side of the wave rotor. Hence the vorticity produced in this instance (gradual closing process) is not as strong as in the gradual opening situation. Larosiliere & Mawid (1993) have explained how the wave structure changes with the rotational speed of a shock tube. While showing the analogy between the flow dynamics in a rotational shock tube with that taking place in a wave rotor channel, they have stated that with increased rotational speed (his analysis

is with respect to a “wheel Mach number” defined as $M_{\Omega} = \Omega R_T / a_{\infty}$) the propagation speed of pressure waves increase due to the higher temperature consistent with higher centrifugal forces. They have observed that the interface becomes oblique prior to any interaction with the reflected shock or rarefaction fronts due to the generation of baroclinic vorticity. This is due to the interaction between the interface (which provides density gradient) and the reflected pressure waves from the channel walls (which provides pressure gradient). If the pilot fuel jet or the hot gas jet enters the channel when the pressure wave reflections are still present, that can cause baroclinic vorticity and enhance local fuel-air mixing. The smearing of the pressure waves near the closing wall and the gradual coalescing of the pressure waves into a shock wave is clearly identifiable in the gradually closing wall case (Figure 6.11). However, the wave traveling times did not show any significant difference in the two cases. Figure 6.12 shows the vorticity deposition on the walls due to gradual closing of the combustion channel in to the exit port. It is interesting to note how this deposited vorticity convects along the leading wall of the channel (Figures 6.12 and 6.13). This will affect the subsequent injection processes in a WRCVC as discussed in Chapter 8.



(a) (b)
 Figure 6.10. Pressure Contours of (a) Instantaneous and (b) Gradual Opening of a Channel (Larosiliere, 1993).

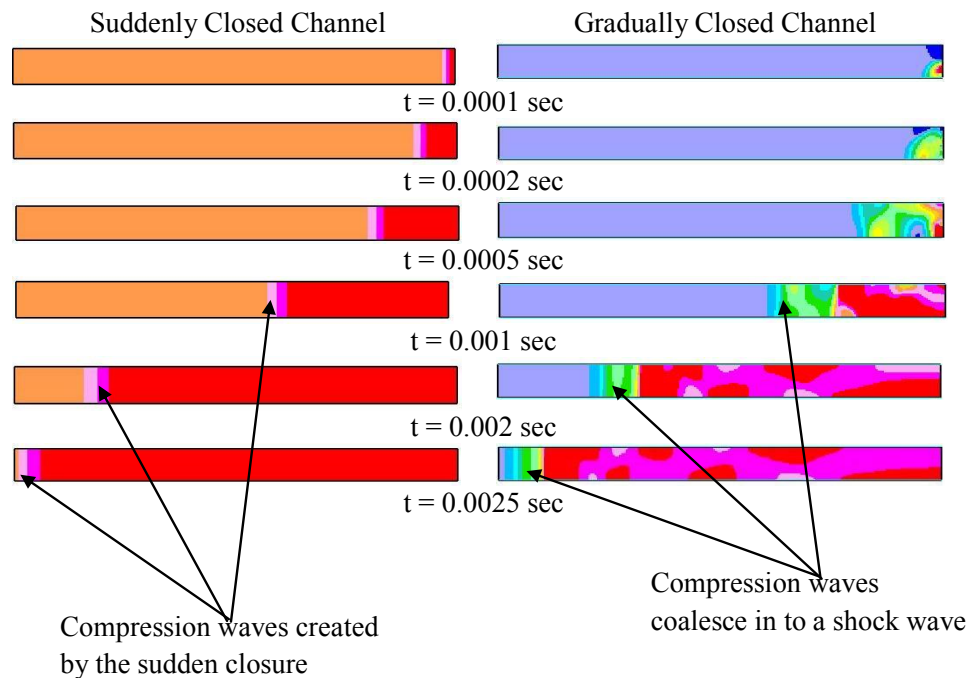


Figure 6. 11. Pressure Contours of Instantaneous and Gradual Closing of a Combustion Channel.

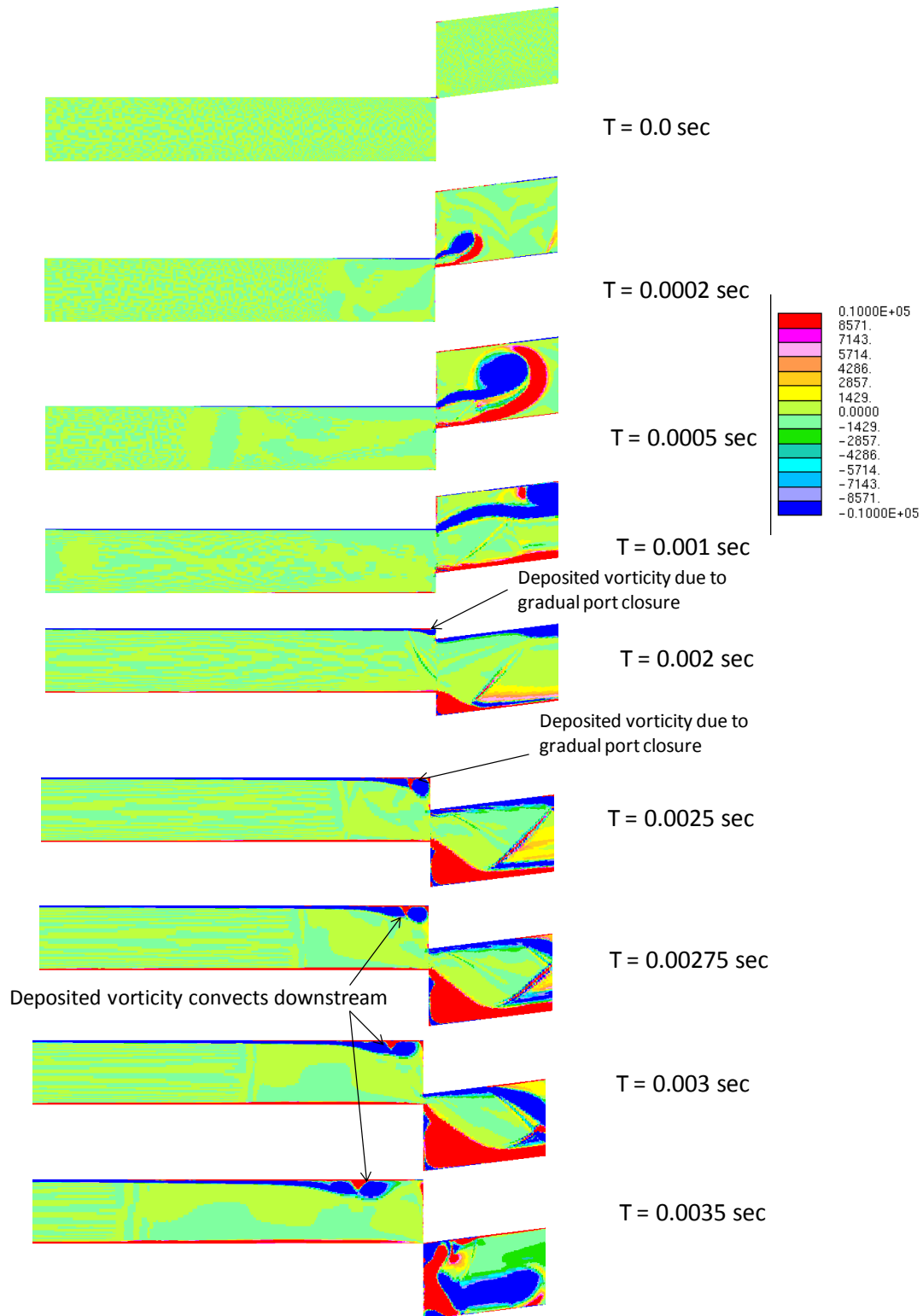


Figure 6.12. Vorticity Contours of Gradual Opening and Closing Processes of a Channel into a Port.

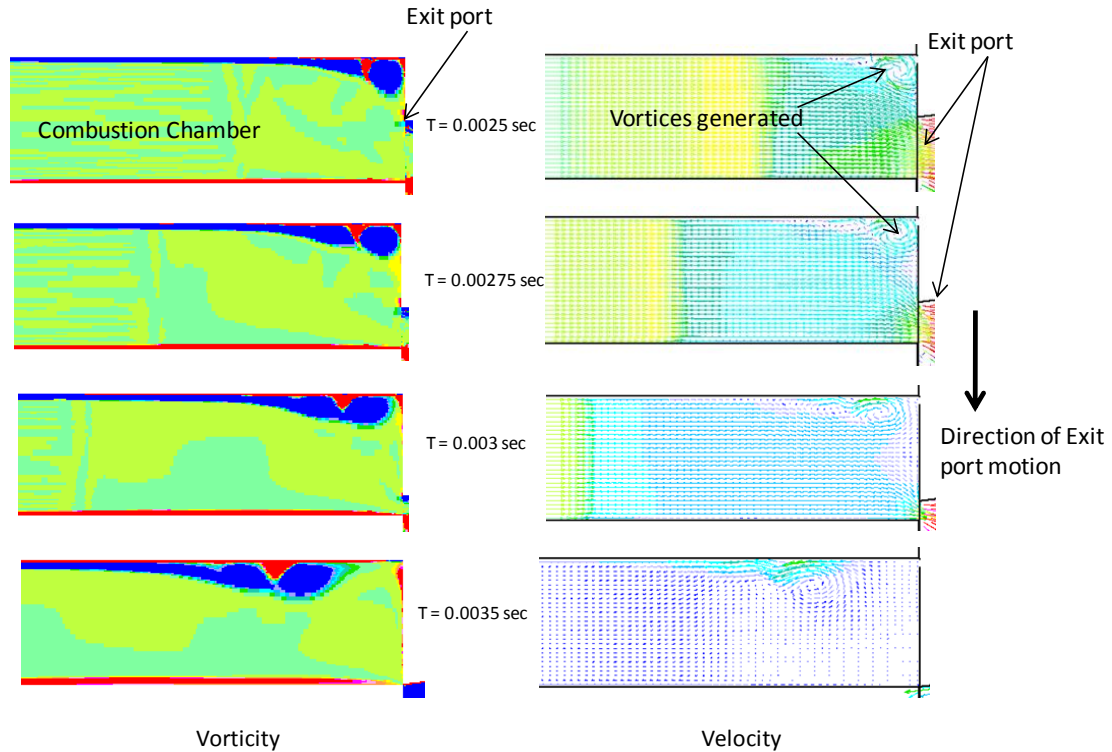


Figure 6.13. Convection of the Deposited Vorticity along the Leading Wall.

The vortices generated at the leading wall, upon exit port closure, can be seen in Figure 6.13. The exit port starts opening to the combustion channel, emptying it as shown in Figure 6.14. The exit port is made to travel vertically down relative to the combustion channel. The combustion channel pressure was initialized higher than the exit port and hence an expansion fan can be seen to traveling into the channel, lowering the pressure in it while emptying the channel. It can be seen from the density contours in Figure 6.14, how these expansion waves start out curved, attached to the leading wall and the end wall and subsequently become planar downstream of the channel. Similarly Figure 6.15 shows how curved, non-planar compression waves are formed when the exit port closes

the combustion channel gradually. This behavior is similar to what Larosiliere (1993) predicted on the gradual closing process as depicted in Figure 6.10.

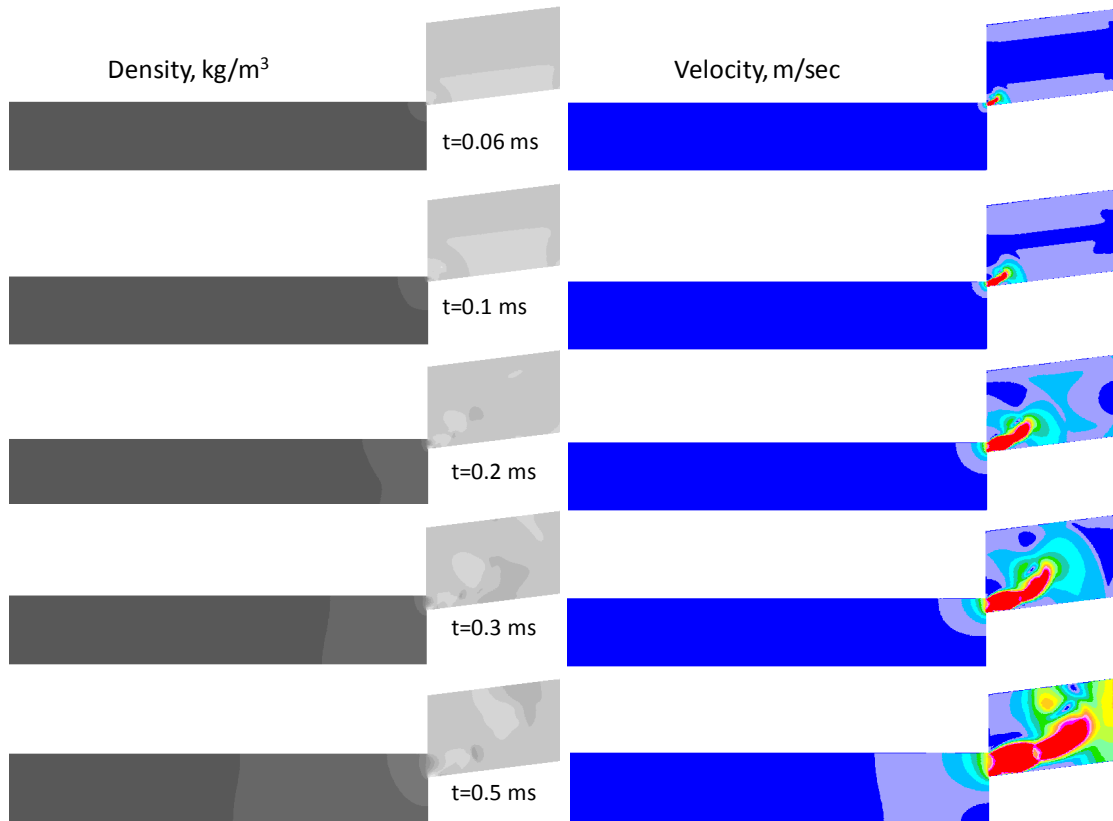


Figure 6.14. Gradual Opening Process.

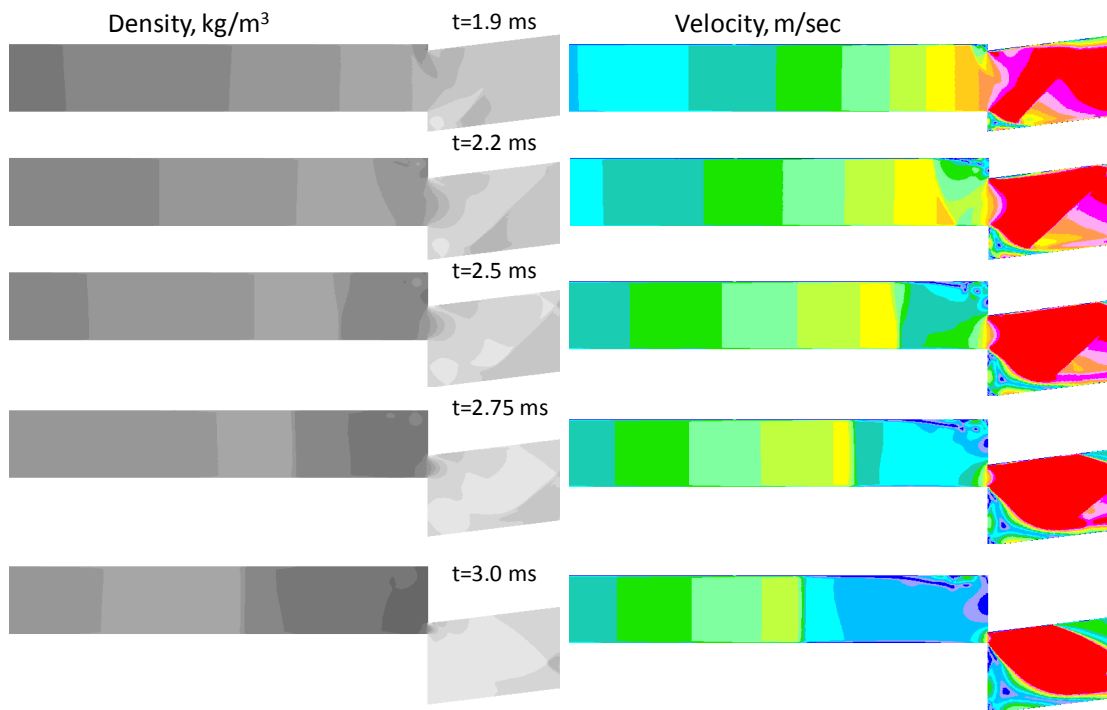


Figure 6.15. Gradual Closing Process.

CHAPTER 7. TRANSIENT TRANSLATING JETS IN A WRCVC.

7.1 Introduction

WRCVC uses transient translating jets for ignition and possibly for pilot fueling, as explained in Chapter 4. The modeling approaches and the numerical analysis performed for the transient jets is the subject of this chapter. Pilot fuel injection modeling will be presented in the first half of the chapter followed by the modeling of hot gas jet used for ignition of the combustible mixture. Both jets are modeled as 2D, non-reacting, turbulent, transient, and translating gas jets on a combustion chamber fixed reference frame in this chapter. Several injector orientations are presented for the pilot fuel injection analysis, followed by a discussion of the effect of various parameters governing jet behavior and mixing. The hot gas jet analysis presents some important large scale vortex structures which seem to govern the mixing process of a translating jet. The chapter is concluded with an analysis which evaluates the relative importance of jet momentum, injected gas type, and the injection pressure on these vortex structures and fluid mixing.

7.2 Pilot Fuel Injection Analysis

Pilot fuel injection can be used to avoid misfiring in a WRCVC in the event a combustible mixture is not available near the ignition source. As explained in Chapter 4, some pilot fuel may be introduced to provide an ignitable zone near the ignition source (hot gas jet) at the carrier wall (e.g. exit side end wall in Figure 4.1), in those situations when primary fuel supplied from the inlet side wall does not reach close enough to the exit side end wall. The misfiring occurred due to the unavailability of combustible mixture near the ignition source (when pilot fuel injection is not used) is the subject of Chapter 9, where experimental data and numerical predictions are presented. The mixture enriching process by the use of pilot fuel, thereby avoiding misfiring is discussed in this section.

Figure 7.1 corresponds to a test case where fuel was supplied from primary fuel injectors 3-6 (Figure 2.7) only and did not result in combustion. The red color region in Figure 7.1 shows the combustible mixture in the combustion channels while the blue color regions represent air without fuel. This combustible mixture representation is from a 1D gas dynamic and combustion model (Elharis, et al., 2011) which shows how the combustible mixture supplied from the inlet of the WRCVC may not reach the vicinity of the igniter, resulting in misfire. Pilot fuel injection was not used in this 1D analysis, which might have helped to ensure ignition and combustion.

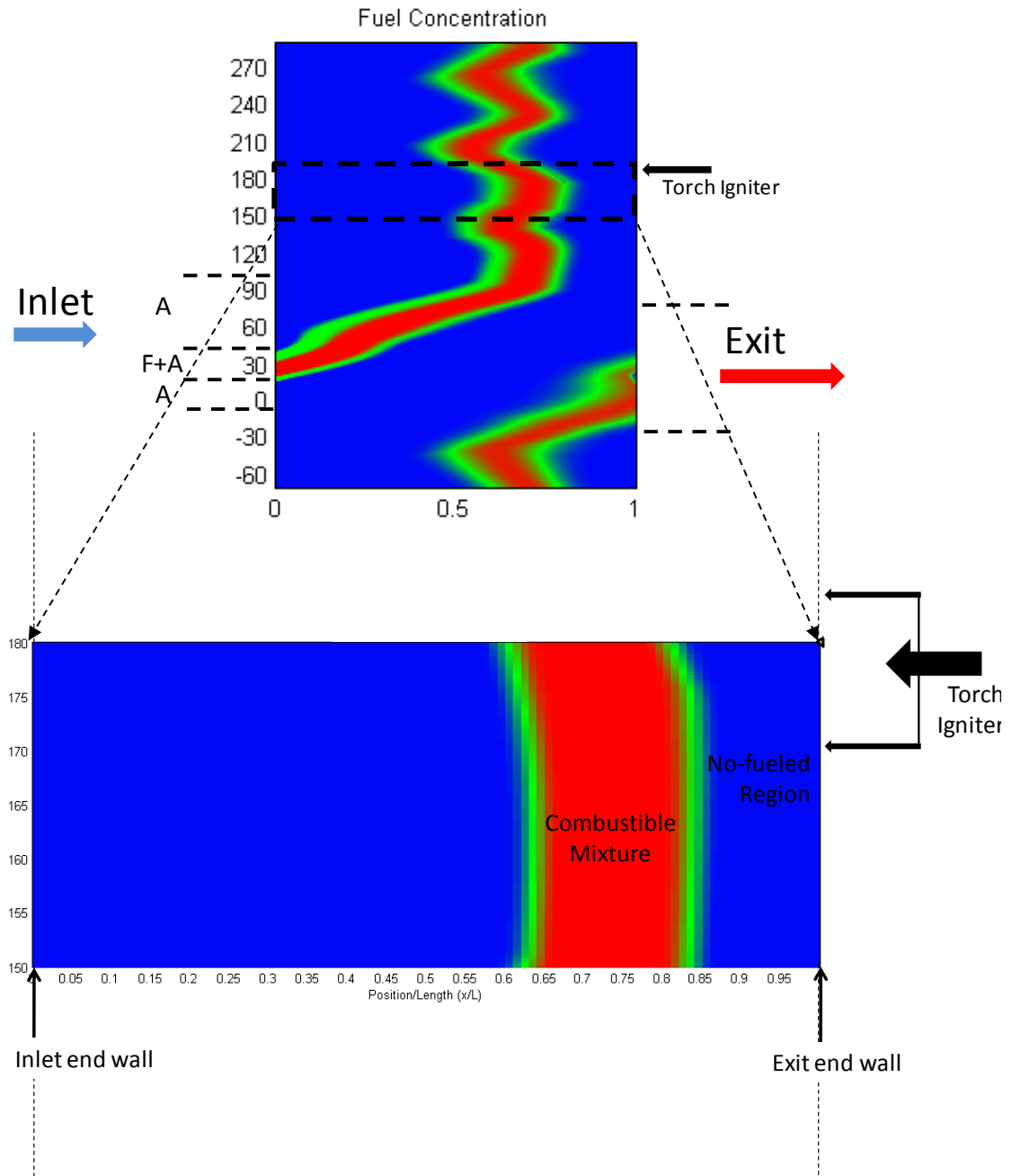


Figure 7.1. Combustible mixture (red), supplied from the inlet side did not reach the exit end wall, as predicted by 1-dimensional time dependent gas dynamics. Pilot fuel was not used in this case.

7.2.1. Injector Orientation

Three injectors orientations were tested numerically to understand the effect of injector orientation for fuel air mixing: axially oriented injector, an injector aligned 30° to the axial direction and directed towards the top wall of the channels (named Reverse-slant Injector) and an injector aligned 30° to the axial direction and directed towards the bottom wall of the channels (named Forward-slant Injector). The region of interest of three consecutive combustion chambers is shown in Figure 7.2, in the form of color-scale plots of the injected gas mass fractions at different times from these three injectors. Three channels were modeled with the middle one behaves close to actual conditions, while the leading and trailing channels suffer from artifacts due to flow starting and stopping in the injector passage.

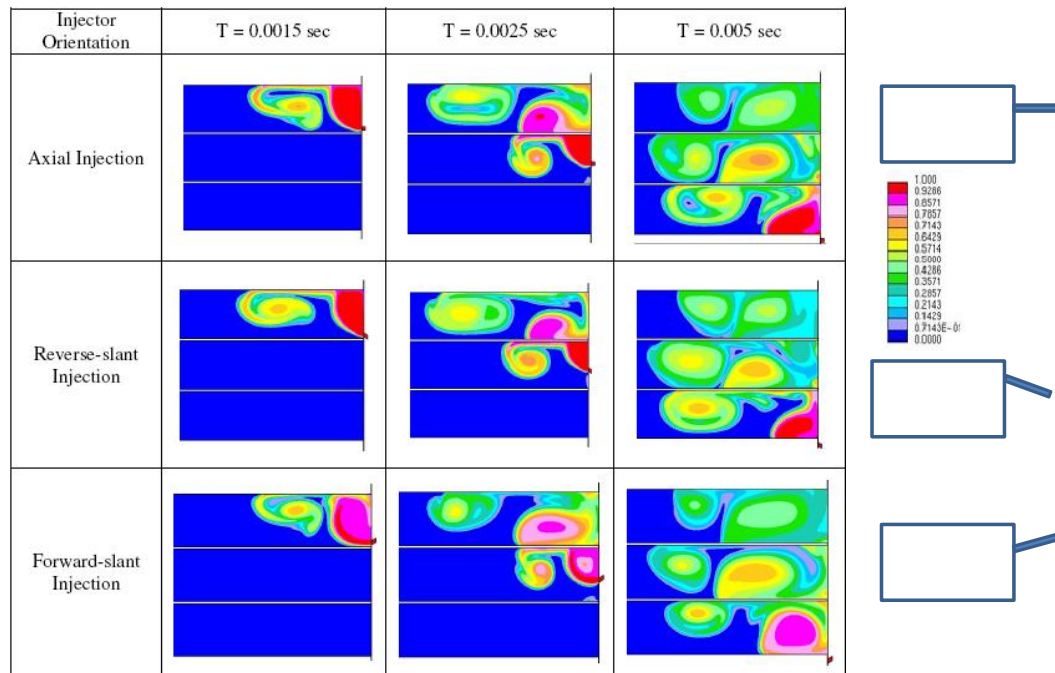


Figure 7.2. Temporal Variation of Fuel Concentration with Different Injector Orientations.

It can be seen from Figure 7.2 that nearly identical flow field in fuel-air mixing is obtained for axial injection and reverse-slant injection. In both cases, the coherent structures seem to be similar. Two counter rotating vortices dominate fuel-air mixing in the channel. One vortex is formed near the top wall of the channel and convected along the channel for sometime before it starts moving downward towards the bottom wall. The other vortex is formed at the exit-end wall and convected downward before moving forward along the bottom wall. The two vortices meet eventually in the lower half of the channel. However, fuel injected from the forward-slant injector is concentrated more towards the bottom wall than the other two cases and the forward moving vortex is smaller compared to the other cases. Three-dimensional aspects need to be analyzed to decide if an angular injector has indeed any advantages compared to an axial one in terms of local fuel-air mixing. This is not analyzed in this thesis.

7.2.2. Effect of Exhaust Port Closing to Subsequent Gas Injection

In the actual WRCVC, the combustion channels open to the injector sometime after the exit port closes. The gradual closing of the combustion channel from the exit port influences the pilot fuel-air mixing process. While partially open, the flow must separate from the wall to exit through the initial opening, creating a recirculation zone. This closing generates a hammer shock, with initially curved pressure waves generated coalescing into a shock wave, which compresses the combustion channel gas. When the channels are exposed to the injector, the fluid in the vicinity of the injector is at rest. This can be seen by comparing the fuel mixing characteristics in the combustion channels closing to the exit port before the injector and a hypothetical case when the exit port

would not exist (Figure 7.3). In this analysis, the channels were initialized with a velocity and the left ends (inlet side, not shown in Figure 7.4) were modeled using total pressure boundary conditions. These total pressure boundaries were changed into no-slip wall boundaries just before the hammer shock arrives at the left end, to recreate the correct flow conditions in the WRCVC.

A single combustion channel and the exit port were modeled in 2D to understand the vorticity deposition on the combustion channel walls due to the gradual exit port closing (Figure 7.5). The computations were done with a moving exit port and a stationary combustion channel, as opposed to a rotating combustion channel with a stationary exit port in the actual WRCVC. This decision to analyze the problem with a coordinate system fitted to the combustion channel was solely numerical. The computations start when the combustion channel is closed to the exit port. The exit port starts moving vertically down, opening itself into the combustion channel, and then closing to it subsequently. (Figure 7.5). It can be seen that vorticity was deposited on the channel walls when the combustion channel was gradually closing to the exit port. Also there is a larger amount of vorticity deposited on the leading wall and it is being convected to the left. This is the reason for the enhanced penetration of pilot fuel gas along the leading wall as can be seen from Figure 7.3 in the case of pilot fuel injection with a preceding exit port.

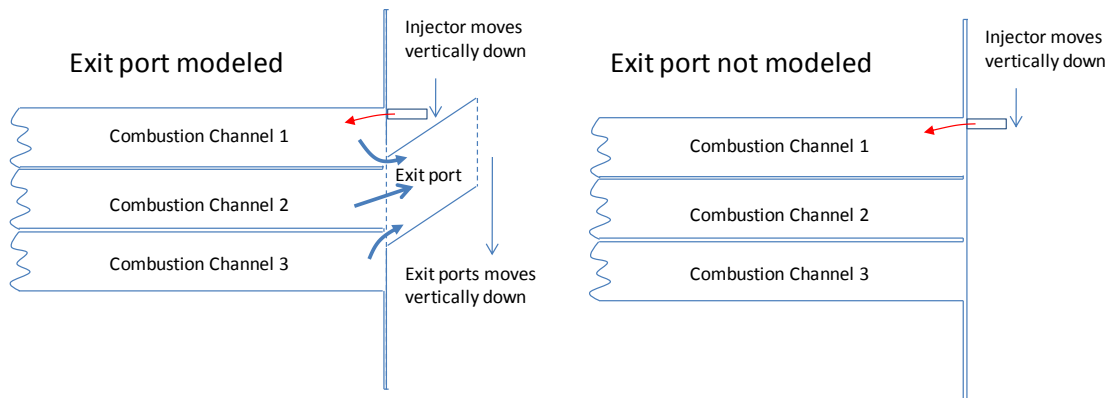


Figure 7.3. Schematic of the Numerical Setup to Evaluate the Effect of Preceding Exit Port to Fuel-Air Mixing by the Pilot Fuel Injector. The Numerical Simulations of the same are shown in Figure 7.4. The Entire Lengths of the Combustion Channels are not shown.

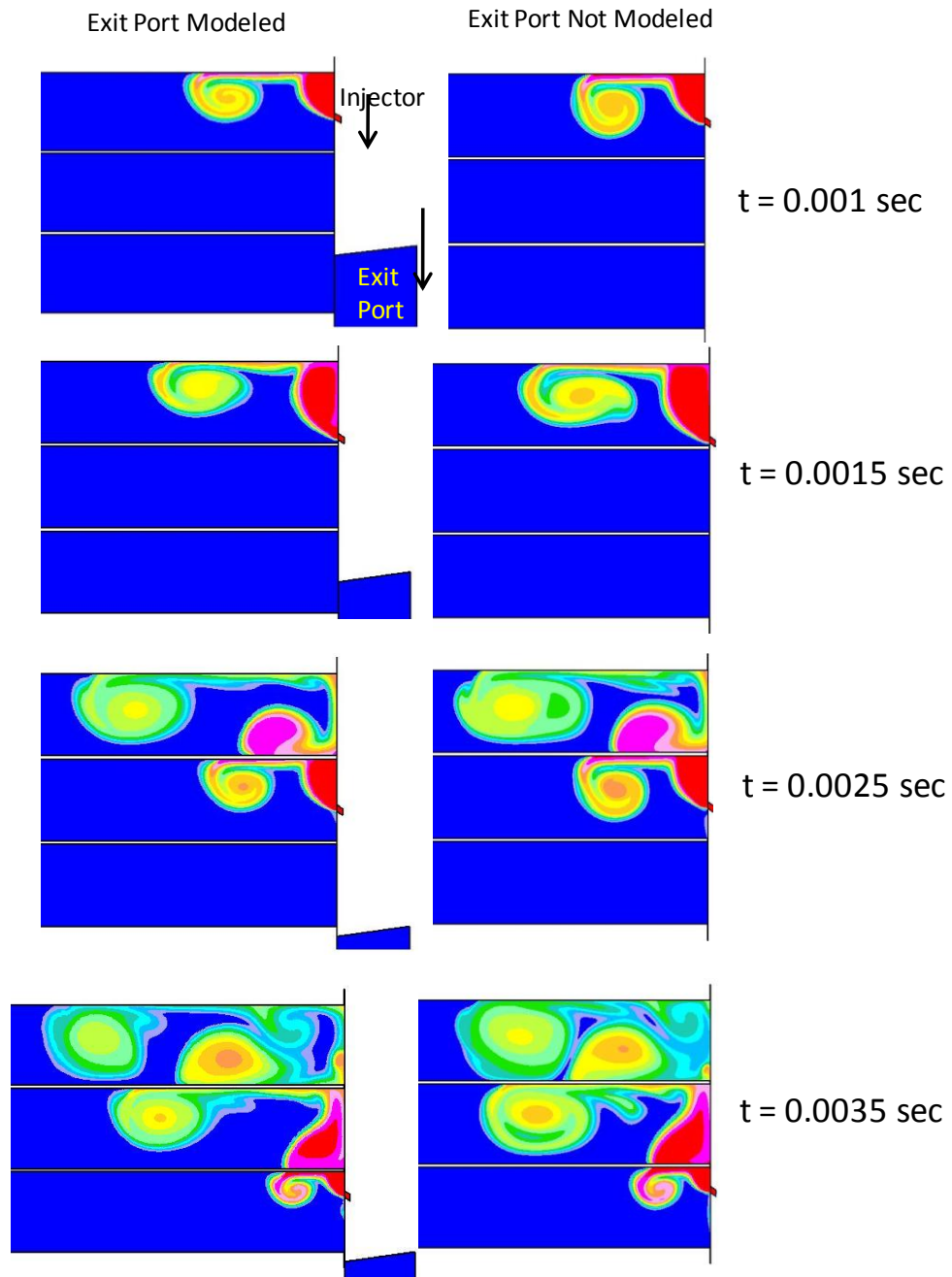


Figure 7.4. Effect of Gradual Closing Process of the Exit Port on Pilot Fuel Injection. The Schematic of the Numerical Setup is shown in Figure 7.3. The Entire Lengths of the Three Combustion Channels are not shown. The Exit Port Moves Vertically down and hence is seen as Disappearing from the latter time step figures.

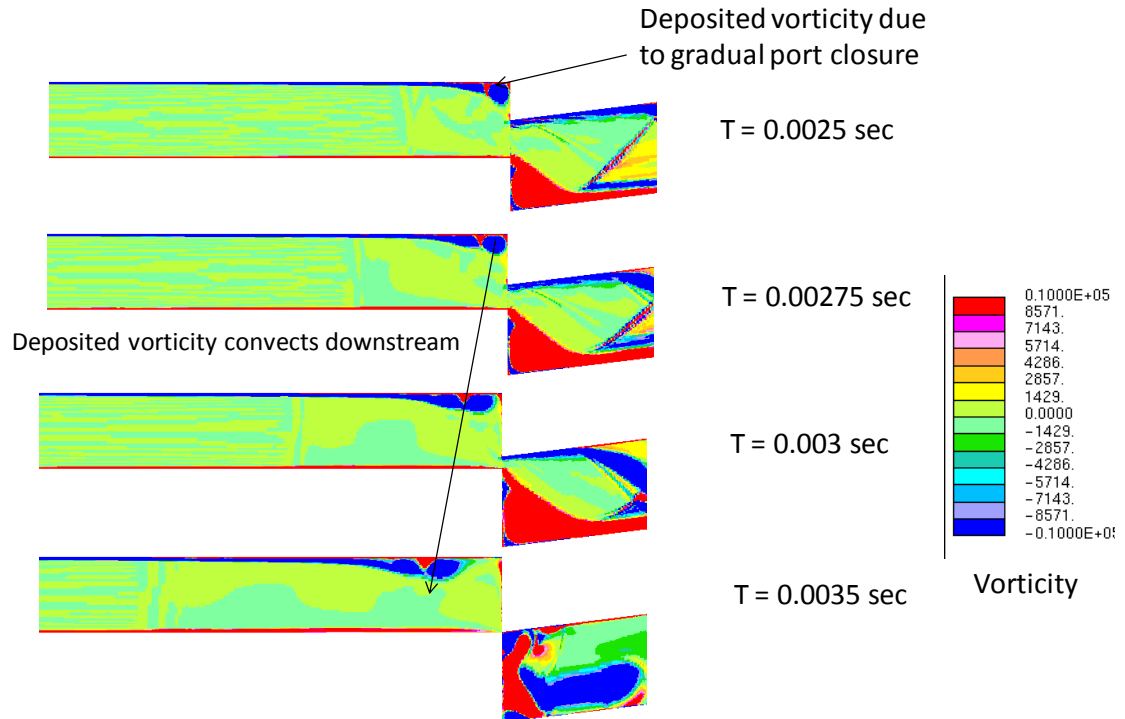


Figure 7.5. Vorticity Depositions and Convection on the Combustion Channel Leading Wall due to Exit Port Closure.

7.2.3. Effect of Jet Width and Pressure Ratio

In this chapter, the effect of changes in mass flow rate and the injection pressure are analyzed. The mass flow rate from the injector in the three dimensions is kept constant by changing the width to height ratio and the injection pressure accordingly, thereby analyzing the effects of injection pressure. While keeping the injection pressure and the injector height the same, varying injector width will vary the mass flow rate. The injector is choked in all cases analyzed here which are shown in Table 7.1. The actual injector used in WRCVC testing had a circular cross section. However 2D injector corresponds to

a slot injector in 3D as shown in Figure 7.6. The injector height shown in Table 7.1 is hypothetical and does not have any practical implication as a slot injector was not used. The numerical value of it was only used in the calculation of the mass flow rate through the injector. Changing the injector width has more effect on fuel-air mixing than changing the injection pressure. The reason for this is thought to be as follows: The coherent structures which govern the mixing are restrained by the channel confinement and their movement is affected by the relative movement of the injector relative to the channel. These factors dominate over the effect of injection pressures on the fuel-air mixing and its effect is minimized. On the other hand, injector size is related to the size of the coherent structures formed, and hence is directly affecting fuel-air mixing. These claims might only be valid for the conditions tested here and more extensive analysis is needed before generalization.

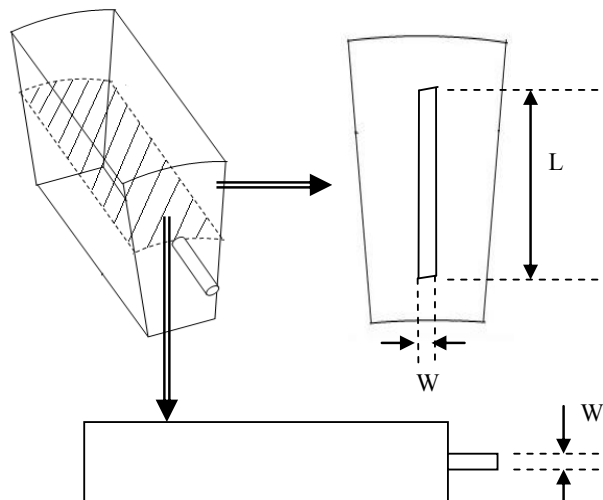


Figure 7.6. Simulation Domain (shown in dashed line) with the Pilot Fuel Injector.

Table 7.1. Test Cases.

Test Cases	Injection Pressure (kPa)	L (in)	W (in)
Case 1	724	0.16	0.2
Case 2 – vary mass flow, const. injection pressure	724	0.16	0.1
Case 3 – vary injection pressure, const. mass flow	1241	0.09	0.2

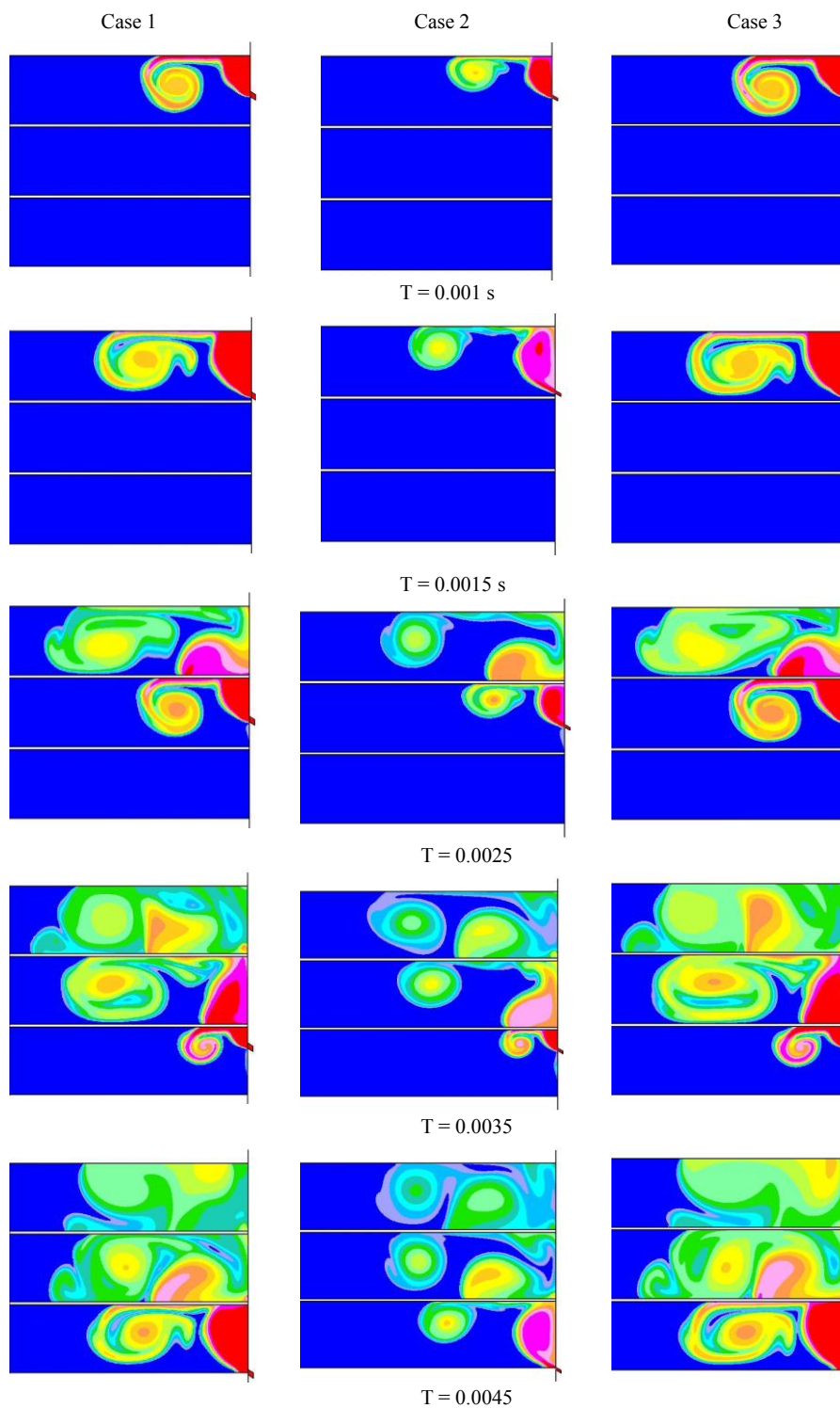


Figure 7.7. Fuel-Air Mixing Predictions for Different Test Cases (refer Table 7.1).

7.3 Hot Gas Injection Analysis

The rate and extent of mixing of the hot gas and the combustible fuel-air mixture is analyzed using 2D numerical modeling. The temporal temperature distribution of the mixture is analyzed to attempt to anticipate the ignition characteristics. The spatial and temporal temperature variation in the channel upon injection is studied for different hot gas mass flow rates and for different combustion channel combustible mixtures. This helps to understand the injection conditions (velocity, jet temperature) required to raise the temperature of the combustible mixture to its ignition temperature. Homogenous combustible mixtures are considered in this work. A schematic of the computational domain for the hot gas igniter of the WRCVC, modeled in 2D is shown in Figure 7.8(b). To illustrate that the process occurs identically in each channel, three adjacent combustion channels are considered for this analysis.

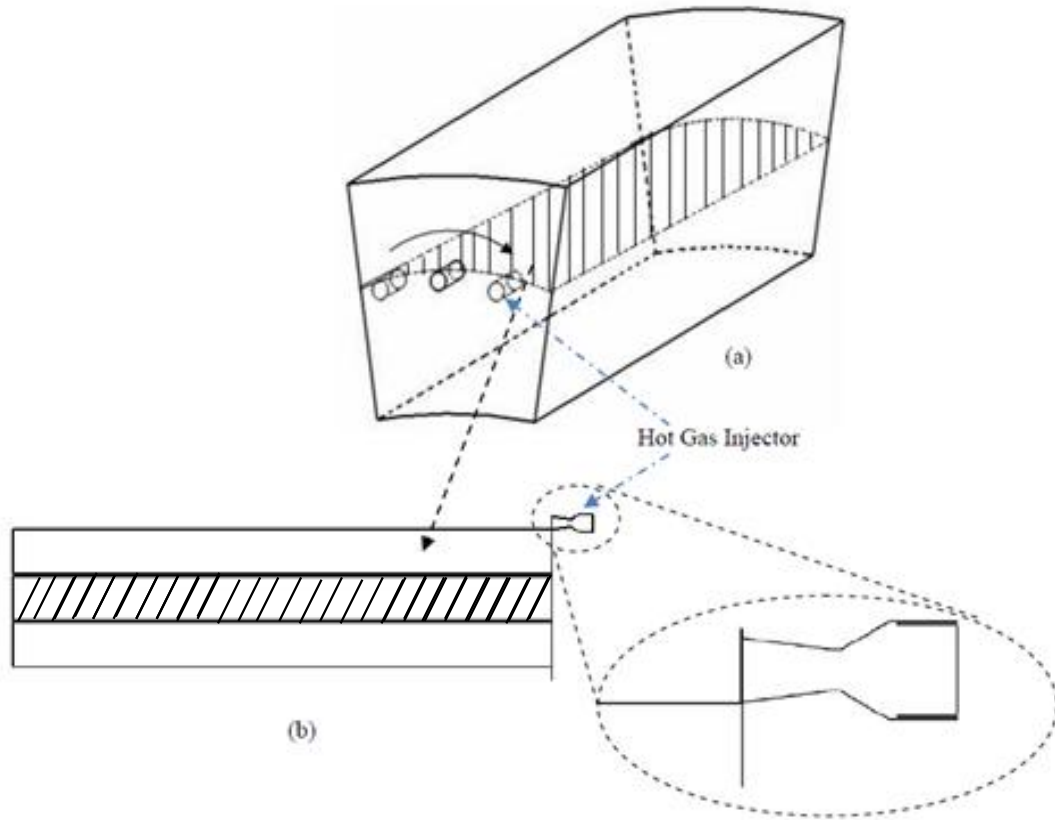


Figure 7.8. Schematics of the Injector Traversing the Combustion Channels.

7.3.1. Vortex Dynamic Dominated Mixing

The 2D modeling of traversing jet flow dynamics and mixing process presented in this chapter reveals very interesting vortex dynamic behavior:

- a. Existence of multiple counter-rotating vortices
- b. Interaction of these vortices
- c. Interaction of the vortices with confining walls
- d. Motion of vortices due to the interactions

Some of these phenomena have been studied in prior work separately, but not together. Saffman (1992) analyzed analytically the inviscid motion of two counter-rotating vortices inside a channel in the absence of a convective flow. Dritschel (1995) analytically studied the interaction of two vortices in the absence of bounding walls. The current problem is too complex to model analytically. Computational analysis provides some insight into the behavior of these vortices, which control the ignition. Sketches of the main vortex behavior and interactions are given schematically in Figure 7.9, based on observation of the 2D computations. Some of the vortices and their behavior may dominate the flow, depending on the selected injection parameters.

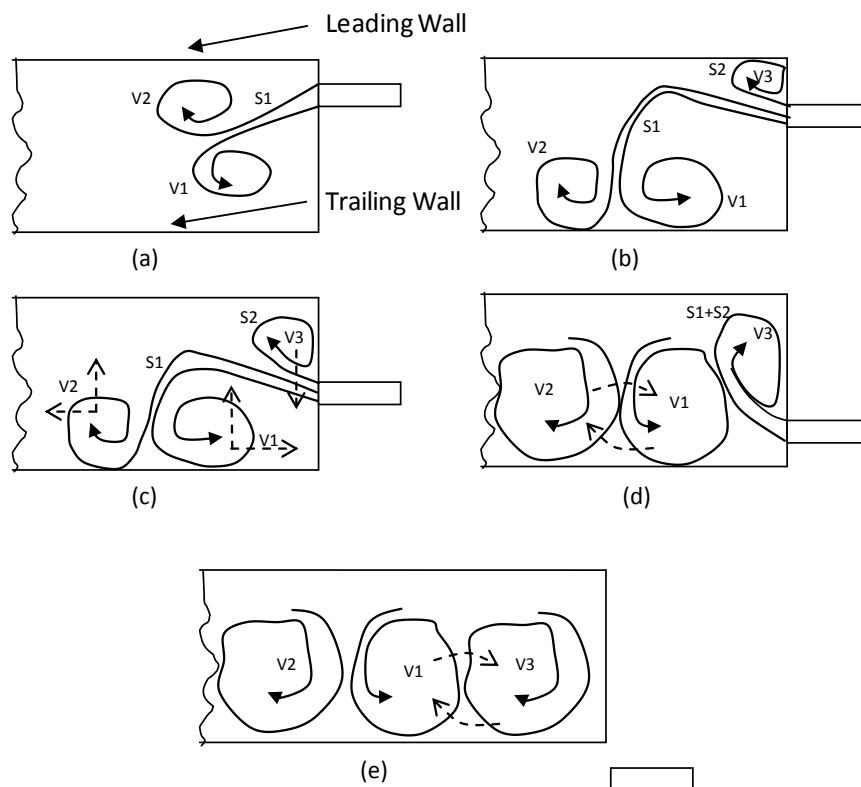


Figure 7.9. Vortex Dynamic Interactions of the Translating Jet Injector.

Upon start of injection, two counter rotating vortices (labeled V1 & V2 in Figure 7.9) are formed. These vortices are fed by stream S1 which is initially oriented towards the trailing wall, but changes direction subsequently to be oriented towards the leading wall (Figure 7.9(a) and 7.9(b)). The initial orientation of S1, apparently in the direction of least resistance, soon changes due to the presence and movement of vortex V1, and a third vortex V3 forms. Mass flow into vortices V1 and V2 via S1 continues even after the two vortices reach the trailing wall. The motion direction of the vortices V1 and V2 after reaching the trailing wall is shown in Figure 7.9(c). Stream S1 is terminated by the upward moving vortex V1 and thenceforth the mass injected is fed primarily into vortex V3. This process is dependent on the momentum in stream S1. When the momentum is higher (later illustrated with Case 4 in Figure 7.14) it is more difficult for the vortex V1 to terminate stream S1. The interaction of the vortices and their mass exchange is shown in Figures 7.9(d) and 7.9(e). The final size, location, and the interaction of the vortices depend on the injector width and injection momentum. Several smaller scale vortices are shed in this process, which are not shown in the schematic above.

There is as yet no systematic experimental study of traversing confined transient jet known to the author. However, there is a new experimental effort by a colleague of the author that has yielded preliminary results that appear to support the above description. Vortex structures from a traversing injector, have been experimentally observed by Murphy (unpublished) using high speed video imaging. This is currently ongoing work at the CPRL, IUPUI. In this setup, a moving hot jet is injected into a long stationary combustion channel to simulate a hot gas igniter. Figure 7.10 shows the development of

the gas jet injected into the stationary combustion channel while the injector rotates relative to the combustion channel. The qualitative similarity of the experimental images and the prediction of the flow structures using the numerical model are very encouraging. It should be noted that the numerical predictions in Figure 7.10 and the experimental high speed images in Figure 7.11 are not carried out for similar in-chamber and hot gas jet conditions. Hence direct comparison of jet penetration and vortical structure sizes should not be made between these. The presentation of these results is intended to give only a qualitative idea about the general behavior of a transient, translating hot gas jets injected into long combustion chambers.

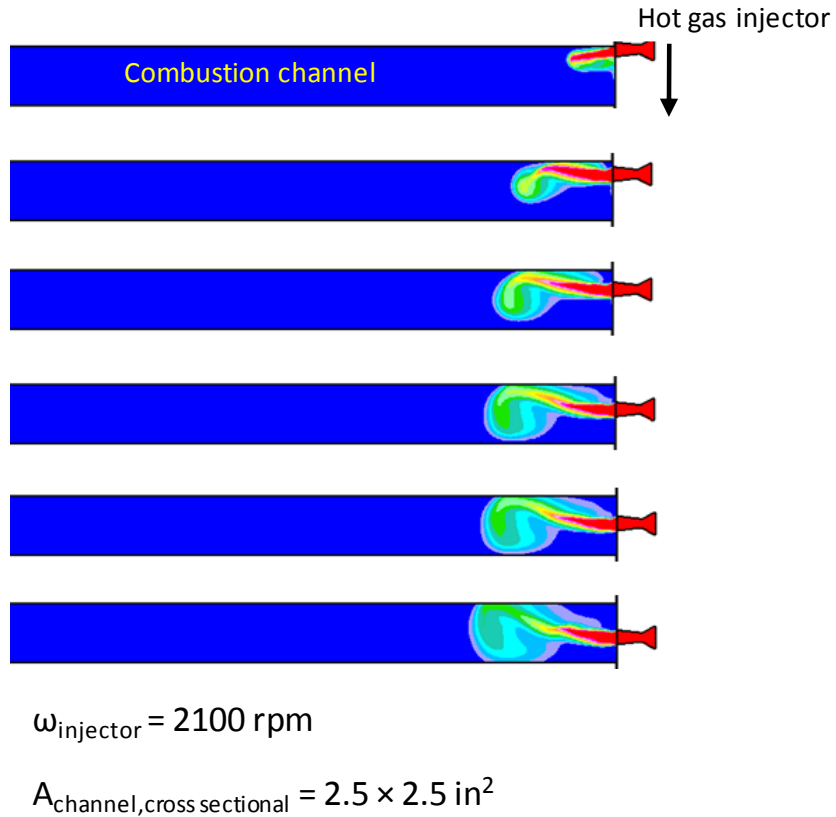


Figure 7.10. 3D Numerical Predictions (Wijeyakulasuriya and Nalim, 2011) of the Developing Vortex Structures from a Traversing Injector into a Long Combustion Channel.

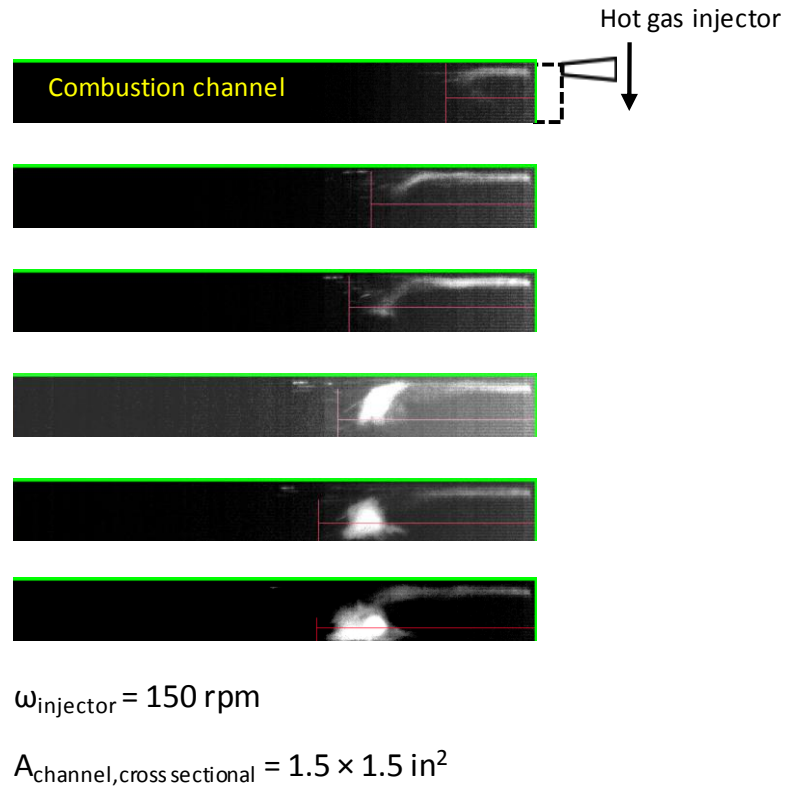


Figure 7.11. Experimental High Speed Video Images (unpublished) of the Developing Vortex Structures from a Traversing Injector into a Long Combustion Channel.

The dimensions of the hot gas injector (igniter), used in the WRCVC test rig (Matsutomi et al, 2010) are shown in Figure 7.12. It has a converging-diverging shape intended to generate supersonic flow, and is provided with a air film for cooling.

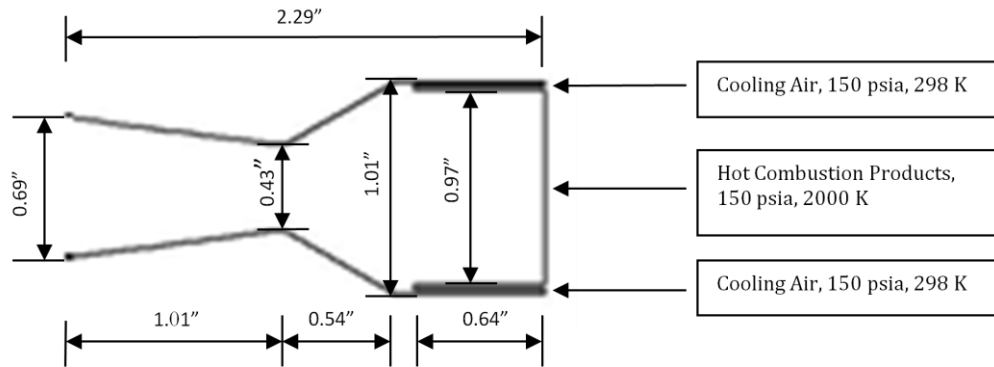


Figure 7.12. Igniter Dimensions and Boundary Conditions.

The temporal development of the predicted injected gas mass fraction is shown in Figure 7.13. The nozzle shown in Figure 7.12 injects hot gas (N_2) into atmospheric air (injecting lighter gas into heavier gas). The formation of the counter rotating vortices V1 and V2 at the start of the injection and V3 towards the end of the injection process is observed. The complex interaction and small scale vortex shedding from the three main vortices are also shown clearly. The behaviors shown in Figures 7.9, 7.10, 7.11 and 7.13 are dependent on many parameters such as injector size relative to the combustion channel (expansion ratio of the jet, defined as the ratio between combustion chamber width to nozzle exit width), injection pressure, and temperature relative to the combustion channel conditions. The first pair of vortices is formed before the jet reaches the midpoint of its traverse, and the third is formed after that, due to the offset jet momentum. This fundamental dynamic of a traversing jet is different from a transient stationary jet with otherwise similar geometry or confinement. An experimental and numerical comparison of this difference is presented in Figures 4.7 and 4.8 in Chapter 4. In the WRCVC context, this appears to imply that any pilot fuel injected will remain close to the end-wall in preparation for

ignition. Further, this shows the importance of correctly modeling the jet as traversing and not as an equivalent stationary transient jet.

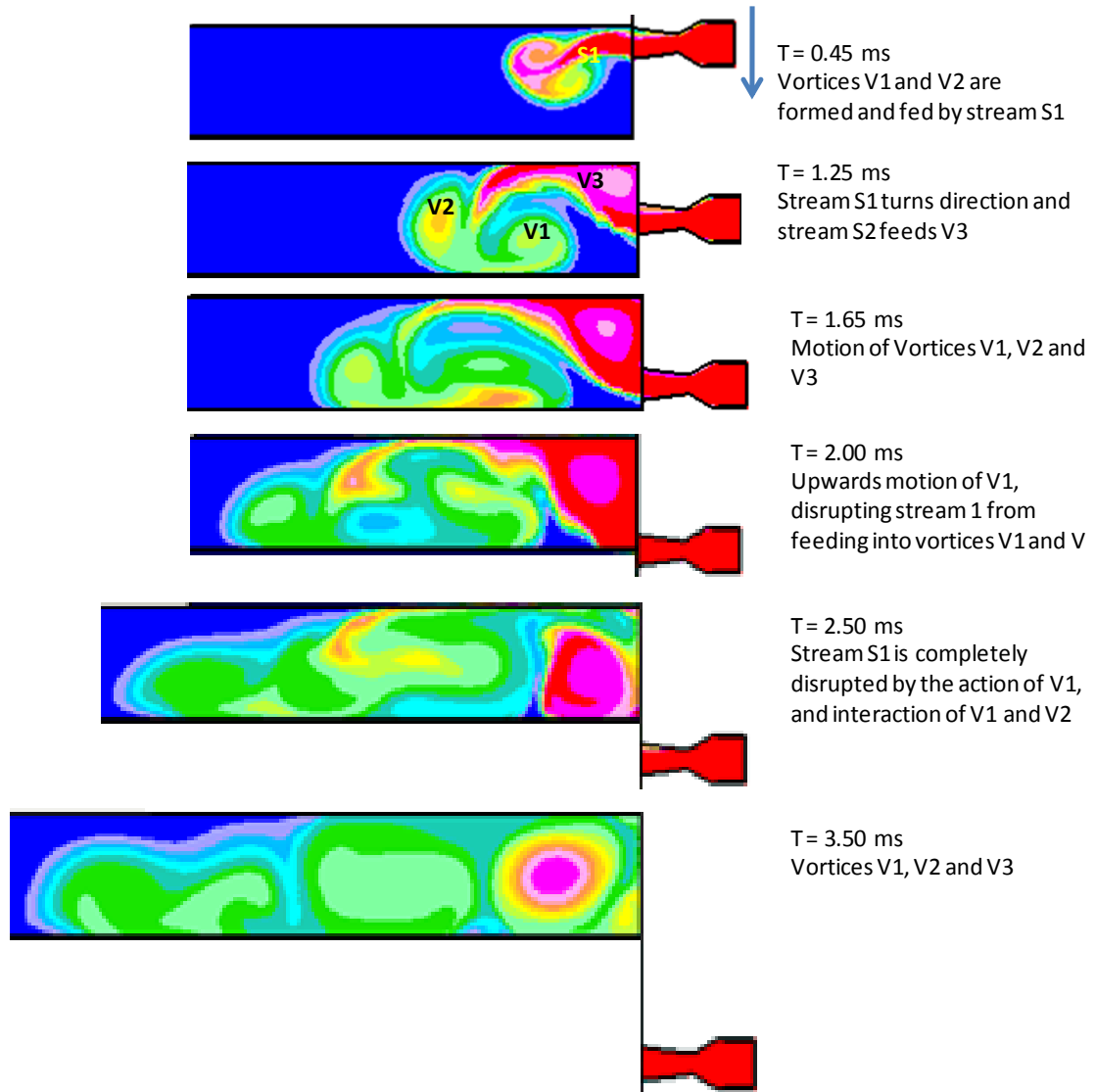


Figure 7.13. Vortex Formation and Interaction from a Translating Injector (Time from the Start of Injector Opening into the Combustion Channel). The Arrow on Top shows the Direction of Injector Motion.

7.3.2. Effect of Jet Momentum, Injection Pressure and Injected Gas Type

Having identified the large-scale vortex structures which govern the hot gas jet behavior and mixing with the chamber gasses, the effects of changing jet parameters on these structures and on axial penetration of the jet are analyzed next. Five cases were considered to understand the mixing process of the injected gas with the combustion channel fluid (Table 7.2). Several parameters were varied to understand the effect of each them. The boundary condition at the inlet to the nozzle is such that the initial mass flow specified (using U , ρ , and T) is held constant across the boundary. Cases 1, 2, and 4 have the same initial density and temperature, while varying the velocities and thus mass flow rates. Several effects can be evaluated by comparing Cases 1, 2, and 4. Since the mass flow is varied by different velocities, the effect of changing the momentum flow is clearly identified. In Cases 1 and 2, the nozzle throat is not always choked, while in Case 4, choked flow at the nozzle throat exists throughout the computation, allowing assessment of the effect of supersonic outflow versus subsonic outflow from the nozzle. To evaluate the effect of density, CO_2 was used as the injected gas (Cases 3 and 5). Case 3 has the same mass flow rate and injection temperature as Case 4, with only an adjustment in initial injection pressure to compensate for the different molecular mass. A slightly lower penetration in Case 3 can be seen compared to Case 4.

Table 7.2. Test Cases.

Case	Injected Gas	Inlet Boundary Conditions			\dot{m} (kg/s)	$\left(\frac{P_{injection}}{P_{injection}} \right)_{k,t}$
		U (m/s)	ρ (kg/m ³)	T (K)		
Case 1	N ₂	28.5	1.3	2200	0.058	6.16
Case 2	N ₂	72.3	1.3	2200	0.150	6.16
Case 3	CO ₂	145.4	1.3	2200	0.300	3.92
Case 4	N ₂	145.4	1.3	2200	0.300	6.16
Case 5	CO ₂	95.0	0.3	2200	0.072	1.00

It may be observed from Figure 7.14 that increased momentum flow rate (calculated at the jet inlet) increases penetration for constant initial injection pressure. The time of jet impingement on the trailing wall is very much dependent on the momentum flow rate injected and higher flow rates reduce the impingement time. However, it is interesting to note that the place of impingement on the trailing wall is approximately the same in all these cases and that might be dependent on combustion channel width, geometry of the injector, and/or the translational speed of the injector relative to the combustion channel.

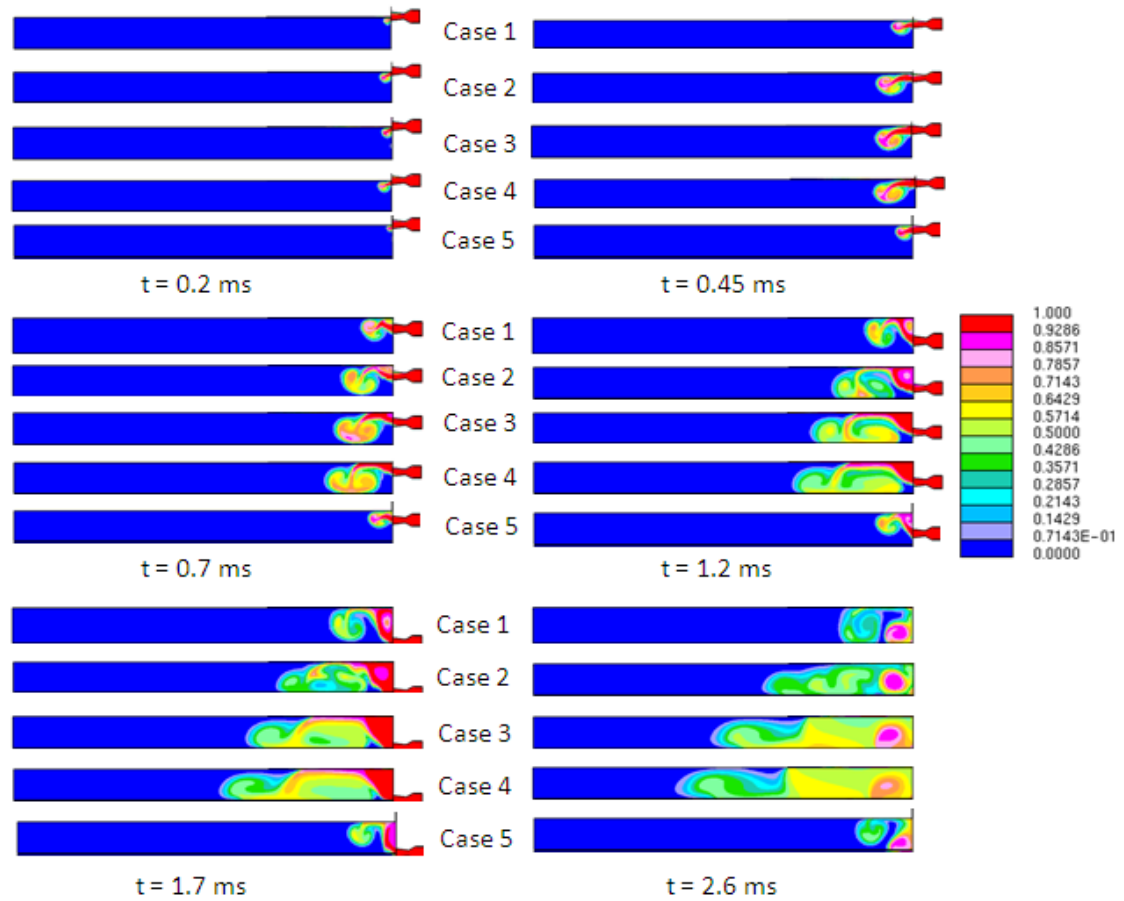


Figure 7.14. Flow Pattern shown by Injected Gas Mass Fraction during Traverse of Injector.

The vortex behavior in all the cases is similar, although certain features dominate in some cases. For example, vortex V1 in Case 4 dominates and suppresses the development of vortex V3. Vortex V2 is suppressed in Case 1 due to the wall effects and low flow velocities. Hence, upon impingement on the trailing wall, rather than moving away from the injection side end wall, V2 gets absorbed/engulfed into vortex V1.

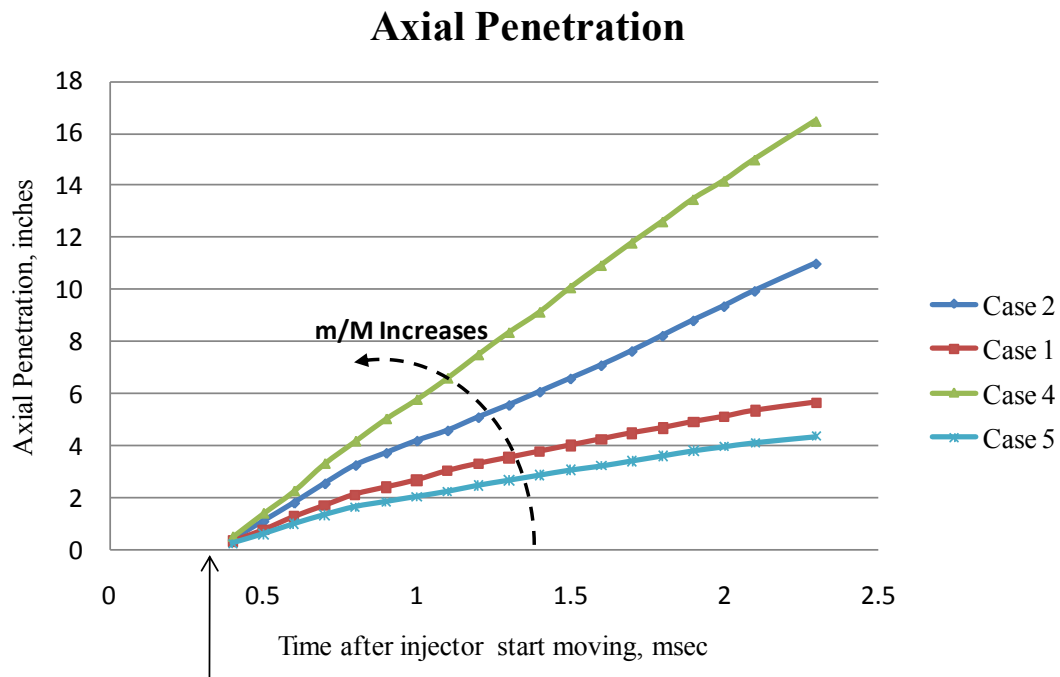
Two types of transient translating gas jets that may be found in a WRCVC are discussed in this chapter. The pilot fuel injector which may be used to inject a small amount of fuel

to enrich the near igniter mixture to avoid misfiring was analyzed numerically using 2D CFD. Different jet orientations were discussed in their ability to mix the injected fuel with in-channel gasses. The effect of the channel closing to the preceding exit port was shown to have an effect on the subsequent gas injection from the pilot fuel injector, in that the vorticity deposited on channel walls enhanced axial jet penetration. The hot gas jet was analyzed next which may be used to ignite the combustible mixture. Several important vortex dynamics behaviors were identified and discussed in relation to fluid mixing. Three major large scale vortices were seen to influence gas mixing in the combustion channel. Finally the effect of jet momentum, injected gas type, and injection pressure on the behavior of these large scale vortex structures and gas mixing were analyzed.

7.4 Jet Penetration from a Confined Traversing Hot Gas Injector

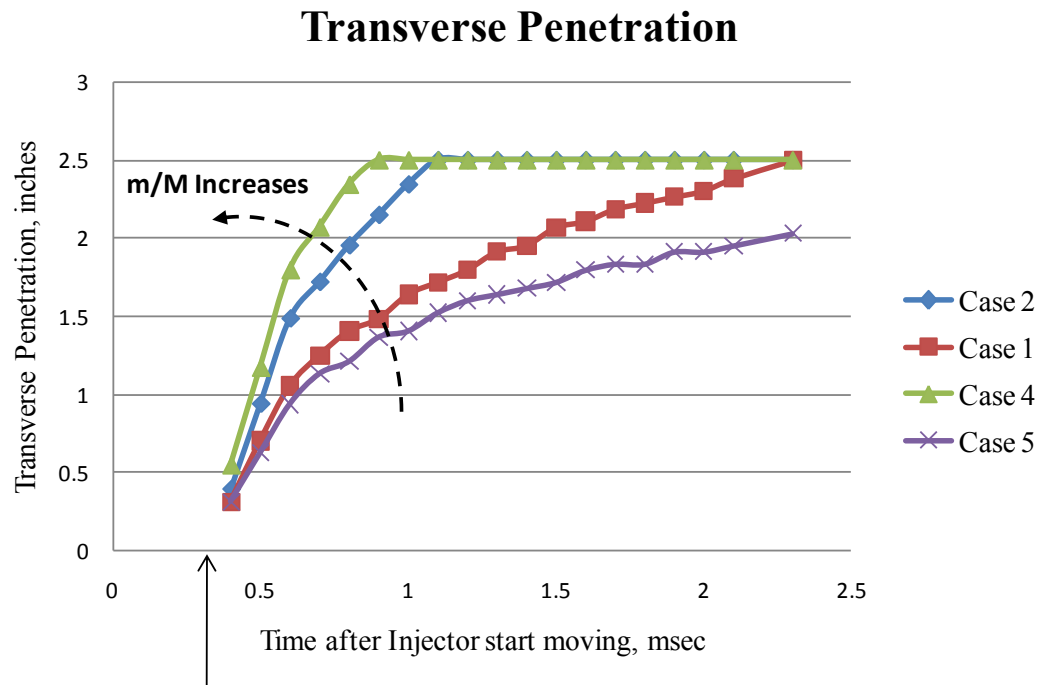
Analyzing and quantifying jet penetration in traversing jet flows is not straight forward, unlike in simple jet flows, where a distinct potential core exists at the jet exit. In a confined traversing jet, the jet exit conditions are highly transient due to the motion of the injector and the interaction of exit flow with moving vortices inside the confined channel. These vortex interactions were sometime seen to decrease the effective exit area of the jet as well. This highly unsteady nature of the jet exit conditions in a confined traversing jet, makes it difficult to correlate jet behavior to its exit parameters such as exit momentum, pressure and Mach number. These parameters are highly variable in a confined traversing jet and vary considerably across the exit area of the jet. In this section the confined traversing jet behavior is described using the jet inlet boundary conditions which were

held constant throughout the computation. Four cases from Table 7.2 were used to present the axial and transverse jet penetration. The axial and transverse jet penetrations are seen to increase with the increase of the quantity ‘mass flow rate (m) / Molecular weight of injected gas (M)’ (Figures 7.15 and 7.16).



Injector start opening into
the channel ($t=0.34$ msec)

Figure 7.15. Axial Penetration of a Confined Traversing Jet for varying m/M .
 m = Mass flow rate, M = Molecular weight of injected gas.



Injector start opening into
the channel ($t=0.34$ msec)

Figure 7.16. Transverse Penetration of a Confined Traversing Jet for varying m/M .
 m = Mass flow rate, M = Molecular weight of injected gas.

In the four cases presented in Figures 7.15 and 7.16, the jet exit Mach numbers were subsonic throughout their traverse past the channel although there was larger variations across the width if the jet exit. The channel width used in these simulations was 2.5 inches which can be seen as the maximum transverse penetration in Figure 7.16. It can be seen that Cases 2 and 4 with higher m/M values reach the trailing wall within 1 ms of injector traverse (before the injector traverse half the channel width) and Case 5 with the lowest m/M value did not reach the trailing wall by the time injector traversed past the

channel. In the cases with lower penetrations, such as cases 1 and 5, vortex V2 (refer Figure 7.9) was weaker and instead of moving downstream, gets engulfed in vortex V1. In all these cases a converging-diverging injector was used where the exit flow was over-expanded. Care should be taken when trying to generalize these results to other types of injector flows as the penetration is primarily depended on the vortex interactions with each other, walls, and the jet exit flow. These interactions in turn depend on the level of confinement, speed of jet traverse and the jet flow conditions. A higher momentum jet exit flow will strengthen the vortex V2 by supplying more mass into it. Further it will not get suppressed by vortex V1 (Figure 7.17 a). These interactions will increase jet penetration. Further it is desirable for the jet to be perfectly expanded or better under expanded, as the increased pressure at the jet exit will not allow vortex V1 to reach near the jet exit and affect the exit flow (Figure 7.17a). Lower jet momentum and/or over expanded jet exit flows can reduce the effective jet exit area as shown in Figure 7.17b.

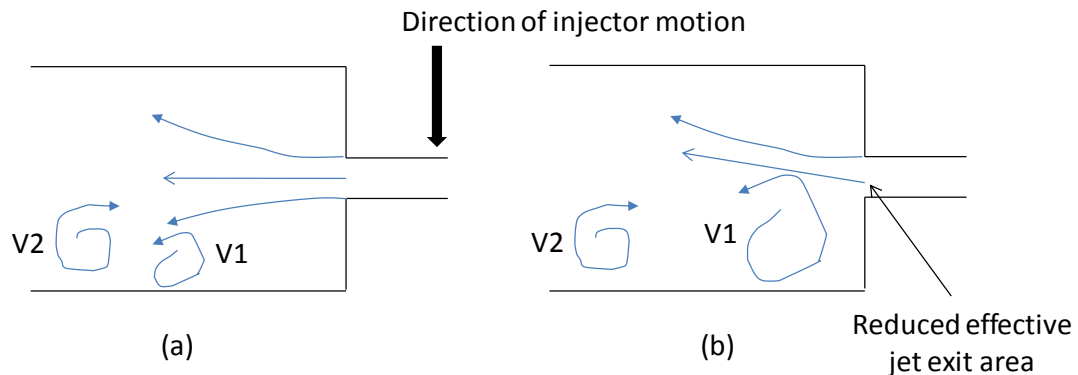


Figure 7. 17. Interaction of Jet Exit Flow with Vortex V1.

CHAPTER 8. EFFECT OF MIXTURE NON-UNIFORMITY ON IGNITION SUCCESS.

8.1 Introduction

As explained briefly in the introductory chapters of this thesis, axial combustible stratification in a WRCVC channel is viewed as an important aspect in achieving reliable ignition, part-load operability, combustion efficiency and low harmful emissions. In a WRCVC, where the combustible mixture is filled from one end and ignited from the opposite end, it is important to control the fuel concentration near the ignition source. Low fuel concentration can exist due to burned gas from previous cycle which was not fully purged and the air (without fuel) from the inlet duct supplied before the combustible mixture to provide purging without spillage of combustible mixture (buffer air). Elharis et al. (2010 & 2011) used a quasi one-dimensional gas dynamic and combustion model to predict the filling process and the combustible mixture distribution in the WRCVC combustion channels, prior to ignition. However this one-dimensional model did not have a mixing model to predict the mixed conditions of the in-channel gas and the injected hot gas.

The ignition locations were arbitrarily chosen (Elharis et al., 2010) in the absence of such a mixing model. The predicted combustible mixture distribution in the combustion channel using the one-dimensional model, is used in this chapter, to set up a two-dimensional model to predict the mixing between cold-combustible and injected hot gas for ignition. Average equivalence ratio and potential ignition location(s) are predicted from these two-dimensional mixing computations, which are then used in the one-dimensional model to predict combustion. This combined methodology helps in improving the near-igniter combustible mixture representation, and hence achieves realistic combustion predictions from the cost effective one-dimensional model. These combustion (or misfire) predictions are validated against experimental data from a wave rotor combustor.

8.2 Test Cases Analyzed

Depending on the air mass flow rate achieved, the combustible mixture may partially spill into the exit port (shown in Figure 2 (a)), reach very close to the exit wall, or stop short of the exit side end wall. This third scenario will leave an unfueled region near the ignition source (Figure 2 (b)). The one-dimensional code currently has only a gradient-diffusion mixing model and does not predict the fluid mixing near the ignition source, which is convection dominated. Hence, the final equivalence ratio near the ignition source after the inter-mixing between the “fueled,” “unfueled,” and the injected hot gases, cannot be predicted using this one dimensional code. It can be seen from Figure 8.1 that the combustible mixture introduced from the inlet port remains in the channel with the same equivalence ratios, in the absence of strong axial mixing.

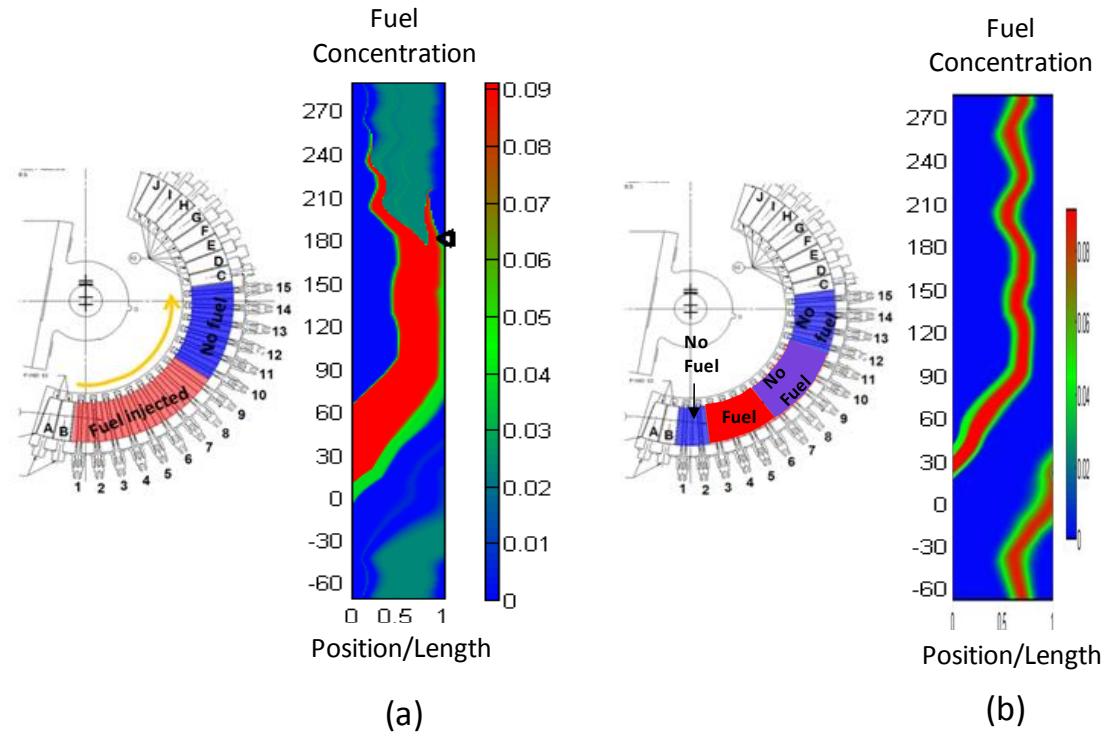


Figure 8.1. Different Fuel Filling setups and One-Dimensional Code Predictions for Axial Combustible Stratification; the Color Red represents the Combustible Mixture of a known Equivalence Ratio and Blue represents Air without Fuel. (a) Active Fuel Injectors 1 – 9, Successful Combustion Detected, and (b) Active Fuel Injectors 3 – 6, resulted in Failed Combustion.

The work presented in the current chapter starts with the “fueled/unfueled” length from the one-dimensional predictions of contour maps of fuel concentration (Figure 8.2) and model mixing by the hot jet injection process using high fidelity two-dimensional CFD. Once mixing of cold combustible gas and the hot ignition gas is complete, the resultant average equivalence ratio in the vicinity of the exit end wall is extracted from these 2D CFD predictions, and may be used to replace the gas near exit end wall region in the one-dimensional code. Thus, the mixture near the ignition source is more representative of the

mixed, cold combustible, and hot gas. Further, the 2D prediction of the temperature after mixing is studied with the local equivalence ratios, thereby arriving at possible ignition locations. These locations are used in the one-dimensional model as the ignition locations to start combustion. The resultant pressure traces from combustion are used to compare against the experimental data.

Table 8.1. Conditions and Configurations for Test Cases. Local Equivalence Ratio is the estimated Local Fuel-Air Ratio for the Fueled Region, divided by the Stoichiometric Fuel to Air Ratio.

Case	Overall equivalence ratio	Air flow	Fuel flow	Torch flow	Intake Air Pressure	Local equivalence ratio	Combustion	RPM	Active Fuel Injectors	Fuel Type
		lbm/s	lbm/s	lbm/s	psia					
A	0.86	8.2	0.48	0.17	19.15	1.44	Yes	2086	1 - 9	C ₂ H ₄
B	0.39	8.3	0.22	0.17	19.70	1.47	No	2100	3 - 6	C ₂ H ₄

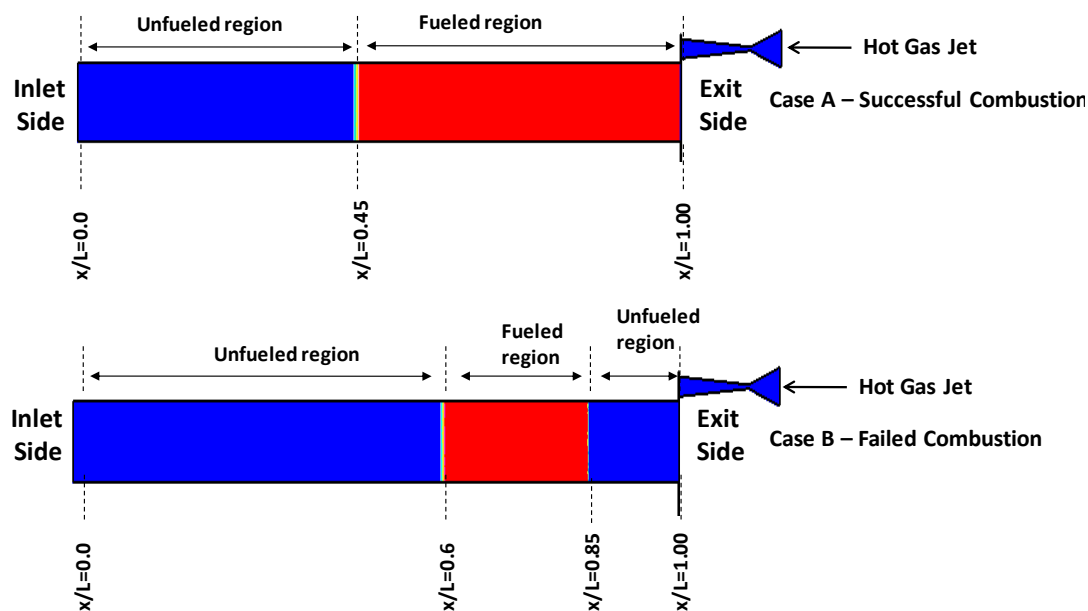


Figure 8.2. The Two Test Cases Analyzed. The Different Region limits are based on One-dimensional Model predictions of actual WRCVC Test Cases.

The two test cases discussed in this chapter, is given in Table 8.1. Case A given in Table 8.1 resulted in successful combustion, where its total flow rate was 1.3 lbm/sec with an overall equivalence ratio of 0.86. The fuel was supplied using injectors 1-9 in the inlet duct, giving rise to a local equivalence ratio of 1.44. This local equivalence ratio was calculated using the fuel supplied and the air in the locality of the active fuel injectors. It can be seen from Figure 8.2, that the combustible mixture reached the exit side end wall. Case B which failed to combust had a total flow rate of 1.05 lbm/sec, with an overall equivalence ratio of 0.39. The fuel was supplied through injectors 3-6 in the inlet duct. The one-dimensional prediction of the combustible mixture distribution inside the combustion channel for case B is shown in Figure 8.2. The combustible mixture is seen

to be in the region of $x/L=0.6$ and $x/L=0.85$ giving rise to a local equivalence ratio of 1.47. It can be seen how a ‘buffer layer (unfueled region)’ exists within 5 inches of the exit side end wall.

The two-dimensional simulations were started using the combustible distributions given by the one-dimensional code as initial conditions for the combustion channel. The hot gas ignition jet is introduced to the combustion channels which had the combustible mixture distribution given by the one-dimensional code and the ignition location and timing was deduced based on the two-dimensional mixing predictions. Combustion or ignition was not modeled in these two-dimensional simulations. The mixing and temperature data was transferred into the one-dimensional code in terms of local ‘mixed’ equivalence ratio and ignition locations based on mixture temperature after the mixing event. Combustion was modeled in the one-dimensional code using these data to verify the success of combustion which was experimentally observed. Experimental point measurements of pressure inside the combustion channels are used to validate the above one-dimensional predictions with inputs from the two-dimensional mixing analysis.

8.3 One Dimensional Numerical Code

The code simulates flow and combustion in a single combustion channel of WRCVC rotating one complete revolution, with time-varying boundary conditions modeled to match the port timings and gas properties. Internal combustion is modeled as deflagration, driven by axial turbulent diffusion, with ignition locations that mimic the torch ignition. It uses Roe’s method (Paxson, 1992) to solve the governing equations, which are

formulated, with dimensionless parameters (Nalim, 2000). The code includes effects of heat transfer, friction, axial turbulent diffusion, and chemical reaction. Additionally, there is special treatment of the regions near channel ends for leakage and partially open channels. The combustion mode is deflagration (Nalim & Paxson, 1997) and modeled using two-step chemical reactions (Elharis, 2011) in the simulations reported here. A detailed discussion about the method of integration, submodels, and boundary conditions of the problem are discussed in detail in previous publications (Nalim & Paxson (1997), and Nalim (1999). The use of this code to predict the WRCVC test conditions which were verified by WRCVC experiments are given by Elharis et al., (2010), Elharis et al., (2011) and Elharis (2011).

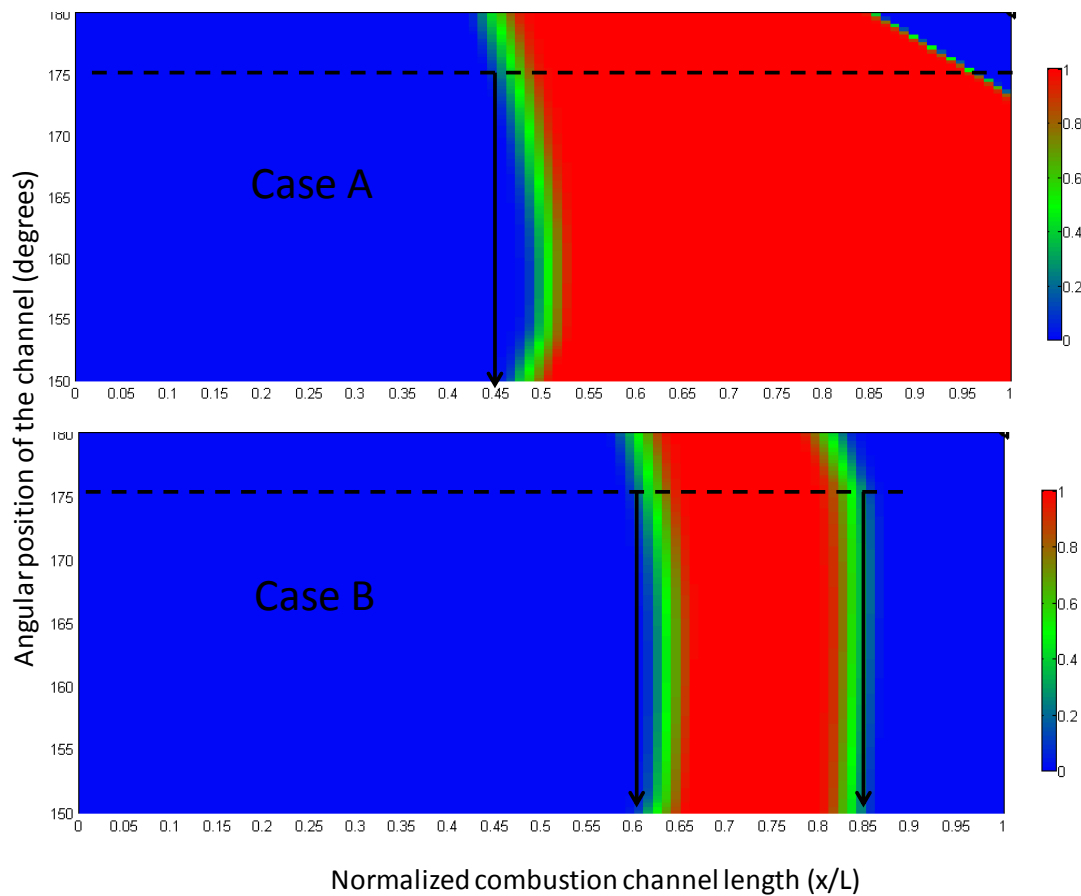


Figure 8.3. One-dimensional Combustible Mixture Distribution Predictions of Cases A and B. The Color Red represents the Combustible Mixture with known Local Equivalence Ratios and Blue, the Air without Fuel. The Vertical Axis, which shows the Angular Position of the Combustion Channel, is zoomed near to the Hot Gas Jet Region (175°).

8.4 Two Dimensional Mixture Non-uniformity Analysis

The simulations were initialized with different lengths (L) of unfueled and fueled regions of known local equivalence ratios as specified in Table 8.1 and shown in Figure 8.2. The injected gas is selected as CO_2 at the adiabatic flame temperature of the mixture being burnt in the prechamber to generate this jet, which enters through the hot gas injector. The measured static pressure (Matsutomi et al., 2010) is also used as a boundary condition at injector inlet. The fueled/unfueled regions were modeled with sharp planar boundaries, between the fuel and no-fuel regions. Although not very realistic considering the mixing which can take place between combustible mixture and other gasses inside the combustion channels, this assumption was adopted in this work. A more realistic approach, including a gradient in combustible equivalence ratio on either sides of the fueled region, which is not considered in this thesis, will require multi-dimensional modeling of the inflow, which is beyond the scope of this thesis. The two-dimensional computations presented here did not include the inlet port and the exit port, but only three combustion channels, hot gas injector, and the clearance gap between the combustion channels and the igniter.

8.4.1. Case A – Successful Combustion

An experimental test case where combustion occurred successfully was selected to show the effectiveness of this combined methodology of predicting ignition location based on two-dimensional mixing analysis. Figure 8.4 presents the time accurate contours of fuel mass fraction when the hot gas jet is injected. Combustion is not modeled in this two-dimensional computation. The simulation starts with the initial combustible mixture

distribution given by the one-dimensional simulation. The combustion channel was initialized with the measured pressure behind the reflected hammer shock wave and the corresponding ideal gas temperature calculated. The injector starts moving at $t=1.0$ ms, while the simulations start at $t=0.0$ ms. This time (first 1ms) is necessary to exclude the initial pressure wave (due to the mismatch between the initial conditions and boundary conditions) from the solution domain and to get the hot gas interface past nozzle exit. This way, when the injector gets aligned with the combustion channel, hot gas flows into the channel without any unrealistic pressure waves due to startup transients. The injector is aligned/opened to the combustion channel for 1.9 ms. It can be seen (in Figure 8.4, contour plot at time $t=1.00$ ms) how the injected gas comes into the combustion channel through the gap between the combustion channel (stationary in the combustion channel frame of reference) and injector (moving in the combustion channel frame of reference) even before the injector starts opening into the channel. From experimental pressure and ion sensor data, it was approximated that combustion started in the combustion channel at $t=0.4$ ms after the igniter start opening into the combustion channel. This time corresponds to 5° of rotor rotation at 2100 rpm. It can be seen from Figure 8.4, at $t=1.4$ ms, that there is a major counter rotating vortex pair which mixes injected hot gas and the combustible mixture inside the channel. The average equivalence ratio (calculated considering the injected gas as air) of the gas which has a temperature greater than 780 K was calculated to be 0.6. This is shown in Figure 8.5.

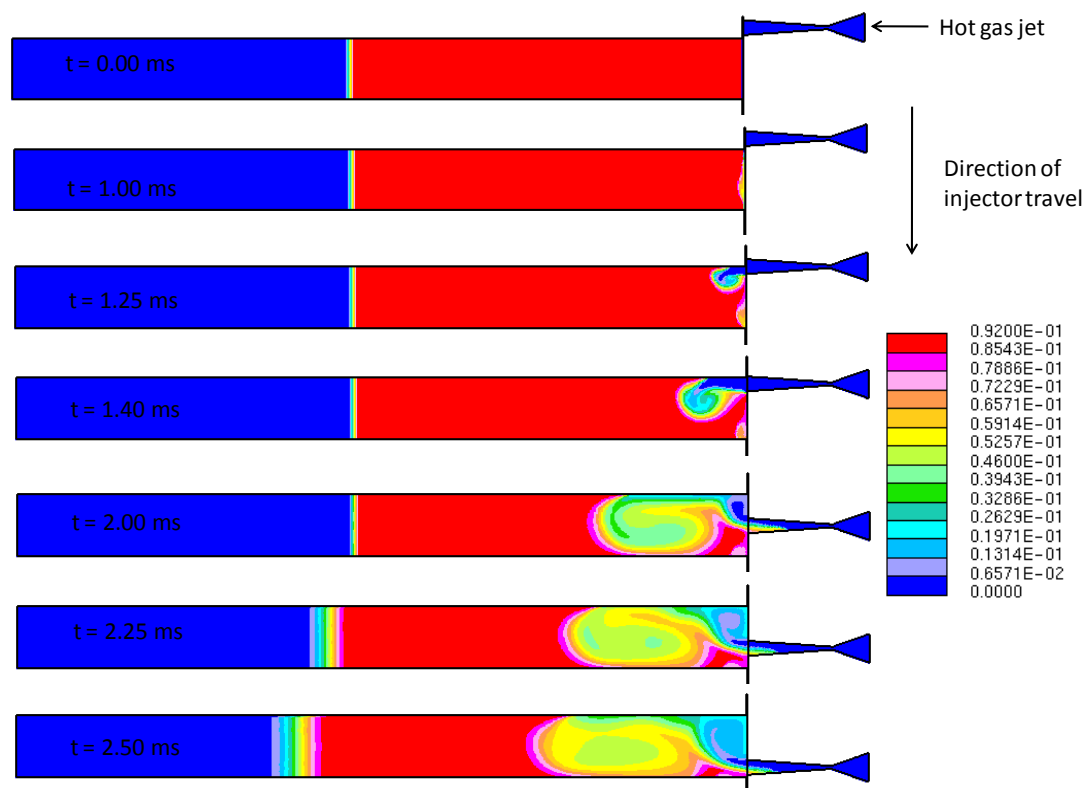


Figure 8.4. C_2H_4 (fuel) Mass Fraction of Case A. In the Color Scheme, 0.092 corresponds to an Equivalence Ratio of 1.44.

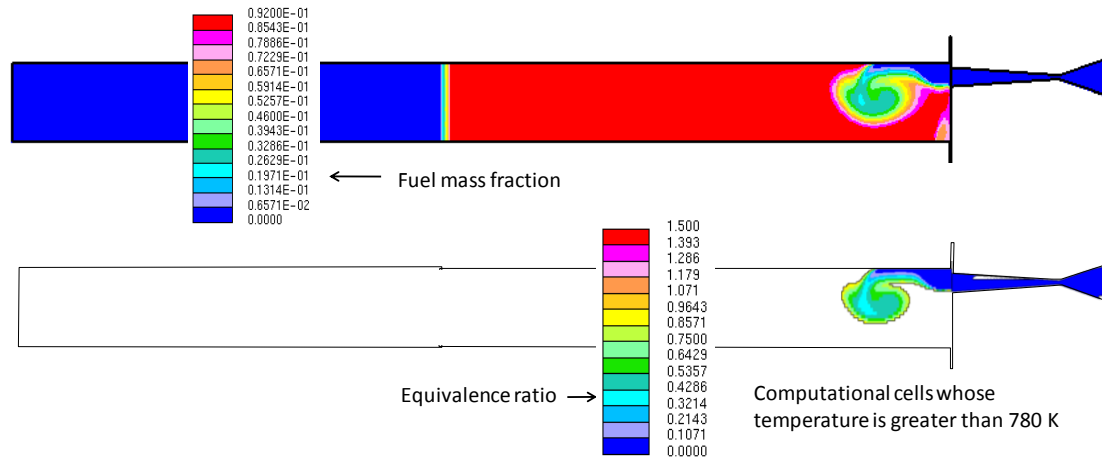


Figure 8.5. Mixing of Combustible Mixture and the Injected Gas is Dominated by Two Counter Rotating Vortices at $t=1.4$ ms (top). The Equivalence Ratio of the Cells whose Temperature is greater than 780 K at $t=1.4$ ms (bottom). The Combustion starts at $t=1.4$ ms.

This average equivalence ratio represents the mixed state of the combustible mixture with the injected hot gas. Hence this value (0.6) was used in the one-dimensional code near the igniter (2.5 inches from the exit side end wall) to better represent the mixed state of gasses. The highest temperatures were in the centers of the two counter rotating vortices which were at locations $x/L = 0.9$ and 0.94 at $t=1.4$ ms. The following discussion provides justification of the possibilities of these locations and time as ignition locations and ignition time. Modified equivalence ratio, in which the hot gas injected, was taken as air in calculating the equivalence ratio is presented in Figure 8.6 for different times during injection process. The average modified equivalence ratio at $t=1.4$ ms is estimated to be ~ 0.6 which is the ethylene-air equivalence ratio for which the lowest ignition delay time prevails when ignited by a hot gas jet (Perera, et al., 2010, Perera, 2010).

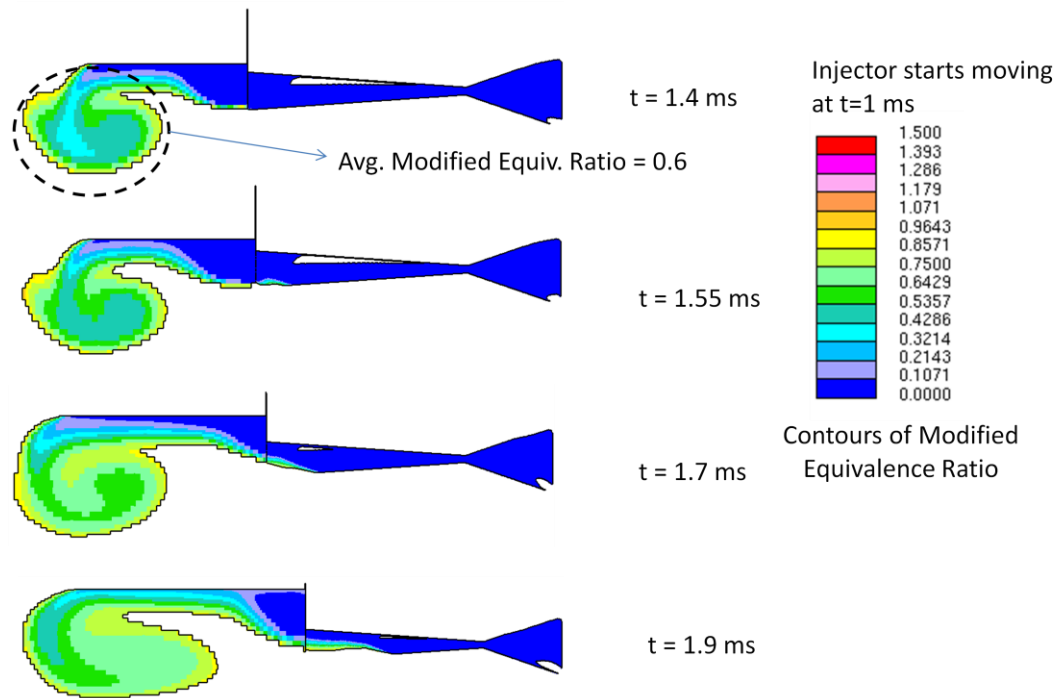


Figure 8.6. Modified Equivalence Ratio. Only the Cells whose Temperature is greater than 780 K is shown.

The contours of modified equivalence ratio are shown in Figure 8.6 for computational cells whose temperature is greater than 780 K. Assuming the time scales for chemical kinetics are much smaller than the mixing time scales, The mixture at $t = 1.4$ ms presents the most possibility for ignition. The average modified equivalence ratio of the cells whose temperatures are greater than 780 K is larger than 0.6 in earlier times than $t = 1.4$ ms and hence would have a comparatively larger ignition time delay.

Assuming hot gas did not come into the combustion channel through the cross channel gap, the ignition can only be initiated by the hot gasses from the torch igniter when it opens into the channel. The channel starts opening into the torch igniter as 168° in WRCVC experiments (Matsutomi et al., 2010). If combustion was initiated as predicted, after a mixing time of 0.5 ms (6°), at $x/L = 0.9$, the flame would have been felt at the closest ion sensor, IP12 which is at $x/L = 0.77$, after another 6° if the apparent flame speed (flame speed relative to the channel walls) was 713 ft/sec as predicted by Elharis et al., (2010). This means that IP12 should sense the flame at 180° . If flame was initiated at $x/L = 0.94$ as predicted, IP12 should sense the flame at 182° . Out of 30 representative combustion test cases, in 3.4% of them, IP12 started to sense the flame between 180° - 182° (Figure 8.7). Hence the predicted ignition locations and time can be taken as realistic. These locations were used as the possible ignition locations in the one-dimensional code to initiate combustion. The data taken into the one-dimensional code, to better represent a mixed state of gas prior to combustion is given in Figure 8.6.

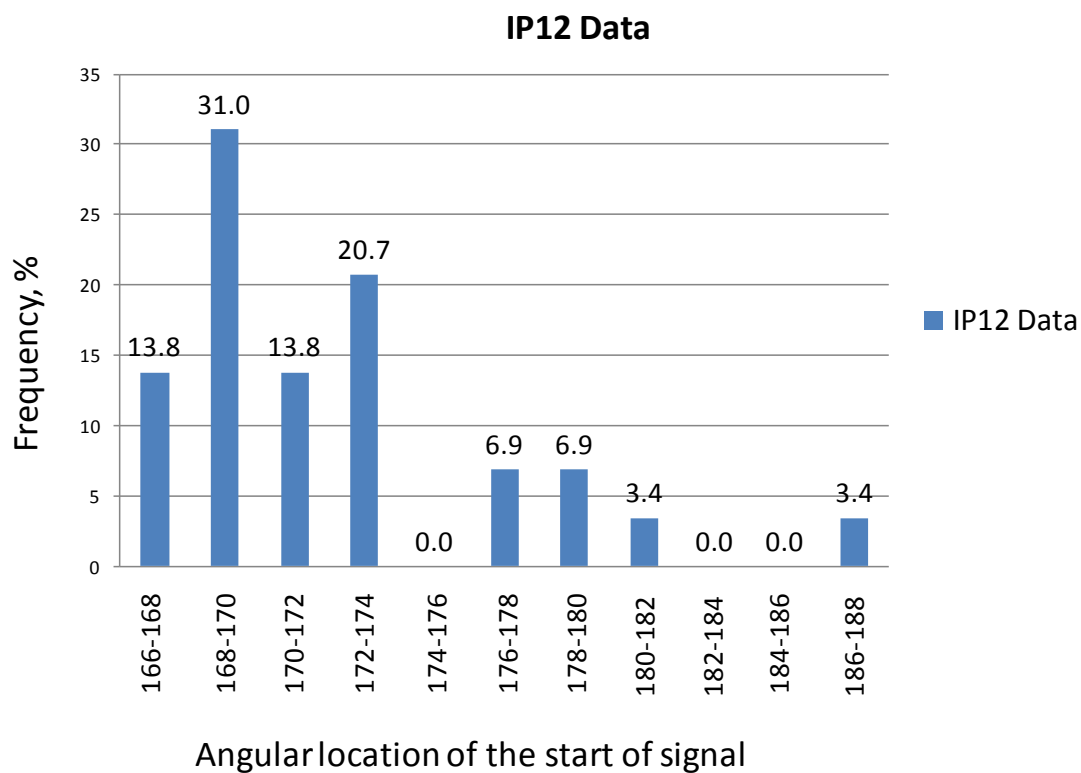


Figure 8.7. Frequency of the Start of Signal sensed by IP12.

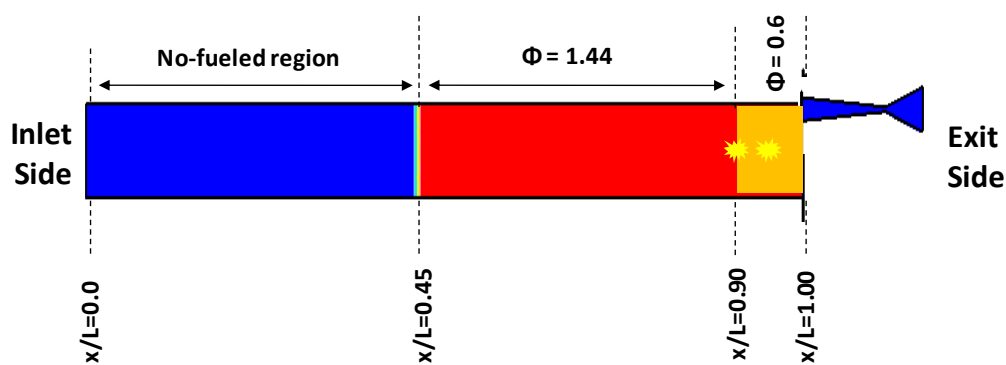


Figure 8.8. The Mixed State of Gas with Modified Equivalence Ratios and Possible Ignition Locations.

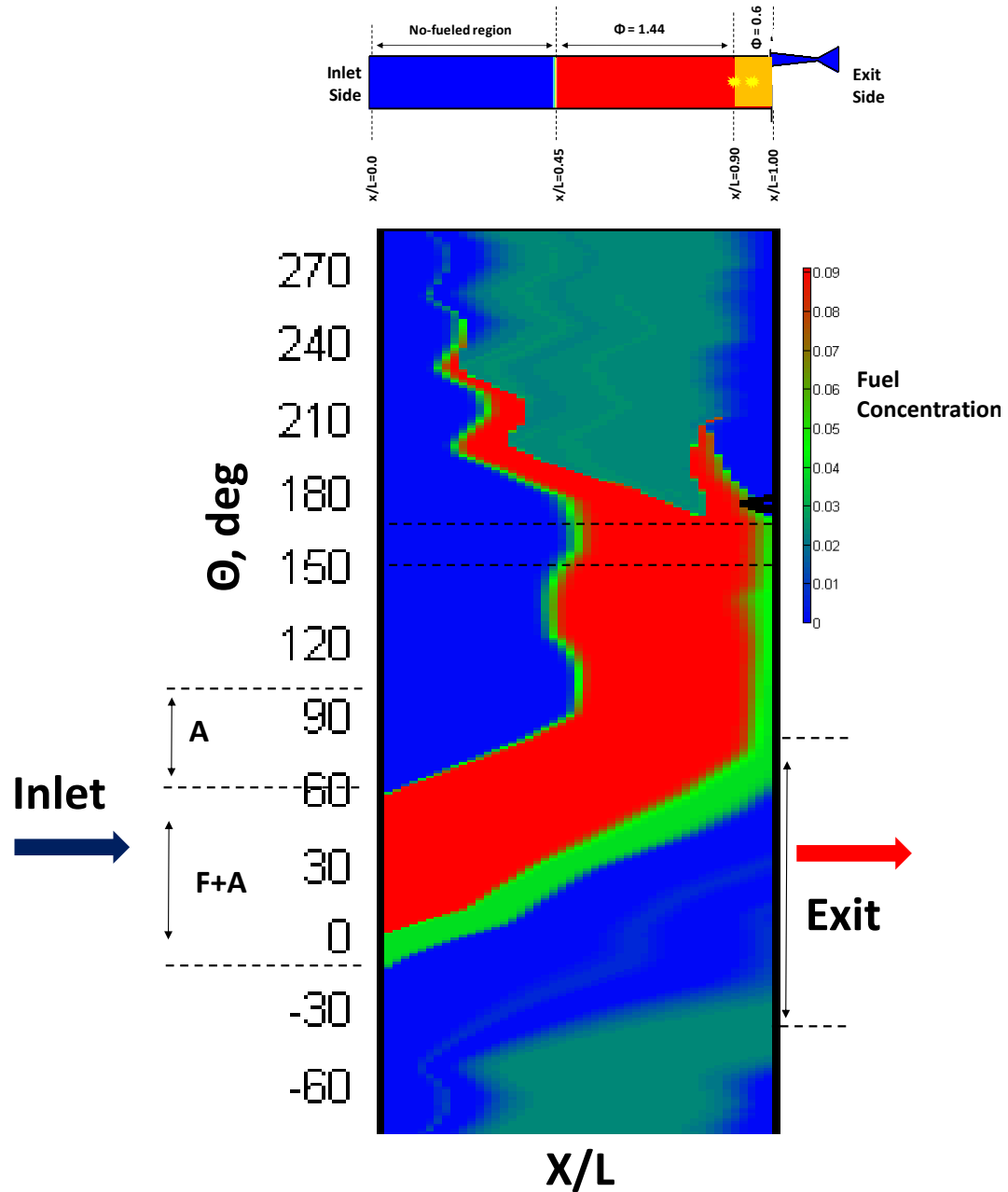


Figure 8.9. 1D Combustion Modeling with the Inputs from the 2D Mixing Predictions for Case A. The Dotted Black line in the 1D Contour Plot shows the Position of the Channel in Comparison to the 2D model.

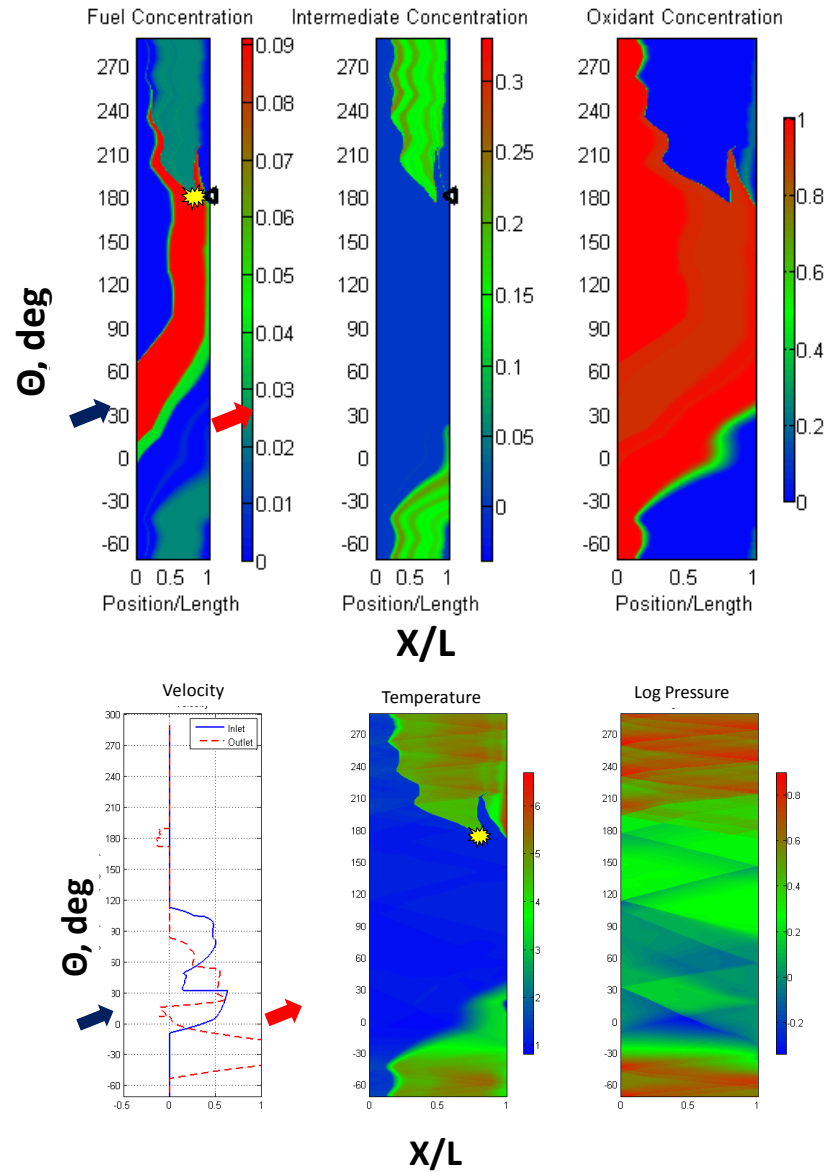


Figure 8.10. 1D Predictions of Concentrations of Fuel, Intermediate Species of Combustion, and Oxidant, Inlet and Outlet Plane Velocities, Normalized Temperature, and Logarithm of Static Pressure. The Predicted Ignition Location is Marked in Plots of Fuel Concentration and Normalized Temperature. The Igniter Location is shown by Black Arrows in Plots of Fuel Concentration and Concentration of Intermediate Species. The Vertical Axis is Rotational Angle and the Horizontal Axis represents Distance Along the Channel, Normalized by Channel Length.

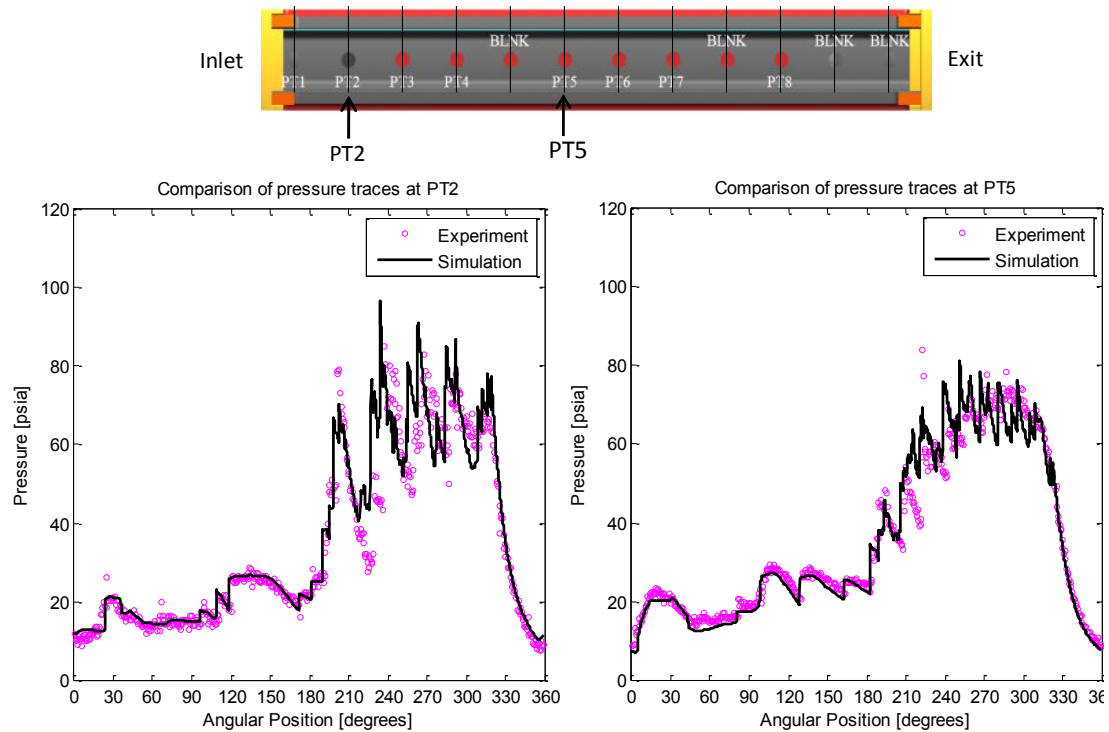


Figure 8.11. In-Channel Pressure Comparisons at PT2 and PT5 for the Successful Firing Case. A representative Experimental Cycle was selected for this Comparison.

Figure 8.9 shows transient 1D predictions of concentrations of fuel, intermediate species of combustion, oxidant, inlet and outlet plane velocities, normalized temperature, and logarithm of static pressure. The simulation represents the plotted quantities inside one combustion channel subjected to time varying boundary conditions to simulate the rotation of the channel past different ports. The occurrence of successful combustion is apparent from these plots. The plot of logarithmic pressure shows the propagation of the pressure waves inside the combustion channel. The comparison of measured transient channel pressure at locations (marked PT2 in Figure 8.11) close to the inlet port and in the middle of the channel to the predictions of the 1D code with the inputs of 2D mixing

analysis is shown in Figure 8.11. The agreement is satisfactory, having predicted almost all of the pressure fluctuations and the peak pressures accurately.

8.4.2. Case B – Failed Combustion

Figure 8.12 presents the time accurate contours of fuel mass fraction when the hot gas jet is injected in Case B. Combustion is not modeled in this computation. The simulation starts with the initial combustible mixture distribution given by the one-dimensional simulation. The combustion channel was initialized with the measured pressure behind the reflected hammer shock wave and the corresponding ideal gas temperature calculated. The injector starts moving at $t=1.0$ ms, while the simulations start at $t=0.0$ ms. From experimental pressure and ion sensor data, it was known that this case failed to combust. The injector traverses the combustion channel in 1.9 ms and the channel opens to the exit after 10 ms (not modeled in this simulation) from the start of hot gas injection, at 2100 rpm. It can be seen from Figure 8.12, that the hot gas jet merely ‘pushes’ the combustible mixture rather than getting mixed with it due to the buffer layer in between. The gas mixing seems more due to diffusion than by convection. The level of diffusion observed in the simulations is affected by the initial turbulence intensity prescribed in the combustion channel which was equal to 1%.

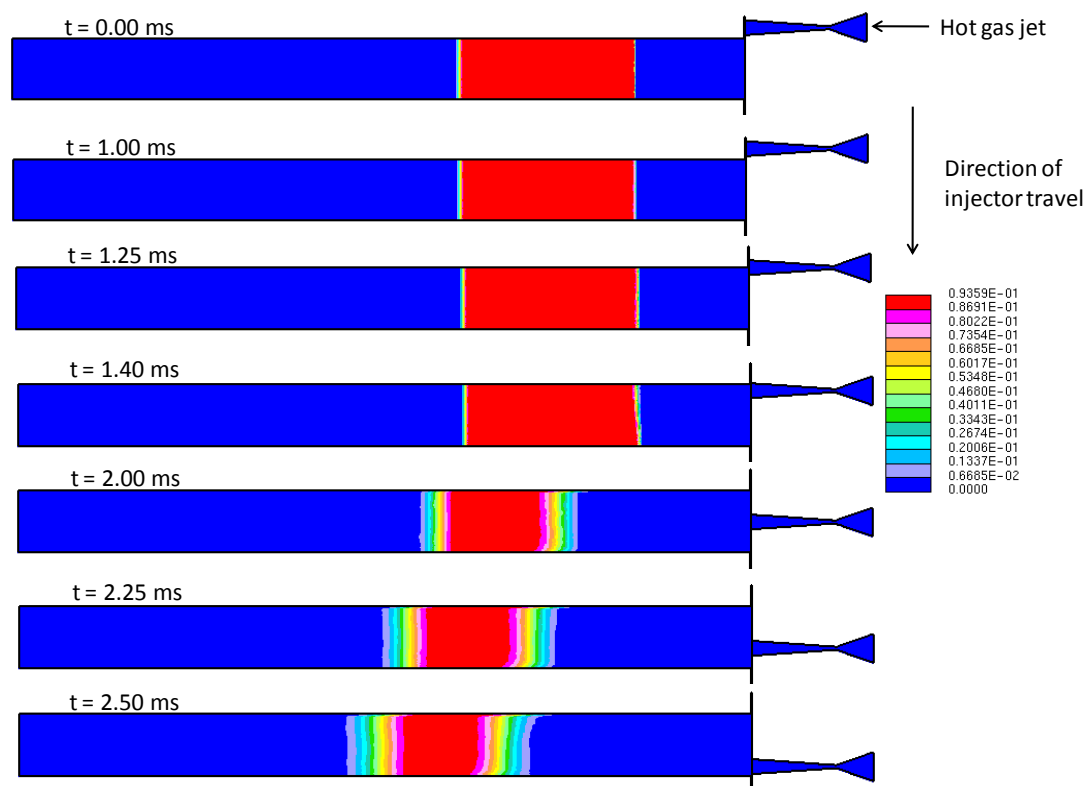


Figure 8.12 C_2H_4 (fuel) Mass Fraction of Case B. In the Color Scheme, 0.094 Corresponds to an Equivalence Ratio of 1.47. Injector Starts Moving at 1.00 ms.

It can be seen from Figure 8.13 that the equivalence ratio of the gas whose temperature is greater than 780 K is very small due to the buffer layer in between. The hot gas does not reach the combustible mixture as a result of this buffer layer. The maximum equivalence ratio of the mixed gas (which has a temperature greater than 780 K) is 0.06 which is too lean to support ignition. The failure of combustion in this case, as seen from experiments can be easily explained from Figures 8.13-8.17. The one-dimensional code predictions of (failed) combustion are given in Figures 8.15-8.17. The inputs given to the one-dimensional code from this mixing calculation is shown in Figure 8.13. The intermediate species and oxidant concentrations in Figure 8.16 further support the absence of

combustion in this case. The equivalence ratios of the channel gas after mixing with the hot gas, predicted from the 2D simulations cannot be directly patched into the 1D code. The equivalence ratio of the inlet combustible mixture is varied (keeping the total fuel and air mass flow rates constant at the measured values) to get a similar mixture downstream of the combustion channel. The inlet static pressure is varied in the 1D code to obtain the measured mass flow rate at the desired distribution. Figure 8.17 shows the comparison of measured in-channel pressure and the 1D prediction of pressure at the same location, PT2.

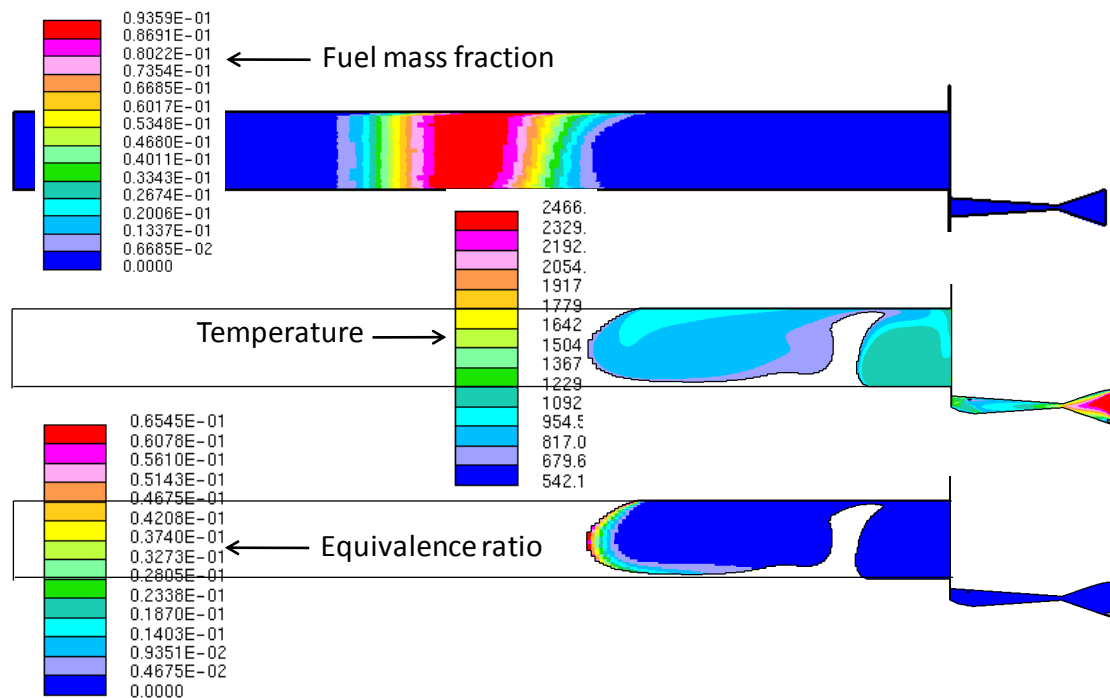


Figure 8.13. The Temperature and Equivalence Ratio of the Mixed Gasses. Equivalence Ratios were calculated in Cells with Temperature greater than 780 K.

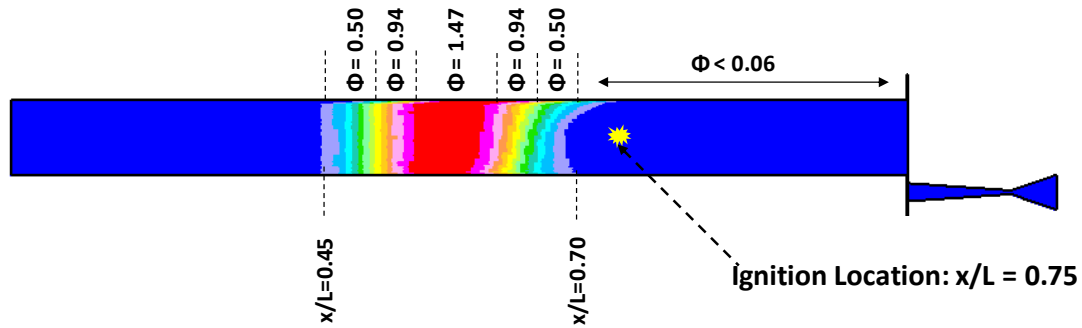


Figure 8.14. The Mixed State of Gas with Modified Equivalence Ratios and possible Ignition Location for Case B.

The 1D predictions of fuel concentration in Figure 8.15 shows how the fuel enters the WRCVC from the left end and fills the combustion channel. As given in Table 8.1, injectors 1-2 and 7-15 do not supply fuel and only injectors, 3-6 supply fuel, which is shown in Figure 8.15. This fuel supply setup kept a large unfueled region near the ignition source and hence prevented from igniting. Fuel concentration plots show how it leaves via the exit port without getting combusted. The concentrations of intermediate species and the oxidant also shows that this case failed to ignite.

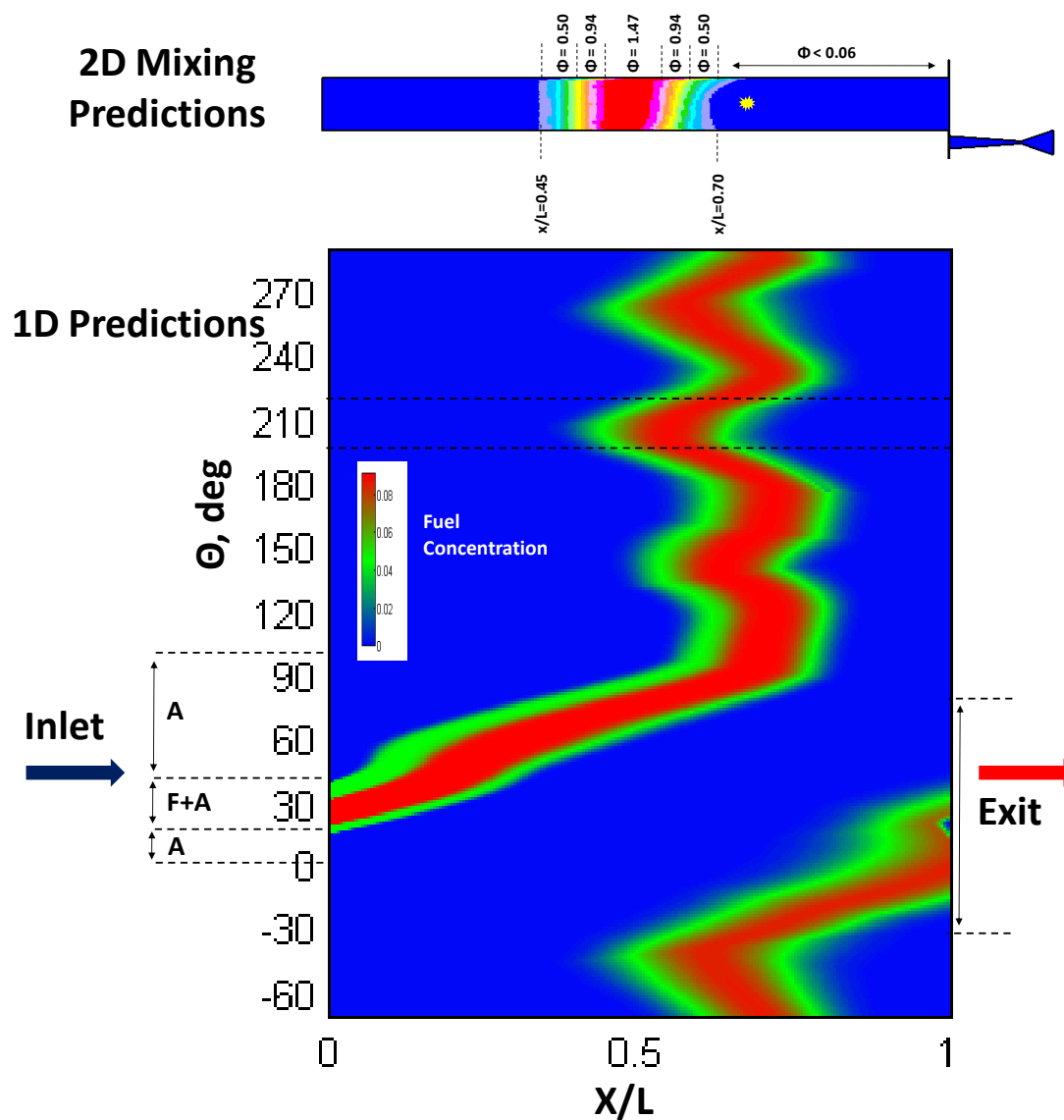


Figure 8.15. 1D Combustion Modeling with the Inputs from the 2D Mixing Predictions for Case B. The dotted black line in the 1D Contour Plot shows the Position of the Channel in Comparison to the 2D Model.

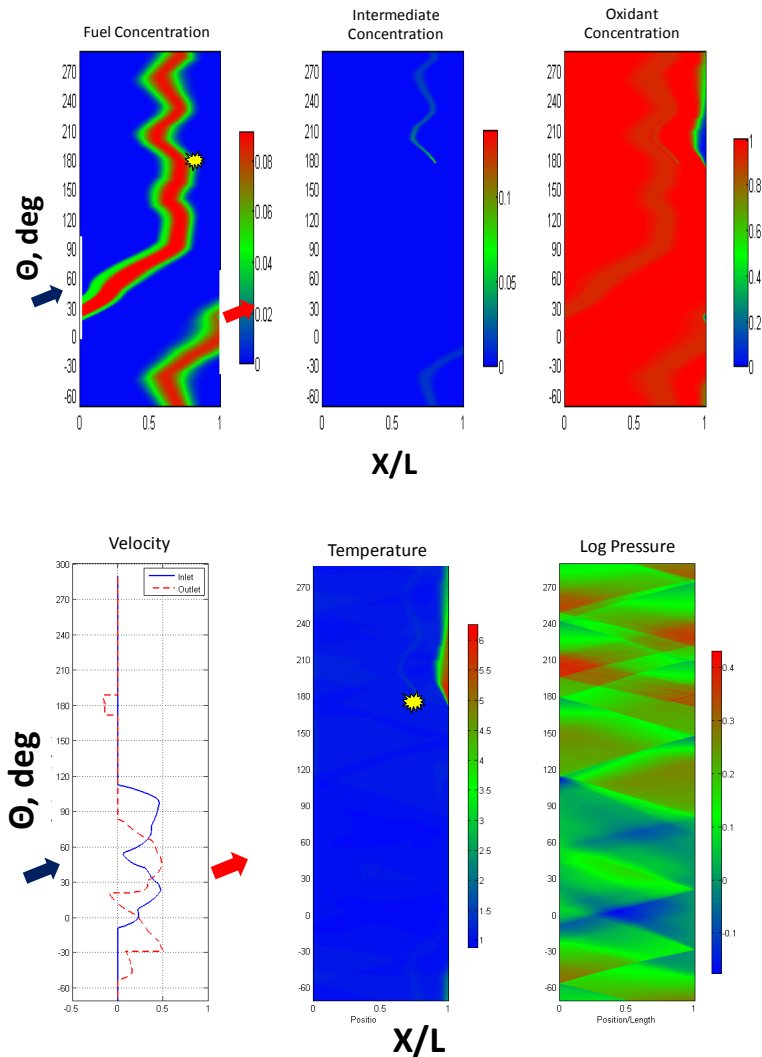


Figure 8.16. Transient 1D Predictions of Concentrations of Fuel, Intermediate Species of Combustion, Oxidant, Inlet and Outlet Plane Velocities, Normalized Temperature, and Logarithm of Static Pressure of Case B. The Predicted Ignition Location is marked in Plots of Fuel Concentration and Normalized Temperature. The Igniter Location is shown using Black arrows in Plots of Fuel Concentration and Concentration of Intermediate Species. The Vertical Axis is Rotational Angle (and also time) whereas the Horizontal Axis represents Distance along the Channel, normalized by Channel Length.

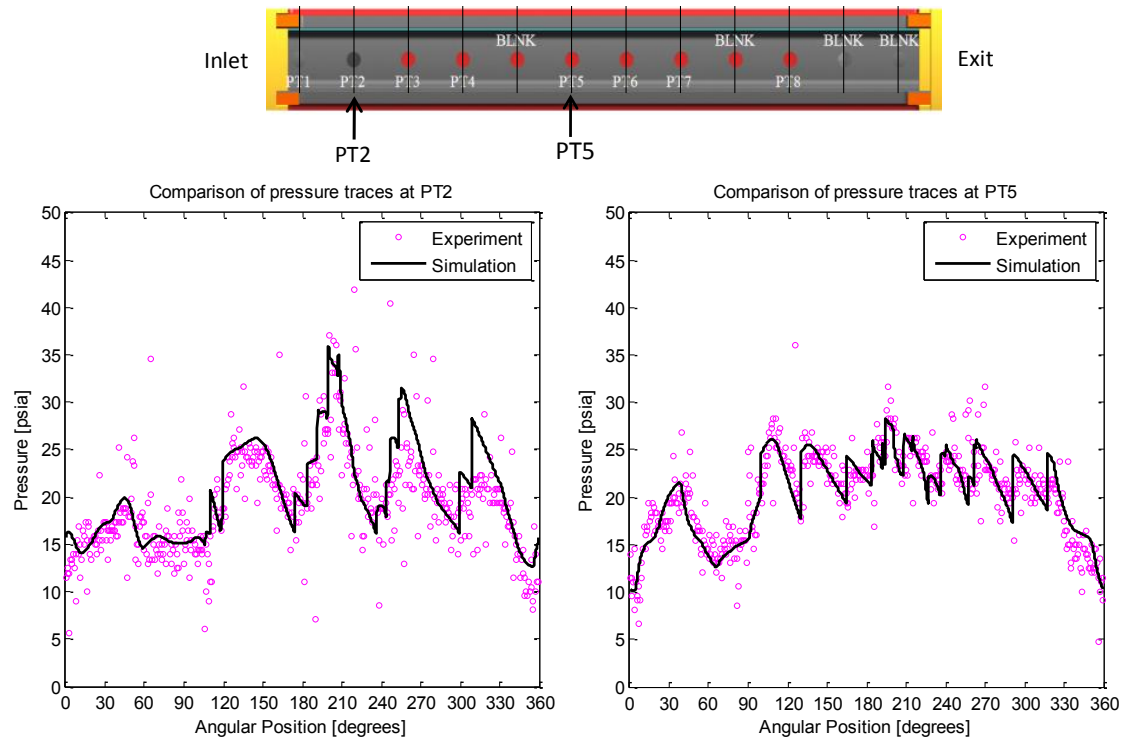


Figure 8.17. In-channel Pressure Comparisons at PT2 and PT5 for the Failed Firing Case. A representative Experimental Cycle was selected for this Comparison.

The injected gas mass fraction of case A in the ‘ignition region’ at $t=1.4$ ms can be used to calculate the ‘high temperature mixedness (HTM)’ of the gas. HTM is an index which can be used to understand the potential for ignition of a combustible mixture based on the mixture temperature and equivalence ratio. This is explained in detail in Chapter 10. An interesting and useful analysis would be to perform two-dimensional mixing analysis for several combustion cases, for which experimental data is available on the time of ignition initiation. The location and intensity of gas mixing can be predicted by the two-dimensional analysis, and these can be used in conjunction with the experimentally determined ignition times to calculate/fine-tune the HTM index which will give insights

into the local equivalence ratio and mixture temperature of an 'ignitable' mixture. This fine-tuned HTM index can then be used to predict the ignition delay times of mixtures using two-dimensional mixing data, in the absence of experimental data. The HTM index presented in Chapter 9 is a temporal value, representing the entire high temperature combustible mixture within defined temperature and equivalence ratio bounds. Since the two dimensional mixing predictions show that there are dominant vortices in the domain which has the highest temperatures and modest equivalence ratios, it will be interesting to define a spatial HTM index and monitor its variation in time. This kind of an analysis might be more effective in predicting ignition location and time, since this track the 'ignitable mass' in a lagrangian perspective. Careful and innovative analysis techniques are necessary in capturing the same 'ignitable mass' in time and space from an Eulerian analysis as given in this thesis. However this is not dealt with in this thesis.

CHAPTER 9. DESIGNING A TWO-DIMENSIONAL NOZZLE.

9.1 Gas Dynamic Design of a 2D Nozzle

Careful attention must be made in approximating a three-dimensional nozzle with a two-dimensional model. The 2D injector can be designed either to supply the same mass flow rate per unit depth of the injector, thereby varying the upstream pressure, or keeping the same upstream pressure as the 3D case varying mass flow rate. If the downstream flow characteristics from the injector and the pressure drop across it are important parameters to hold constant, the injector dimensions needs to be recalculated. The injector used as the torch igniter in WRCVC (Matsutomi, 2010) is a converging-diverging nozzle with circular cross sections. As explained in chapter 6, the available computer resources did not allow doing several 3D simulations in a timely manner and hence 2D approximations which give much quicker results were attractive. The methodology used to design the 2D injector to better approximate the 3D injector is explained first. Then, axial penetration results from both 2D and 3D injectors are presented to verify the design hypothesis. The expansion ratio the gas experiences and the momentum flow rate at the nozzle exit (when the injector is at the middle of the combustion channel) were kept the same as in the 3D case when designing the 2D injector.

Since the mass flow rate per unit area and temperature are kept the same, the Mach number is expected to be the same at the nozzle exit. Hence the exit width of the nozzle ($b_{\text{diverging}}$ in Figure 12.1) is kept at the same value of 0.61 inches (same as in the 3D computation) relative to the channel width of 2.5 inches. From 3D simulations, the exit Mach number at nozzle exit was found to be 2.5 at the mid channel position. The lengths of converging and diverging sections have been optimized to get the same pressure drop across and the exit Mach number as the 3D simulations.

9.1.1. Diverging Section

Once the exit width ($b_{\text{diverging}}$) was chosen, throat width (a) was selected to give a known Mach number at the exit at a known length ($L_{\text{diverging}}$) of the diverging section. The equations solved are given below: The Mach number of the flow in the diverging section is assumed to depend only on area change and friction of the nozzle walls. Hence, the Mach number change along the length of the nozzle is given by Equation 9.1, which is simplified in Equation 9.2:

$$\frac{dM}{dx} = \frac{M \left(1 + \frac{\gamma-1}{2} M^2 \right)}{1-M^2} \left(-\frac{1}{A} \frac{dA}{dx} + \frac{\gamma M^2}{2} \frac{4\bar{f}}{D} \right) \quad (9.1)$$

$$\frac{dM}{dx} = \frac{M \left(1 + \frac{\gamma-1}{2} M^2 \right)}{(1-M^2)\gamma(x)} (-\tan \alpha + \gamma M^2 \bar{f}) \quad (9.2)$$

A fourth-order Runge Kutta algorithm was used to solve Equation 9.2, to obtain the desired Mach number at $x=L_{\text{diverging}}$. This was an iterative process as throat width was not known in priori. An average friction factor \bar{f} was selected based on the friction factors

at the inlet, throat, and exit of the nozzle, calculated according to the Reynolds numbers from the 3D simulation. The average friction factor was calculated to be 0.0045. The inlet width was calculated for a known throat width, length ($L_{\text{converging}}$) and choked flow at the throat.

9.1.2. Converging Section

Once the nozzle throat width was calculated, the same procedure was followed for the converging section to calculate the inlet width of the nozzle ($b_{\text{converging}}$). The equation is as follows:

$$\frac{dM}{dx} = \frac{M \left(1 + \frac{\gamma-1}{2} M^2 \right)}{(1-M^2)y(x)} (\tan \alpha + \gamma M^2 \bar{f}) \quad (9.3)$$

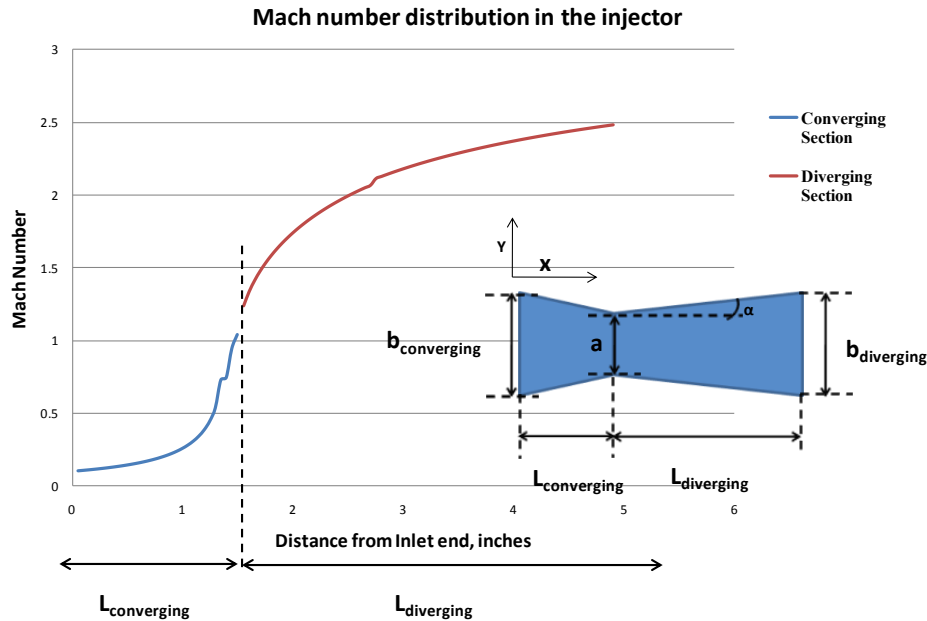


Figure 9.1. Mach Number Distribution in the Nozzle.

The designed 2D nozzle was intended to provide similar penetration characteristics of the 3D nozzle which affect the mixing between the injected gas and channel gas. The comparison of 2D and 3D penetration of the injected gas jet for similar boundary conditions are shown in Figure 9.2. Time zero corresponds to the start of injector motion. The simulation starts before that and the injector flow is diverted to a separate region (not shown here) to exclude the startup transient effects from affecting the solution. Once the flow establishes in the injector, the injector is made to move and time is recorded from 0.0 ms. The injector moves at 1704 inches/sec linearly across the face of the combustion channel. Only the 3D injector is shown in Figure 9.2 to show the location of the injectors. The black curve corresponds to the 0.01 iso-surface of the injected gas mass fraction in 2D case. The colored lined corresponds to the same in the 3D case.

The combustion chamber is numerically isolated from the injector when the injector goes past the chamber and the simulation is terminated. It is acknowledged that the 2D injector is best compared with a 3D slot injector, although a hole-type injector was used in 3D to be consistent with the one used in related WRCVC experiments (Matutomi et al., 2010). The work presented in Figure 9.2 was done in support of these experiments and this 2D injector was designed to represent the actual 3D hole-type injector used in the experiments, so that faster results can be obtained in two dimensions.

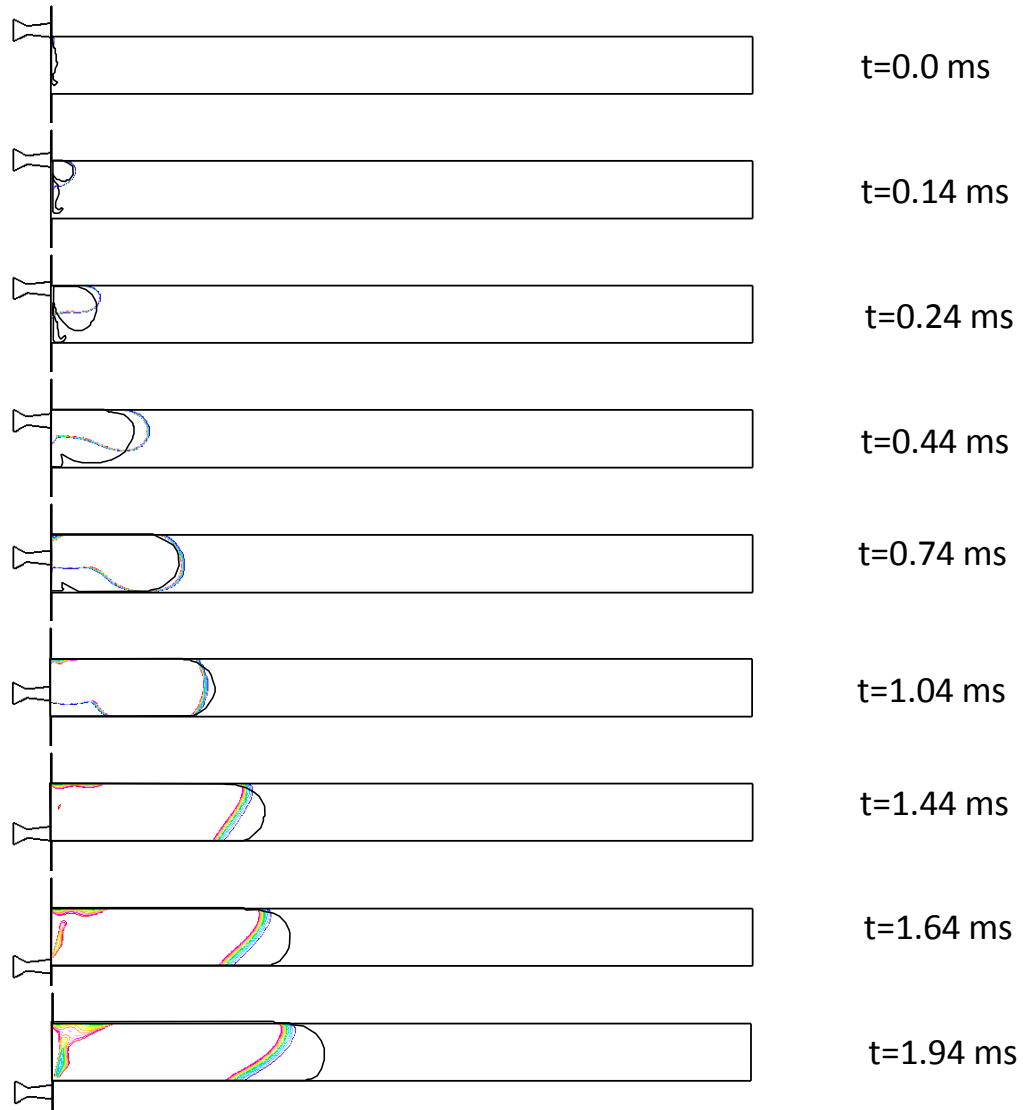


Figure 9.2. Penetration of 2D and 3D Jets. Only the 3D Injector is shown (black Curve inside the Combustion Channel corresponds to the 0.01 Iso-surf of the Injected Gas Mass Fraction in the 2D Jet and the Colored Lines correspond to the 0.01 Iso-surf of the Injected Gas Mass Fraction in the 3D Jet Computations).

As seen in Figure 9.2, the 2D jet is able to predict axial penetration patterns comparable to the 3D predictions for the same boundary conditions. However, predictions start to deviate when the jet travels beyond the middle of the channel. The 2D jet is seen to penetrate more in the circumferential direction (in the direction of injector travel) than the 3D jet. During the last half of its travel, the 2D jet is seen to penetrate more than the 3D jet, axially.

9.2 Effect of Initial Injection Pressure Ratio

Axial penetration and mixing of the injected gas from the 2D injector is studied at different momentum flow rates at the injector inlet. The cases considered are summarized in Table 9.1. The combustion channel was initialized with the measured pressure behind the reflected hammer shock in the WRCVC experiments (Matsutomi et al., 2010, Elharis et al., 2010), for all cases. The temperature was calculated using isentropic relations. The mass flow rate and total temperature (at injector inlet) were kept constant by varying the total pressure and Mach number at injector inlet (Figure 9.3). The mass flow rate was selected to be the same as the torch igniter flow rate used in the WRCVC experiments (Matsutomi, et al., 2010). Also the injection total pressure used in the experiments is as same as in Case 3 in Table 9.1

Table 9.1. Initial and Boundary Conditions of Test Cases used in Numerical Computations.

Mass flow rate (kg/sec)		0.075				
Gas constant (J/kg-K)		287				
Nozzle inlet area (m ²)		5.58e-04				
Total temperature (K)		2315				
Specific heat ratio		1.4				
Initial/back pressure (Pa)		172370				
		Nozzle inlet boundary conditions				
Case	Total inlet Pressure (Pa)	Pressure ratio	Density (kg/m ³)	Velocity (m/s)	Static Temperature (K)	Mach number
1	517107	3	0.77	176	2300	0.18
2	689476	4	1.03	131	2306	0.14
3	861845	5	1.29	105	2310	0.11
4	1034214	6	1.55	87	2311	0.09

Once the pressure ratios were selected, Equation 9.1 was used to calculate the Mach number for constant mass flow rate, nozzle inlet area, total inlet temperature, and inlet area. The penetration of the jets in Cases 1 to 4 is compared in Figure 9.4 using contour plots of the injected gas mass fraction. The times shown in Figure 9.4 are from the start of injector travel. It can be seen from Table 9.1, Case 1 has the highest momentum and Case 4 the lowest. However, due to the increase in inlet pressure from Case 1 through 4, the inlet density is increasing accordingly from Case 1 through 4. The nozzle inlet boundary condition is applied in such a way that the supplied density, velocity and temperature are used to calculate the mass flow rate (which is the same for all cases) which is kept constant across the inlet boundary. Velocity, static temperature, and density are allowed to vary at the boundary. It is interesting to note that the axial jet penetration does not vary much in these cases. This similarity in penetration can be attributed to the exit Mach number of the nozzle and the pressure loss across the nozzle. These parameters

were seen to stay the similar during most of the injector travel for the inlet total pressures selected. The nozzle throat remained choked for entire travel of the injector in all cases.

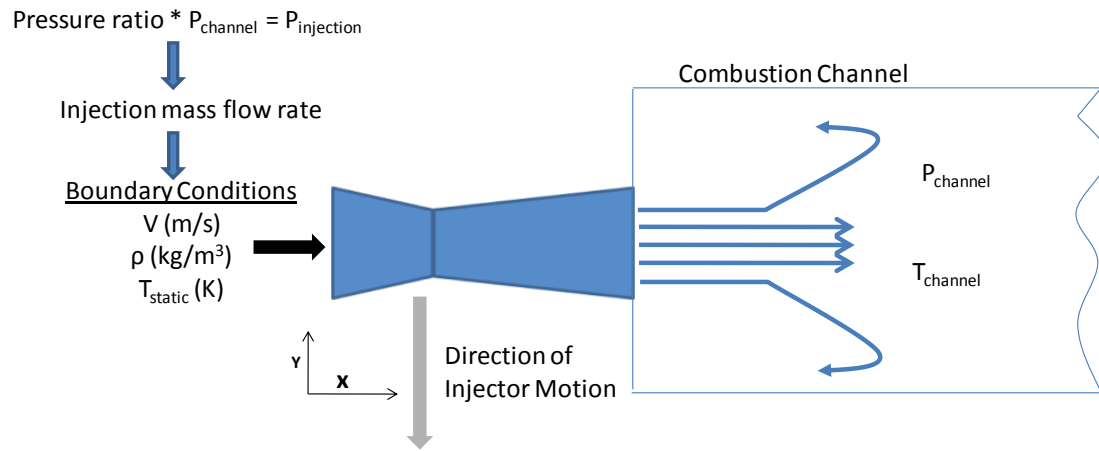


Figure 9.3. Boundary Conditions and Problem Setup in the Computations of 2D Hot Gas Jet Injecting in to a Long Combustion Channel to assess the Effect of Initial Injection Pressure on Jet Penetration and Mixing Effectiveness with in Channel Gas.

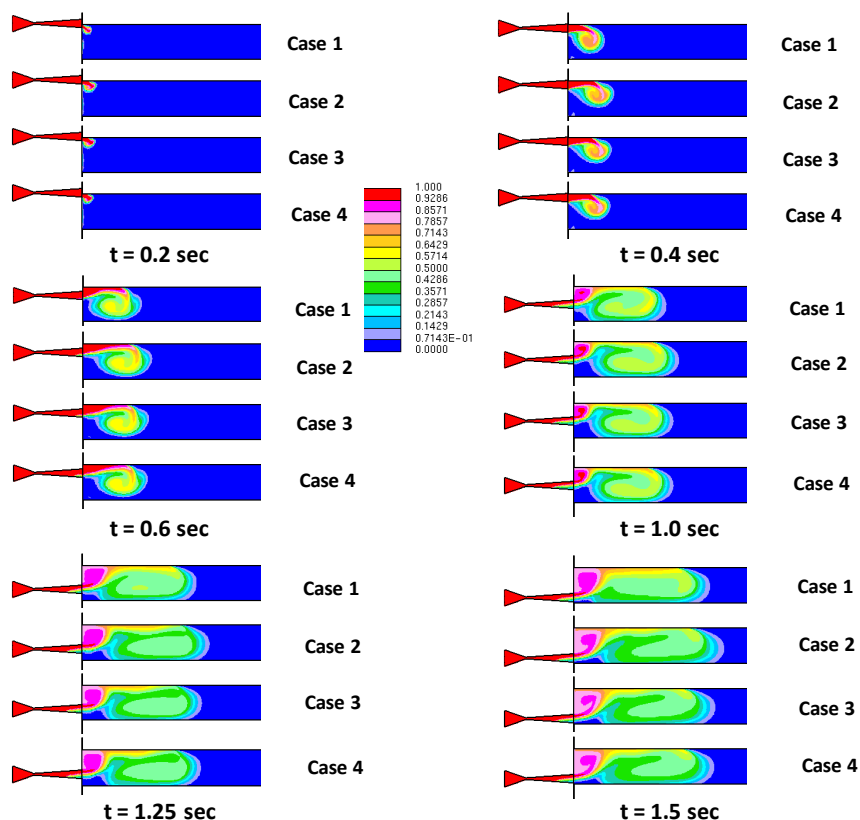


Figure 9.4. Comparison of Axial Jet Penetration from the 2D Nozzle for Different Inlet Momentum Flow Rates. Only part of the Combustion Channel is shown.

Quantification of the level of mixing is important in understanding the ignitability and subsequent burning characteristics of the combustible mixture. However this is a challenging task in transient flow problems where the level of mixedness of gasses varies with time. A typical example is the combustible mixture trapped inside an IC engine combustion chamber, whose local equivalence ratio keeps changing with time due to the gas motion inside. A common approach used in the IC engine community is to track the local equivalence ratio in time. The analysis gets even more complex when mass is added into the control volume transiently, as in the case of hot gas injection for ignition in a

WRCVC. The ignition of combustible mixture requires a high-temperature mixture to be formed whose composition contains sufficient fuel and sufficient oxygen, and may be influenced by admixing of recently combusted gas containing active radicals. When the mass added into the system is expected to ignite the mixture, tracking the local equivalence ratio alone will not suffice. The variation of the local temperature of the combustible mixture and the heat transfer to the surrounding gas becomes equally important in deciding its ignitability. Hence a new quantity called the “high-temperature mixedness (HTM)” was defined which takes into account the local temperature and the mixture quality of the gas. At any given time during the injection process, the fraction of the injected gas whose temperature is above a known limit (780 K) is selected. From this selected ‘hot mass,’ the gas whose mass fraction is between known limits is again selected. The ratio between this selected mass and the total injected gas mass is termed HTM at that time:

$$\text{high temperature mixedness} = \frac{\langle m_{LL \leq Y_{HG} \leq UL} \rangle \text{ for } T_{cell} > T_{Critical}}{m_{HG, Total}} \quad (9.4)$$

Unlike in IC engine related work, a clear definition of the equivalence ratio cannot be used for mixing quantification when a burnt gas is added to the fuel-air mixture for ignition. The fuel-air mixture gets diluted from this already burnt gas and hence the definition of equivalence ratio gets affected. Hence HTM was defined using injected gas mass fraction rather than equivalence ratio. If injected gas mass fraction is known at a location, at any given time, fuel and air concentrations can also be known from species

balance equations. This usage of injected gas mass fraction avoids having to ‘redefine’ a definition for equivalence ratio to be used in situations when the fuel-air mixture is diluted from gasses brought in for ignition.

Several authors in the past have used similar definitions to define and analyze transient mixing behavior. Nanda & Abraham (2002) quantified the mixing of injected fuel with combustion chamber gas in a diesel engine, by using the injected mass at any instant, normalized by the total amount of injected mass. They grouped the injected mass into three zones: rich, flammable, and lean. The lean fraction is that part of the injected gas (fuel vapor) which has an equivalence ratio less than 0.5; the flammable fraction is that fraction of the fuel vapor which has an equivalence ratio between 0.5 and 2.0, and the rich fraction is the amount of fuel vapor which has an equivalence ratio greater than 2.0. The limits of these zones had been arbitrarily chosen. Abraham and Bracco (1989) present these different mixing zones, referring to them as f (fraction) - θ (crank angle) plots.

A numerical technique used for modeling combustion, called “multi-zone modeling” uses a similar approach of mixing quantification. The combustible mixture in reacting flow simulations are grouped into zones according to their equivalence ratios and temperatures. At each time-step, the grouping of the computational cells into zones is performed in a way that guarantees that the grouped cells have similar thermodynamic and chemical properties. Temperature is the most representative variable of the thermodynamic state of a cell. In addition, the equivalence ratio, ϕ , provides information about the composition

and how far combustion has progressed in the cell. Taking this into consideration, Babajimopoulos et al., (2005) used the following steps in grouping the computational cells into T/ ϕ zones as following:

- All cells in the combustion chamber are sorted from lowest to highest temperature and are divided into five temperature zones. These zones were selected in such a way that each zone contains a prescribed fraction of the mass within the chamber (5%, 10%, 20%, 30% and 35%, going from the coldest to the hottest zone).
- The cells in each temperature zone were sorted from lowest to highest ϕ . Starting from the cell with the lowest ϕ , the cells of the temperature zone are divided into as many zones as needed, so that the maximum ϕ range in each zone is $\Delta\phi_{\max} = 0.02$.
- The last steps are to take any T/ ϕ zones which contain more than 1% of the cylinder mass, sort the cells in these zones by temperature, and divide them into smaller temperature zones, so that, in the end, the mass fraction in each zone does not exceed 1%.

Once the T/ ϕ zones were selected as above, the zone temperatures, pressures, and compositions are computed as the average of cells within each zone. Then each zone reacts as a single zone (with averaged values of temperature, pressure and composition) constant volume chemical reactor for the time from “t” to “t+ Δt ”. Changes in composition and internal energy are mapped back onto the cells associated with the zone (Babajimopoulos et al., 2005). Aceves et al. (2000 & 2001) introduced a sequential multi-

zone modeling approach. This multi-zone model of HCCI combustion assumes a decoupling of the turbulent mixing process and chemistry prior to and during the main heat release. The cells with similar pressure and temperature histories are grouped into a relatively small number of zones (10–100). The chemical kinetics solver is then applied to this small number of zones, instead of the large number of cells used in the CFD code, offering a great advantage in computational time compared with a full integration of a chemical kinetics code and a CFD code. The multi-zone model has been successful in the prediction of combustion process parameters, such as peak cylinder pressure and burn duration (Babajimopoulos, 2005).

Flowers et al. [26] modified the multi-zone model to include mixing effects, by introducing a coupled CFD/multi-zone model. Instead of a one-way mapping of the CFD temperature distribution onto the multi-zone chemical kinetics solver, their method was modified to have mapping back and forth throughout the cycle. The advantage is that the fluid mechanical processes are still calculated on a high-resolution grid, while the computationally intensive chemical kinetics processes can be solved within a small number of zones. The goal of the study was to investigate the mixing of cold gases from the crevices and the boundary layer with the hot gases in the core during the ‘post main heat release’ oxidation. It was found that there is diffusion of CO and fuel from the lowest temperature regions into the hotter gases in the core and that the fuel continues to react during the expansion stroke. In addition, the predictions of HC and CO emissions were improved compared with the sequential multi-zone model. Babajimopoulos et al. (2005) extended the sequential CFD/multi-zone model for open-cycle applications and

investigated the mixing of residual gases with the fresh charge. In order to address the composition inhomogeneity during the chemistry calculation; the fuel–O₂ equivalence ratio was used as an additional criterion for grouping cells into zones.

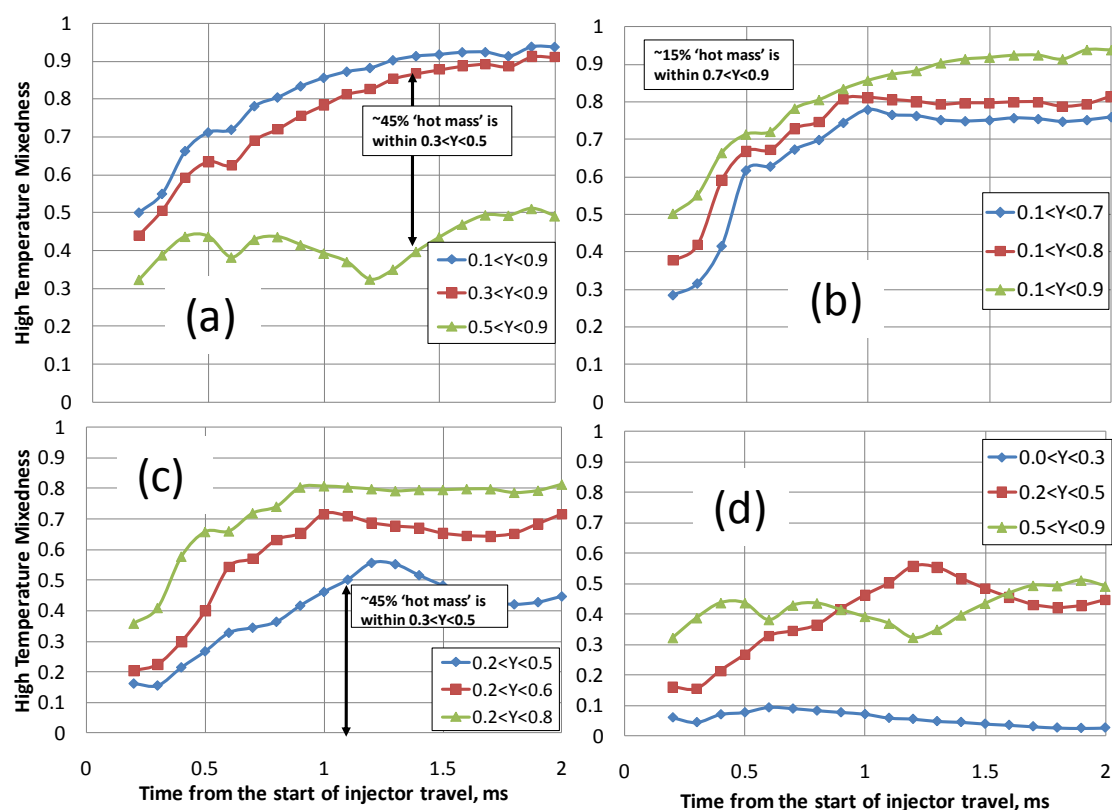


Figure 9.5. High temperature mixedness of Case 4.

The plots in Figure 9.5 present HTM (in vertical axis) against the time from the start of injection of hot gas (in horizontal axis). HTM with different lower limits and same upper limit of injected gas mass fractions are plotted on top left in Figure 9.5. HTM with the same lower limit and varying upper limits are plotted on top right in Figure 9.5. Two different such selections are plotted on the bottom of figure 9.5 to better understand the level of mixedness and ignition potential of gassed inside the combustion channels. These

plots help understand the level of mixing inside the combustion channels. Once the temperatures and mass fractions needed for ignition of a certain fuel is known, these plots can be used to determine the ignition success inside the combustion channel. For example, for a particular fuel, if the temperature of the mixture should be above 780 K (arbitrarily chosen) and the hot gas mass fractions should be within $0.3 < Y < 0.5$ (arbitrarily chosen), the plots in Figure 9.5 can be used in the following way to understand the ignition success.

The time evolution of HTM which is shown in Figure 9.5(a) varies the lower mass fraction limit and keeps the upper limit at 0.9. It can be seen that HTM for mass fraction limits $0.1 < Y < 0.9$ and $0.3 < Y < 0.9$ is similar and approaches $HTM=0.9$ while the HTM of $0.5 < Y < 0.9$ is quite low comparatively. This shows that ~45% of the ‘hot injected mass’ (normalized by instantaneous total mass injected) lies between mass fraction limits of $0.3 < Y < 0.5$. The upper limit of mass fraction is varied while keeping the lower limit of mass fraction at 0.1 in Figure 9.5(b). The effect of upper limits chosen 0.7 – 0.9 is seen to have a minimum effect on HTM; supporting the idea that majority of the mass injected has low mass fractions. HTMs between the mass fraction lower limit of 0.2 and upper limits of 0.5 - 0.8 are shown in Figure 9.5(c). This depicts the fact that ~45% of the injected mass (normalized by instantaneous total mass injected) is within the mass fraction limits $0.2 < Y < 0.5$. However it can be seen from Figure 9.5(d) the injected mass within limits $0.0 < Y < 0.3$ is very small and hence supports the claim that about ~45% of the mass injected is within mass fraction limits $0.3 < Y < 0.5$. According to the ignition criteria assumed, Case 4 has ~45% of the injected mass within $0.3 < Y < 0.5$ and above

780K, and hence conducive for ignition. However, the locations of this “ignitable mass” cannot be deduced from Figure 9.5, and contour plots of injected gas mass fractions have to be looked into.

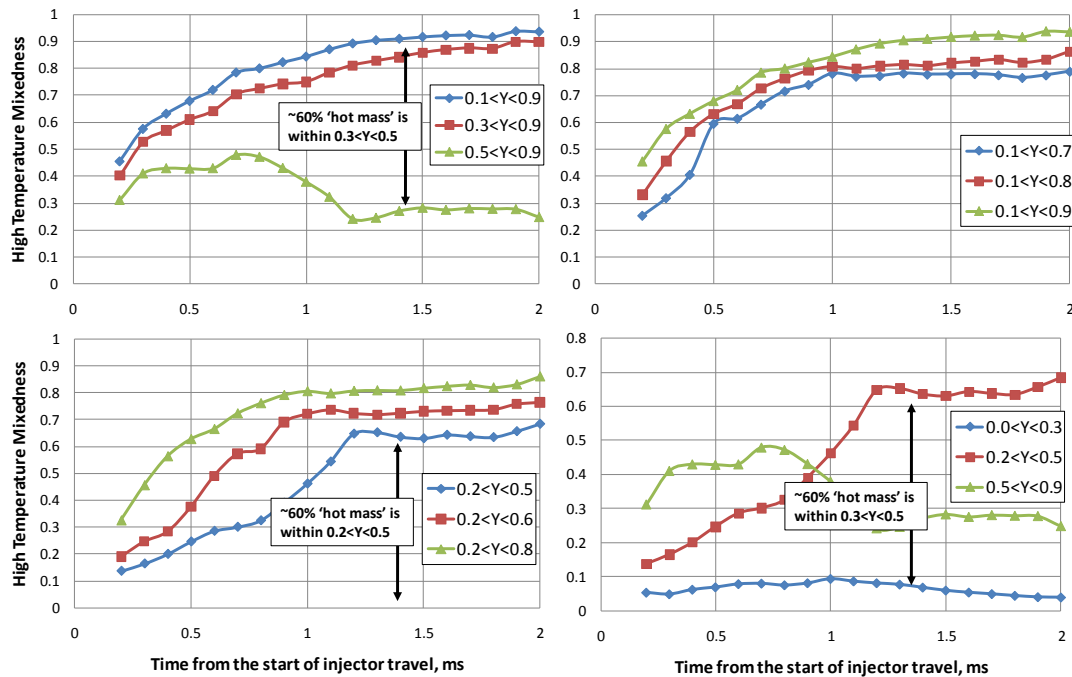


Figure 9.6. High Temperature Mixedness of Case 3.

A similar analysis shows that ~60% of the injected gas is within mass fractions $0.3 < Y < 0.5$ and is above a temperature of 780K for Cases 1, 2, & 3. HTM between $0.3 < Y < 0.5$ is increasing beyond 1.2 ms in Cases 1, 2, & 3, where as it is seen to decrease in Case 4.

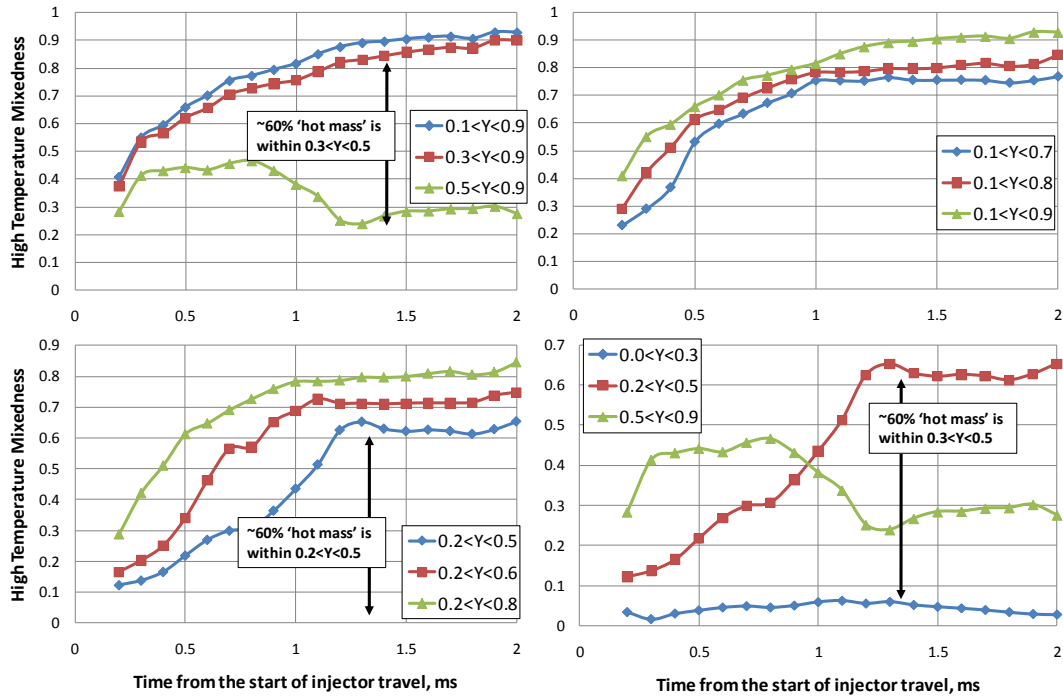


Figure 9.7. High Temperature Mixedness of Case 2.

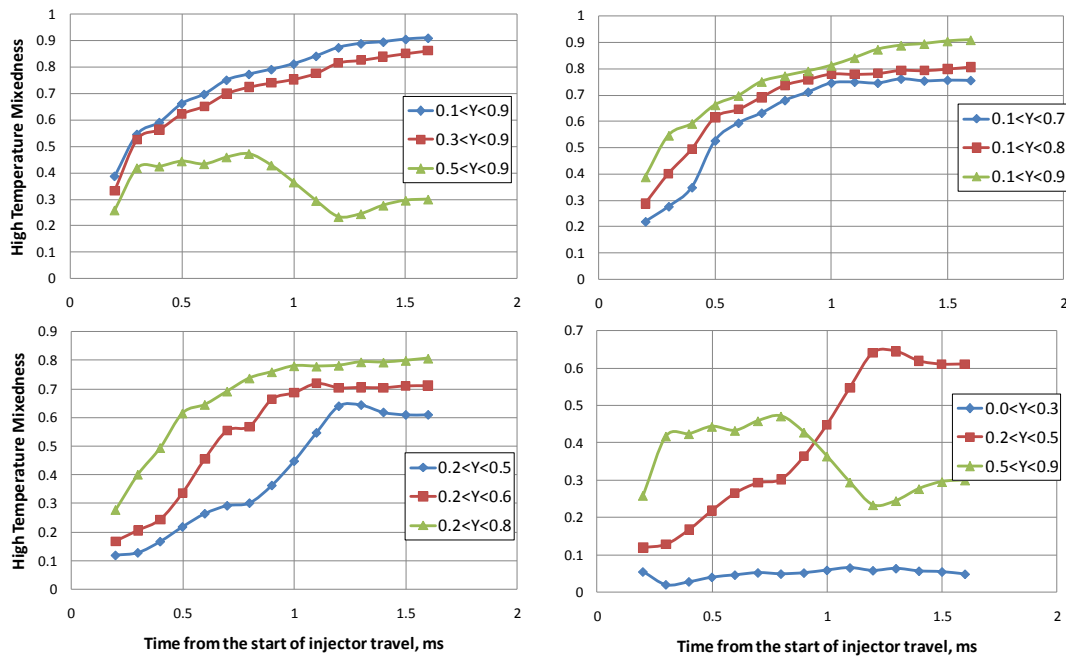


Figure 9.8. High Temperature Mixedness of Case 1.

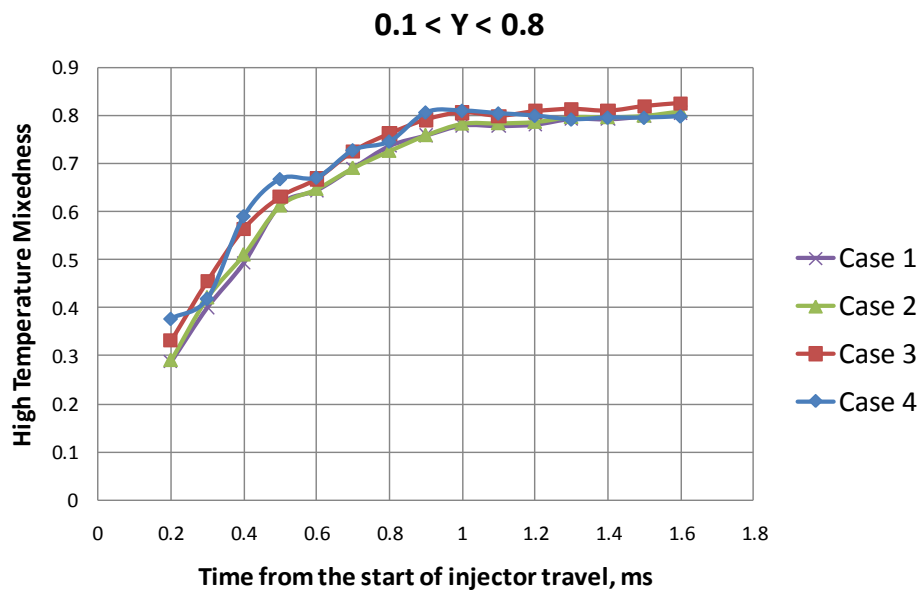


Figure 9.9. Time Evolution of the High Temperature Mixedness for Injected Gas.

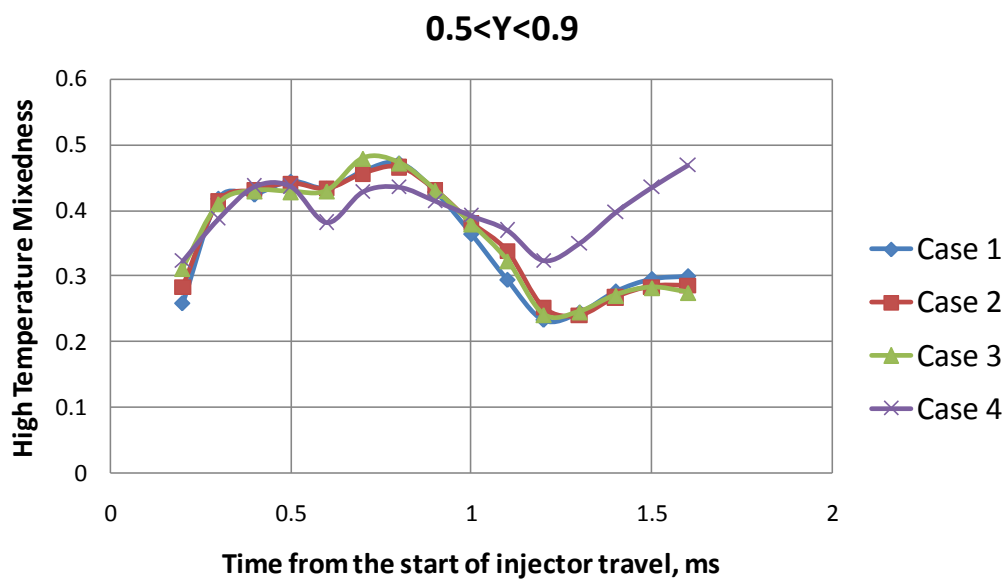


Figure 9.10. Time Evolution of the High Temperature Mixedness for Injected Gas Mass Fractions $0.5 < Y < 0.9$.

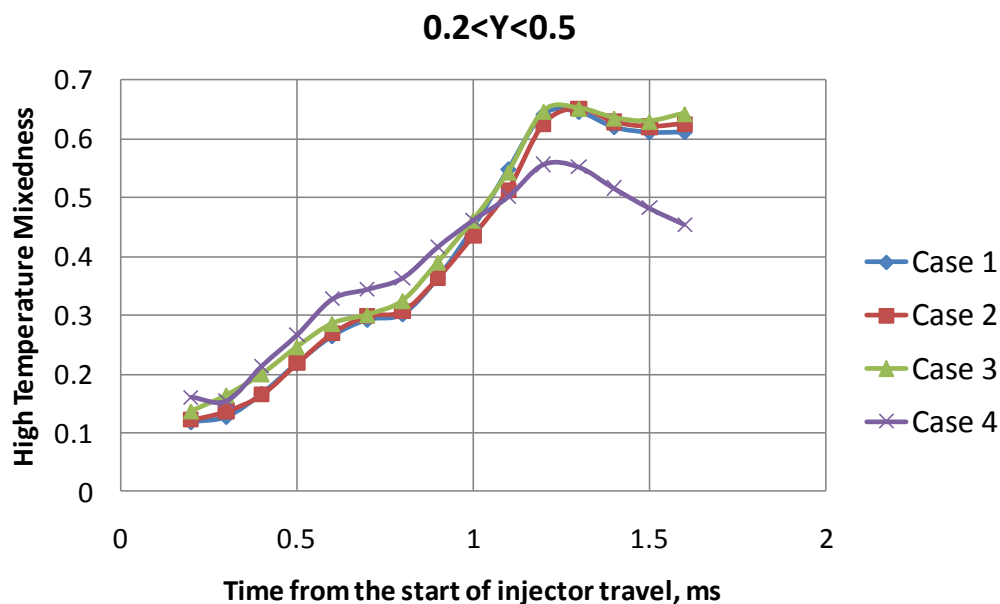


Figure 9.11. Time Evolution of the High Temperature Mixedness for Injected Gas Mass Fractions $0.2 < Y < 0.5$.

A series of comparisons of HTM is presented for the four cases considered in Figures 9.9, 9.10, and 9.11. It can be seen from Figure 9.11 how the HTM for Cases 1, 2, and 3 approaches a value of 60% while for case 4 it approaches 45% for mass fraction limits $0.2 < Y < 0.5$. According to the assumed ignition conditions (mass fraction of injected gas to be within $0.3 < Y < 0.5$ and temperature to be more than 780 K), cases 1 – 3, where the injector inlet pressures were 3, 4, and 5 times that of the channel pressure respectively, would have a higher ignition success than Case 4, whose injector inlet pressure was 6 times that of channel pressure.

CHAPTER 10. HOT GAS INJECTION ANALYSIS IN 3D.

10.1 Introduction

The 3D time-dependent analysis of the mixing between the hot gas jet and the combustion channel gas is presented in this chapter. The hot gas injector (torch igniter) used in the WRCVC test rig (Matsutomi, 2010) is a converging-diverging (C-D) nozzle which delivers a supersonic hot gas jet into the combustion channels as they rotate past it. For simplicity and to reduce the computational time of the simulation, the geometry of the WRCVC combustion channel (Figure 10.1) was approximated by a passage of square cross section, and a combustion channel-fitted reference frame was used. Two partial channels (one leading and one trailing) were added as shown in Figures 10.1 & 10.2. The two partial channels were introduced to be able to model with some accuracy the gradual opening and closing processes of the injector into the channel, while keeping the computational cost lower than for modeling multiple full channels. Two test conditions were analyzed: A) an injector with a square and uniform cross-section injecting into the combustion channels initially at atmospheric conditions (Figure 10.2) and B) an injector modeled as a C-D nozzle injecting into the combustion channel initially at a pressure and temperature which are comparable to conditions behind the reflected hammer shock (Figure 10.1). This hammer shock is generated due to stopping the in-channel flow when the combustion channel closes to the exit port.

Note that this fluid action is not included in the simulations presented in this section, in that it is completed prior to the injection of hot gases for ignition. No grid independence study has been carried out for the 3D analysis due to the extreme high cost of these simulations. Rather, the 2D grid which produced grid independent results (Figures 7.4 and 7.6) has been extruded in the third dimension to obtain the 3D mesh. Reasoning is given for the approximation of the circular cross sectional C-D nozzle with a square cross sectional one.

10.2 Problem Setup in 3D

The simpler Case A is discussed first. The dimensions of the channel with the straight (simplified) injector are shown in Figure 10.2. The 2D representation of the injector nozzle uses the simplified geometry shown in Figures 10.2 & 10.3, which is physically equivalent to a slot of indefinite length replacing the square hole considered in 3D. The plane used for the 2D computation is the θ -z plane of the 3D channel, as shown by hashed lines in Figure 7.6. All models (2D and 3D) have a moderate clearance gap between the moving injector and the stationary combustion channels, equal to 0.01 in.

The current simulations given in this section do not include combustion and only analyze fluid mixing between the injected hot gas and in-channel gas. The gas was modeled as compressible and a widely used RANS turbulence model SST $k-\omega$ was used to model turbulence with standard wall functions used to model near wall regions. The 3D grid which had ~2,000,000 cells was uniform in the r & θ directions, and was stretched in the z -direction to have more cells in the near injector region. The same grid density as in the

mid plane (θ - z) of the 3D grid was used for the 2D grid (with straight injector) which has $\sim 200,000$ cells. The direct comparison of 2D and 3D results is ambiguous when the 3D injector is not a slot injector, covering the entire depth of the channel, as explained in Chapter 10. In the current computations, the boundary conditions are kept the same in both 2D & 3D cases. This ensured nearly the same Reynolds & Mach numbers at the injector exit. An alternate comparison, not adopted here, might be to keep the mass flow rate per unit depth of the channel the same in both cases.

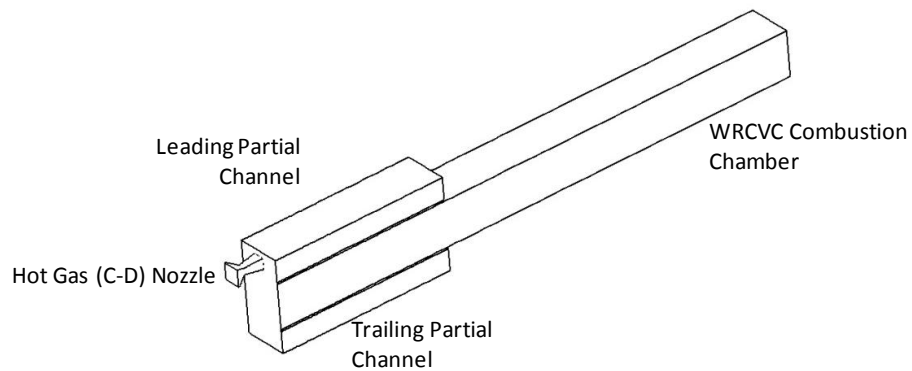


Figure 10.1. Simulated Domain in 3D with the C-D Nozzle.

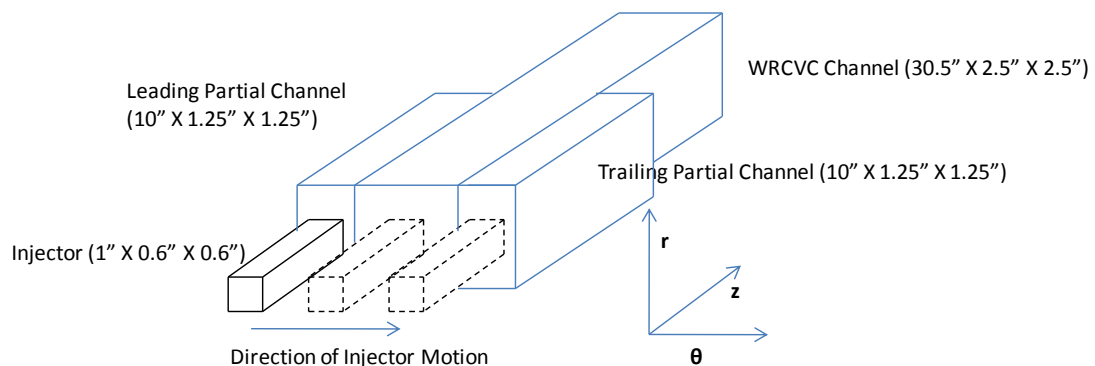


Figure 10.2. Simulated WRCVC Domain in 3D with a Simplified Nozzle Geometry.

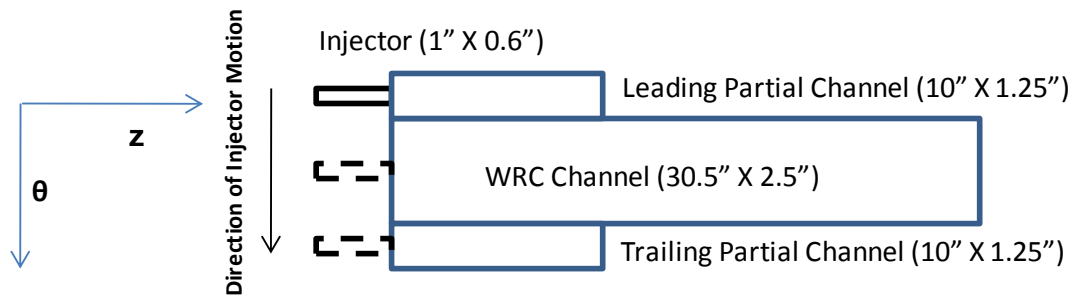


Figure 10.3. 2D Representation of the Computational Domain for the simplified Nozzle Geometry.

The C-D injector in Case B corresponds closely to actual WRCVC test rig operating conditions. The C-D nozzle with circular cross sections is approximated by a C-D nozzle with square cross sections, providing for a simpler grid while keeping the areas and the lengths of the nozzle the same. This simplicity was in the mesh motion where rectangular cells of the square cross section nozzle sliding over the rectangular cells of the combustion channel proved to be more stable numerically than the tetrahedral cells of the circular cross section nozzle. This approximation did not introduce any appreciable difference to jet penetration and shape as can be seen from Figure 10.4. Figure 10.4 presents a comparison between a stationary square cross section C-D nozzle injecting into a channel and a round cross section C-D nozzle injecting into a similar channel. The contours shown are mass fractions of injected gas. The circular injector has same dimensions as the one used in WRCVC experiments (Matsutomi et al., 2010). The square injector was designed to have same cross sectional areas at the inlet, throat, and exit as of the circular injector. The lengths of converging and diverging sections are also kept the

same between the two. In these transient numerical simulations, the injectors were stationary in order to keep the computational cost low. Comparisons of the area averaged mass flow rates, mach numbers and static pressures at the nozzle exit are plotted in Figures 10.5, 10.6, and 10.7 respectively. It can be seen from Figure 10.5 that mass flow rate stays the same between the two cases except from time 1.5 sec to 3.0 sec, where the mass flow rate of circular cross section injector is slightly higher. However, they converge back to the supplied boundary value of 0.78 kg/sec after 3.0 sec. This difference in mass flow rates during times 1.5 sec and 3.0 sec can be explained by looking at the Mach numbers and static pressures at the nozzle exits. The area averaged Mach number of the square cross section injector drops from 1.8 to 0.6 at $t=1.5$ sec, while that of circular cross sectional nozzle drops only to 1.2 and stays at that value till $t=3.0$ sec.

A plausible explanation for this behavior is that the back pressure sensed by the gas coming out of injector exit is increasing at a faster rate in the square cross section injector compared to that of the circular cross section injector. Since the combustion channel dimensions and all the boundary and initial conditions were kept the same, it is concluded that the pressure waves reflecting off of confining channel walls are arriving at the injector exit faster, in the square cross section injector compared to the circular cross section injector. This is only possible if the pressure waves from the square cross section injector diverge more than in the circular cross section injector as shown schematically in Figure 10.8. Hence they reflect back at the exit faster in the square cross section injector case than in the circular cross section injector case.

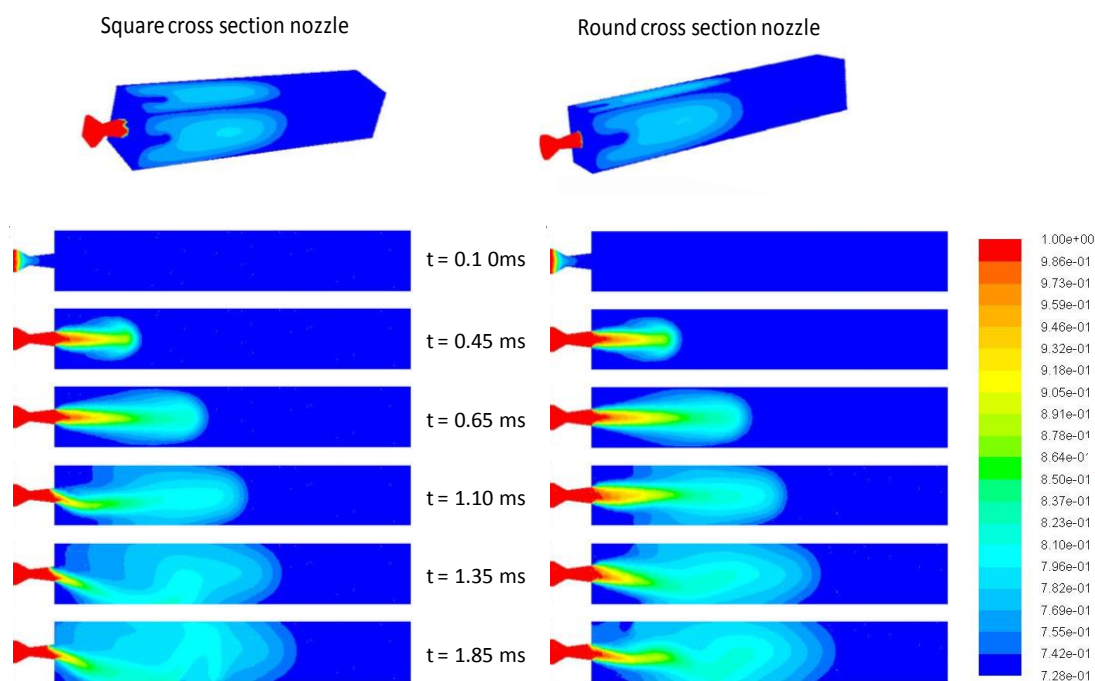


Figure 10.4. Comparison of Jet Penetration and Jet Shape from a Round Cross Section and Square Cross Section Nozzle (Stationary). The Contours are Injected Gas Mass Fraction (Figure credit: Rohitahwa Kiran at Michigan State University).

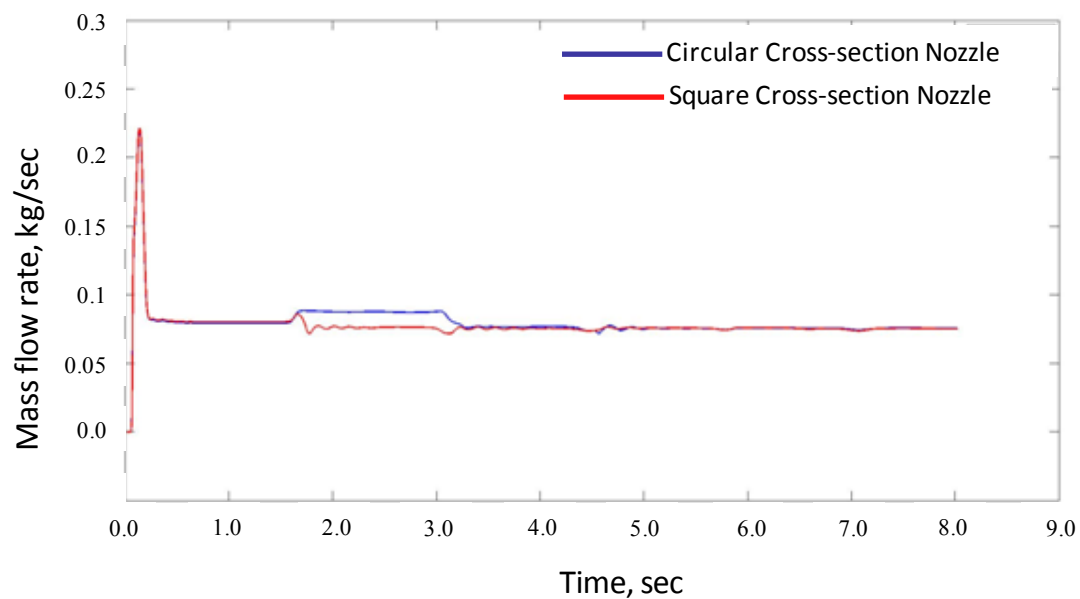


Figure 10.5. Comparison of the Area Averaged Mass Flow Rates at the Nozzle Exits.

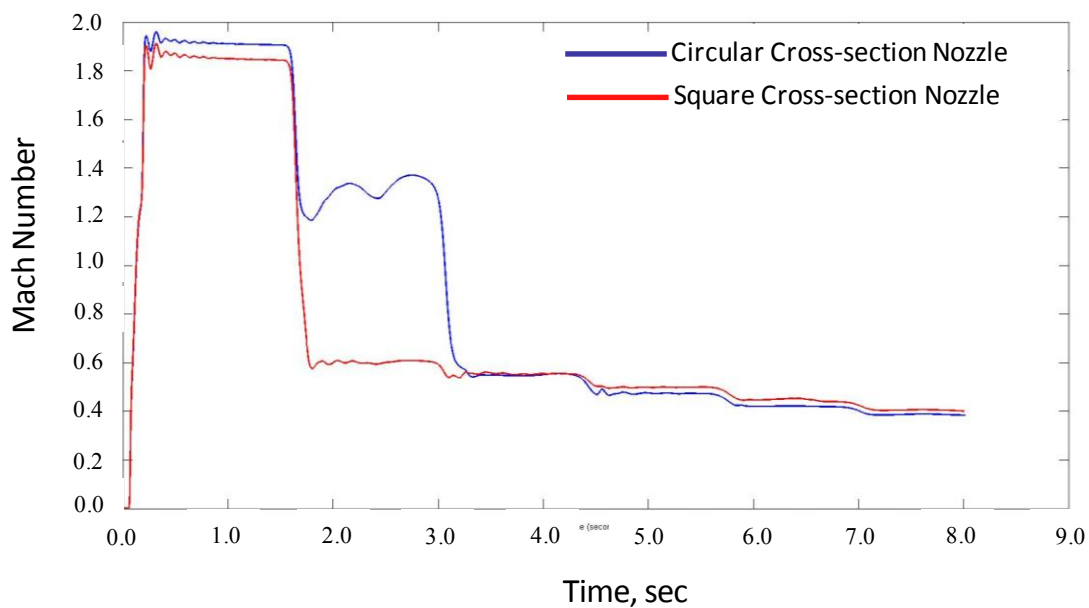


Figure 10.6. Comparison of the Area Averaged Mach Numbers at Nozzle Exits.

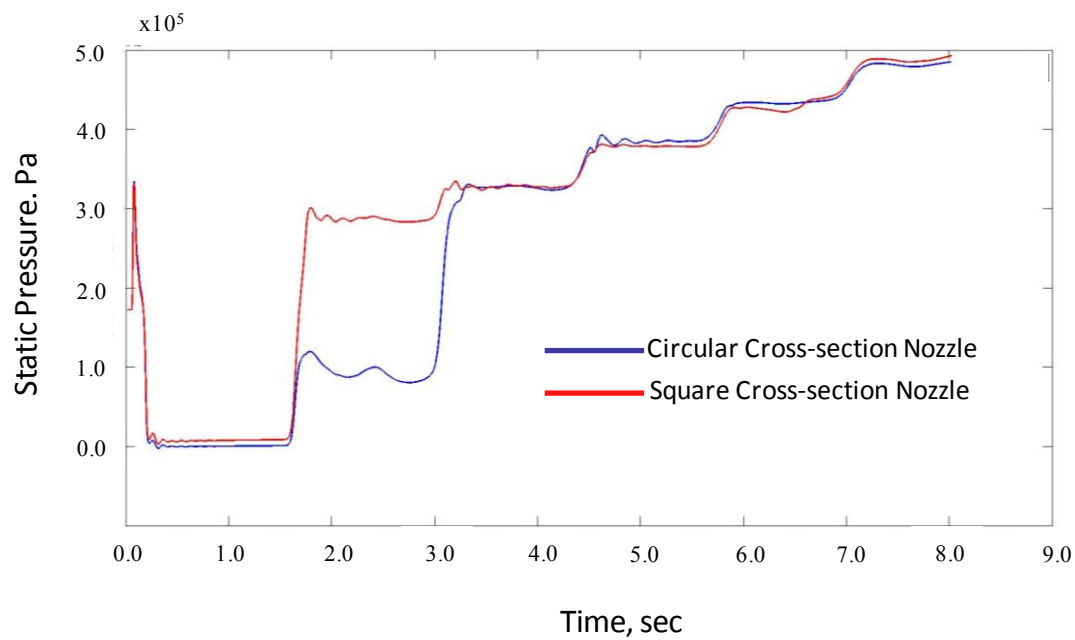


Figure 10.7. Comparison of the Area Averaged Static Pressures at Nozzle Exits.

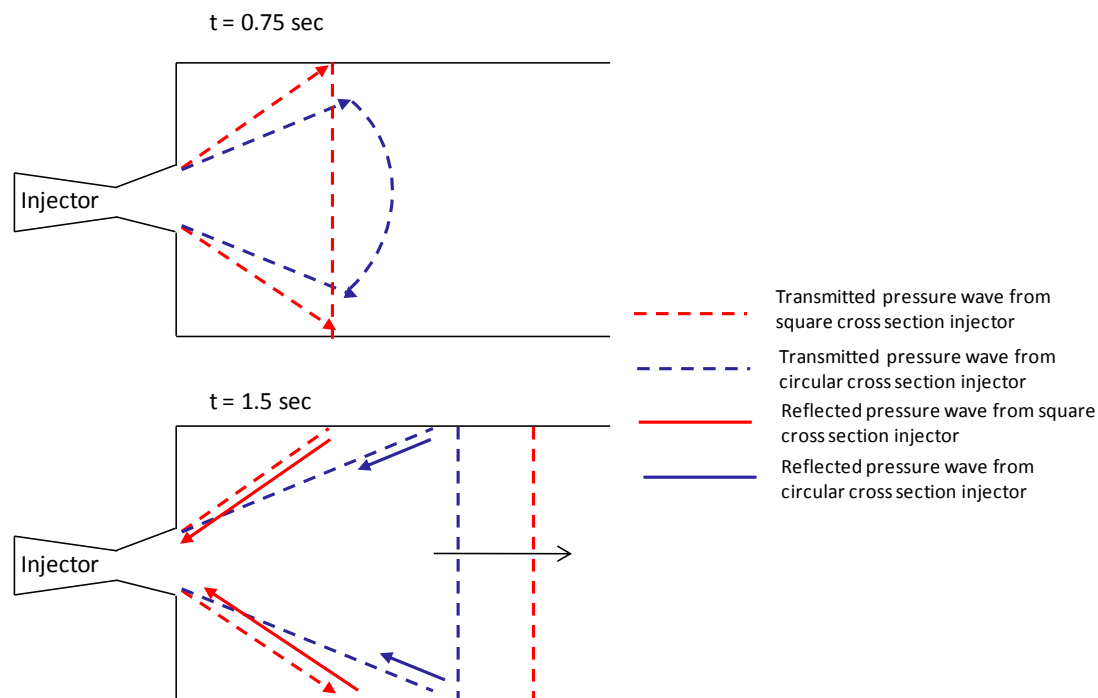


Figure 10.8. Schematic of Transmitted and Reflected Pressure Waves depicting the Rise of Back Pressure in the Square Cross Section Injector sooner than that in the Circular Cross Section Injector.

Hence the flow from the square cross section injector can be taken equal to that of the circular cross section injector is sufficient time was given for the pressure waves to reflect off of the confining walls and to raise the back pressure at the nozzle exit. For this reason and due to the simplicity and robustness of mesh motion in the square cross section nozzle (here after referred to as the 3D injector), it was used in this thesis after allowing sufficient time for the flow to develop as from a circular cross section injector.

The measured mass flow rate from actual WRCVC experiments is used at the inlet of the 3D injector. The combustion chambers were initialized with the pressure, measured behind the reflected hammer shock before the introduction of the hot gas jet for ignition. The 2D C-D injector, designed in Chapter 10 is used to compare the 2D and 3D penetration predictions. The computational predictions of the flow field are analyzed to get a better idea of the jet penetration, cross-channel flow through the clearance gap and gas mixing. A good understanding of all these phenomena is very important for the successful design and operation of WRCVC.

It was shown before that in the initial testing of the WRCVC (Matsutomi et al., 2010 and Elharis, et al., 2010), certain combustible mixtures failed to ignite, which might be due to insufficient fuel concentration near the ignition source, which in turn depends on the level of mixing between hot gases injected and the cold combustible mixture. This was already analyzed in Chapter 9 in detail. The experimental tests also indicated that ignition in the combustion chambers were taking place prior to their arrival at the injection point which could be due to hot gas flowing through the clearance gap. The phenomena can thus be termed early ignition. This analysis will not include the effect of centrifugal forces or other effects of rotation, as the injector is assumed to traverse the chamber in a straight line, rather than rotate past it as in the actual WRCVC.

10.3 The Transient Confined 3D Gas Jet

The 3D transient confined gas jet, as it enters into the combustion chamber (during the partial opening period) is seen to spread more in the transverse r -direction than it spreads in the θ -direction (Injector moves in the θ -direction). This appears to be due to the fact that the jet is being blocked by the leading wall when it is being opened to the channel. The gas bounces off of the leading wall onto either side, in the r -direction. Vortex '1' in Figure 10.9 is blocked by the leading wall, when the injector is at position 'A' (Figure 10.9). The vortices drawn in Figure 10.9 are only in three orthogonal planes, but the jet spreads in all directions as shown in the 3D iso-surface illustration of the computed jet in Figure 10.10.

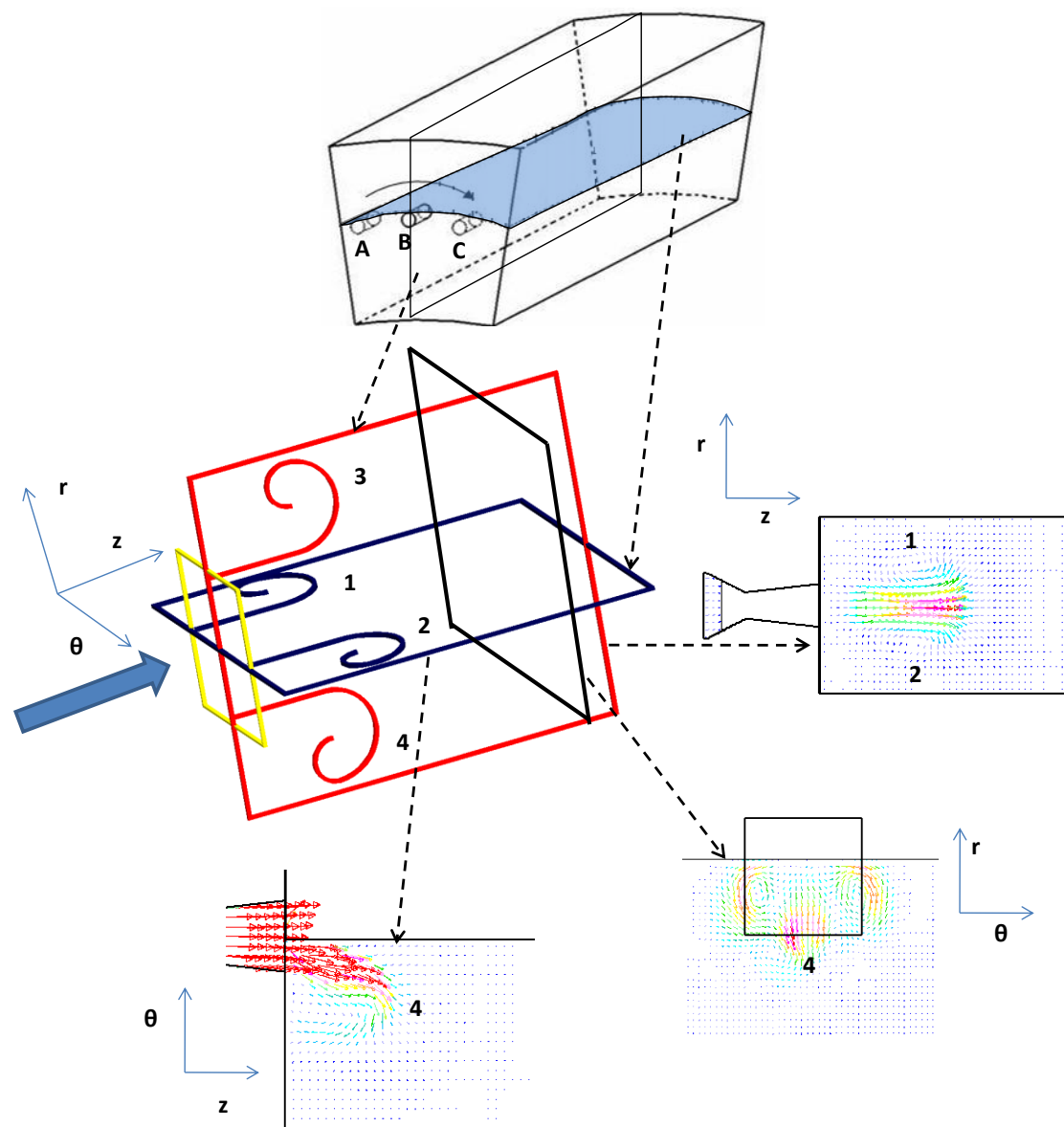


Figure 10.9. Vortex Structures when the Injector is partially opened to the Channel (Vortex '3' is suppressed by the leading wall).

The three-dimensional nature of the jet coming into the channel is shown in Figure 10.10 using the iso-surface of injected gas mass fraction equal to 0.01. The jet tends to develop along the leading wall of the channel like a “pointed mushroom,” and dips down towards the trailing wall, only when the injector has traversed half the channel width. The jet does not develop symmetrically, although large asymmetries are not seen.

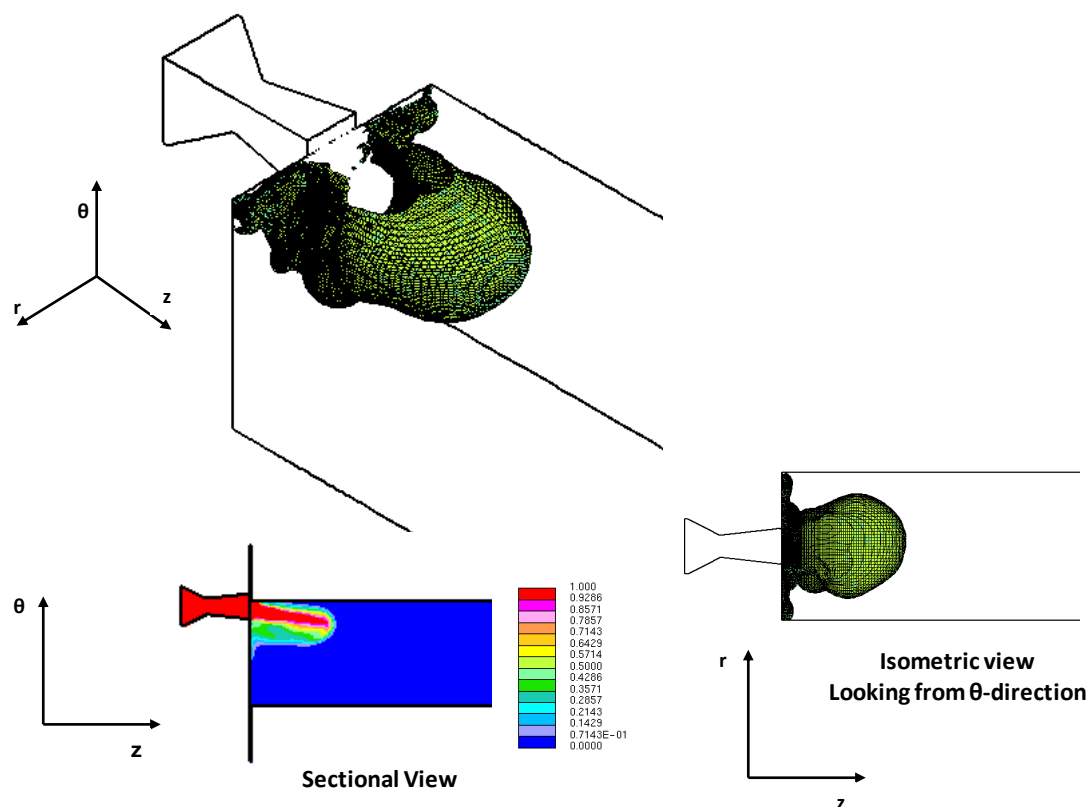


Figure 10.10. Three-dimensional view of the Jet entering the Channel. (Contours shown are the 0.01 Iso-surface of Injected Mass Fraction and Color Scale shows the Injected Mass Fraction).

In order to further understand the vortex structures which govern the mixing process, sectional views of the injected gas mass fraction in r-z plane is presented in Figure 10.11 for a single injector location. Two vortices in the r-direction and a single vortex in the θ -direction (the other one is suppressed by the leading wall) can be seen to dominate mixing of injected hot gas with the cold combustion channel gas. The time selected ($t=0.91$ ms) correspond to the earliest ignition time seen experimentally, for the test case analyzed here. Hence Figure 10.11 shows how the hot gaseous jet might have behaved just before the initiation of combustion in this selected cycle. Plots in r-z plane are plotted for different values of θ and hence only certain cross-sections capture the nozzle flow.

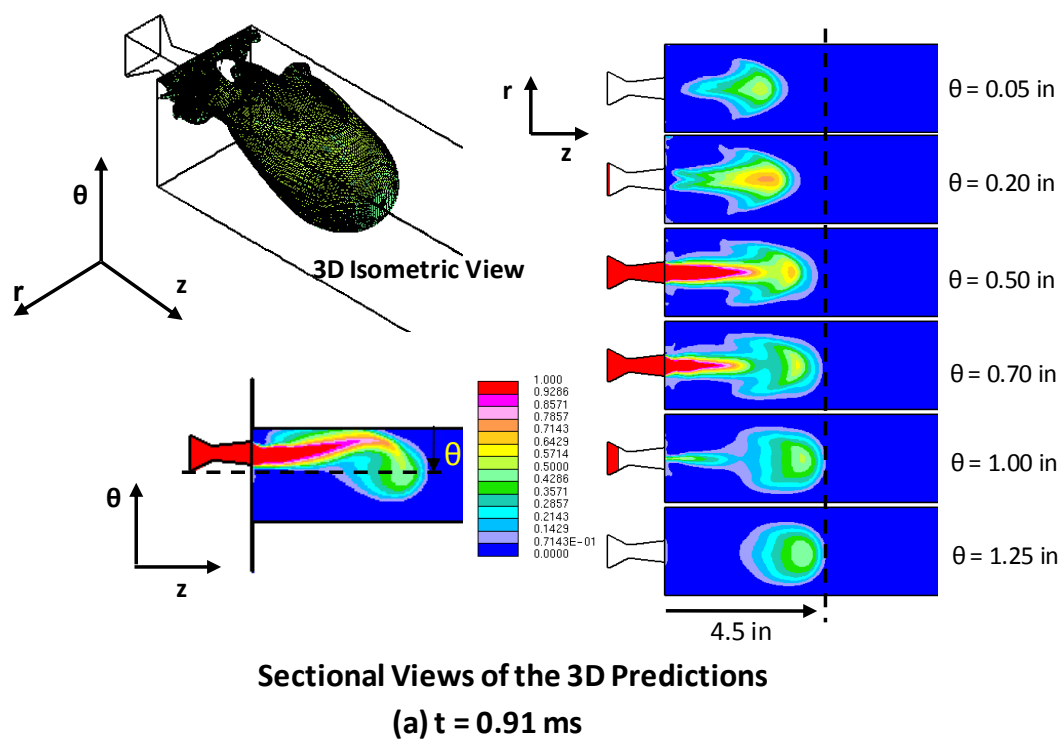


Figure 10.11. Fluid Mixing Assisted by 3D Vortices ($t=0.91$ ms). Injector start opening to Channel at $t=0.35$ ms. The θ Dimension within the Channel is parallel to the direction of Injector Motion.

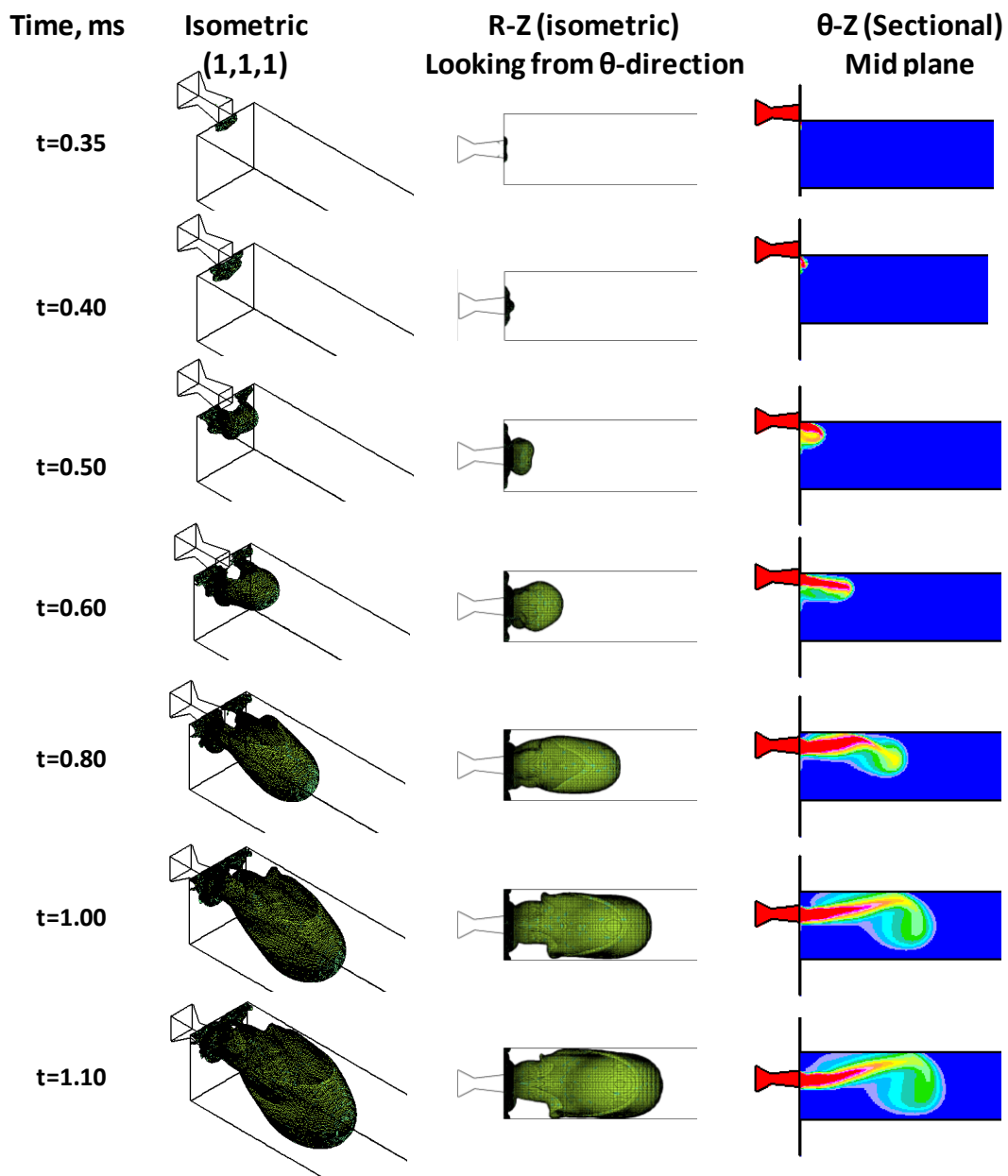


Figure 10.12. The Development of the 3D Jet Depicted by 0.01 Iso-surf of the Injected Gas Mass Fraction (Time is measured from the Start of the Injector Motion, from the Middle of Leading Partial Channel).

10.4 Jet Penetration

The simulations were initialized when the injector was at the middle of the leading partial channel which corresponded to $t = 0$ sec. The initialization and boundary conditions are summarized in Table 10.1. The specified velocity and density at the nozzle inlet were only used to calculate the mass flow rate, which was kept constant across the boundary, while the pressure, density and velocity were allowed to vary. The inlet velocities of the straight injector nozzles (Cases 3 and 4) were selected to be approximately equal to the outlet velocities from the C-D nozzles (Cases 1 and 2) at stationary conditions.

The flow progression in the main channel is now described using the straight injector (constant cross sectional area) simulation, cases 3 and 4 in Table 10.1. As the jet forms and penetrates, it is noted that the penetration of the 2D jet (case 4) is comparable to the 3D jet (case 3) in the initial part of jet injection process, (Figure 10.13) although the jet penetration prediction in case 4 becomes larger than that of case 3 in the latter part of injector travel (Figure 10.14).

It is noted that in Case 3, colder ambient gas ‘backfills’ the region already traversed by the jet (Figures 10.14 and 10.16), which is not seen in Case 4. This is expected, because the 3D injector in Case 3 does not completely fill the regions on either side in the r-direction, and this leaves cold gas that can migrate elsewhere. Identifying possible “cold” regions is important in studying the development, propagation, and subsequent completion of the combustion process inside the WRCVC.

Table 10.1. Initial and Boundary Conditions

Case	1 (3D, C-D nozzle)	2 (2D, C-D nozzle)	3 (3D, Straight nozzle)	4 (2D, Straight nozzle)
Initial Conditions in the main channel				
Pressure, kPa	172	172	100	100
Temperature, K	347	347	298	298
Velocity, m/s	0	0	0	0
Boundary Conditions (at nozzle inlet)				
Velocity, m/s	94.3	94.3	1222	1222
Density, kg/m ³	1.23	1.23	1.3	1.3
Temperature, K	2311	2311	2311	2311
Boundary Conditions (nozzle walls)				
Type	No-slip	No-slip	No-slip	No-slip
Velocity, m/s	43	43	43	43
Boundary Conditions (channel walls)				
Type	No-slip	No-slip	No-slip	No-slip
Velocity, m/s	0	0	0	0

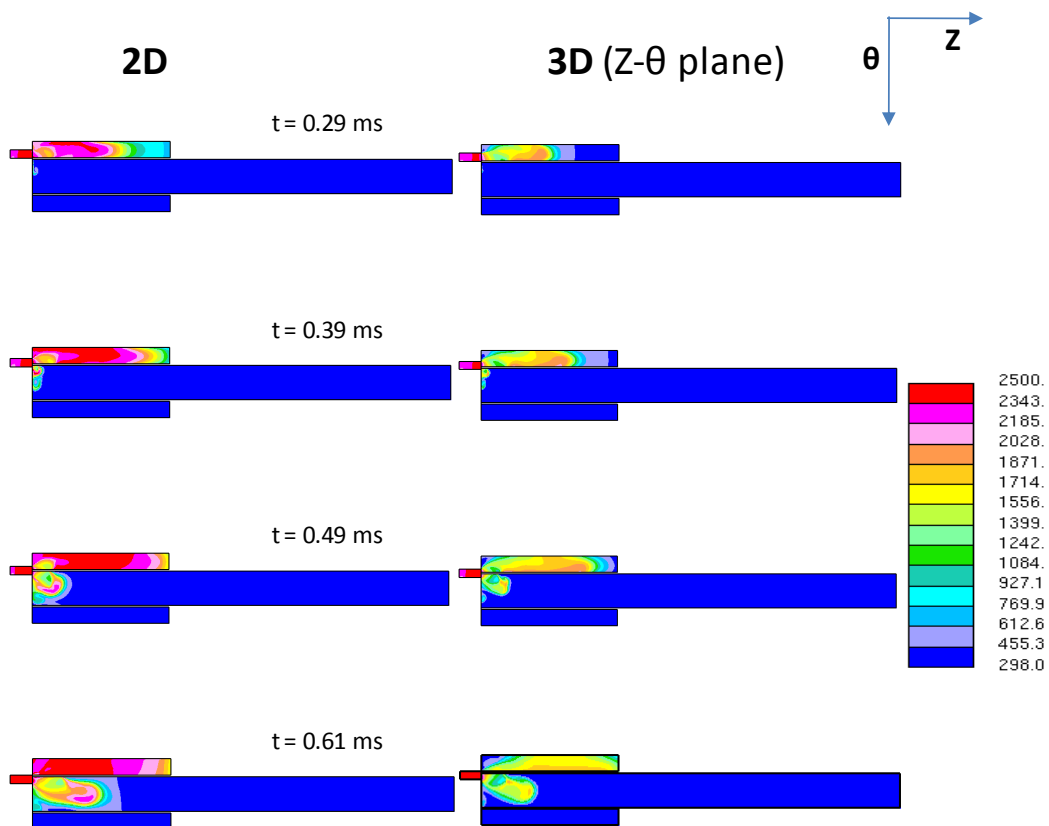


Figure 10.13. Comparison of 2D and 3D Cases in the Initial Phase of Injector Motion. Contours of Absolute Temperature (K) are shown.

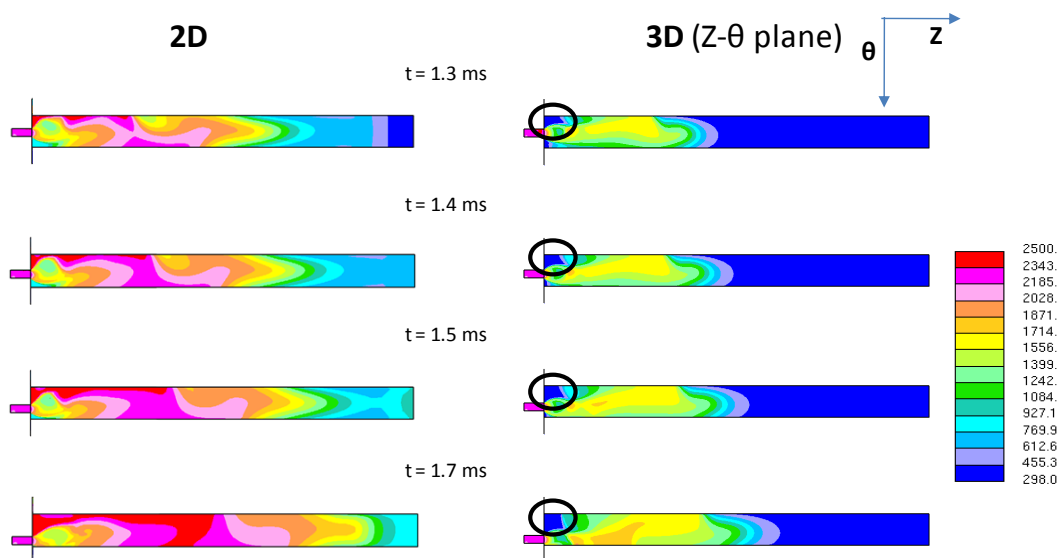


Figure 10.14. Comparison of 2D and 3D Cases in the latter part of Injector Motion (Partial Channels are not shown). Contours of Absolute Temperature (K) are shown (Black Circles show colder Ambient Gas returns to the path of the 3D predictions).

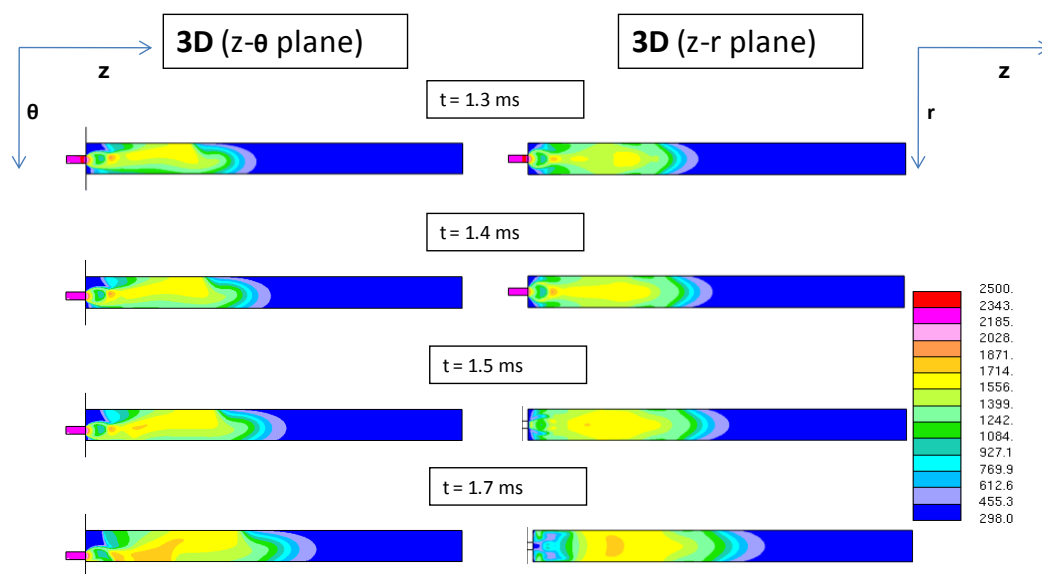


Figure 10.15. Comparison of Jet Penetration in Two Orthogonal Planes in the 3D Case. (Partial Channels are not shown). Contours of absolute temperature (K) are shown.

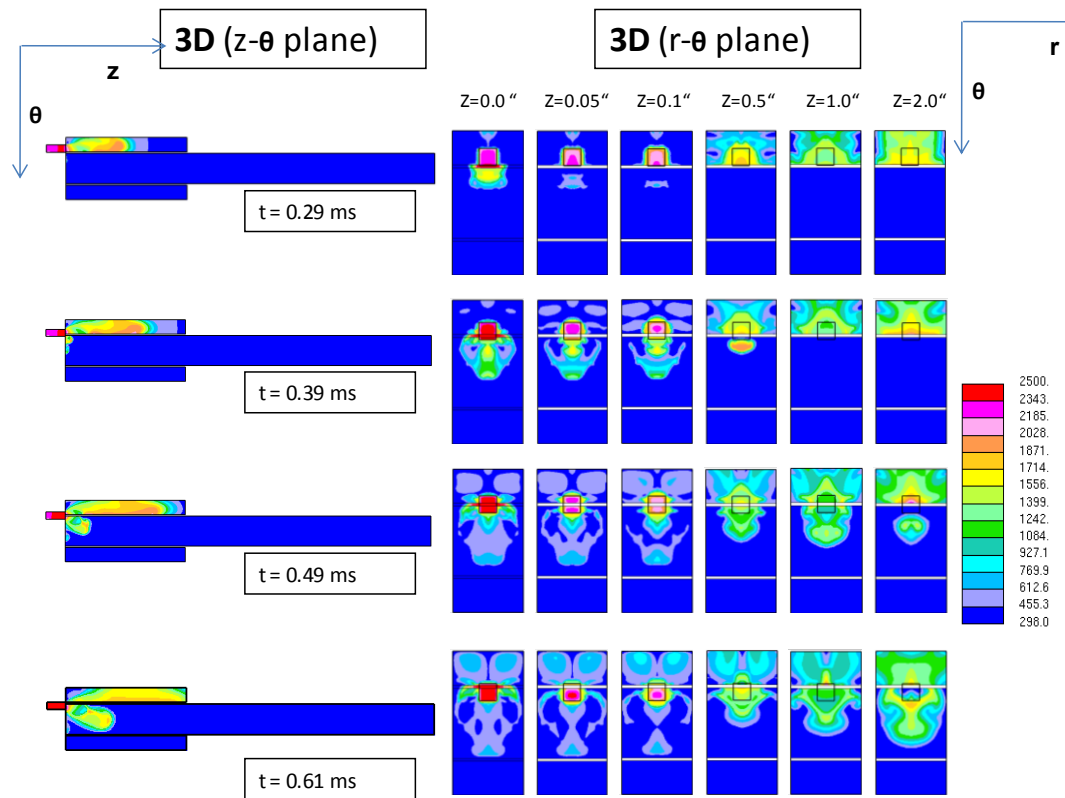


Figure 10.16. Cross-channel Clearance. Contours of Absolute Temperature (K) are shown. The Clearance Gap is 0.01" starting from $Z=0.0$ ".

The development of the 3D jet (Case 3) in r - θ plane is shown in Figure 10.16. One important thing seen here is the arrival of hot gasses into the main combustion channel through the cross channel gap before the injector starts injecting into the main channel. The leading and trailing half channels are shown in this figure as well. The jet develops symmetrically in the r - θ plane which was not seen in the jet in Case 1.

The hot gas jet is over-expanded in the jet in Case 1 and exits at an average Mach number of 1.5. The penetration of the jet into the channel is due to the momentum of the jet rather than the static pressure difference. The maximum predicted penetration of the jet is ~7 in. which is about 23% of the combustion channel length. In the context of a WRCVC ignited by a hot gaseous jet, low penetration might be favorable in that it results in low cold combustible mixture entrainment and hence retain high jet temperatures. This predicted jet penetration length can be verified using the in-rotor thermocouple data as shown in Figure 10.17. Thermocouple data for two test cases during the time when the torch igniter was turned on (before combustion) is presented in this figure. Thermocouples TC8 – TC10 which were within 7 inches from the exit side end wall can be seen to have recorded higher temperatures than the rest of the thermocouples (TC1-TC7). Due to the low frequency of the thermocouples used, the recorded temperatures are average values over multiple cycles.

It can be seen from Figure 10.18 that the axial penetration of the two jets of Cases 1 and 2 are comparable, although the 2D jet in Case 2 tends to spread faster in the circumferential direction (in the direction of injector travel). Cold regions near the leading end wall can be seen to develop in the Case 1 where the injected gas fail to migrate, similar to what's seen in Figures 10.14 and 10.16.

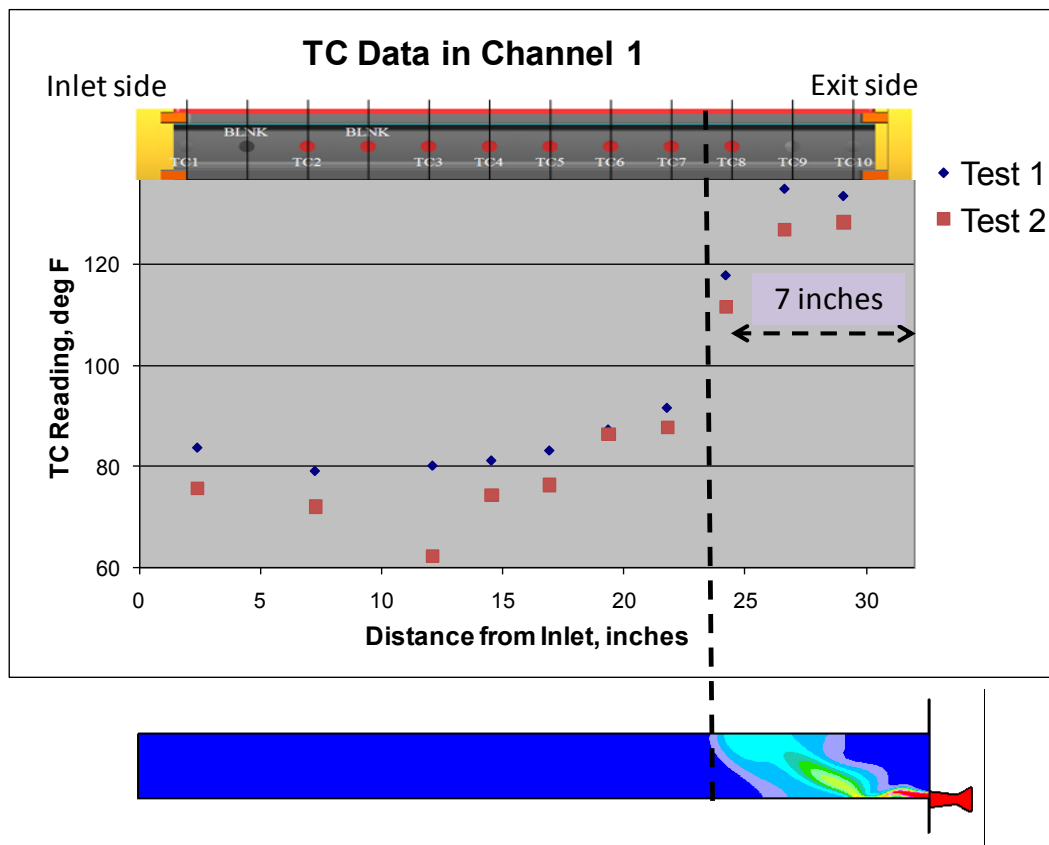


Figure 10.17. In-channel Thermocouple (TC) Data for Two Experimental Tests, during the Period when the Torch Igniter was turned on (prior to combustion) and the 3D Axial Jet Penetration Predictions from Case 1.

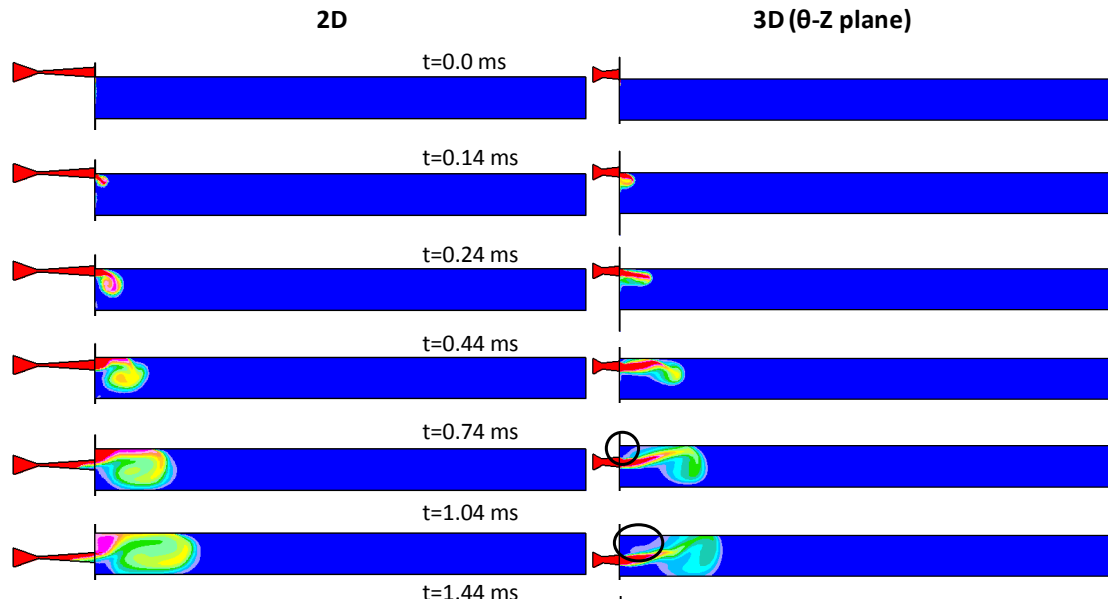


Figure 10.18. Comparison of 3D (Case 1) and 2D (Case 2) Jet Penetration from the C-D injector. Contours of injected gas mass fraction are shown.

10.5 Gas Mixing

Assessing the level of mixedness between the injected hot gas and the colder chamber gas is challenging due to the transient mass addition process as explained in Chapter 10. The injected gas mixes rapidly with the chamber gas upon injection and changes the injected gas mass fraction in space and time. Similar to the definition of HTM used in Chapter 10, it is attempted here to use the predicted injected gas mass fraction to understand the level of mixing inside the chamber, by comparing against the total mass of hot gas injected. However the temperature of the gas was not used as a selection criterion unlike in HTM. The ‘level of mixing’ or the ‘mixedness’ of injected hot gas with the chamber gas is defined to be the ratio of hot gas mass existing at mass fractions within a chosen range to the total mass of injected hot gas. The limits for this range of injected gas mass fraction

are selected based on the problem analyzed. The mixedness of the injected gas at different times, for different injected gas mass fraction limits are shown in Figure 10.19, and given in Equation 10.1:

$$\text{mixedness} = \frac{m_{LL \leq Y_{HG} \leq UL}}{m_{HG, Total}} \quad (10.1)$$

The distribution of injected gas mass fraction within the chamber is quantified in Figure 10.19 by plotting the predicted mixedness as a function of time as the injector moves across the channel. Hot gas began entering the channel at 0.29 ms before the injector aligns with the top edge of the chamber at 0.35 ms. This is due to the cross-channel flow through the clearance gap. When comparing the graphs for $0.1 < Y < 0.9$ and $0.3 < Y < 0.9$ (Figure 10.19 bottom figure), it is clear that majority of the injected mass has low mass fractions ($Y = 0.1 - 0.2$). By comparing curves for $0.1 < Y < 0.8$ and $0.2 < Y < 0.8$ (Figure 10.19, top figure), it can be further inferred that the mass with mass fractions in the vicinity 0.1 is greater than the mass with mass fractions in the vicinity 0.2. It is interesting to note how curves in Figure 10.19 (top figure) tend to converge after 1ms (injector is at the midpoint of chamber at 1.24ms) which indicates that these upper limits of the injected gas mass fraction does not affect the mixedness very much as long as the lower limit selected is the same. This in fact explains that the majority of mass in these mixtures were near the lower limits after 1ms. Overall, it can be concluded that majority of the injected mass has a lower mass fraction as time progresses which indicates rapid mixing between injected gas and chamber gas.

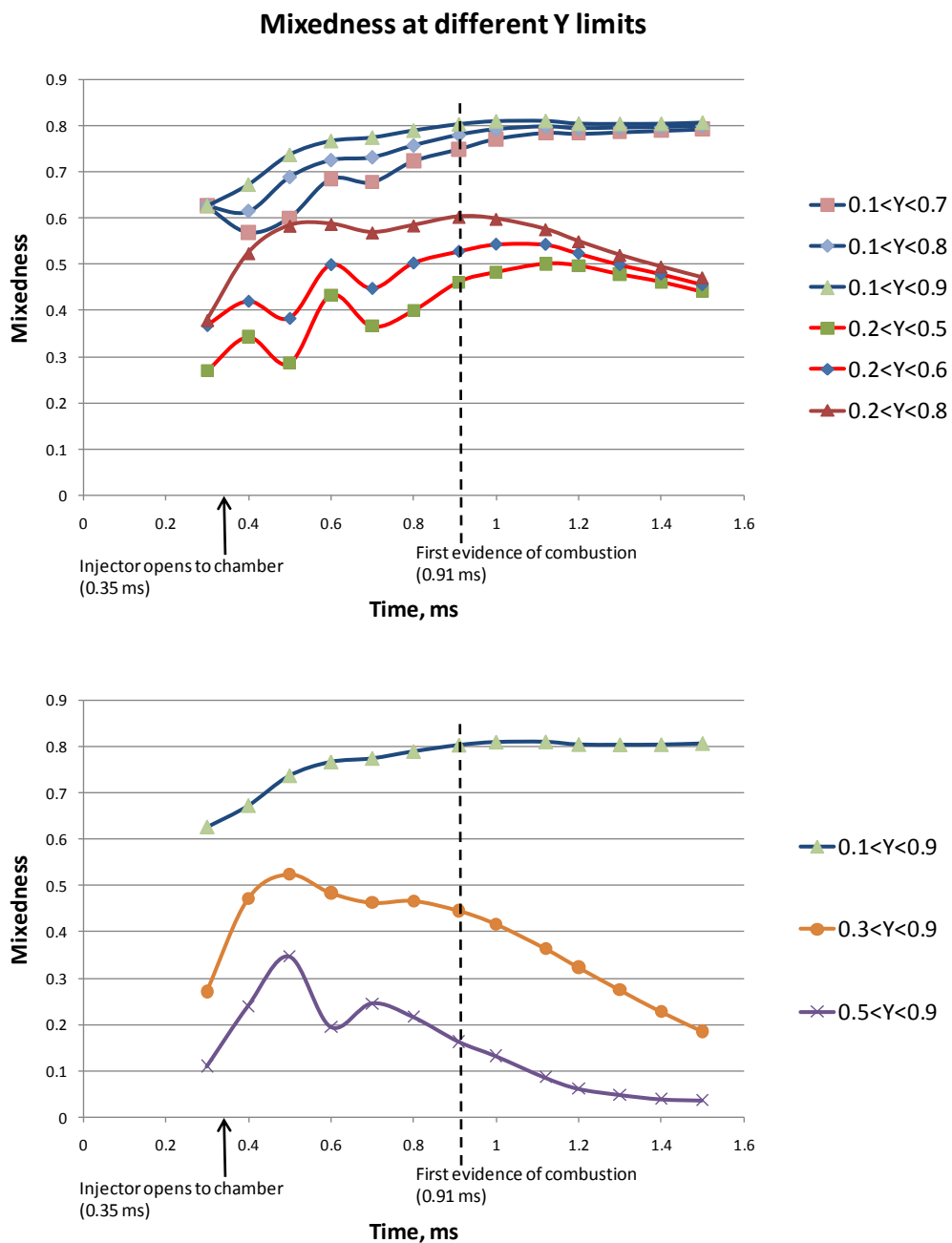


Figure 10.19. Level of Mixing of Injected Gas with Chamber Gas. Y is the Injected Gas Mass Fraction.

The variation of high temperature mixedness (HTM) over is shown in Figure 10.20. In Figure 10.20, the HTM between the limits $0.1 < Y < 0.9$, $0.1 < Y < 0.8$, and $0.1 < Y < 0.7$ is seen to converge as was seen in Figure 10.19. However the HTM was decreasing over time unlike an increase over time in mixedness as was seen in Figure 10.19. This means that majority of 'high temperature' mass, is still in the vicinity of $Y=0.1$ rather than at higher mass fractions, and the amount of 'high temperature mass' which is below $Y=0.1$ is increasing with time. If the 'high temperature mass' which is above the limit $Y=0.1$ was increasing in time, the HTM curves in Figure 10.20 (top figure) would have increased in HTM scale rather than decreasing. Although the bottom figure in Figure 10.19 indicates a vast difference in mixedness for curves $0.1 < Y < 0.9$ and $0.3 < Y < 0.9$, the difference in the HTM for the same limits do not show such a difference. This can be interpreted as follows: even though the majority of the mass was the vicinity of $Y=0.1$ not all that mass had a high enough temperature (780 K to 2500 K). In fact, the injected mass with sufficiently high temperature was in the vicinity of $Y=0.3$, although this mass was losing its temperature very quickly due to entrainment of colder chamber gas.

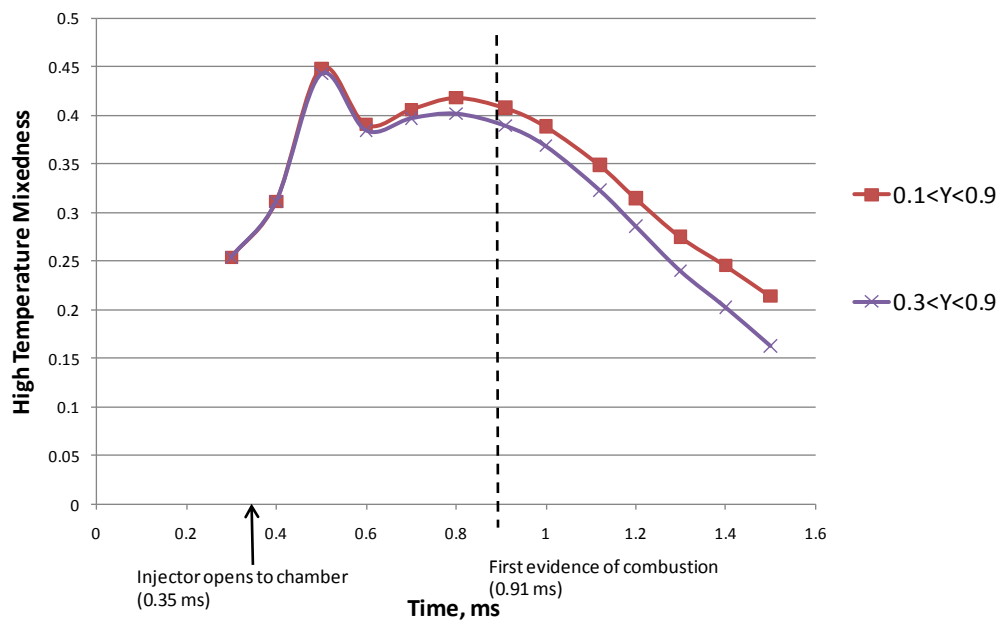
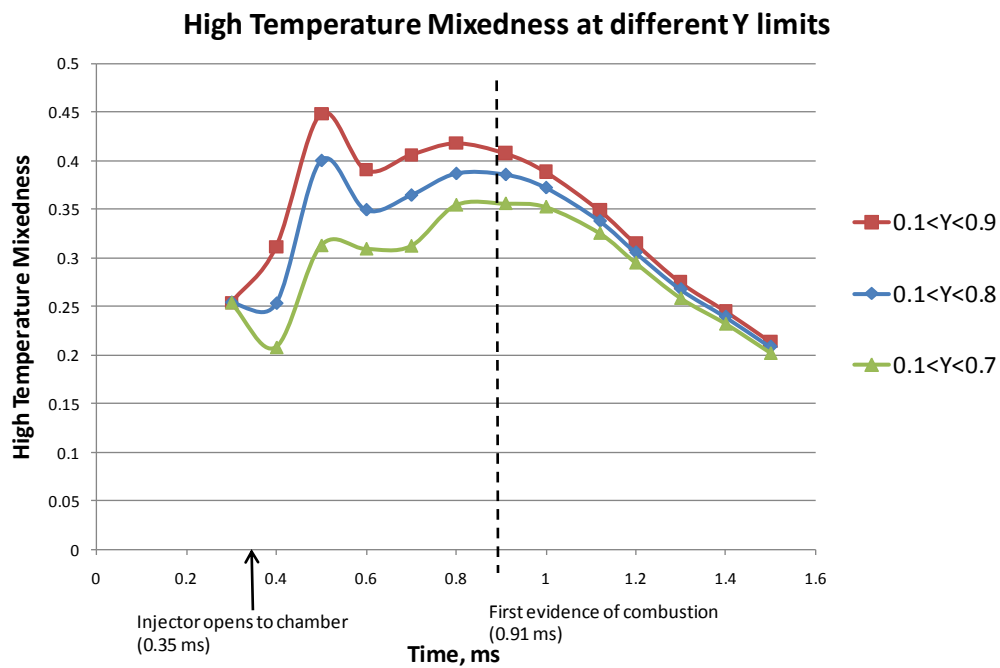


Figure 10.20. Level of Mixing of Injected Gas with Chamber Gas, that resulted in High Temperature Mixtures.

CHAPTER 11. CONCLUSIONS AND RECOMMENDATIONS

This thesis provides an analysis of the mixing behavior of a gas injected into a long channel, while the injector traverses across the channel. URANS simulations were used in 2D and 3D to analyze the salient flow structures which govern the mixing behavior. Experimental evidence on the behavior of the large scale structures of the mixing process qualitatively supports the predictions. Major conclusions are summarized under the four major topics analyzed in this thesis. Recommendations for the effective operation of the pilot gas injection and the hot gas injection processes, based on the findings of this thesis are presented at the end.

11.1 Conclusions

1. Conclusions related to the fluid dynamics of mixing in a confined traversing jet
 - Numerical modeling of the translating jet is important in understanding the flow physics governing the mixing process. The translating jet behavior cannot be approximated by a stationary jet.
 - The behavior of the large-scale flow structures governing the mixing process from a translating jet is quite different from that of a stationary jet. The motion of counter rotating vortices that make up these structures enhances mixing.

- The motion of the counter rotating vortices inside the confined channel and their interactions with the channel walls restricts the injected mass to be in the vicinity of the jet carrier wall.
- The jet momentum and the channel cross sectional area compared to the injector exit area are important parameters governing the vortex size and strength and hence mixing. Higher jet momentum increases the jet penetration while reducing channel width will reduce penetration.
- A counter-rotating vortex pair is formed upon the initial entry of the jet in to the channel. The vortex turning towards the leading side wall will be suppressed by the presence of the wall when the jet momentum is low. The development of this vortex is important to axial penetration of the jet away from the injector carrier wall. Suppressing this at lower jet momentums and narrower combustion channel width will reduce jet penetration. Enhancing this vortex at higher jet momentum and wider combustion channel widths will increase jet penetration.
- Limited jet penetration is advantageous in pilot fuel injection in a WRCVC which will result in a fuel-rich combustible mixture near the ignition source.
- Low jet momentum and penetration can be advantageous in the hot gas injection process as well, in that the cold ambient gas entrainment will be reduced. This will preserve hot jet temperatures which will aid ignition.
- The jet exit conditions are highly transient and vary considerably during the injector traverse. This makes it difficult to correlate the jet penetration behavior to the jet exit conditions.

- Axial and transverse jet penetration was found to increase with the increase of the ratio 'mass flow rate / molecular weight' of the injected gas.
- The mixing of fuel with the hot gas jet is decided also by the length of the unfueled buffer layer existing near the ignition source. The hot gas jet is expected to penetrate this layer and reach the combustible mixture to ignite it. However from the finding presented in this thesis, it is clear that the translating jet mixes rapidly with the surrounding gas compared to a stationary jet. Hence higher jet momentum, narrower jet exit areas compared to the width of the channel, and lower translating speeds are necessary if the translating jet is expected to penetrate further to ignite a combustible mixture.
- It is also shown that vorticity is deposited on walls when the combustion channel is gradually closing into the exit port. These vortices are seen to move along the walls of the combustion channel which affects subsequent gas injection.
- Insightful information was obtained from the 3D translating jet simulations which were different to the 2D predictions. The spread of the jet in the third dimension resulted in creating cold surrounding gas to be pushed closed to the injector carrier wall. This might affect adversely for ignition and/or combustion efficiency.
- The cross channel flow was also predicted by both 2D and 3D simulations which showed this gas comes in to the channel as a wall jet along the injector carrier wall and stays in the vicinity of it without much penetration. This fact was experimentally verified, in that 'early ignition' was detected in some combustion channels of the WRCVC prior to its alignment with the igniter. This was only possible if the high pressure, high temperature gasses from the previous

combusting channel came in to the current one. However this early combustion due to this cross channel flow was not observed to take place beyond one combustion channel. In other words back propagation of combustion was not seen. This was due to the unavailability of combustible mixture in the vicinity of the igniter side end wall. The gasses which came through the gap stayed in the vicinity of the wall and cooled rapidly as it mixed with unfueled, cold gasses.

2. Developed a methodology to support the 1D WRCVC code to better predict the ignition location and time
 - A methodology is proposed to better predict ignition locations inside the combustion channel. This was done by using the two dimensional gas mixing simulation data to predict the mixed state of the mixture and its temperature. This predicted equivalence ratio and the temperature of the gas in the vicinity of the injector after being mixed with the hot gas was used in a transient one dimensional code to model combustion and gas dynamics inside the WRCVC channel in a more economical manner. The resultant predictions of transient pressure inside the combustion channel were compared to the experimental data and were found to match very well.
 - This improved the capabilities of the 1D code by providing mixed state conditions prior to combustion.
 - The proposed methodology provides better estimates for ignition locations and times that can be used in the 1D code.

3. Presented a definition to quantify the mixing from a transient traversing confined jet which aids to determine its ignition potential
 - A new definition is proposed to quantify the degree of mixing of the injected gas with chamber gases. 'High Temperature Mixedness (HTM)' takes into account the transient mass fraction of the injected gas and its temperature to represent the state of mixing. The injected gas which has a higher temperature than a threshold temperature is selected first. This 'hot mass' is again screened according to its mass fraction. The fraction of this hot mass which has its mass fraction between two known limits is divided by the total hot gas mass injected to obtain HTM. This index identifies when and where in the combustion channel, ignitable gas is present. Carefully planned experimental data is necessary in identifying the threshold temperatures and injected gas mass fraction limits which results in ignition of different fuels. This is not done in this thesis and is proposed as a vital future research area.
 - Once an ignition criteria is known, HTM can be used to identify the fractions of hot mass within certain mass fractions of injected gas, and how they evolve in time.

4. Compared the 2D and 3D predictions of gas mixing from a confined traversing jet
 - The spread of the 3D jet in the third dimension resulted in creating cold surrounding gas to be pushed closed to the injector carrier wall. This was not predicted in the 2D computations

- The cross channel flow comes in to the channel as a wall jet along the injector carrier wall and stays in the vicinity of it without much axial penetration
- Early combustion was not observed to take place beyond one combustion channel in the experiments. This was due to the unavailability of combustible mixture in the vicinity of the igniter side end wall

11.2 Recommendations

Some recommendations are made for effective operations of the pilot fuel and torch igniter jets in the WRCVC test rig (Matsutomi et al., 2010).

A. Pilot Fuel Injector

Requirements:

1. Mix with the combustion channel gas in such a way as to create an ignitable mixture in the vicinity of the hot gas injector.
2. Not expected to penetrate much axially and get diluted by the un-fueled mixture.

Recommendations:

1. Since the pilot fuel is not expected to penetrate much axially, a low momentum jet is desired. A lower 'mass flow rate / molecular weight' of the injected gas ratio at the jet inlet will result in low axial jet penetration, as the vortex which turns towards the leading end wall would be weaker.
2. If a converging-diverging nozzle is being used as the injector, getting the flow to over expand in the nozzle will also aid in reducing axial penetration. This will

help vortex V1 (Figure 7.9) to retract towards the injector carrier wall which is responsible for reducing the axial penetration.

3. An increase in jet traversing speed will decrease axial penetration.

B. Hot Gas Injector / Torch Igniter

Requirements:

1. Mix with the combustion mixture in the channel in such a way as to create an ignitable mixture.
2. Depending on the fuel stratification technique used, it might be expected to penetrate further into the channel axially.

Recommendations:

1. If the hot gas is required to penetrate axially, a higher momentum jet is desired. A higher 'mass flow rate / molecular weight' of the injected gas ratio at the jet inlet will result in higher axial jet penetration, as the vortex V2 (Figure 7.9) would be stronger.
2. If a converging-diverging nozzle is being used as the injector, getting the flow to under expand in the nozzle will aid in increasing axial penetration. This will prevent vortex V1 (Figure 7.9) from suppressing the exit flow and reducing the effecting exit flow area.

3. For given jet conditions, a reduction in jet traversing speed will increase axial penetration. For example, if the WRCVC is operated at the design speed of 4200 rpm with the same torch igniter conditions, the axial penetration of the gas into the combustion channel is predicted to be lower than that obtained at 2100 rpm.

The traversing jet experiment available in CPRL, IUPUI can be used effectively to experimentally investigate the behavior of the traversing jet. High speed video imaging, schlieren imaging, and high frequency pressure data can be used to capture and identify the salient flow features which can verify the numerical predictions presented in this thesis. A systematic and detailed study, varying the injector flow conditions, injector geometric conditions, injector traversing speed, and confinement ratio is required to arrive at empirical correlations of jet penetration, jet tip velocity, and mass entrainment rate of a traversing, confined, turbulent jet.

LIST OF REFERENCES

LIST OF REFERENCES

- Abraham, J., "Entrainment Characteristics of Transient Gas Jets," *Numerical Heat Transfer, Part A*, Vol. 30, 1996, pp. 347–364.
- Abraham, J., Bracco, F. V., "Fuel-Air Mixing and Distribution in a Direct-Injection Stratified-Charge Rotary Engine," International Congress and Exposition, SAE 890329, Detroit, MI, Feb 27 – March 3, 1989.
- Nandha, K. P., Abraham, J., "Dependence of Fuel-Air Mixing Characteristics on Injection Timing in an Early-Injection Diesel Engine," SAE 2002 World Congress, SAE 2002-01-0944, Detroit, MI, March 4 – 7, 2002.
- Abrahamsson, H., Johansson, B. & L'ofdahl, L. "An Investigation of the Turbulence Field in the Fully Developed Three-dimensional Wall-Jet," Internal Rep 97/1, Chalmers University of Technology, Sweden, 1997.
- Aceves, S. M., Flowers, D. L., Martinez-Frias, J., Smith, J. R., Westbrook, C. K., Pitz, W. J., Dibble, R., Wright, J. F., Akinyemi, W. C., and Hessel, R. P., "A sequential fluid-mechanic chemical-kinetic model of propane HCCI combustion, SAE paper 2001-01-1027, 2001.
- Aceves, S. M., Flowers, D. L., Westbrook, C. K., Smith, J. R., Pitz, W., Dibble, R., Christensen, M., and Johansson, B., "A multi-zone model for prediction of HCCI combustion and emissions," SAE paper 2000-01-0327, 2000.
- Akbari, P., Nalim, M. R., and Mueller, N., "A Review of Wave Rotor Technology and its Applications," 2004 ASME International Mechanical Engineering Congress, IMECE2004-60082, Nov. 13-19, 2004, Anaheim, California, USA.
- Akbari, P., Nalim, M. R., and Snyder, P. H., "Numerical Simulation of Deflagrative and Detonative Combustion Wave Rotors," 42nd AIAA/ASME/SAE/ASEE Joint Propulsion Conference and Exhibit, AIAA 2006-5134, Sacramento, California, 9-12 July 2006.

Akbari, P., Nalim, M.R., Wijeyakulasuriya, S.D., and Muller, N., "Wave Disk Engine for Micro-Scale Power Generation," *44th AIAA/ASME/SAE/ASEE Joint Propulsion Conference & Exhibit*, AIAA 2008-4879, Hartford, CT, July 2008.

Arcoumanis, C., Cossali, E., and Whitelaw, J. H., "Measurement of tip penetration of confined high-density transient jets by laser beam deflection," *Experiments in Fluids*, Vol. 6, 1988, pp. 422-424.

Attard, W. P., Fraser, N., Parsons, P., and Toulson, E., "A Turbulent Jet Ignition Pre-Chamber Combustion System for Large Fuel Economy Improvements in a Modern Vehicle Powertrain," SAE Technical Paper 2010-01-1457, 2010.

Babajimopoulos, A., Assanis, D. N., Flowers, D. L., Aceves, S. M., and Hessel, R. P., "A fully coupled computational fluid dynamics and multi-zone model with detailed chemical kinetics for the simulation of premixed charge compression ignition engines," *International Journal of Engine Research*, Vol. 6, 2005, pp. 497-512.

Baker, J. A., and Skinner, G. B., "Shock-Tube Studies on the Ignition of Ethylene-Oxygen-Argon Mixtures," *Combustion and Flame*, Vol. 19, No. 3, December 1972, pp. 347-350.

Baldwin, B. S. and Lomax, H., "Thin Layer Approximation and Algebraic Model for Separated Turbulent Flows", AIAA Paper 78-257, 1978.

Baldwin, B.S. and Barth, T.J., "A One-Equation Turbulence Transport Model for High Reynolds Number Wall-Bounded Flows," NASA TM 102847, 1990.

Bogdanoff, D. W., "Compressibility Effects in Turbulent Shear Layers," *AIAA Journal*, Vol. 21, No. 6, 1983, pp. 926-927.

Bouzada, B. E., Wijeyakulasuriya, S. D., Nalim, M. R., "Improved compressible jet shear layer modeling using RANS models for confined and impinging jets," *40th Fluid Dynamics Conference and Exhibit*, Chicago, IL, June 2010.

Bradshaw, P., Ferriss, D. H., and Atwell, N. P., "Calculation of Boundary Layer Development Using the Turbulent Energy Equation," *Journal of Fluid Mechanics*, Vol. 28, Pt. 3, 1967, pp. 593-616.

Brown, C. J., and Thomas, G. O., "Experimental Studies of Shock-Induced Ignition and Transition to Detonation in Ethylene and Propane Mixtures," *Combustion and Flame*, Vol. 117, No. 4, June 1999, pp. 861-870.

Bruszkak, A. E., Burgess, D., and Wijnen, M. H., "Reaction Kinetics in Hot-gas Ignition of Ethane-Air," *Combustion and Flame*, Vol. 7, 1963, pp. 245-251.

- Burcat, A., Lifshitz, A., Scheller, K., and Skinner, G. B., "Shock-Tube Investigation of Ignition in Propane-Oxygen-Argon Mixtures," *13th Symposium (International) on Combustion*, Vol. 13, No. 1, 1971, pp. 745-755.
- Cato, R. J., and Kuchta, J. M., "Hot Gas Ignition Temperatures of Hydrocarbon Fuel Vapor-Air Mixtures," Bureau of Mines, AD0643518, 1966.
- Cheng, G. C., "The Effect of Streamline Curvature and Swirl on Turbulence Modeling in Curved Ducts," Ph.D. Dissertation, The University of Kansas, Lawrence, Kansas, 1990.
- Cheng, G. C., and Farokhi, S., "On Turbulent Flows Dominated by Curvature Effects," *ASME Journal of Fluids Engineering*, Vol. 114, March 1992, pp. 52-57.
- Corliss, J. M., Putnam, A. A., Murphy, M. J., and Locklin, D. W., "NO_x Emissions from Several Pulse Combustors," *105th ASME Winter Annual Meeting*, ASME Paper 84-JPGG-APC-2, New Orleans, 1984.
- Craft, T. J., and Launder, B. E., "On the Spreading Mechanism of the Three-Dimensional Turbulent Wall Jet," *Journal of Fluid Mechanics*, Vol. 435, pp. 305-326, 2001.
- Crow, S., and Champagne, F., "Orderly Structure in Jet Turbulence," *Journal of Fluid Mechanics*, Vol. 48, 1971, pp. 547-591.
- Davidenko D. M., "Numerical Modeling of Inert and Reacting Compressible Turbulent Jets," *13th AIAA/CIRA International Space Planes and Hypersonic Systems and Technologies Conference*, AIAA-2005-3237, May 2005, pp. 16-20.
- Davis, M. R., and Winarto, H., "Jet Diffusion from a Circular Nozzle above a Solid Plane," *Journal of Fluid Mechanics*, Vol. 101, No. 1, 1980, pp. 201-221.
- De Zilwa, S. R. N., Khezzar, L., Whitelaw, J. H., "Flows through plane sudden-expansions," *International Journal for Numerical Methods in Fluids*, Vol. 32, 2000, pp. 313-329.
- Drikakis, D., "Study of Compressible Flow Bifurcation Phenomena in Sudden Expansion," *Proceedings of the Third ECCOMAS, Computational Fluid Dynamics Conference*, 9-13 September 1996, Paris, France.
- Dritschel, D. G., "A General Theory of Two-Dimensional Vortex Interactions," *Journal of Fluid Mechanics*, Vol. 293, 1995, pp. 269-303.
- Eidelman, S., "The Problem of Gradual Opening in Wave Rotor Passages," *Journal of Propulsion and Power*, Jan.-Feb. 1985, Vol. 1, No. 1, pp. 23-28.
- El Tahry, S.H., "k-ε Equation for Compressible Reciprocating Engine Flows," *Journal of Energy*, Vol. 7, No. 4, pp. 345-353, 1983.

Elharis, T. M., Wijeyakulasuriya, S. D., and Nalim, M. R., “Two-Step Modeling of Stratified Charge Combustion in a Wave Rotor Combustor,” *47th AIAA/ASME/SAE/ASEE Joint Propulsion Conference & Exhibit*, San Diego, CA, Jul 2011.

Elharis, T. M., Wijeyakulasuriya, S. D., Nalim, M. R., “Analysis of Combustion and Energy Transfers in a Wave Rotor,” *49th AIAA Aerospace Sciences Meeting*, Orlando, FL, 4-7 January 2011.

Elharis, T. M., Wijeyakulasuriya, S. D., Nalim, M. R., Izzy, Z., “Wave Rotor Combustor Aero-thermodynamic Design and Model Validation based on Initial Testing,” *46th AIAA/ASME/SAE/ASEE Joint Propulsion Conference & Exhibit*, Nashville, TN, 25-28 July 2010.

Elharis, T.M., “A Multi-step Reaction Model for Stratified-Charge Combustion in Wave Rotors,” M.S.M.E. Thesis, Department of Mechanical Engineering, Indiana University-Purdue University, Indianapolis, 2010.

Fanil, B., and Dash, R., “Three-Dimensional single and multiple jets,” *Journal of Hydraulic Engineering*, Vol. 109, No. 2, February 1983, pp. 254-269.

Fearni, R. M., Mullin, T., and Cliffe, K. A., “Nonlinear flow Phenomena in a Symmetric Sudden Expansion,” *Journal of fluid Mechanics*, Vol. 211, 1990, pp. 595 – 608.

Fink, Z. J., and Vanpée, M., “Overall Kinetics of Hot Gas Ignition,” *Combustion Science and Technology*, Vol. 11, No. 5-6, 1975, pp. 229-238.

Fujisawa, N., and Shirai, H., “Mean Flow and Turbulence characteristics of Three-Dimensional Wall Jet along Plane Surface,” *Transactions of Japan Society for Aeronautical and Space Sciences*, Vol. 32, 1989, pp. 35-46.

Gemmen, R. S., Richards, G. A., Janus, M. C., “Pressure-Gain Combustion for Gas Turbines,” *Advanced Coal-Fired Power Systems '95 Review Meeting*, Morgantown, West Virginia, June 27-29, 1995.

Gussak, L. A., “High Chemical Activity of Incomplete Combustion Products and a Method of Prechamber Torch Ignition for Avalanche Activation of Combustion in Internal Combustion Engines,” SAE Technical Paper 750890, 1975.

Hidaka, Y., Kataoka, T., and Suga, M., “A Shock-Tube Investigation of Ignition in Ethylen-Oxygen-Argon Mixtures,” *Bulletin of the Chemical Society of Japan*, Vol. 47, No. 9, 1974, pp. 2166-2170.

Hill, B., “Measurement of Local Entrainment Rate in the Initial Region of Axisymmetric Turbulent Air Jets,” *Journal of Fluid Mechanics*, Vol. 51, 1972, pp. 773–779.

- Hutchins, T. E., and Metghalchi, M., "Energy and Exergy Analyses of the Pulse Detonation Engine," *Journal of Engineering for Gas Turbines and Power*, Vol. 125, October 2003, pp. 1075-1080.
- Jones, W. P., and Launder, B. E. "The Prediction of Laminarization with a Two-Equation Model of Turbulence", *International Journal of Heat and Mass Transfer*, Vol. 15, 1972, pp. 301-314.
- Kawanabe, H., Naito, Y., Kosaka, H., and Shioji, M., "CFD Analysis of a High-speed Unsteady Jet," *Heat Transfer-Asian Research*, Vol. 36, No.1, 2007.
- Kentfield, J. A. C., "Performance Implications of Gas-Turbine Pressure-Gain Combustors," *27th AIAA/ASME/SAE/ASEE Joint Propulsion Conference & Exhibit*, AIAA-91-1879, Sacramento, California, 24-26 June, 1991.
- Kentfield, J. A. C., "Thermodynamics of Airbreathing Pulse-Detonation Engines," *Journal of Propulsion and Power*, Vol. 18, No. 6, November–December 2002.
- Kentfield, J. A. C., and Fernandes. I. C. V., "Further Development of an Improved Pulse Pressure Gain, Gas-Turbine Combustor," ASME Paper No. 90-GT-84, 1984.
- Kentfield, J. A. C., and Speirs, B. C., 1991, "A Multi-Inlet Core for Gas Turbine, Pulse, Pressure-Gain Combustors," ASME Paper No. 91-GT-304.
- Kentfield, J. A. C., and Yerneni, P., 1985, "Pulsating Combustion Applied to a Small Gas Turbine," ASME Paper No. 85-GT-52.
- Kentfield, J. A. C., and O'Blenes, M., "Methods for Achieving a Combustion-Driven Pressure-Gain in Gas Turbines," *Journal of Engineering for Gas Turbines and Power*, Vol. 110, No. 4, October 1998. (also ASME Paper No. 87-GT-126)
- Kentfield, J.A.C. and Fernandes. L.C.V., "Improvements to the Performance of a Prototype Pulse, Pressure-Gain, Gas Turbine Combustor," *Journal of Engineering for Gas Turbines and Power*, Vol. 112, 1990, pp. 67-72.
- Khalil, E.E., Spalding, D.B., and Whitelaw, J.H., "The Calculation of Local Flow Properties in Two-Dimensional Furnaces," *International Journal of Heat and Mass Transfer*, Vol. 18, 1975, p.775.
- Lamoureux, N., Paillard, C. E., and Vaslier, V., "Low Hydrocarbon Mixtures Ignition Delay Times Investigation Behind Reflected Shock Waves," *Shock Waves*, Vol. 11, No. 4, January 2002, pp. 309-322.

Lampinen, M. J., Turunen, R., and Koykka, M., "Thermodynamic Analysis of a Pulse Combustion System and Its Application to Gas Turbines," *International Journal of Energy Research*, Vol. 16, 1992, pp. 259-276.

Larosiliere, L.M., "Three-Dimensional Numerical Simulation of Gradual Opening in a Wave Rotor Passage," 29th Joint Propulsion Conference and Exhibit, AIAA-93-2526, Monterey, California, 28-30 June, 1993.

Larosiliere, L.M., and Mawid, M., "Analysis of Unsteady Wave Processors in a Rotating Channel," 29th Joint Propulsion Conference and Exhibit, AIAA-93-2527, Monterey, California, 28-30 June, 1993.

Launder, B. E., and Rodi, W., "The Turbulent Wall Jet Measurements and Modeling," *Annual Review of Fluid Mechanics*, Vol. 15, 1983, pp. 429-459.

Launder, B. E., and Sharma, B. I. "Application of the Energy Dissipation Model of Turbulence to the Calculation of Flow Near a Spinning Disc", *Letters in Heat and Mass Transfer*, Vol. 1, No. 2, 1974, pp. 131-138.

Launder, B.E. and Spalding, D.B., *Mathematical Models of Turbulence*, Academic Press, London and New York, 1972.

Launder, B.E., Morse, A., Rodi, W., and Spalding, D.B., "Prediction of Free Shear Flows-A Comparison of the Performance of Six Turbulence Models," NASA SP 321, Vol. 1, 1973.

Lifshitz, A., "Chemical Reactions in Shock Waves and Detonations," *Handbook of Shock Waves*, Academic Press, New York, 2001, Chap. 16.5.

Lim, W. H. E., "Gasdynamic Inlet Isolation in a Rotating Detonantion Engine," MSc Dissertation, Naval Postgraduate School, December 2010.

Lumley, J.L., "Rational Approach to Relations between Motions of Differing Scales in Turbulent Flows," *The Physics of Fluids*, Vol.10, No. 7, 1967, p. 1405.

Matsutomi, Y., Meyer S. E., Wijeyakulasuriya, S. D., Izzy, Z., Nalim, M. R., Shimo, M., Kowalkowski, M., Snyder, P. H., "Experimental Investigation on the Wave Rotor Combustor," *46th AIAA/ASME/SAE/ASEE Joint Propulsion Conference & Exhibit*, Nashville, TN, 25-28 July 2010.

Mayinger, F., Jordan, M., Eder, A., Zaslanko, I.S., karpov, V. P., and Frolov, S. M., "Flame-Jet Ignition of fuel-Air Mixtures. Experimental Findings and Modeling," *17th International Colloquium on the Dynamics of Explosions and Reactive Systems* (ICDERS), Heidelberg, Germany, July 25-30, 1999.

- Menter, F. R., "Two-Equation Eddy-Viscosity Turbulence Models for Engineering Applications," *AIAA Journal*, Vol. 32, No. 8, August 1994, pp. 1598-1605.
- Morel, T. and Mansour, N., "Modeling of Turbulence in Rapidly Compressed Flows," SAE Paper 820040, 1982.
- Morse, A.P., Whitelaw, J.H., and Yianneskis, M., "The Influence of Swirl on the Flow Characteristics of a Reciprocating Piston-Cylinder Assembly," Imperial College Mechanical Engineering Dept. Rept. FS/78/24, 1978.
- Muller, J. L., "Theoretical and Practical Aspects of Resonant Combustion Chambers in Gas Turbines," *Journal of Mechanical Engineering Science*, Vol. 13, No. 3, 1971, pp. 137-150.
- Murase, E., Hanada, K., Yun, J. H., and Oppenheim, A. K., "Radical Emission and Fluorescence Measurements in Pulsed Flame Jet," *4th international Symposium on Diagnostics and Modeling of Combustion in Internal Combustion Engines (COMODIA)*, Kyoto, Japan, July 20-23, 1998, pp. 399-404.
- Murase, E., Ono, S., Hanada, K., and Oppenheim, A. K., "Pulsed Combustion Jet Ignition in Lean Mixtures," SAE Technical Paper 942048, 1994.
- Murphy, K., M.S.M.E. Thesis, Department of Mechanical Engineering, Indiana University-Purdue University, Indianapolis, unpublished.
- Naguib, A. M., and Koochesfahani, M. M., "On wall-pressure sources associated with the unsteady separation in a vortex-ring/wall interaction," *Physics of Fluids*, Vol. 16, No. 7, July 2004, pp. 2613-2622.
- Nalim, M. R., "Thermodynamic Limits of Pressure Gain and Work Production in Combustion and Evaporation Processes," *Journal of Propulsion and Power*, Vol. 18, No. 6, 2002, pp. 1176-1182.
- Nalim, M.R., "Assessment of Combustion Modes for Internal Combustion Wave Rotors," *Journal of Engineering for Gas Turbines and Power*, Vol 121, No. 2, 1999, pp. 265-271.
- Nalim, M.R., "Longitudinally Stratified Combustion in Wave Rotors," *Journal of Propulsion and Power*, Vol 16, No. 6, 2000, pp. 1060-1068.
- Nalim, M.R., and Paxson, D.E., "A Numerical Investigation of Premixed Combustion in Wave Rotors," *Journal of Engineering for Gas Turbines and Power*, Vol 119, No. 3, 1997, pp. 668-675.

- Nalim, M.R., and Pekkan, K., "Internal Combustion Wave Rotors for Gas Turbine Engine Enhancement," *Proceedings of the International Gas Turbine Congress*, Tokyo, Japan, 2003.
- Newman, B. G., Patel, R. P., Savage, S. B., and Tjio, H. K., "Three-Dimensional Wall Jet Originating from a Circular Orifice," *Aeronautical Quarterly*, Vol. 23, 1972, pp. 188-200.
- Oppenheim, A. K., Teichman, K., Hom, K., and Stewart, H. E., "Jet Ignition of an Ultra-Lean Mixture," SAE Technical Paper 780637, 1978.
- Pagé J., "Contribution à l'Etude des Jets Turbulents Axisymétriques à Masse Volumique Variable," Thèse de Doctorat, Université d'Orléans, France, 1998.
- Papamoschou, D., and Roshko, A., "The Compressible Turbulent Shear Layer: An Experimental Study," *Journal of Fluid Mechanics*, Vol. 197, 1988, pp. 453-477.
- Patel, S., and Drikakis, D., "Numerical Effects on the Predictions of Flow Instabilities in Channels with Sudden-Expansion," *Proceedings of IMECE 2003, ASME International Mechanical Engineering Congress*, Washington, D. C., November 15-21, 2003.
- Paxson, D.E., "A General Numerical Model for Wave Rotor Analysis," NASA TM-105740, 1992.
- Perera, U. I., Wijeyakulasuriya, S. D., Nalim, M. R., "Hot Jet Ignition Delay Time and Localization Analysis for Ethylene-Air," *49th AIAA Aerospace Sciences Meeting*, Orlando, FL, 4-7 January 2011.
- Perera, U. L. I. U., "Experimental Investigation into Combustion Torch Jet Ignition of Methane-Air, Ethylene-Air, and Propane-Air Mixtures," M.S.M.E. Thesis, Department of Mechanical Engineering, Indiana University-Purdue University, Indianapolis, 2010.
- Piechna J., Akbari P., Iancu F., and Muller N., "Radial-flow wave rotor concepts, unconventional designs and applications" *Proceedings of IMECE04, 2004 ASME International Mechanical Engineering Congress*, IMECE2004-59022, Anaheim, CA, 13-19 November, 2004.
- Pope, S. B., "An Explanation of the Turbulent Round-Jet/Plane-Jet Anomaly," *AIAA Journal*. Vol. 16, No. 3, 1978, pp. 279-281.
- Poroseva, S. V., and Bezar, H., "On the Ability of Standard k- ϵ Model To Simulate Aerodynamic Turbulent Flows," *Computational Fluid Dynamics Journal*, Vol. 9, 2001, pp. 464-470.
- Porter, C. D., "Valveless-Gas-Turbine Combustor with Pressure-Gain," ASME paper number 58-GTP-11, 1958.

Ramos, J.I. and Sirignano, W.A., "Axisymmetric Flow Model with and without Swirl in a Piston Cylinder Arrangement with Idealized Valve Operation," SAE Paper 800284, 1980.

Reynolds, W.C., "Modeling of Fluid Motions in Engines—An Introductory Overview," *Combustion Modeling in Reciprocating Engines*, edited by J.N. Mattavi and C.A. Amann, Plenum Press New York, 1980, pp. 41-68.

Ricou, F., and Spalding, D., 1961, "Measurements of Entrainment by Axisymmetrical Turbulent Jets," *Journal of Fluid Mechanics*, Vol. 11, pp. 21–32.

Rodi, W., "The Prediction of Free Turbulent Boundary Layers by Use of a Two-Equation Model of Turbulence," Ph.D. Dissertation, University of London, England, 1972.

Rodi, W., "The prediction of free turbulent boundary layers by use of a 2-equation model of turbulence," Ph.D. Thesis, Imperial College, University of London, 1972.

Rose, P. H., "Potential Applications of Wave Machinery to Energy and Chemical Processes," *Proceedings of the 12th International Symposium on Shock Tubes and Waves*, Jerusalem, July 16–19, 1979, pp. 3-30.

Rossi, L. F., "Vortex Computations of Wall Jet Flows," Proc. 1st Annual Forum on Vortex Methods for Engineering Applications. Feb. 1995.

Rubel, A., "On the Vortex Stretching Modification of the $k-\epsilon$ Turbulence Model: Radial Jets," *AIAA Journal*, Vol. 23, No. 7, July 1985, pp. 1129-1130.

Russo, R. M., "Operational Characteristics of a Rotating Detonation Engine using Hydrogen and Air," MSc Dissertation, Air Force Institute of Technology, June 2011.

Saffman, P. G., *Vortex Dynamics*, 1st ed., Cambridge University Press, New York, 1992.

Sarkar, S., "The Stabilizing Effect of Compressibility in Turbulent Shear Flows," *Journal of Fluid Mechanics*, 1995, Vol. 282, pp. 163-186.

Sheen, H. J., Chen, W. J., and Wu, J. S., "Flow patterns for an annular flow over an axisymmetric sudden expansion," *Journal of Fluid Mechanics*, Vol. 350, 1997, pp. 177-188.

Sheen, H. J., Chen, W. J., and Wu, J. S., "Flow Patterns for an Annular Flow over an Axisymmetric Sudden Expansion," *Journal of Fluid Mechanics*, Vol. 350, 1997, pp. 177 – 188.

Shreeve, R.P. and Mathur, A., eds., "Proceedings of the 1985 ONR/NAVAIR Wave Rotor Research and Technology Workshop," NPS-67-85-008, Naval Postgraduate School, Monterey, California, 1985.

Simmons, R. F., and Wolfhard, H. G., "Some Limiting Oxygen Concentrations for Diffusion Flame in Air Diluted with Nitrogen," *Combustion and Flame*, Vol. 1, No. 2, 1957, pp. 155-161.

Smith, A.M.O. and Cebeci, T., "Numerical solution of the turbulent boundary layer equations", Douglas aircraft division report DAC 33735, 1967.

Snyder, P. H., "Wave Rotor Demonstrator Engine Assessment," NASA-CR-198496, 1996.

Snyder, P. H., Elharis, T. M., Wijeyakulasuriya, S. D., Nalim, M. R., Matsutomi, Y., and Meyer, S. E., "Pressure Gain Combustor Component Viability Assessment Based on Initial Testing ," *47th AIAA/ASME/SAE/ASEE Joint Propulsion Conference & Exhibit*, San Diego, CA, Jul 2011.

Song, L., Abraham, J., "Entrainment Characteristics of Transient Turbulent Round, Radial and Wall-Impinging Jets: Theoretical Deductions," *Journal of Fluid Engineering*, Vol. 125, July 2003, pp. 605-612.

Spalart, P. R. and Allmaras, S. R., "A One-Equation Turbulence Model for Aerodynamic Flows", AIAA Paper 92-0439, 1992.

Tanaka, T., and Tanaka, E., "Experimental Study of a Radial Turbulent Jet: 1st Report, Effect of Nozzle Shape on a Free Jet," *Bulletin of the Japan Society of Mechanical Engineers*, Vol. 19, No. 133, 1976, pp. 792-799.

Tarzhanov, V. I., Telichko, I. V., Vil'danov, V. G., Sdobnov, V. I., Makarov, A. E., Mukhin, S. L., Koretskii, I. G., Ogarkov, V. A., Vlasov, V. V., Zinchenko, A. D., Vorob'ev, A. V., Grachev, A. N., Matkin, V. A., and Potashnikov, V. A., "Detonation of Propane-Air Mixtures under Injection of Hot Detonation Products," *Combustion, Explosion and Shock Waves*, Vol. 42, No. 3, 2006, pp. 336-345.

Tennekes, H. and Lumley, J.L., *A First Course in Turbulence*, MIT Press, 1974.

Thring, M. W., editor, *Pulsating Combustion – The Collected Works of F. H. Reynst*, Pergamon Press, Oxford, United Kingdom, 1961.

Toulson, E., Watson, H. C., and Attard, W. P., "Gas Assisted Jet Ignition of Ultra-Lean LPG in a Spark Ignition Engine," SAE Technical Paper 2009-01-0506, 2009.

Toulson, E., Watson, H. C., and Attard, W. P., "Modeling Alternative Prechamber Fuels in Jet Assisted Ignition of Gasoline and LPG," SAE Technical Paper 2009-01-0721, 2009.

Valentino, M., Jiang, X., Zhao, H., “A Comparative RANS/LES Study of Transient Gas Jets and Sprays under Diesel Conditions,” *Atomization and Sprays*, Vol 17, No. 5, 2007, pp. 451-472.

Valle, R. M., Cândido de Sá, D. C., and RamalhoFilho, F. A., “Constructive Parameters Analysis of combustion Pre-Chamber Adapted in Torch-Ignition System of Otto Cycle Engine,” SAE Technical Paper 2003-01-3713, 2003.

Van Dolah, R. W., Zabetakis, M. G., Burgess, D. S., and Scott, G. S., “Ignition or the Flame-Initiation Process,” *Fire Technology*, Vol. 1, No. 1, 1965, pp. 32-42.

Vanpée, M., and Wolfhard, H. G., “Comparison between Hot Gas Ignition and Limit Flame Temperatures,” *ARS Journal*, Vol. 29, No. 7, 1959, pp. 517-519.

Vutthivithayarak, R., Braun, E. M., Lu, F. K., “Examination of the Various Cycles for Pulse Detonation Engines,” *47th AIAA/ASME/SAE/ASEE Joint Propulsion Conference & Exhibit*, AIAA 2011-6064, San Diego, California, 31 July - 03 August 2011.

Wall, T., Nguyen, H., Subramanian, V., Mai-Viet, T., and Howley, P., “Direct Measurements of the Entrainment by Single and Double Concentric Jets in the Regions of Transition and Flow Establishment,” *Transactions of the Institution of Chemical Engineers*, Vol. 58, 1980, pp. 237–241.

Wallesten, J., and Chomiak, J., “Investigation of Spark Position Effects in a Small Pre-Chamber on Ignition and Early Flame Propagation,” SAE Technical Paper 2000-01-2839, 2000.

Walraven, F., “Operational Behavior of a Pressure Wave Machine with Constant Volume Combustion,” Asea Brown Boveri, Technical Report CHCRC 94-10, 1994.

Weber, R., “A Pressure-Wave Machine with Integrated Constant-Volume Combustion,” Swiss Energy Research Report 1977–1997, National Foundation of Energy Research, Switzerland, Project No. 426, 1997, pp. 142–153.

Westbrook, C. K., and Dryer, F. L., “Chemical Kinetic Modeling of Hydrocarbon Combustion,” *Progress in Energy and Combustion Science*, Vol. 10. No. 1, 1984, pp. 1-57.

Wijeyakulasuriya, S. D., Nalim, M. R., “Multidimensional Modeling of Gas Mixing in Transient Translating Confined Turbulent Jets,” *49th AIAA Aerospace Sciences Meeting*, Orlando, FL, 4-7 January 2011.

Wijeyakulasuriya, S. D., Perera, U. I., and Nalim, M. R., “Mixing and Ignition Potential of a Transient Confined Turbulent Jet in a Wave Rotor Constant Volume Combustor,” *46th AIAA/ASME/SAE/ASEE Joint Propulsion Conference and Exhibit*, Nashville, TN, 25-28 July 2010.

Wijeyakulasuriya, S. D., Perera, U. I., Nalim, M. R., "Mixing and Ignition Potential of Transient Confined Turbulent Jet in a Wave Rotor Combustor," *46th AIAA/ASME/SAE/ASEE Joint Propulsion Conference & Exhibit*, Nashville, TN, 25-28 July 2010.

Wijeyakulasuriya, S.D., Nalim, M.R., "Gas Injection Strategies in Confined Subsonic Cross-flow for Wave Rotor Fueling," AIAA 2008-4867, *44th AIAA/ASME/SAE/ASEE Joint Propulsion Conference & Exhibit*, Hartford, CT, July 2008.

Wijeyakulasuriya, S.D., Nalim, M.R., "Transient Translating Gas Jets in Confined Channels," AIAA 2009-4987, *45th AIAA/ASME/SAE/ASEE Joint Propulsion Conference & Exhibit*, Denver, CO, 2-5 August 2009.

Wijeyakulasuriya, S.D., Nalim, M.R., "Transient Translating Gas Jets in Confined Channels," AIAA 2009-4987, *45th AIAA/ASME/SAE/ASEE Joint Propulsion Conference & Exhibit*, Denver, CO, 2-5 August 2009.

Wilcox, D. C., "Reassessment of the Scale Determining Equation for Advanced Turbulence Models," *AIAA Journal*, Vol. 26, No. 11, 1988, pp. 1299–1310.

Wilcox, D. C., and Alber, I. E., "A Turbulence Model for High Speed Flows," *Proceedings of the 1972 Heat Transfer and Fluid Mechanics Institute*, Stanford Univ. Press, Stanford, CA, 1972, pp. 231–252.

Wilcox, D. C., *Turbulence Modeling for CFD*, 2nd ed., DCW Industries, Inc., La Cañada, CA, 1998.

Witze, P. O., and Dwyer, H. A., "The Turbulent Radial Jet," *Journal of Fluid Mechanics*, Vol. 75, No. 3, 1976, pp. 401-417.

Wolfhard, H. G., "The Ignition of Combustible Mixtures by Hot Gases," *Jet Propulsion*, December 1958, pp. 798-804.

Würmel, J., Silke, E. J., Curran, H. J., Ó Conaire, M. S., and Simmie, J. M., "The Effect of Diluent Gases on Ignition Delay Times in the Shock Tube and in the Rapid Compression Machine," *Combustion and Flame*, Vol. 151, No. 1-2, October 2007, pp. 289-302.

Yamaguchi, S., Ohiwa, N., and Hasegawa, T., "Ignition and Burning in a Divided Chamber Bomb," *Combustion and Flame*, Vol. 59, 1985, pp. 177-187.

VITA

VITA

Education**Doctor of Philosophy in Mechanical Engineering**

Purdue University, West Lafayette, IN

GPA **3.81/4.0**

Jan. 2008 - Dec. 2011

*Thesis: Transient and traversing gas jet modeling for pressure-gain combustion applications***Master of Science in Mechanical Engineering**

Purdue University, Indianapolis, IN

GPA **3.91/4.0**

Aug. 2006 - Dec. 2007

*Thesis: Gas injection strategies in confined subsonic cross flow for wave rotor combustor fueling***Master of Science**

University of Moratuwa, Sri Lanka

Jan. 2005 - Nov. 2007

*Thesis: Multidimensional moving mesh simulation of scavenge process in a small two-stroke engine***Bachelor of Science in Mechanical Engineering**

University of Moratuwa, Sri Lanka

Dec. 2000 - Aug. 2004

Work Experience

- Research Engineer, Convergent Sciences, Inc. (August 2011 – Present)
- Research Associate, Turbo-machinery Lab, Department of Mechanical Engineering, Michigan State University (May 2011 – August 2011)
- Research Assistant, Combustion and Propulsion Research Lab, School of Mechanical Engineering, Purdue University, Indianapolis, IN (January 2010 – April 2011 and August 2006 – December 2007)
- Research Assistant, School of Mechanical Engineering, Purdue University, West Lafayette, IN (January 2008 – December 2009)
- Research Assistant, Department of Mechanical Engineering, University of Moratuwa, Sri Lanka (January 2005 – July 2006)

Awards & Honors

- Merit Award on research from National Science Foundation, Sri Lanka (2010)
- IUPUI Fellowship for PhD from Purdue School of Engineering & Technology (2008-2009)
- IUPUI Fellowship for MSME from Purdue School of Engineering & Technology (2006-2007)
- Multiple grants totaling over \$37K from agencies such as MURI and Rolls Royce (2007-2010)

PUBLICATIONS

PUBLICATIONS

Conference Papers with Refereed Extended Abstract

1. **Wijeyakulasuriya, S. D.**, Nalim, M. R., "Multidimensional Modeling of Gas Mixing in Transient Translating Confined Turbulent Jets," *49th AIAA Aerospace Sciences Meeting*, Orlando, FL, 4-7 January 2011
2. Perera, U. I., **Wijeyakulasuriya, S. D.**, Nalim, M. R., "Hot Jet Ignition Delay Time and Localization Analysis for Ethylene-Air," *49th AIAA Aerospace Sciences Meeting*, Orlando, FL, 4-7 January 2011
3. Elharis, T. M., **Wijeyakulasuriya, S. D.**, Nalim, M. R., "Analysis of Combustion and Energy Transfers in a Wave Rotor," *49th AIAA Aerospace Sciences Meeting*, Orlando, FL, 4-7 January 2011
4. **Wijeyakulasuriya, S. D.**, Perera, U. I., Nalim, M. R., "Mixing and Ignition Potential of Transient Confined Turbulent Jet in a Wave Rotor Combustor," *46th AIAA/ASME/SAE/ASEE Joint Propulsion Conference & Exhibit*, Nashville, TN, 25-28 July 2010
5. Matsutomi, Y., Meyer S. E., **Wijeyakulasuriya, S. D.**, Izzy, Z., Nalim, M. R., Shimo, M., Kowalkowski, M., Snyder, P. H., "Experimental Investigation on the Wave Rotor Combustor," *46th AIAA/ASME/SAE/ASEE Joint Propulsion Conference & Exhibit*, Nashville, TN, 25-28 July 2010
6. Elharis, T. M., **Wijeyakulasuriya, S. D.**, Nalim, M. R., Izzy, Z., "Wave Rotor Combustor Aero-thermodynamic Design and Model Validation based on Initial Testing," *46th AIAA/ASME/SAE/ASEE Joint Propulsion Conference & Exhibit*, Nashville, TN, 25-28 July 2010
7. Bouzada, B. E., **Wijeyakulasuriya, S. D.**, Nalim, M. R., "Improved compressible jet shear layer modeling using RANS models for confined and impinging jets," *40th Fluid Dynamics Conference and Exhibit*, Chicago, IL, June 2010.
8. **Wijeyakulasuriya, S.D.**, Nalim, M.R., "Transient Translating Gas Jets in Confined Channels," AIAA 2009-4987, *45th AIAA/ASME/SAE/ASEE Joint Propulsion Conference & Exhibit*, Denver, CO, 2-5 August 2009.
9. **Wijeyakulasuriya, S.D.**, Nalim, M.R., "Gas Injection Strategies in Confined Subsonic Cross-flow for Wave Rotor Fueling," AIAA 2008-4867, *44th AIAA/ASME/SAE/ASEE Joint Propulsion Conference & Exhibit*, Hartford, CT, July 2008.
10. Akbari, P., Nalim, M.R., **Wijeyakulasuriya, S.D.**, Muller, N., "Wave Disk Engine for Micro-Scale Power Generation," AIAA 2008-4879, *44th AIAA/ASME/SAE/ASEE Joint Propulsion Conference & Exhibit*, Hartford, CT, July 2008.
11. **Wijeyakulasuriya, S.D.**, Nalim, M.R., "Simulation of Scavenging in a Small Two-Stroke Gasoline Engine Typical in South Asia," SAE 07APAC-113, 14th Asia Pacific Automotive Engineering Conference (APAC-14), Hollywood, CA, Aug 2007.

12. **Wijeyakulasuriya, S. D.**, Elharis, T. M., and Nalim, M. R., “Effect of Mixture Nonuniformity on Hot-Jet Ignition in a Wave Rotor Combustor,” *47th AIAA/ASME/SAE/ASEE Joint Propulsion Conference & Exhibit*, San Diego, CA, Jul 2011.
13. Elharis, T. M., **Wijeyakulasuriya, S. D.**, and Nalim, M. R., “Two-Step Modeling of Stratified Charge Combustion in a Wave Rotor Combustor,” *47th AIAA/ASME/SAE/ASEE Joint Propulsion Conference & Exhibit*, San Diego, CA, Jul 2011.
14. Snyder, P. H., Elharis, T. M., **Wijeyakulasuriya, S. D.**, Nalim, M. R., Matsutomi, Y., and Meyer, S. E., “Pressure Gain Combustor Component Viability Assessment Based on Initial Testing ,” *47th AIAA/ASME/SAE/ASEE Joint Propulsion Conference & Exhibit*, San Diego, CA, Jul 2011.
15. Pierluissi, A., Pierluissi, A. F., **Wijeyakulasuriya, S. D.**, Zhu, L., “Multi-dimensional one-way FSI Modeling of a Notional Multi-Lobed Mixer,” *47th AIAA/ASME/SAE/ASEE Joint Propulsion Conference & Exhibit*, San Diego, CA, Jul 2011.

Journal Articles in Review

1. Elharis, T. M., **Wijeyakulasuriya, S. D.**, Nalim, M. R., “Wave Rotor Combustor Aerothermodynamic Design and Model Validation based on Initial Testing,” *Journal of Propulsion and Power*, in review, 2011.

Theses

1. **Wijeyakulasuriya, S. D.**, “Transient and Traversing Gas Jet Modeling for Pressure-gain Combustion Applications,” Ph.D. thesis, December 2011.
2. **Wijeyakulasuriya, S.D.**, “Gas Injection Strategies in Confined Subsonic Cross Flow for Wave Rotor Fueling,” MSME thesis, School of Mechanical Engineering, Purdue School of Engineering and technology, Indianapolis, December 2007.
3. **Wijeyakulasuriya, S.D.**, “Multidimensional Moving Mesh Simulation of Scavenge Process in a Small Two-Stroke Engine,” MSc thesis, Department of Mechanical Engineering, University of Moratuwa, Sri Lanka, November 2007.

Non-Refereed Conference Abstracts

1. **Wijeyakulasuriya S. D.** and M.R. Nalim “Multi-Dimensional Moving Grid Simulation of Scavenging in a Small Two-Stroke Gasoline Engine Typical in South Asia,” University of Moratuwa Engineering Research Unit Symposium, Oct 2007.